ISSN 2458-973X

JSCMT

Journal of Sustainable Construction Materials and Technologies

Volume 9
Number 4
Year 2024

YTU PRESS

www.jscmt.yildiz.edu.tr

ISSN 2458-973X

JSCMT

Journal of
Sustainable Construction
Materials and Technologies

Volume 9 Number 4 Year 2024

HONORARY EDITORIAL ADVISORY BOARD

Tarun R. Naik, *University of Wisconsin-Milwaukee, Center for By-Products, USA*

EDITOR-IN-CHIEF

Orhan Canpolat, *Yıldız Technical University, İstanbul, Türkiye*

CO-EDITORS

Rakesh Kumar, *Central Road Research Institute, New Delhi, India*

Benchaa Benabed, *Université Amar Telidji Laghouat, Algeria*

LANGUAGE EDITORS

Muhammed Bayram, *Texas State University***,** *USA*

Ömer Faruk Kuranli, *Yıldız Technical University, Türkiye*

ASSISTANT EDITOR

Ekin Paylan, *Kare Publishing, Türkiye*

EDITORIAL BOARD

Togay Ozbakkaloglu, *College of Science and Engineering Ingram School of Engineering Texas State University, TX, United States;* ***Messaoud Saidani,*** *Associate Head of School, School of Energy, Construction and Environment, Coventry University, UK;* ***Xiaojian Gao,*** *Harbin Institute of Technology, HIT · School of Civil Engineering, China;* ***Muammer Koç,*** *Hamad bin Khalifa University, Sustainable Development College of Science and Engineering (HBKU), Qatar;* ***Mustafa Şahmaran,*** *Hacettepe University, Engineering Faculty Civil Engineering Department, Türkiye;* ***Sudharshan N. Raman,*** *Monash University Malaysia, Civil Engineering Discipline, School of Engineering, Malaysia;* ***Roman Rabenseifer,*** *Slovak University of Technology, Department of Building Construction, Faculty of Civil Engineering, Bratislava, Slovakia;* ***Shengwen Tang,*** *Wuhan University, School of Water Resources and Hydropower Engineering, China;* ***Soofia Tahira Elias Özkan,*** *Middle East Technical University, Department of Architecture, Türkiye;* ***Manuel F. M. Costa,*** *Centre of Physics of Minho and Porto Universities, University of Minho, Portugal;* ***Ali Naji Attiyah,*** *University of Kufa, College of Engineering – Department of Civil Engineering, Iraq;* ***Murat Ateş,*** *Tekirdağ Namık Kemal University, Department of Chemistry, Faculty of Arts and Sciences, Türkiye;* ***Ghazi Al-Khateeb,*** *Jordan University of Science and Technology, Depatment of Civil Engineering, College of Engineering, Jordan;* ***Huachao Yang,*** *College of Energy Engineering, Zhejiang University, Hangzhou, China;* ***Sepanta Naimi,*** *Altinbas University, Department of Civil Engineering, Türkiye;* ***Siyu Ren,*** *Nankai University, School of Economics, China*

ISSN 2458-973X

JSCMT
Journal of Sustainable Construction Materials and Technologies

Volume 9 Number 4 Year 2024

CONTENTS

Research Articles

J Sustain Const Mater Technol, Vol. 9, Issue. 4, pp. 305–314, December 2024

Journal of Sustainable Construction Materials and Technologies
Web page info: https://jscmt.yildiz.edu.tr
DOI: 10.47481/jscmt.1607459

Research Article

Sustainability evaluation of highway sign support by field testing and finite element analysis

Talat SALAMA*, Drew VOGHEL

Department of Manufacturing and Construction Management, Central Connecticut State University, New Britain, USA

ARTICLE INFO

Article history
Received: 24 March 2024
Revised: 24 November 2024
Accepted: 05 December 2024

Key words:
Highway sign supports, finite element analysis, field test

ABSTRACT

The primary objective of this study is to evaluate the sustainability of highway sign supports through field testing and finite element analysis. The study aims to develop a predictive maintenance model to evaluate the service life of these structures. Sign support systems are important structures in the Connecticut Department of Transportation (CTDOT) bridge management system. Periodic sustainability inspections and maintenance activities are needed as a long-term, cost-effective maintenance strategy. The research involved non-destructive field testing of a cantilever-type highway sign support, followed by finite element modeling using Highway Sign Structures Engineering (HSE) by SAFI software. Data from accelerometers, strain gauges, and anemometers were collected and analyzed to validate the model. The experimental setup was done in collaboration with CTDOT. The data was collected and analyzed, and it was used to verify the three-dimensional finite element (FE) model developed, which was used to test the structure's design capacity. The study found that the sign support structure experienced significant wind loading on a few occasions, with stress levels reaching about 20% of its elastic limit. The finite element model accurately predicted structural behavior under design load conditions, demonstrating its potential for predictive maintenance applications.

Cite this article as: Salama, T., & Voghel, D. (2024). Sustainability evaluation of highway sign support by field testing and finite element analysis. *J Sustain Const Mater Technol*, 9(4), 305–314.

1. INTRODUCTION

This research performed a non-destructive field test of a highway sign support to develop a finite element model simulating the structure for behavior analysis due to limited state loads. The advancements in sensor technology and data analysis have provided new opportunities for real-time monitoring and predictive maintenance of these structures. The experimental setup was in collaboration with the Connecticut Department of Transportation (CTDOT), where the project focused on field instrumentation and testing of a highway sign support that was a cantilever-type structure. The data was collected and analyzed, and it was used to verify the three-dimensional finite element (FE) model developed, which was used to test the structure's design capacity. The research shows the potential to increase the service life of sign support structures, which is currently set at 34 years.

An event occurred on I-190 SB in Worcester, Massachusetts, that underscores the importance of this project. On August 9th, 2022, a cantilevered sign support collapsed on the roadway, obstructing the low-speed and middle lanes (Fig. 1). Thankfully, no motorists were injured, and the Massachusetts Department of Transportation (MassDOT) had the road cleared the following day [1]. Still, such an incident illustrates the potential risk associated with these structures and what can happen if they are not regularly maintained.

***Corresponding author.**
*E-mail address: talats@ccsu.edu

Published by Yıldız Technical University Press, İstanbul, Türkiye

Figure 1. Collapsed sign support.

This and other similar instances highlight the need for improved maintenance and monitoring of highway sign supports. A Federal Highway Administration (FHWA) study reported that poorly maintained sign supports can become hazardous, especially when vehicles strike [2]. The study underscores the importance of regular inspections and preventive maintenance to ensure the structural integrity of these supports. The study published guidelines emphasizing the critical role of maintenance in preventing accidents caused by damaged or missing signs. These guidelines recommend regular cleaning, vegetation control, and timely repairs to maintain the effectiveness and safety of highway sign supports [2].

Recent studies have shown that regular maintenance and inspection can significantly extend the service life of highway sign supports. For instance, a survey by Tuhin highlighted the importance of structural integrity and regular inspections to prevent failures [3]. Another study by Patel (2024) discussed the design improvements and maintenance strategies for highway sign supports to enhance their durability [4].

The American Association of State Highway and Transportation Officials (AASHTO) has also updated its guidelines for the structural supports of highway signs, luminaires, and traffic signals, emphasizing regular maintenance and advanced materials [5]. These updates reflect the latest research and technological advancements in the field, providing a more robust framework for maintaining highway sign support.

A survey focusing on asset management, design process, inspection frequency, material usage, and failure types was drafted and circulated to all the Departments of Transportation (DOTs) to investigate sign support structures effectively. Data from each response was recorded, organized, and interpreted to assess the common issues affecting sign support structures and the effective management practices of these structures. The first step in the development process of the survey was to assemble and review current practice, technical literature, research findings of recently completed and ongoing projects, and procedures and codes addressing highway sign support on deterioration models, asset management, evaluation, and testing. The review focused on recent sign support risk assessment and field-testing developments.

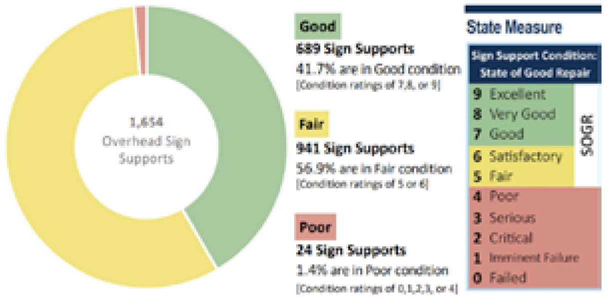

Figure 2. CTDOT Sign support inventory with performance scale.

Documents published by state DOTs standardizing elements of their sign support assets are evidence of sound asset management. Several DOTs have published Transportation Asset Management Plans (TAMPs) to secure federal funds and comply with federal legislation, specifically the Moving Ahead for Progress in the 21st Century (MAP-21) Act and the Fixing America's Surface Transportation (FAST) Act [6]. Responsible for approximately 1,654 sign supports, CTDOT has established performance measures (Fig. 2) and maintenance programs to manage sign support assets better. Supports with a score of 0 have failed; a score of 9 indicates that the support is in excellent condition. Assets receiving scores between 5 and 9 are said to be in a State of Good Repair (SOGR).

The NCHRP Report, 494 Structural Supports for Highway Signs, Luminaries, and Traffic Signals, includes a section discussing inspection, retrofit, repair, and rehabilitation of fatigue-damaged support structures. The Federal Highway Association (FHWA) assesses support as reasonable and fair but is a poor system. Recent data suggests that 41.7% are in good condition, 56.9% are in fair condition, and 1.4% are in poor condition [7]. CTDOT's TAMP combines each rating system so that sign supports in good condition correspond to scores 9-7, sign supports in fair condition correspond to scores 6 and 5, and sign supports in poor condition correspond to scores 4-0 [6].

The sign supports maintained by CTDOT are categorized by type, where 643 are cantilevered, 617 are entire spans, and 394 are bridge-mounted [6]. A fourth type is the butterfly support. The kind of support determines the inspection interval, where full-span supports are inspected every 6 years, and the cantilever and the bridge-mounted supports are inspected every 4 years. If a support is fabricated out of aluminum, it shall be inspected every two years, no matter the type of support [8].

A clearly defined maintenance schedule and an organized method for logging inspection data are crucial to asset management. Other DOTs have implemented standardized documents, defining installation and inspection methods, signing support selection criteria, and repairing manuals [9]. The Wisconsin Department of Transportation (WisDOT) has published a table of available sign support types and selection criteria for each support [9]. WisDOT also has a chapter in its Facilities Development Manual dedicated to standardized sign support structure designs and selection processes [10]. These standardized designs help contractors fabricate a reliable sign support structure without redesigning the whole structure every time a job comes out to bid. Also included on WisDOT's website is a list of Load and Resistance Factor Design (LRFD) Standardized Overhead Sign Structure Plans [11]. Nebraska Department of Roads (NDOR) published a complete inspection and installation manual for sign supports and high mast lighting [12]. NDOR's manual includes pictures of best practices concerning torquing, anchor bolt plumpness, plate connection tolerances, corrosion prevention, and other necessary installation and inspection considerations. Michigan Department of Transportation is the only state DOT that has published a repair manual for sign support structures, indicating that most DOTs would replace the whole structure entirely rather than make repairs [12]. A supplemental literature review was also conducted on fatigue stresses, as these forces are attributed to most sign support structure failures [13].

Life cycle planning is driven by one underlying principle: timely investments in an asset result in improved condition over a more extended period and lower long-term cost. CTDOT uses age-based deterioration curves based on a 34-year service life to execute life cycle planning. The condition-based models need more development to be successfully implemented, so the age-based approach is strictly adhered to. Once a sign support has reached the end of its 34-year service life, they are replaced. If an age-based modeling approach is being used, it is essential to have a database documenting how old the assets are. According to the Minnesota Department of Transportation data, 73% of its overhead sign support structures are between 0 and 40 years old [14], which backs up CTDOT's 34-year service life expectancy claim.

Setting long-term performance goals and proper life cycle planning assists in scheduling sign support replacement and repair. CTDOT's TAMP outlines some performance targets for sign support management. In 2019, it was projected that 96.6% of sign supports would be in an SOGR by the end of 2020, and 95.2% of sign supports would be in a SOGR by the end of 2022. A 10-year goal was also established by CTDOT's TAMP, which set out to achieve a SOGR for 90% of sign supports. The decrease in the percentage of sign supports in an SOGR around 2026 is due to a large number of supports reaching their life expectancy simultaneously (Fig. 3). CTDOT's TAMP maintains that funding for sign supports will be approximately $4 million per year, with the replacement of 40% of sign supports in poor condition funded by other projects. It is noteworthy that 100% of the funds in the sign support budget go towards replacement. Perhaps allocating some of those funds towards repair could be more economical.

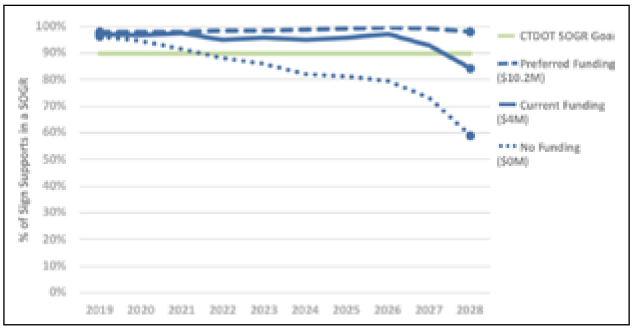

Figure 3. CTDOT Sign support performance projections.

CTDOT estimates that it costs $140,000 to replace a cantilever support, $250,000 to replace a full-span support, and $50,000 to replace a bridge-mounted support [2]. Since these assets are not cheap, selecting those that need replacement the most is crucial. While common sense would say those supports scoring lowest on the SOGR scale will be replaced first, replacement criteria are not entirely condition-based. Sign supports are often replaced because the sign panel size increases due to changes in FHWA's Manual on Uniform Traffic Control Devices (MUTCD) for Streets and Highways requirements. A bigger sign panel requires support stronger than the existing support. Sometimes, projects that alter the roadway can lead to the replacement of excellent support. Other times, sign support projects are issued by location, so every sign support along the designated corridor will be replaced regardless of its condition. These non-condition-based replacements create the potential for waste and excess cost, resulting in economic loss.

To combat the adverse effects of non-condition-based replacements, CTDOT's TAMP outlines five investment strategies: (1) Program sign support projects based on poor conditions, (2) Reduce the number of sign supports by putting signs next to the road whenever possible, (3) Increase efforts to maintain the sign panel size by decrease the sign legend spacing, (4) Overdesign sign supports with an augmented factor of safety so they can support next-generation sign panels, and (5) Reduce the number of bridge mounted sign supports to decrease dead load supported by the bridge and lower inspection costs.

Failure rates of sign support systems are scarce. Each study for the project showed that significant structure collapse occurs infrequently and can be avoided with preventative analysis and a predictive failure model. Sign support asset management is a topic that has not been extensively studied [15]. However, developing predictive deterioration models for sign support systems is feasible by identifying key factors such as materials, age, location, and wind loading. As cars and trucks pass under signs, the wind gradually wears off them on the sign supports.

Specifically, the supports' welded joints are the primary degradation point. Failure analysis of the highway sign structure and design improvement showed that hairline fractures occur due to wind loads. Kipp et al. [16] also revealed that analyzing the structures under various wind loads is more practical than a pure static load, as varying wind speeds can cause more damage to structures over time. The study attempted to model

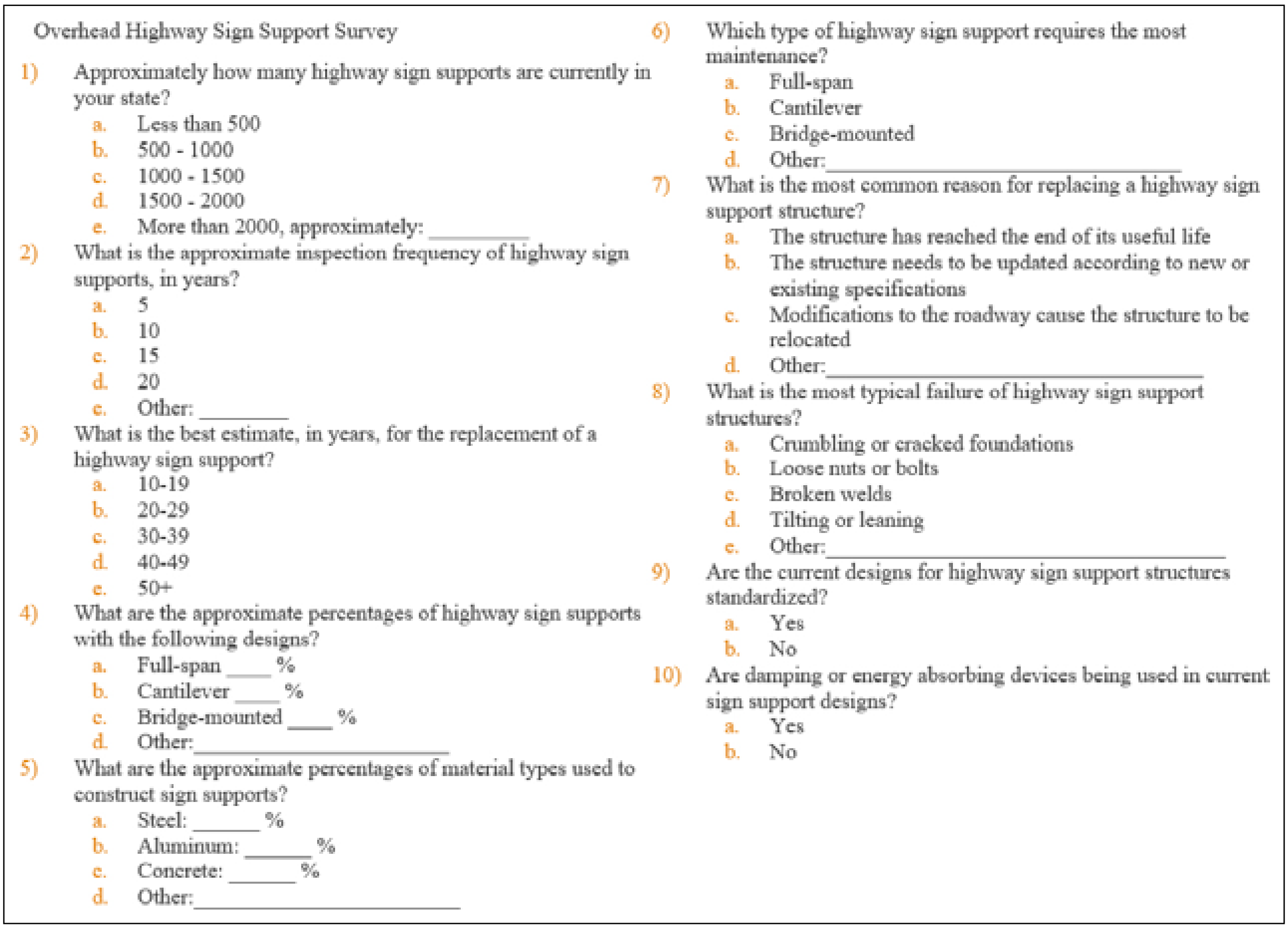

Overhead Highway Sign Support Survey

1) Approximately how many highway sign supports are currently in your state?
   a. Less than 500
   b. 500 - 1000
   c. 1000 - 1500
   d. 1500 - 2000
   e. More than 2000, approximately: __________
2) What is the approximate inspection frequency of highway sign supports, in years?
   a. 5
   b. 10
   c. 15
   d. 20
   e. Other: _________
3) What is the best estimate, in years, for the replacement of a highway sign support?
   a. 10-19
   b. 20-29
   c. 30-39
   d. 40-49
   e. 50+
4) What are the approximate percentages of highway sign supports with the following designs?
   a. Full-span ____ %
   b. Cantilever ____ %
   c. Bridge-mounted ____ %
   d. Other:_______________________
5) What are the approximate percentages of material types used to construct sign supports?
   a. Steel: ______ %
   b. Aluminum: ______ %
   c. Concrete: ______ %
   d. Other:_______________________
6) Which type of highway sign support requires the most maintenance?
   a. Full-span
   b. Cantilever
   c. Bridge-mounted
   d. Other:_______________________________
7) What is the most common reason for replacing a highway sign support structure?
   a. The structure has reached the end of its useful life
   b. The structure needs to be updated according to new or existing specifications
   c. Modifications to the roadway cause the structure to be relocated
   d. Other:_______________________________
8) What is the most typical failure of highway sign support structures?
   a. Crumbling or cracked foundations
   b. Loose nuts or bolts
   c. Broken welds
   d. Tilting or leaning
   e. Other:_______________________________
9) Are the current designs for highway sign support structures standardized?
   a. Yes
   b. No
10) Are damping or energy absorbing devices being used in current sign support designs?
   a. Yes
   b. No

Figure 4. Overhead highway sign support survey sent to the nation DOTs.

wind effects on different sign support systems and identify their weak points for future repair schedules. It was concluded that the two critical points in the structure were the midpoint of the span and the base of the columns. The probability of failure and reliability of the curves should depend on the lanes and the average daily traffic under each structure. This study also validated using predictive computer modeling for measuring sign support wind degradation.

Looking more at the types of sign supports specifically, field testing and analysis of aluminum highway sign trusses looked at how existing designs can be modeled to increase their wind load capacity. The study by Barle et al. [17] showed this to be the case by examining cantilever-type and Type-III overhead sign supports. The conclusion was that increasing the drag coefficient on these structures could reduce the wind load. By analyzing these, we can see that minor modifications to sign supports have a significant impact.

Different types of sign supports have varying tolerances for wind capacity and respond differently to stresses. Two studies support this conclusion: by Yang et al. [18] and by Ehsani et al. [19]. These two papers conclude that monotubes rely on stiffness for reliability rather than strength criteria, while the opposite is true for box truss structures. Therefore, the type of sign support affects reliability if all other factors are equal.

The idea of conducting regular inspections of aging models can identify problems before they occur. Al Shboul et al. [20] analyzed predictive failure models and showed that simulating wind speeds can comprehensively approach predictive failure. This work supports the findings of Barle et al. [17], who concluded that variable wind speeds cause more wear and tear than static wind speeds. The conclusions drawn by Al Shboul et al. [20] were used to detect two severe fractures in signs that would have otherwise gone unnoticed. This discovery was due to new inspection practices [21]. While the study is more technical, the hypothesis suggests that wind is among the highest risk factors for sign support degradation, primarily caused by passing traffic underneath.

Reviewing related peer literature and their methods reinforces the study's validity. Two key research publications on the topic are "Road Asset Management Systems" by Miller et al. [22] and "Analysis of Traffic Sign Asset Management Scenarios" by Harris et al. [23]. These two publications provided the basis for the approach to asset management and categorization. Kruse et al. [24] demonstrated how asset management using technology such as GIS information can be effective. Their study supports the subsequent research, highlighting the advantages of using advanced software to monitor assets. Combined with a predictive failure model, this can result in a more efficient maintenance plan.

2. METHODOLOGY

2.1. Survey

Studying the existing literature on sign support management and structural analysis facilitated sound project design. A survey focusing on asset management, design process, inspection frequency, material usage, and failure types was drafted and circulated to all DOTs to investigate sign support structures effectively. Each step, from writing the survey to sensor installation and data treatment, required us to draw upon knowledge from articles discussing fatigue stress, reports covering inspection procedures, and drawings standardizing sign support design. After sufficient literature review, the survey was drafted (Fig. 4) and distributed to all the United States Departments of Transportation. Data from each response was recorded, organized, and interpreted to assess the common issues affecting sign support structures and the effective management practices of these structures.

Survey circulation was conducted by contacting three to five individuals from each State DOT affiliated with a traffic engineering division, a structures division, or a maintenance division. Because sign supports are often considered an ancillary asset, they usually fall under the jurisdiction of the previously mentioned divisions. Any trends relating to material usage, inspection techniques, design considerations, and failure modes were identified.

The response rate was 46%, and graphical representations were constructed to show specific trends in the data. The scatterplot (Fig. 5) plots inspection frequency against the number of sign support structures. Each data point on the scatterplot represents a DOT who participated in the survey. The y-axis represents the years passed between inspections, and the x-axis represents the number of sign support structures a given DOT maintains. A linear regression was used to graph a line that best fit the recorded data. Although the linear regression produces a relatively low R^2 value, it's important to note that a DOT with as many as 34 times the sign support structures performs inspections at a similar frequency.

The pie chart (Fig. 6) shows DOT estimates for sign support life expectancy. Each section of the pie chart constitutes a percentage of DOT response and corresponds to an approximate life expectancy. 72% of DOTs claim sign support structures can remain in service after 40 years, potentially underestimating the service life estimated in CTDOT's TAMP. Those DOTs reporting an estimated sign support service life expectancy greater than 50 years also commented on its response that repeated maintenance would be performed on the structures before programming a replacement. Other DOTs, however, reported that structures would be replaced before significant maintenance was required. Other notable findings reported in survey responses include: (1) 29% of DOTs reported that 25% to 48% of their sign supports were constructed of aluminum, while the other 71% reported over 93% of sign supports were constructed of steel, (2) a revision to an anchor bolt tightening procedure has reduced hardware section loss due to corrosion, (3) Inspections are being prioritized based on asset condition and location. Those structures in a worse condition which require more maintenance and structures located in areas exposed to adverse external factors (i.e., flood plains, snow belts) are being inspected at a higher frequency, and (4) Other DOTs report annual inspection of bridge-mounted sign supports indicating that these particular assets are high maintenance.

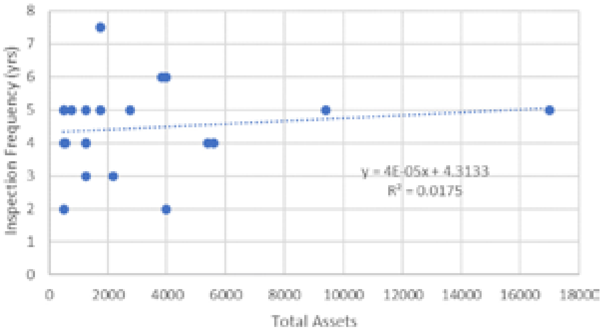

Figure 5. DOT Inspection frequency scatterplot.

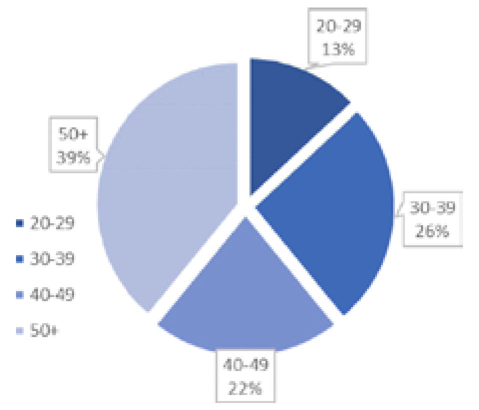

Figure 6. Sign support life expectancy pie chart.

After polling the United States DOTs, it is apparent that some DOTs are more diligent in managing assets beyond pavements and bridges, like sign supports, than others [9]. Reading through various Transportation Asset Management Plans published by different DOTs and analyzing survey responses has brought the most effective management strategies to the surface.

The current modeling approach utilized by CTDOT is an age-based approach rooted in the service life of the actual sign panel—not the sign support. After 17 years, the sign panel is due for a replacement. Once the sign panel is replaced twice, CTDOT determines that the sign support structure should also be replaced, resulting in a 34-year service life. The current age-based modeling approach may shorten the service life of sign support structures. The project's primary objective is to develop and verify condition-based models better. The condition-based models need more development to be successfully implemented, so the age-based approach is currently the only option. Once a sign support has reached the end of its 34-year service life, they are replaced. The experimental effort of this project is meant to provide the CTDOT with a condition-based model to consider adopting.

Figure 7. CTDOT Asset no. 21740.

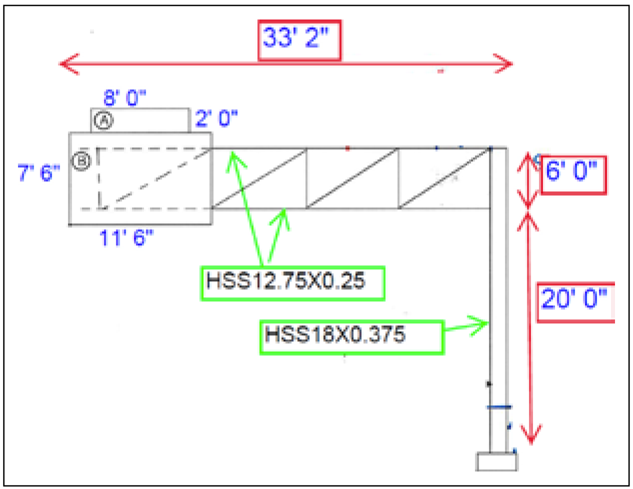

Figure 8. Dimensions schematic of sign support 21740.

2.2. Instrumentation and Field Test

The CTDOT bridge management and maintenance team coordinated the non-destructive condition assessment field test. This task evaluated the compiled database of sign supports in Connecticut and sorted the inventory to identify suitable candidates for equipment installation. The efforts were closely coordinated with CTDOT representatives, key stakeholders such as transportation enforcement and maintenance, and planning authorities.

In 2022, CTDOT sign support asset 21740, located over I-384 in Manchester, Connecticut, was chosen for the field test portion of the project (Fig. 7). The sign support type is a Truss Arm Cantilever made of steel. This task involved the use of a data acquisition system and instrumentation that included (1) Anemometers to obtain wind velocity and direction, (2) Accelerometers to obtain the acceleration response of the structure, and (3) Strain Gauges to measure the strain response of the structure. The accelerometer type has a 5g sensitivity option for dynamic structural testing in tough field conditions. Four strain gauges were installed at the base of the pole of the overhead sign support structure, four strain gauges at the top arm of the lattice structure holding the arm, and one accelerometer and one anemometer at the top arm. Figure 8 shows the dimensions schematic of the sign support. The equipment supplier field staff required one bucket truck provided by CTDOT for use during the installation day. The instruments remained connected to the structure for six months to collect data continuously.

Figure 9. Graph of the top strain gauges data for channel 1 - Up and down positions.

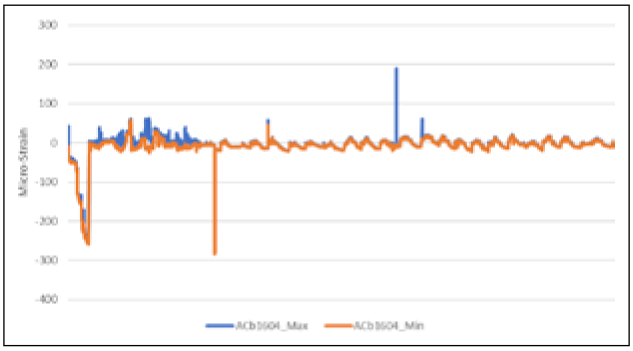

Figure 10. Graph of the top strain gauges data for channel 2 – East and west positions.

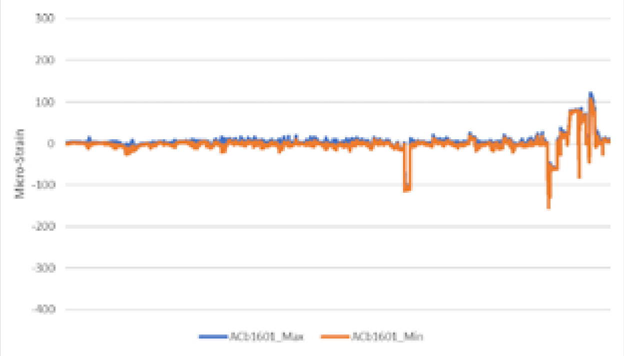

Figure 11. Graph of the bottom strain gauges data for channel 3 – North and south positions.

3. RESULTS AND DISCUSSION

3.1. Field Test Results

The instrumentation system was installed and active for six months, starting in November 2022. The data acquisition system (DAS) collected the data from the various sensors and saved it onto the system's hard drive. The drive was accessible remotely through a modem that transmitted the data online and made it available through a software application.

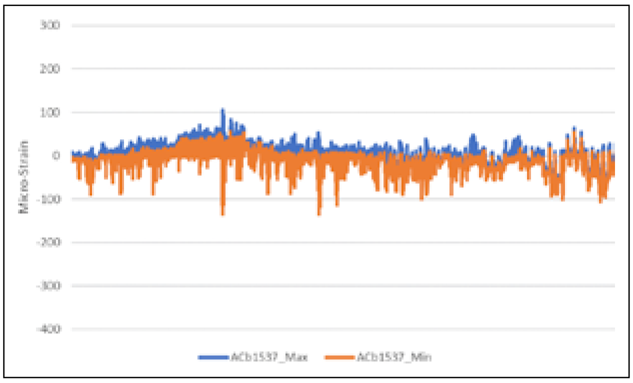

Figure 12. Graph of the bottom strain gauges data for channel 4 – East and west positions.

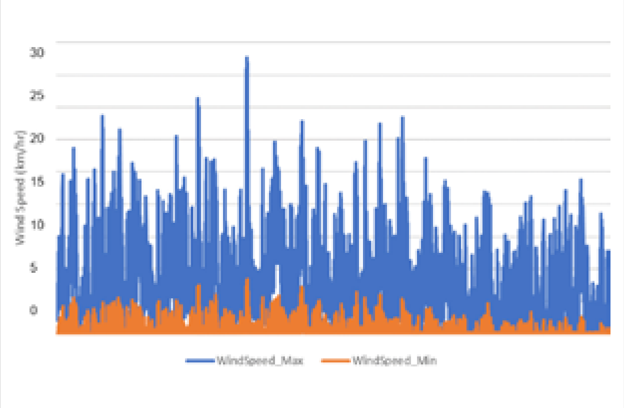

Figure 13. Graph of wind speed sensor.

Table 1. Experimental absolute maximum strain and stress values compared to yield limit

		Micro-strain	Ratio	Percentage	Stress MPa (ksi)
Strain limit		1,724			345 (50.0)
Top strain	Up-Down	386	0.224	22.4%	77 (11.2)
Top strain	East-West	281	0.163	16.3%	56 (8.2)
Bottom strain	North-South	155	0.090	9.0%	31 (4.5)
Bottom strain	East-West	133	0.077	7.7%	27 (3.9)

The following graphs, Figure 9, Figure 10, Figure 11, and Figure 12, provide the strain gauge data over time. Figure 13 presents the wind speed data over the same time frame.

The experimental results show that the top horizontal arm experienced higher strains than the bottom of the vertical pole. Further, the maximum strain was experienced only once and reached a value of 380 micro-strain. Otherwise, the strain range was between 50 micro-strain and 130 micro-strain.

Table 1 compares the experimental data and the yield limit, showing that the maximum strain reached after months of testing and exposure to wind load was only 22.4% of the elastic yield capacity of the structure. This indicates the strength and resilience of this sign support structure and that significant potential strength remains in the structure.

3.2. Finite Element Modeling and Verification

A finite element model (FEM) was developed to analyze the sign support that was field tested under various design loads as specified by the American Association of State Highway and Transportation Officials (AASHTO) – LRFD, titled 'Structural Supports for Highway Signs, Luminaires, and Traffic Signals (LTS),' [5]. This task focused on improving the reliability of methods for determining traffic loading on sign supports. The field data collected was utilized to build the FEM three-dimensional sign support structure using the software Highway Sign Structural Engineering (HSE), created by the Structural Engineering Software company SAFI.

Verifying the FE model with the experimental data provided the opportunity to understand better the behavior of the sign support and the loading influence. The model was developed, and the wind load applied was the average value of 28 km/hr (45 mph) obtained from the wind speed data. The limit state values (Fig. 14) show that the vertical pole has a value of 0.18 (18%) of the actual pole capacity, within a 10% difference compared to the experimental data. Similarly, the top horizontal cantilever arm has a limit state value of 0.10 (10%) of the capacity, which is, on average, about 8% less than the experimental data.

These results show that the model is accurate and can be used to predict the behavior of the sign support at complete design load capacity. The second model was then developed with the whole design load applied by the AASHTO LRFD-LTS code, which accounts for the wind load at the region where the sign support is, namely Hartford, Connecticut. The analysis results depend on including or excluding fatigue stress in the limit state load combinations. Fatigue has a significant impact on the results, as seen in Figure 15 and Figure 16. Fatigue stress is so substantial that some sections exceed their limit state.

The study's findings are based on a specific type of highway sign support structure (cantilever-type) and may not directly apply to other sign supports. The results may vary for different designs, materials, and environmental conditions. The finite element analysis model relies on certain simplified assumptions to make the problem workable. These assumptions include idealized material properties, boundary conditions, and load applications, which may not fully capture the complexities of real-world scenarios. The FEA model was validated using data from a single field test. While the model agreed well with the test data, further validation with additional field tests on different structures would strengthen the confidence in the model's predictions. Addressing these limitations in subsequent studies

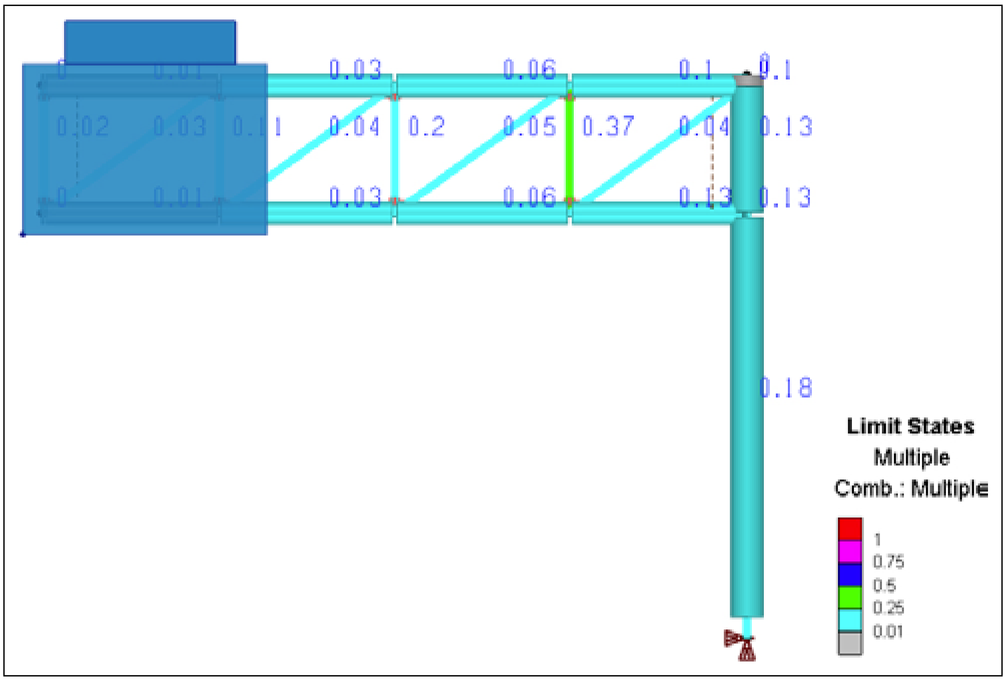

Figure 14. FE Model analysis due to wind load of 28 km/hr (45 mph) to simulate experimental data.

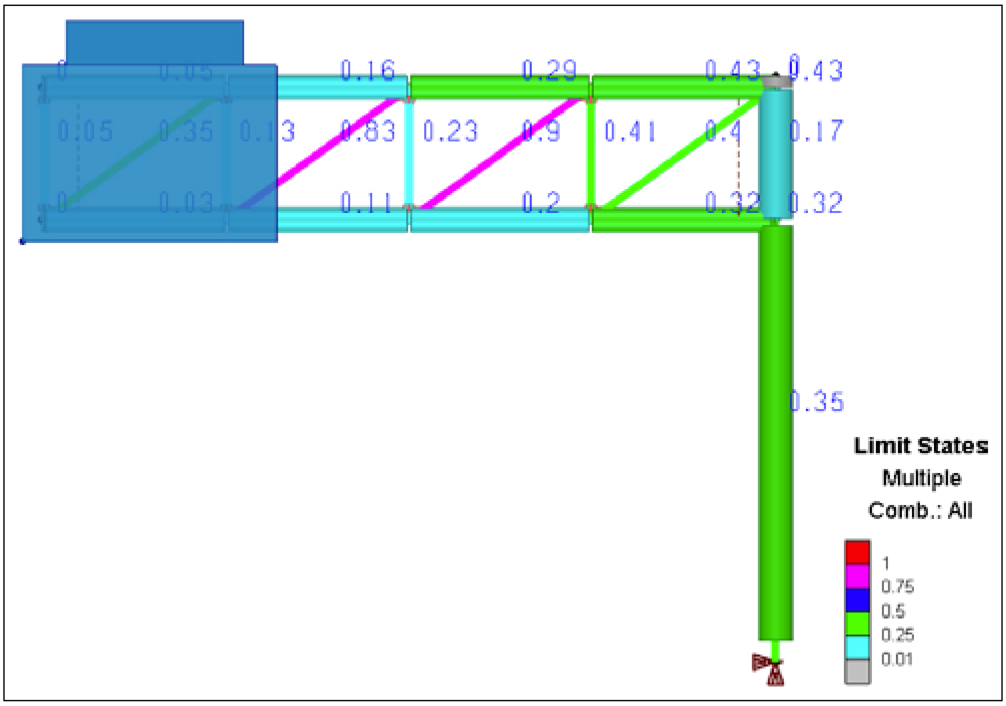

Figure 15. Limit states for all load combinations where results exclude fatigue.

will help to refine the models and improve the reliability of the findings, ultimately contributing to the development of more robust and sustainable highway sign support systems.

4. CONCLUSIONS

The research evaluated sign support management strategies, including repair manuals, Transportation Asset Management Plans, standardized drawings, and structure selection criteria. The researchers gathered and analyzed survey feedback from DOTs throughout the US. This effort initiated the second phase of the research work that involved the instrumentation and testing of a highway sign support structure.

The sustainability evaluation of highway sign support systems through field testing and finite element analysis has provided valuable insights into these critical infrastructure components' structural integrity and longevity. The study's findings underscore the importance of regular maintenance and inspection to ensure the safety and durability of high-

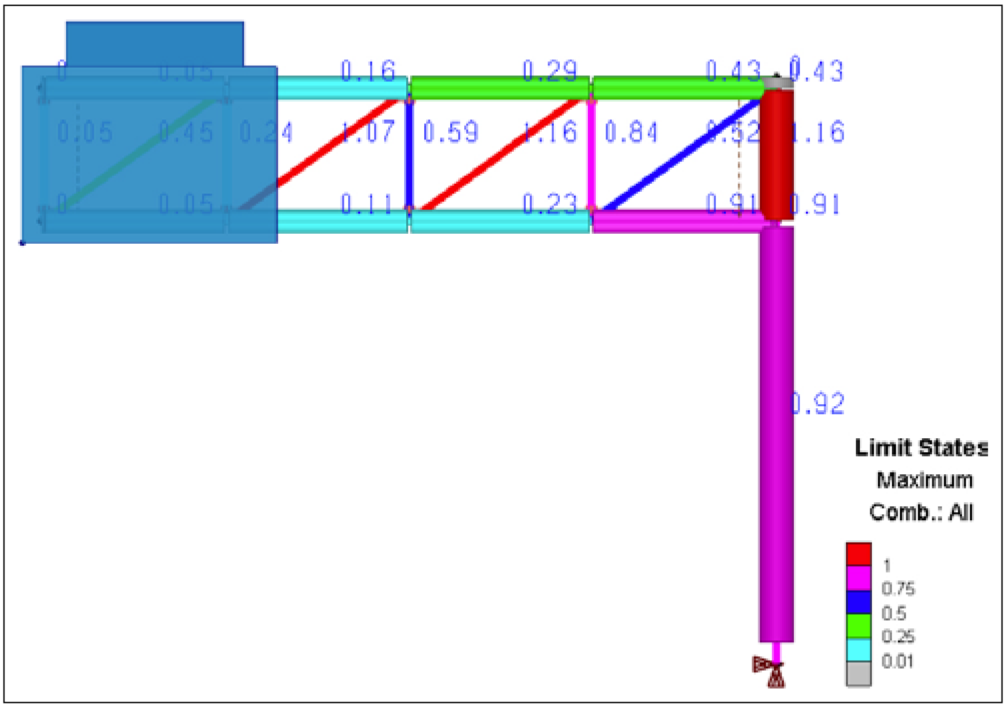

Figure 16. Limit states for all load combinations where results include fatigue.

way sign supports. The field testing in collaboration with the Connecticut Department of Transportation (CTDOT) revealed that the sign support's top horizontal arm experienced higher strains than the bottom of the vertical pole. The maximum strain recorded was 380 micro-strain, which is 22.4% of the elastic yield capacity of the structure. This data highlights the areas of the structure most susceptible to stress and potential failure, providing a basis for targeted maintenance efforts.

The finite element model was developed and verified using the field test data, which accurately predicted the behavior of the sign support under various loading conditions. The model demonstrated that the structure could reach its design capacity, mainly when considering fatigue loading. This finding suggests that the current design standards are adequate but could benefit from enhancements to address long-term fatigue stresses. The research emphasizes the need for a comprehensive asset management approach that includes regular inspections, timely maintenance, and advanced modeling techniques to predict and mitigate potential failures. By adopting these practices, transportation agencies can enhance the safety and reliability of highway sign supports, ultimately contributing to a more sustainable and resilient transportation infrastructure.

The study's recommendations for prioritizing repairs based on the condition and age of the sign support, designing structures to resist long-term fatigue stresses, and conducting further research on different types of sign supports are crucial for extending the service life of these structures. In conclusion, the study provides a robust framework for evaluating the sustainability of highway sign support systems. The combination of field testing and finite element analysis offers a powerful tool for understanding the behavior of these structures under various conditions and making informed decisions about their maintenance and design. Future research should continue to explore the application of these methods to other types of sign supports and to develop more refined models that can further enhance the safety and longevity of highway infrastructure.

ACKNOWLEDGMENTS

The authors wish to acknowledge the support of the Connecticut Department of Transportation in providing the funding used in this research, Grant # SPR-2323, for 2021. The authors also thank the CTDOT for their support and guidance throughout this effort.

ETHICS

There are no ethical issues with the publication of this manuscript.

DATA AVAILABILITY STATEMENT

The authors confirm that the data that supports the findings of this study are available within the article. Raw data that support the finding of this study are available from the corresponding author, upon reasonable request.

CONFLICT OF INTEREST

The authors declare that they have no conflict of interest.

USE OF AI FOR WRITING ASSISTANCE

Not declared.

PEER-REVIEW

Externally peer-reviewed.

REFERENCES

[1] Fortier, M. (2022). *Large highway sign falls right onto I-190 in Worcester*. https://www.nbcboston.com/news/local/large-highway-sign-falls-right-onto-i-190-in-worcester/2803359/

[2] McGee, H. W. (2010). *Maintenance of signs and sign supports: A guide for local highway and street maintenance personnel*. Office of Safety, Federal Highway Administration, U.S. Department of Transportation. Report No. FHWA-SA-09-025.

[3] Tuhin, I. A. (2020). Structural behavior of long span overhead sign support bridges. *Open J Civ Eng, 10*(1), 1-8. [CrossRef]

[4] Patel, P. P. (2024). Design of highway sign supporting structures with various structural systems. *Rec Dev Struct Eng, 4*, 349-357. [CrossRef]

[5] American Association of State Highway and Transportation Officials. (2022). *Interim revisions to the standard specifications for structural supports for highway signs, luminaires, and traffic signals, 6th ed.* LRFDLTS-1-I5.

[6] Connecticut Department of Transportation (CTDOT). (2022). *Highway transportation asset management*. https://portal.ct.gov/dot/bureaus/engineering-and-construction/project-administration/asset-management

[7] Federal Highway Administration. (2020). *Transportation asset management plans case study 7 - managing assets beyond pavements and bridges*. https://www.fhwa.dot.gov/asset/pubs/hif20067_case7.pdf

[8] Zaffetti, R. P. (2018). *Bridge Safety and Evaluation Bridge Safety Memo 2018-02 In-Depth Inspections*. Connecticut Department of Transportation Office of Engineering.

[9] Fouad, F. H., Davidson, J. S., Delatte, N., Calvert, E. A., Chen, S. E., Nunez, E. & Abdalla, R. (2003). *NCHRP Report 494 structural supports for highway signs, luminaries, and traffic signals*. Transportation Research Board.

[10] Wisconsin Department of Transportation. (2021). *Structural inspection manual: Ancillary structures - overhead sign structures and supports*. https://www.fhwa.dot.gov/bridge/pubs/nhi20999.pdf

[11] Wisconsin Department of Transportation. *LRFD standardized overhead sign structure plans*. https://wisconsindot.gov/Pages/doing-bus/eng-consultants/cnslt-rsrces/strct/standard-sign-plans.aspx

[12] Nebraska Department of Roads Materials and Research Division. (2008). *Inspection guide for the installation of high mast lighting and sign structures*. https://dot.nebraska.gov/media/maolwhfi/ndor-inspection-guide-for-installation-of-towers-and-signs.pdf

[13] Gilani, A., & Whittaker, A. (2000). Fatigue-life evaluation of steel post structures. I: Background and analysis. *J Struct Eng, 126*(3), 322-330. [CrossRef]

[14] Minnesota Department of Transportation. (2019). *Highway transportation asset management*. https://www.dot.state.mn.us/assetmanagement/tamp.html

[15] Hensing, D. J., & Rowshan, S. (2005). *Roadway safety hardware asset management systems case studies*. United States: Federal Highway Administration, Office of Safety Research and Development. No. FHWA-HRT-05-073.

[16] Kipp, M. A., Ehsani, M. R., & Bjorhovde, R. (1987). Field testing of highway sign support structures. *J Struct Eng, 113*(4), 850-863. [CrossRef]

[17] Barle, J., Grubisic, V., & Vlak, F. (2011). Failure analysis of the highway sign structure and the design improvement. Eng Fail Anal, 18(3), 1076-1084. [CrossRef]

[18] Yang, J., Culmo, M. P., & Dewolf, J. T. (2004). Stability analysis of truss type highway sign support structures. *Wind Struct, 7*(6), 393-404. [CrossRef]

[19] Ehsani, M. R., & Bjorhovde, R. (1988). Behavior of monotube highway sign support structures. *J Struct Eng, 114*(12), 2755-2772. [CrossRef]

[20] Al Shboul, K. W., Rasheed, H. A., & Alshareef, H. A. (2021). Intelligent approach for accurately predicting fatigue damage in overhead highway sign structures. *Structures, 34*, 3453-3463. [CrossRef]

[21] De Barros, R. C., & Paiva, F. (2018). Seismic and wind response control of cantilevered highway sign support using a TMD. In *2018 13th APCA International Conference on Automatic Control and Soft Computing (CONTROLO)* (pp. 368-373). IEEE. [CrossRef]

[22] Miller, S., Scott, P., Cooper, S., Brown, P., Ingram, P., & Chalmers, H. (2012). Road asset management systems. In *Proceedings of the IET & IAM Asset Management Conference*, London, UK. [CrossRef]

[23] Harris, E. A., Rasdorf, W., Hummer, J. E., & Yeom, C. (2007). Analysis of traffic sign asset management scenarios. *Transp Res Rec, 1993*(1), 9-15. [CrossRef]

[24] Kruse, B. K., & Simmer, T. (2003). *Asset management of roadway signs through advanced technology*. North Dakota State University.

J Sustain Const Mater Technol, Vol. 9, Issue. 4, pp. 315–326, December 2024

Journal of Sustainable Construction Materials and Technologies
Web page info: https://jscmt.yildiz.edu.tr
DOI: 10.47481/jscmt.1608347

Journal of Sustainable Construction Materials and Technologies

Research Article

Flexural behavior of sustainable high-strength RC beams with GGBS and iron filings incorporation

Sawsan Akram HASSAN[1], **Saif Luay ALTAI***[2]

[1]*Department of Civil Engineering, Mustansiriyah University, College of Engineering, Baghdad, Iraq*
[2]*University of Babylon, College of Engineering, Babylon, Iraq*

ARTICLE INFO

Article history
Received: 03 October 2024
Revised: 08 November 2024
Accepted: 01 December 2024

Key words:
Ground granulated blast furnace slag, high-strength concrete, iron filings, peak load, sustainability

ABSTRACT

This experimental study investigates the behavior of sustainable high-strength reinforced concrete (HSRC) beams when cement is partially replaced with ground granulated blast furnace slag (GGBS) and sand with iron filings (IF). Eight rectangular HSRC beams were experienced to four-point loading to examine the effects of these substitutions. The cement was replaced with GGBS at three percentages (10%, 30%, and 50%), with and without a 10% substitution of sand by IF. The results showed that substituting 30% GGBS caused a minor reduction in beam strength, while higher GGBS percentages (above 30%) led to a more significant decrease. However, adding 10% IF improved the beams' strength, demonstrating its potential as a reinforcing material. All beams exhibited similar failure patterns under peak loads. Similarly, the load-deflection behavior of all beams showed consistent patterns across different configurations. However, beams of an optimum replacement consisting of 30% GGBS and 10% IF can support larger values of load-carrying capacity, moment-resisting capacity, and energy absorption than those with other mixtures. The study shows that while GGBS could enhance sustainability, it should be judiciously adopted to maintain structural integrity. Contrariwise, IF shows excellent potential in improving the HSRC beams with improvement in sustainability. It tends to create a balance in material substitution to optimize performance and environmental impacts in concrete structures.

Cite this article as: Hassan, S. A., & Altai, S. L. (2024). Flexural behavior of sustainable high-strength RC beams with GGBS and iron filings incorporation. *J Sustain Const Mater Technol*, 9(4), 315–326.

1. INTRODUCTION

Applications of waste material in RC beams have been developed as a relatively new research area to increase construction sustainability and tackle some environmental problems originating from conventional concrete production. Past research has investigated various waste materials that can be partially used to substitute conventional aggregates or cement in RC beams. In this connection, the clean coal bottom ash and coal fly ash replacement of fine and coarse aggregates demonstrate higher ultimate load and deflection capacities for RC beams [1]. Similarly, researchers have also made attempts to utilize spent garnet as a replacement for fine aggregate, exhibiting enhanced material behavior and reduced failure under impact loads in RC beams [2]. In minor uses, ceramic waste powder tends to decrease environmental impacts and, with that, even CO_2 emissions in higher percentages, almost invariably affecting compressive strength and load-carrying capacity negatively [3]. Other wastes used in tests were granular plastic, crumbed

---

***Corresponding author.**
*E-mail address: eng.saif.hadi@uobabylon.edu.iq

Published by Yıldız Technical University Press, İstanbul, Türkiye

rubber, waste newspaper, and crushed bricks—all of which decreased compressive strength but are still possibly useful for minor structural uses [4, 5]. Recycled concrete aggregate has also shown some strength in maintaining and even improving the mechanical properties of RC beams, obtaining higher compressive strength compared to the ones using natural aggregates [6]. Waste glass and agricultural by-products like rice husk ash have also been applied; these materials give some advantages regarding ductility and sustainability [7, 8]. The addition of fibers, namely polypropylene glass fibers and waste aggregates, further developed the flexural capacity and ductility of the RC beams [9]. All these studies reflect the potentiality of waste materials for reducing environmental impacts and enhancing the RC beams' structural performance, thus promoting greener construction methodologies.

As industrial waste production rises, factory and mechanical plant byproducts are recognized for construction applications. One example is ground granulated blast furnace slag (GGBS), a by-product of blast furnaces in the steel and iron industries. Researchers have explored ways to reduce the environmental footprint of GGBS, enabling its use in concrete structures as a partial or complete replacement for traditional cement. Consequently, depending on the size of the concrete structure and the quantity of GGBS employed, a significant amount of this by-product can be removed from the environment, along with its economic advantages. The partial substitution of GGBS for cement substantially improves the strength of concrete in comparison to normal concrete [10–14]. The compressive strength of concrete rises with an increase in the proportion of GGBS up to a specific limit, i.e., the optimal substitution of GGBS, after which compressive strength diminishes [15–18]. The optimal substitution of GGBS was found to be 55%, according to [15], and [16] reported it to be 10%. However, [17] observed that GGBS exhibits no influence on the concrete strength up to a replacement level of 20%, after which the concrete strength declines. This manifestation is attributed to unreacted GGBS functioning as a filler material.

Furthermore, when utilized in place of some of the cement, GGBS slows down the hydration process, causing a decrease in the strength of the concrete [19]. The compressive strength of a concrete mixture containing cement, fine and coarse aggregates with partial replacement with GGBS, fly ash, and recycled aggregates demonstrates improved results compared to conventional concrete mixes [20]. The flexural behavior of RC beams and the ones with GGBS is comparable [21, 22]. However, the flexural strength of concrete with 60% GGBS content significantly increased compared to 0% GGBS. In comparison, a minor decrease was observed at 40% replacement, and a substantial decrease occurred at 80% replacement [23]. The characteristics of the beams without GGBS closely resemble those in which 70% of the cement is substituted with GGBS [24]. However, for beam specimens with GGBS of 90%, both stiffness and strength were lower than those without GGBS by 16% and 6%, respectively. In RC beams, GGBS as a complete replacement for cement was experimentally examined [25]. The ultimate load of RC beams with GGBS that failed in flexure was 83% of those without GGBS. Recent studies highlight that GGBS significantly enhances the sustainability performance, engineering properties, and life cycle assessment of high-strength self-compacting geopolymer concrete composites, making it an optimal choice for sustainable construction [26–33]. Experimental research has also shown that GGBS enhances the performance of previous concrete, particularly in terms of chloride resistance and sustainability benefits [34].

Iron filing (IF) is another by-product of the milling, filing, or grinding of finished iron products. Numerous studies have investigated replacing sand with fly ash, stone powder, and copper slag. IF is among the waste products that can effectively replace sand in concrete. Iron-containing waste materials were first explored for manufacturing heavy concrete in 2011 [35]. The compressive strength of concrete produced with IF as sand replacement exhibited a 3.5% increase for the 10% replacement level and a 13.5% increase for the 20% replacement level. However, at the 30% replacement level, there was a decrease of 8% [36]. The concrete achieved optimal strength with a 20% substitution of sand with IF and particles of waste glass[37]. The compressive and flexural strength decreased after replacing sand with IF by 20%, which was suggested to be the optimal amount for sand replacement with IF. The highest compressive strength of concrete can be attained with IF at 12%, after which it begins to decline [22]. A previous study [36] found that when sand is replaced with IF, the compressive strength overperforms by 30%. A considerable improvement in compressive strength was attained when the sand was entirely replaced with IF [38].

Previous studies have extensively explored the use of waste materials in RC beams to enhance sustainability and structural performance. However, there are notable gaps in understanding the optimal use of these materials. While materials like coal bottom ash, fly ash, spent garnet, and ceramic waste powder have been investigated, their effects on compressive strength at high replacement levels remain a concern, as they can lead to strength reductions. Using fibers such as polypropylene and glass has also improved flexural capacity and ductility. Still, the specific interactions between these fibers and other waste materials like GGBS and IF are not fully understood. GGBS is recognized as a viable cement substitute, with research indicating that a 55% replacement level optimizes concrete strength. However, too much GGBS can diminish strength, and the ideal balance for strength and sustainability remains unclear. Likewise, while IF has shown promise as a sand replacement, especially in boosting compressive strength, the long-term impacts and ideal replacement ratios to sustain structural integrity need further investigation.

This study seeks to bridge existing gaps by examining the combined influence of GGBS and IF on high-strength reinforced concrete (HSRC) beams, particularly their effects on flexural behavior, crack patterns, energy absorption, and overall structural performance. The research aims to offer deeper insights into the optimal use of these materials to enhance the sustainability and functionality of concrete structures.

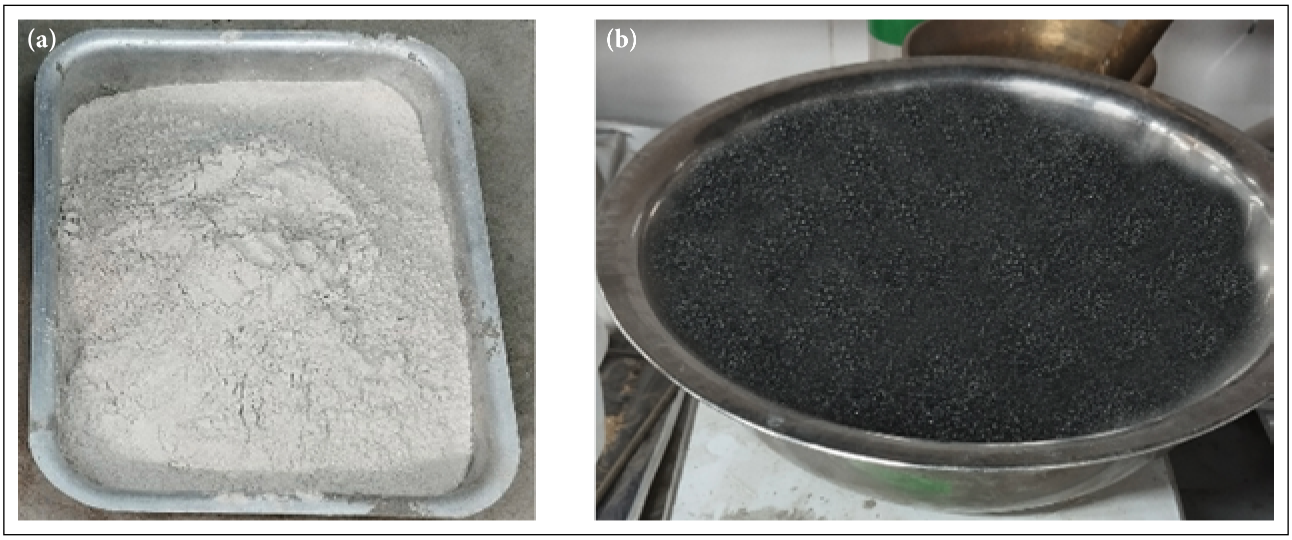

Figure 1. Materials used in the experiments. **(a)** GGBS, **(b)** IF.

Table 1. Materials used in the mixture of each specimen

Specimen ID*	Cement (kg/m^3)	GGBS (kg/m^3)	GGBS/cement (%)	Sand (kg/m^3)	IF (kg/m^3)	IF/sand (%)
BG0F0	570	0	0 %	640	–	–
BG10F0	513	57	10 %	640	–	–
BG30F0	399	171	30 %	640	–	–
BG50F0	285	285	50 %	640	–	–
BG0F10	560	0	0 %	576	64	10 %
BG10F10	504	56	10 %	576	64	10 %
BG30F10	392	168	30 %	576	64	10 %
BG50F10	280	280	50 %	576	64	10 %

*B refers to beam, G (0,10,30,50) refers to GGBS content percentage of cement replacement, and F (0,10) refers to IF percentage of replacement of the sand. GGBS: Ground granulated blast furnace slag; IF: Iron filings.

2. EXPERIMENTAL PROGRAM

2.1. Materials

Cement (Portland cement type I), aggregate, superplasticizer, and various other materials (such as GGBS and IF) were the components used to produce the concrete mixture. The sand and gravel were washed to remove any dust deemed to be unwelcome, after which they were dried and placed in a container prepared for use later. In Figure 1, the GGBS and IF were utilized in the experiments—the use of GGBS and IF were implemented as partial replacements for cement and sand, respectively. Table 1 shows the usage of GGBS and IF as a partial replacement. As shown in Table 1, the following quantities of materials were employed to achieve one cubic of mixing. The amount of water used was 125 kg/m^3. The amount of sand used was 640 kg/m^3, while the amount of gravel used was 1075 kg/m^3. The amount of superplasticizers (EUNIFLOW 260) was 6 kg/m^3. It was determined that the reinforcing bars used in the experiments were made of 45-grade steel (i.e., yield stress 450 MPa) after they were put through the testing procedures outlined in ASTM A370.

2.2. Test Beam Specimens

Eight HSRC beams were cast and tested. The HSRC beams were cast in two sets (four in each). In the first set, HSRC beams were cast to investigate the impact of varying GGBS content percentages on beam strength. In contrast, the second set consists of beams with IF and the exact varying GGBS content percentages as in the first set. After placing the steel frame inside the formwork, which was cleaned and oiled earlier, the concrete was poured into it. The concrete was left inside the formwork for two days to ensure it had enough strength to be unmolded. Beams were constantly sprayed with water and covered with a plastic sheet to keep them as moist as possible. Reinforcing bars of 16mm diameter were used as flexural rebars, while reinforcing bars of 6 mm were used as stirrups. Figure 2 shows the layout of the HSRC beams designed according to the ACI code [39] with flexural reinforcing bars of 2ϕ16 mm and stirrups of 12ϕ6 mm at a spacing of 150mm. Two ϕ 6mm rebars were used at the top to hold the stirrups in place during casting. At 35 days of age, the beams were tested, during which measurements were taken for load in kN and midspan deflection in mm, as well as observations of the mode of failure and crack pattern. Figure 3 shows the beam molded and curing. Three 150 mm by 300 mm cylinders were cast for each beam tested to determine its compressive strength.

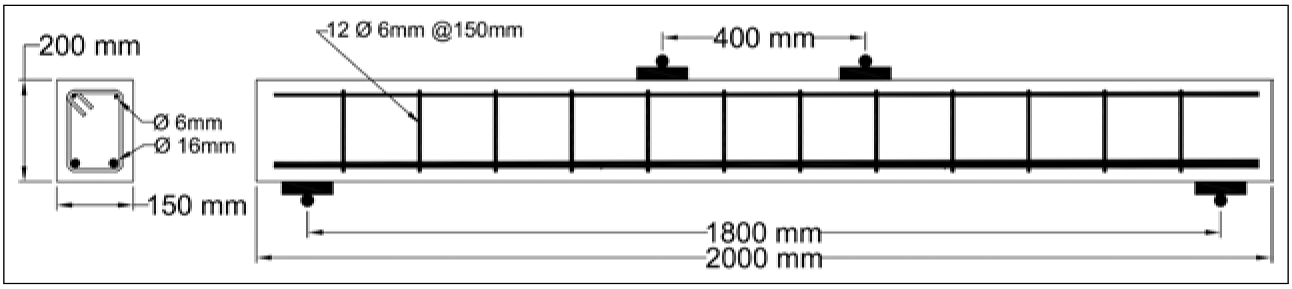

Figure 2. HSRC beam layout.

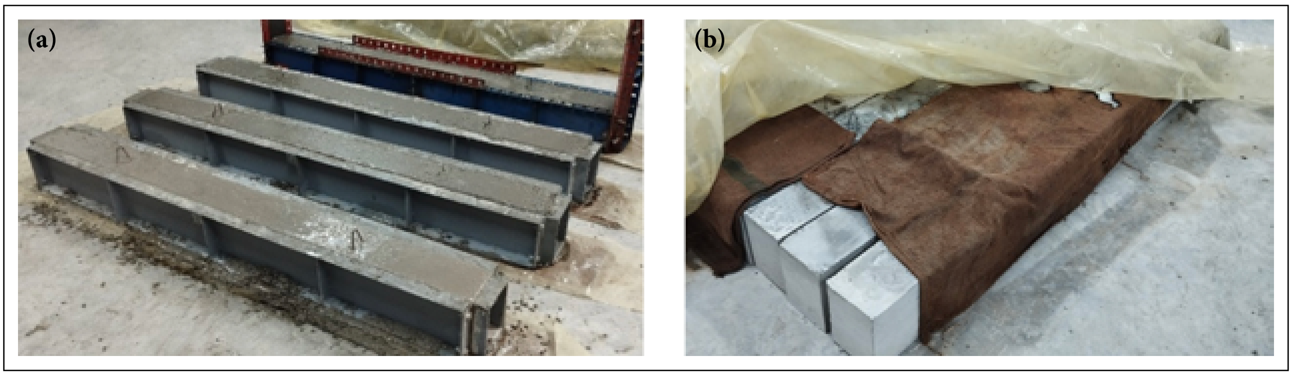

Figure 3. Beam molded and curing. **(a)** Beam molded. **(b)** Curing.

This study divided the beam specimens into two groups according to the materials' composition. In the first group, no GGBS was used, and the IF percentages were 0%, 10%, 30%, and 50% in the four beam specimens, respectively. The second group used a constant 10% GGBS across all beam specimens, with IF percentages of 0%, 10%, 30%, and 50%. GGGBS and IF partially replaced cement and sand in the concrete mix. Six HSRC beams were tested with varying compositions: three contained GGBS at 10%, 30%, and 50%, respectively, while others included 10% IF in addition to GGBS. The control beam, BG0F0, contained neither GGBS nor IF. The beam BG0F10 had 10% IF only. The beams BG10F0, BG30F0, and BG50F0 contained 10%, 30%, and 50% GGBS, respectively, without IF. Conversely, the beams BG10F10, BG30F10, and BG50F10 each included 10% IF alongside their respective GGBS percentages. The weights of cement, sand, GGBS, and IF used in the concrete batches are detailed in Table 1.

2.3. Test Setup

Utilizing a universal loading cell machine with a maximum capacity of 600 kN, a monotonic test was performed on four point-loading beams, as depicted in Figure 4. The ratio of shear span to beam depth was 3.5, which was determined by the fact that each loading point was positioned 200 millimeters away from the center of the beam to induce flexural failure. A dial gauge with an accuracy of 0.02 millimeters was attached to the bottom face of the beam being tested to measure the midspan deflection. Once the tested beam could no longer support additional loads, the testing was terminated because of failure. While the beam was being loaded, the crack pattern was recorded on the surface of the beam that was being tested. A rate of one kilonewton per second was applied to the load. During the process of loading the beam, the load and deflection were measured, and at the same time, the crack pattern was meticulously examined and marked.

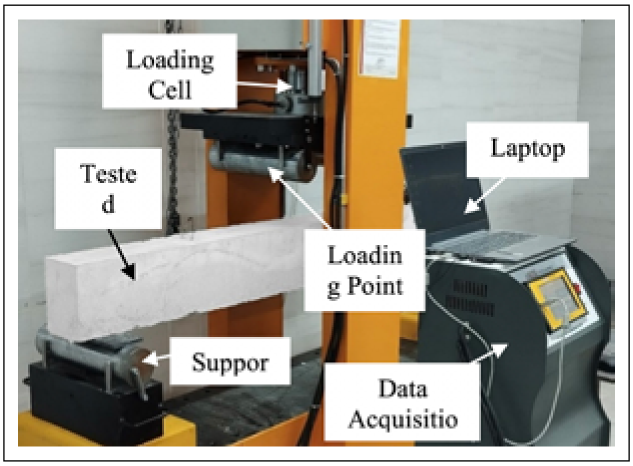

Figure 4. Test setup.

The testing procedure for determining the stress-strain behavior of a concrete cylinder involves using a universal compressive testing machine that applies a compressive load to the cylinder. A dial gauge is attached to measure the longitudinal deformation, as shown in Figure 5. Three cylinders measuring 150 mm by 300 mm were cast for each beam tested to capture stress-strain curves and determine peak compressive strength. This setup enables precise strain measurement, essential for evaluating the concrete's elasticity and compressive strength.

Table 2. Compressive strength of cylinders

Specimen ID	Compressive strength (MPa)
BG0F0	60
BG10F0	64
BG30F0	73
BG50F0	70
BG0F10	61
BG10F10	67
BG30F10	73
BG50F10	71

3. RESULTS AND DISCUSSION

These experiments were conducted to gain a deeper understanding of the sustainability-related behavior of HSRC beams. The following sections detail the experimental results, including crack patterns, load capacity, and deflection curves. These findings are presented in the following sections. Additionally, an explanation is provided for how these results behave.

3.1. Cylinder Specimens

The compressive strength of the average value of the compressive strength of three (150x300) mm cylinders of all the tested beams is shown in Table 2. The baseline specimen (BG0F0) demonstrates a compressive strength of 60 MPa. As additive levels of (GGBS and IF) increase, compressive strength rises notably, peaking at 73 MPa for BG30F0 and BG30F10. This increase suggests enhanced load-bearing capacity due to a denser and more robust concrete matrix. However, when additives (GGBS and IF) reach a higher concentration in both groups, as seen in BG50F0 and BG50F10, the compressive strength declines slightly to 70 MPa and 71 MPa, respectively. This reduction indicates that excessive additives may lead to brittleness, limiting the concrete's overall stability under load.

Regarding the stress-strain response shown in Figure 6, all cylinder specimens initially behave similarly up to around 15 MPa, showing a linear increase in stress as strain is applied, indicating stable load-bearing capacity across mixtures. Beyond this point, however, the effects of additives become more pronounced. Cylinder specimens with 10-30% additives continue to gain compressive strength, peaking around 73 MPa, while those with 0% or excessive additives start to plateau.

3.2. Beam Specimens

3.2.1. Crack Patterns

The HSRC beams, after failure, depicted in Figure 7, show distinct cracking patterns influenced by varying IF ratios and GGBS content. The analysis of these beams revealed that cracks typically initiated at loads between 24 kN and 29 kN, depending on the material composition. Beam Specimens without GGBS, like BG0F0 and BG0F10, began cracking at around 24 kN and 26 kN, respectively. The cracks were closely spaced and propagated quickly, indicating a lower resistance to crack formation and growth. However, the addition of IF in BG0F10 slightly improved crack resistance, delaying the onset of cracking and slightly controlling crack propagation.

Figure 5. Measuring the stress-strain curve (left image is before testing, right image is after testing).

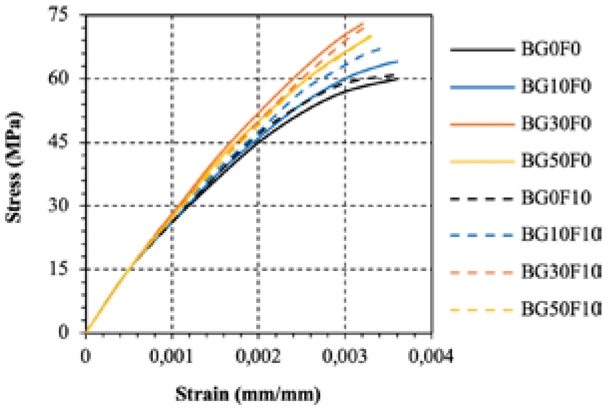

Figure 6. Stress-strain curves of tested cylinders.

Beams incorporating GGBS exhibited enhanced crack resistance, with BG10F0 and BG30F0 showing crack initiation at 27 and 26 kN, respectively. The cracks in these beams were spaced wider apart, reflecting the beneficial effects of GGBS in improving the concrete's microstructure and delaying crack propagation. 30% GGBS optimizes crack resistance by enhancing the microstructure through improved particle packing and reducing voids. This level maintains a balance between cementitious properties and filler effect, which prevents excessive cracking. In contrast, 50% GGBS delays crack initiation further due to enhanced packing but compromises overall strength as the cement matrix becomes overly diluted. When combined with IF, as seen in BG10F10 and BG30F10, the cracking load increased to approximately 28 kN and 29 kN, with the cracks being more controlled and evenly spaced, demonstrating a synergistic effect of the two materials.

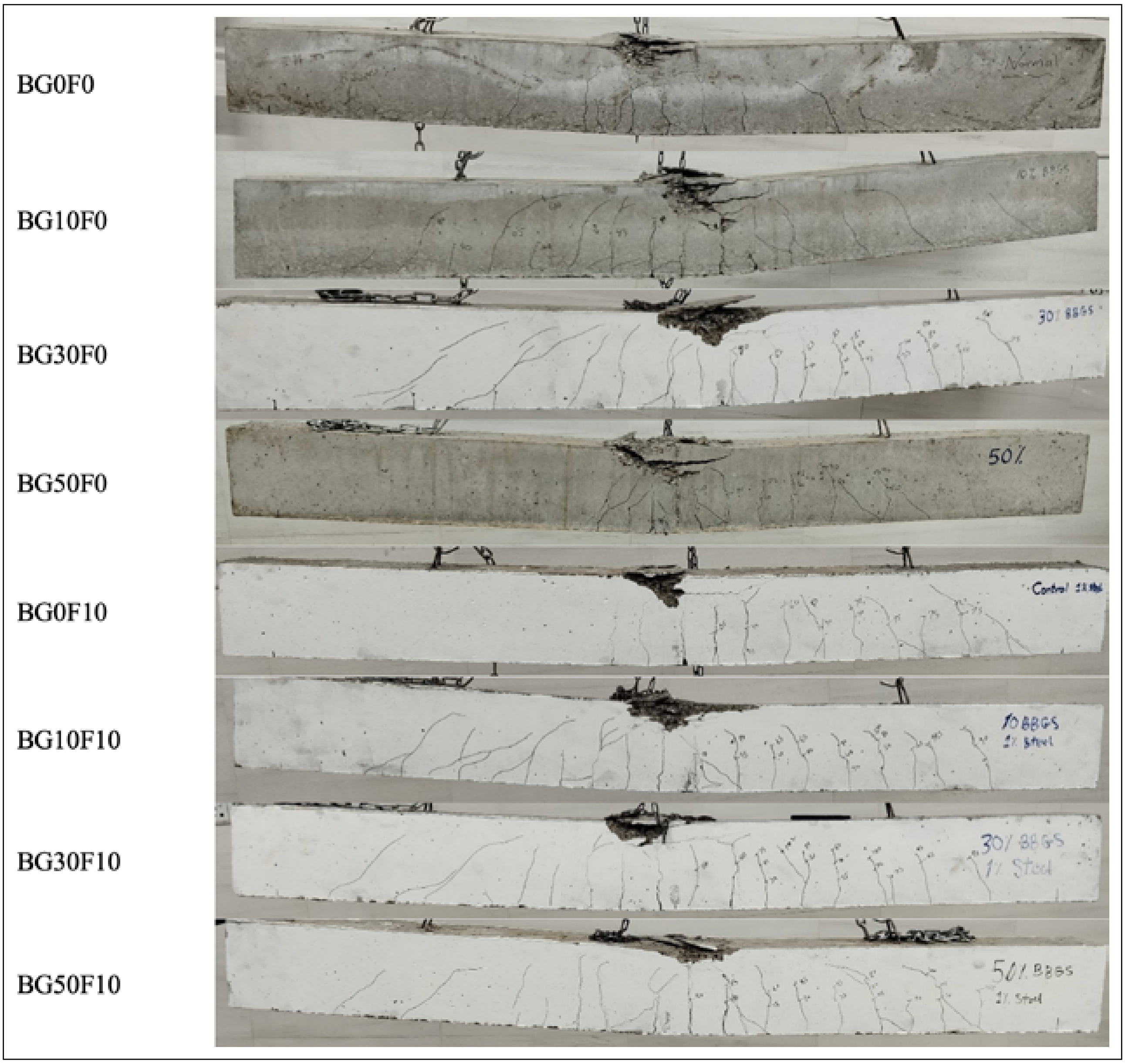

Figure 7. HSRC beams after testing.

The most significant improvement was observed in BG50F0, where the high GGBS content delayed crack initiation to around 29 kN. This specimen exhibited the widest crack spacing and the smallest crack widths, showing the highest resistance to crack propagation even at higher loads. Across all beam specimens, crack propagation slowed significantly once the load exceeded 70 kN to 75 kN, with final failure characterized by widening flexural cracks in the upper-middle span. The variations in cracking patterns across the beam specimens underscore the importance of GGBS and IF in enhancing the structural performance and durability of HSRC beams.

3.2.2. Load Capacity

One of the characteristics studied is the load capacity of the HSRC beams incorporating various GGBS content with or without IF. Table 3 illustrates the peak load results for all HSRC beams. The highest peak load recorded at 123.8 kN was noted for BG30F10, while the lowest peak load measured at 114.1 was observed for BG10F10. The compressive strength of the concrete was somehow diverse due to differences in the GGBS content percentage added to some beam specimens. However, all HSRC beams failed in flexural mode. The experimental results

Table 3. Peak load of tested beams

Specimen ID	Peak load (kN)
BG0F0	122.3
BG10F0	118.6
BG30F0	120.6
BG50F0	112.9
BG0F10	120.7
BG10F10	114.1
BG30F10	123.8
BG50F10	119.3

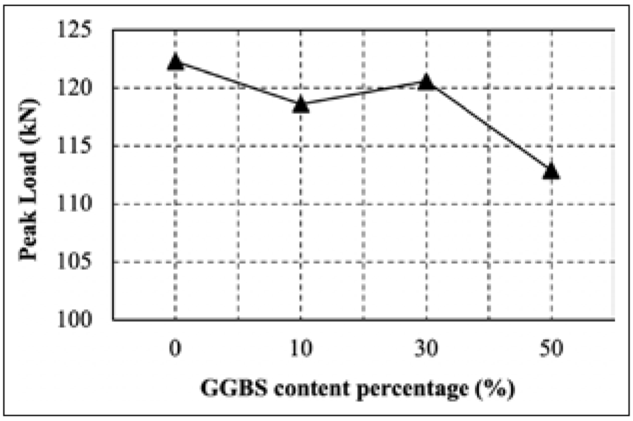

Figure 8. GGBS content percentage vs. peak load of beams with GGBS.

showed that both GGBS and IF undoubtedly influence the behavior of HSRC beams. The optimal performance of 30% GGBS is due to its ability to act as a non-reactive filler that enhances the density without significantly reducing the cement's binding capabilities. However, at 50% GGBS, the dilution of cement content reduces load-bearing capacity. Adding 10% IF further supports the load capacity by reinforcing the tensile properties, effectively distributing stresses, and reducing crack formation. Even though all HSRC beams failed in a flexural mode, loads at which HSRC beams failed were distinguishable.

Furthermore, the experiments revealed that HSRC beams with different percentages of GGBS exhibited slightly different strengths [21, 22]. GGBS is a very fine material and experiences no chemical reactivity. Hence, GGBS functions solely as a filler. Due to the fineness and lack of chemical reactivity of the GGBS, as the percentage of replacement increases, the strength of the HSRC beams gets greater until a certain percentage is reached, at which point the strength starts to decrease [15, 18]. This percentage is called the optimal percentage of replacement. However, it is very challenging to maintain this percentage practically, along with other in-situ circumstances. Suggesting a prescribed percentage that can provide the best strength is better. Three different percentages of GGBS were suggested (i.e., 10%, 30%, and 50%) of the weight of the cement. As the GGBS content percentage increases, the need for water content rises, leading to a drop in compressive strength. In addition, the cement content responsible for the chemical binding of concrete components lessens.

Moreover, the findings from the experiment indicated that when the GGBS content percentage increases, the peak load of the beams drops. The beams BG50F0 and BG10F10 were the only two with the lowest strength compared to all other beams. However, BG30F10 showed the highest strength among all beams. The peak load of the beam (BG50F0) with 50% of GGBS content percentage drops 8% of the control beam. However, the best GGBS content percentage is 30%, unlike what was found by [15, 18]. Because the strength starts to deteriorate as the GGBS content percentage increases after a certain point.

Table 4. Peak load of beams with GGBS

Specimen ID	Peak load (kN)	Compressive strength (MPa)*
BG0F0	122.3	100%
BG10F0	118.6	97%
BG30F0	120.6	99%
BG50F0	112.9	92%

*The calculated percentage relative to the control beam BG0F0. GGBS: Ground granulated blast furnace slag.

When it comes to decision-making, it all comes down to the structural designer, who may prioritize the utilization of GGBS even though it may compromise the strength of the structure.

3.2.2.1. *Effect of GGBS Replacement*

A comparison in terms of load capacity between the HSRC beams utilizing GGBS and those without GGBS is presented in this section. GGBS, acting as a non-reactive fine material, functions as a filler in concrete [17]. The strength increases or stays unchanged as GGBS content percentage rises until reaching a certain point, after which the strength declines [15–18] (Table 3). For HSRC beams, this behavior is noticeable in Figure 8. In addition, replacing the cement with GGBS partially underperforms the beam in terms of peak load. The peak load for beams BG10F0 and BG30F0 is 118.6 and 120.6, respectively, approximately 1-3% less than the control beam (Table 4). However, when utilizing a GGBS content percentage of 50%, the peak load of the beam BG50F0 drops by 8%. This behavior is predicted as the GGBS content percentage increases due to the chemical non-reactivity of the GGBS. This behavior suggests that as the GGBS content percentage exceeds 50%, the load capacity may drop proportionally. The performance at 30% GGBS is near-optimal because it improves the concrete's microstructure without significantly compromising the chemical binding provided by the cement. Exceeding this threshold leads to performance declines as the cement matrix weakens, highlighting the critical balance needed in GGBS content.

3.2.2.2. *Effect of IF Replacement*

One of the main aims of this experiment is to examine the effect of IF content percentage on the behavior of the HSRC beams. The results showed that utilizing IF in the concrete impacted the behavior of the HSRC beams, as shown in Figure 9. Table 5 shows that the peak load of the beam BG0F10 is within only 1% compared to the control beam, even though the compressive strength of the beam BG0F10 was 1% higher than the control beam. The addition of IF shows some improvement in gaining extra strength in comparison to the control beam, even though the control beam with 10% of IF (BG0F10) failed at a load of 1% lower than the control beam (i.e., 120.7 kN) but almost the same displacement (i.e., 33.4 mm). Incorporating 10% IF is particularly beneficial as it enhances tensile properties and reinforces the matrix, helping to control cracks. Unlike higher percentages, which can introduce inconsistencies, this level provides the best results without disrupting the overall

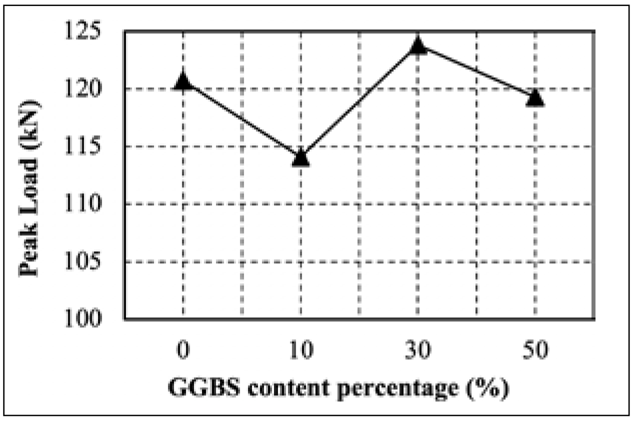

Figure 9. GGBS content percentage vs. peak load of beams with and without IF.

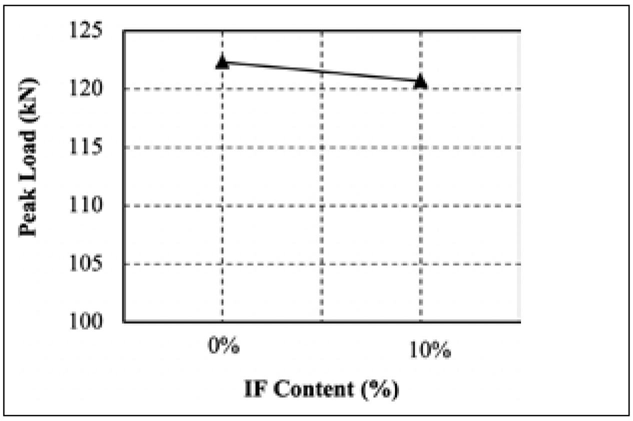

Figure 10. Peak load of beams with IF.

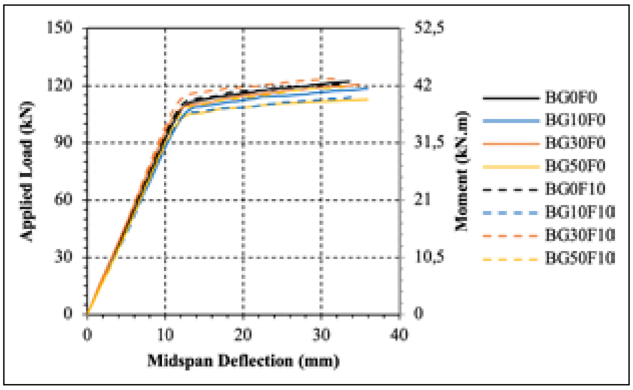

Figure 11. Load-deflection and moment-deflection curves of all HSRC beams.

Table 5. Peak load of beams with GGBS

Specimen ID	Peak load (kN)	Specimen/BG0F0*
BG0F0	122.3	100%
BG0F10	120.7	99%

*The calculated percentage relative to the control beam BG0F0. GGBS: Ground granulated blast furnace slag.

Table 6. Peak load of beams with GGBS

Specimen ID	Peak load (kN)	Specimen/BG0F0*
BG0F0	120.7	100%
BG10F10	114.1	95%
BG30F10	123.8	103%
BG50F10	119.3	99%
BG0F0	120.7	100%

*The calculated percentage relative to the control beam BG0F0. GGBS: Ground granulated blast furnace slag.

structural integrity. The beams (BG30F10 and BG50F10) gained strength of around 2% and 6%, respectively, compared to corresponding beams without IF. The insignificant margin of strength reduction implies the potential advantage of utilizing IF as a partial replacement for sand.

3.2.2.3. Composite Effect of GGBS and IF Replacement

Studying the behavior of HSRC beams with both GGBS and IF is one of the main subjective. The combined effect of GGBS and IF may seem somewhat challenging since it deals with two different materials with different mechanical and physical properties. The combination of 30% GGBS and 10% IF demonstrated the best structural performance due to the complementary effects of improved microstructure and enhanced crack resistance. Higher GGBS percentages, while beneficial for crack delay, slightly reduced overall beam strength, confirming that a balanced approach is necessary for optimal results. Unlike the beams without IF shown in Figure 8, where beams with a higher GGBS content percentage experience a higher drop in peak load than that of the control beam, beams with IF shown in Figure 10 exhibit slightly different behavior. Table 6 illustrates that the peak load of beam BG10F10 drops 5% compared to the control beam. However, with a GGBS content percentage of 30% and an IF content percentage of 10%, the peak load rises by 3% compared to the control beam. When the GGBS content percentage was changed to 50%, the beam BG50F10 failed at a rate of 1% lower than the control beam. The more content of GGBS and IF with less compromise in the strength of the HSRC beams is the most favorable. Hence, HSRC beams with a GGBS content percentage of 50% and an IF content percentage of 10% with a drop in strength of only 1% may appear to be the better choice to keep the strength and utilize as much GGBS and IF as a partial replacement as possible.

3.2.3.Load-Deflection Curves

The relationship between load and moment versus midspan deflection of all eight HSRC beams drawn in Figure 11 reflects the overall behavior of the beams subjected to external loads. The moment is calculated as half of the total load multiplied by the shear span, which is 0.7 m. All HSRC beams exhibit two slopes of stiffness, which is the slope of the tangent. The first steep stiffness characterizes the elastic behavior, whereas the second shallow stiffness denotes the plastic behavior. HSRC beams carry loads during the initial stiffness while experiencing deformations approximately linearly. However, as the beam experiences plastic behavior in the concrete, steel, or both, its ability to sustain loads

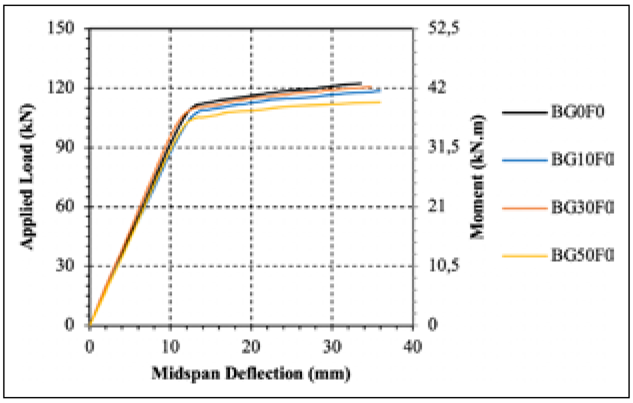

Figure 12. Load-deflection and moment-deflection curves of beams with GGBS.

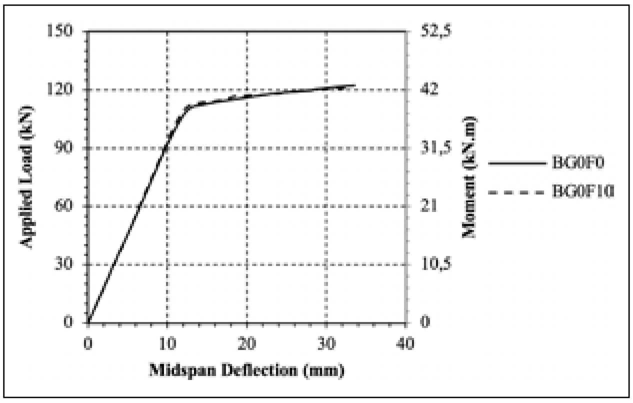

Figure 13. Load-deflection and moment-deflection curves of beams with and without IF.

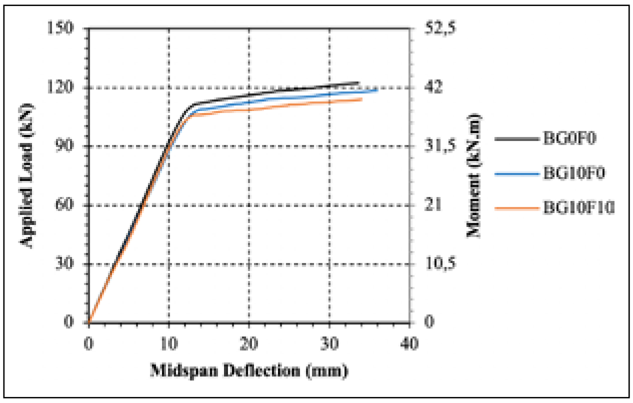

Figure 14. Load-deflection and moment-deflection curves of beams with 10% of GGBS.

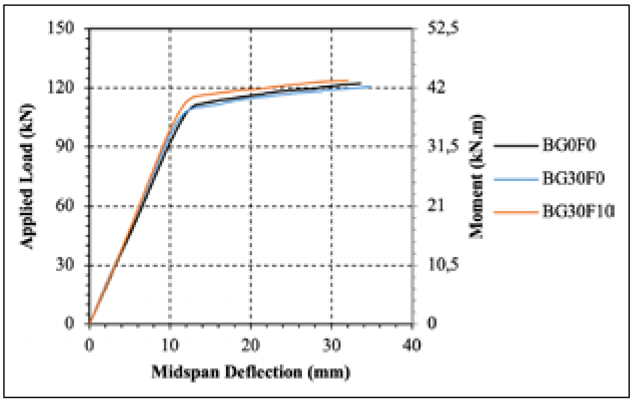

Figure 15. Load-deflection and moment-deflection curves of beams with 30% of GGBS.

uniformly diminishes, significantly reducing beam stiffness. All HSRC beams showed the same behavior, gradually increasing strength up to failure. The following sections present the deflection curves in detail.

3.2.3.1. Effect of GGBS Replacement

The load-deflection curves of the beams BG0F0, BG10F0, BG30F0, and BG50F0 are shown in Figure 12. Partial replacing the cement with GGBS can slightly change the overall behavior of the beams. The results show that the control beam has the highest plastic stiffness compared with other beams. Meanwhile, the beam BG50F0 experiences the lowest stiffness. The considerable proportion of GGBS content results in a decline in compressive strength, thereby contributing to the reduced overall beam strength observed. The plastic stiffness of the beam BG30F0 is higher than the other two beams, BG10F0 and BG50F0.

3.2.3.2. Effect of GGBS Replacement

The load and deflection of the control beam and BG0F10 are shown in Figure 13, which illustrates the relationship between the two. On the whole, the two beams behave in a virtually identical manner. The peak load, on the other hand, varies by one percent. Even though the compressive strength of the beam BG0F10 increases, the beam's behavior does not change due to the 10% IF content percentage. Additionally, due to the similarity in behavior, the engineering community may be encouraged to use the IF as a partial replacement for the sand.

3.2.3.3. Composite Effect of GGBS and IF Replacement

The results demonstrate a subtle variation between the combined influence of GGBS and IF compared to utilizing either material independently. Figure 14 shows the load-deflection curves of the control beam, BG0F10 and BG10F10. The control beam shows higher plastic stiffness than the other two beams. Adding 10% GGBS and IF underperforms the beam, while the beam with only 10% GGBS becomes stiffer. Figure 15 shows the load-deflection of the control beam, BG30F0 and BG30F10. The beam BG30F0 shows a drop in plastic stiffness compared to the control beam. However, an improvement in the plastic stiffness of the HSRC beams was noticed when a 30% GGBS and a 10% IF were utilized. The load-deflection curves of the control beam, BG50F0 and BG50F10, are drawn in Figure 16. The beam BG50F0 shows a distinguishable decrease in plastic stiffness compared to the other two beams. However, the plastic stiffness of beam BG50F10 is greater than BG50F0. This type of response may be due to the interaction of the IF with the concrete, which may improve the overall strength of the beam. It can be concluded that the overall strength of the HSRC beams can be improved by substituting GGBS and IF with a certain percentage.

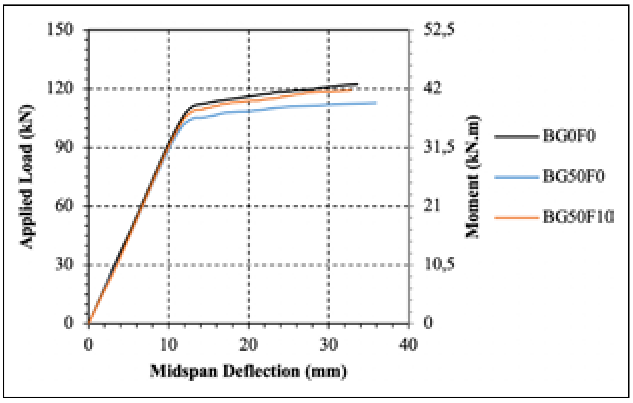

Figure 16. Load-deflection and moment-deflection curves of beams with 50% of GGBS.

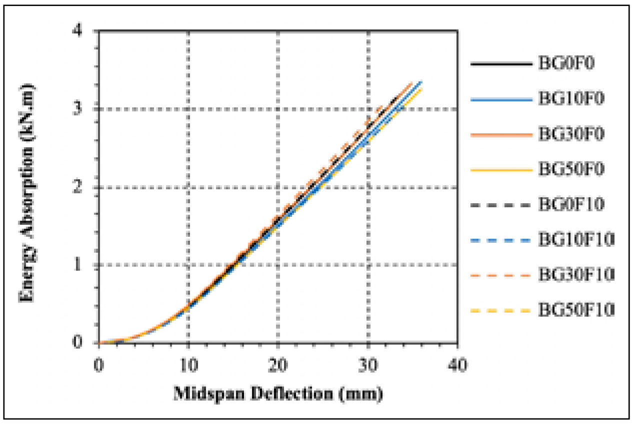

Figure 17. Energy absorption versus deflection curves of all HSRC beams.

3.2.4. Energy Absorption

The energy absorption versus midspan deflection curves for all tested beams, illustrated in Figure 17, offer valuable insights into the energy dissipation capabilities of beams with varied levels of GGBS and IF as partial replacements. Initially, all beams show a linear increase in energy absorption with rising midspan deflection, reflecting a consistent elastic response up to about 10 mm. Beyond this point, energy absorption rises slower as deflection increases, indicating a shift to plastic deformation.

Beams with a 30% GGBS substitution (BG30F0 and BG30F10) demonstrate slightly higher energy absorption at more significant deflections than the control beam (BG0F0) and other specimens. This trend suggests that 30% GGBS optimally enhances energy absorption, potentially due to better microstructural packing and material density. On the other hand, beams with a higher GGBS content (BG50F0 and BG50F10) show a slight decrease in energy absorption, indicating that an excessive GGBS percentage might reduce the material's energy dissipation effectiveness.

The addition of 10% IF in beams shows marginal improvement in energy absorption over the deflection range in beams like BG10F10 and BG30F10, which indicates some reinforcing effects. This is especially the case for the BG30F10, where 30% GGBS combined with 10% IF improves the energy absorption capacity compared to other formulations. All these results suggest that, for a balance between GGBS and IF contents, an optimum allows HSRC beams to dissipate more energy when subjected to loads and to be more deformation-resistant. The best overall performance is achieved by combining the highest percentage of GGBS with 10% IF, showing the possibility of these eco-friendly binders for structural applications requiring high energy dissipation and durability.

4. CONCLUSIONS

This study described the flexural performance of some HSRC beams manufactured to incorporate GGBS and IF as different binders. Extensive experiments were conducted to test conventional and modified HSRC beams due to various treatments to obtain important information about material performance on compressive strength and flexural behaviors. The experimental results indicated that the replacement of cement by 30% GGBS yielded a minimum loss in strength, around 1–3%, compared to the control beam—within the limit for use in structural applications. On the contrary, higher cement replacement by 50% GGBS resulted in a peak load reduction of approximately 8%, which evidenced the adverse effects of the content of GGBS in high percentages. Adding 10% IF to beams with 30% GGBS content increased the peak load by 3% and showed that an interaction between GGBS and IF leads to improved performance of RVA beams. The beams without GGBS (BG0F0) had the highest capacity among all the tested beams.

In contrast, the beams containing 50% GGBS resulted in the most significant reduction, emphasizing the importance of optimizing GGBS content to maintain beam strength. The beams, on the other hand, with a combination of GGBS and IF, showed characteristic resistance to the appearance of cracks and controlled the propagation of cracks to ensure further durability. Indeed, 30% GGBS and 10% IF gave the optimum performance that balanced sustainable issues with strength. Actual results underline that GGBS should not be higher than the optimum 30% replacement to maintain optimum structural integrity, and additional reinforcement benefits could be realized with IF when incorporation was at 10%. Other recommendations for the future include studying the durability of the HSRC beams with GGBS and IF under extreme environmental conditions of high temperature and moisture. A follow-up study may also establish the economic feasibility of using such materials in large-scale building projects, ensuring that GGBS and IF will positively contribute to the environment and be cost-effective when put into practical use.

ETHICS

There are no ethical issues with the publication of this manuscript.

DATA AVAILABILITY STATEMENT

The authors confirm that the data that supports the findings of this study are available within the article. Raw data that support the finding of this study are available from the corresponding author, upon reasonable request.

CONFLICT OF INTEREST

The authors declare that they have no conflict of interest.

FINANCIAL DISCLOSURE

The authors declared that this study has received no financial support.

USE OF AI FOR WRITING ASSISTANCE

Not declared.

PEER-REVIEW

Externally peer-reviewed.

REFERENCES

[1] Ariffin, N. F., Nasrudin, N. N., Alias, A., Lim, N. H. A. S., Hasim, A. M., & Zaimi, M. N. S. (2024). Thermal waste replacement as a sustainable approach to reinforced concrete beam design: A finite element study. *Open Civ Eng J, 18*(1), e18741495285908.[CrossRef]

[2] Rahmat, M. S., Mokhatar, S. N., Razali, B. A., Hadipramana, J., & Hakim, S. J. S. (2023). Numerical modelling of impact loads on rc beams utilizing spent garnet as a replacement for fine aggregate. *J Adv Res Appl Mech, 107*(1), 41-54. [CrossRef]

[3] Özkılıç, Y. O., Althaqafi, E., Bahrami, A., Aksoylu, C., Karalar, M., Özdöner, N., ... & Thomas, B. S. (2024). Influence of ceramic waste powder on shear performance of environmentally friendly reinforced concrete beams. *Sci Rep, 14*(1), 10401. [CrossRef]

[4] Aziz, P. L., & Abdulkadir, M. R. (2022). Mechanical properties and flexural strength of reinforced concrete beams containing waste material as partial replacement for coarse aggregates. Int J Concr Struct Mater, 16(1), 56. [CrossRef]

[5] Özkaynak, H., & Özbay, A. E. Ö. (2019, June 17-18). *The effect of waste newspaper on compressive strength of concrete mortar*. 4th Eurasian Conference on Civil and Environmental Engineering (ECOCEE). Istanbul.

[6] Ellis, L. A., Leon, L. P., & Charran, A. V. (2023). Investigating the use of recycled concrete as aggregates in the construction of structural beams. *West Indian J Eng, 45*(2), 4-13. [CrossRef]

[7] Hama, S. M., Ali, Z. M., Zayan, H. S., & Mahmoud, A. S. (2023). Structural behavior of reinforced concrete incorporating glass waste as coarse aggregate. *J Struct Integr Maint, 8*(1), 59-66. [CrossRef]

[8] El-Sayed, T. A., Erfan, A. M., & El-Naby, R. M. A. (2019). Flexural behavior of RC beams by using agricultural waste as a cement reinforcement materials. *J Eng Res Rep, 7*(1), 1-12. [CrossRef]

[9] Karimi Pour, A., Shirkhani, A., Kırgız, M. S., & Noroozinejad Farsangi, E. (2023). Influence of fiber type on the performance of reinforced concrete beams made of waste aggregates: experimental, numerical, and cost analyses. *Pract Period Struct Des Constr, 28*(2), 04023007. [CrossRef]

[10] Malagavelli, V., & Rao, P. N. (2010). High-performance concrete with GGBS and ROBO sand. *Int J Eng Sci Technol, 2*(10), 5107-5113.

[11] Al-Hamrani, A., Kucukvar, M., Alnahhal, W., Mahdi, E., & Onat, N. C. (2021). Green concrete for a circular economy: A review on sustainability, durability, and structural properties. *Materials, 14*(2), 351. [CrossRef]

[12] Parashar, A. K., Sharma, P., & Sharma, N. (2022). Effect on the strength of GGBS and fly ash based geopolymer concrete. *Materials Today Proceedings, 62*, 4130-4133. [CrossRef]

[13] Liu, Z., Takasu, K., Koyamada, H., & Suyama, H. (2022). A study on engineering properties and environmental impact of sustainable concrete with fly ash or GGBS. *Constr Build Mater, 316*, 125776. [CrossRef]

[14] Panda, R., & Sahoo, T. K. (2021). Effect of replacement of GGBS and fly ash with cement in concrete. In *Lecture Notes in Civil Engineering* (Vol. 75, pp. 811-818). Springer. [CrossRef]

[15] Özbay, E., Erdemir, M., & Durmuş, H. İ. (2016). Utilization and efficiency of ground granulated blast furnace slag on concrete properties-A review. *Constr Build Mater, 105*, 423-434. [CrossRef]

[16] Kumar, V. R. P., Gunasekaran, K., & Shyamala, T. (2019). Characterization study on coconut shell concrete with partial replacement of cement by GGBS. *J Build Eng, 26*, 100830. [CrossRef]

[17] Chandrashekar, V., PS, T., Madhu, K. S., & KB, D. T. P. (2018). Effect on the engineering properties of pervious concrete by partial replacement of cement with GGBS. *GRD J Eng, 3*, 1-7. [CrossRef]

[18] Oner, A., & Akyuz, S. (2007). An experimental study on optimum usage of GGBS for the compressive strength of concrete. *Cem Concr Compos, 29*(6), 505-514. [CrossRef]

[19] Hussain, F., Kaur, I., & Hussain, A. (2020). Reviewing the influence of GGBFS on concrete properties. *Materials Today: Proceedings, 32*, 997-1004. [CrossRef]

[20] Dixit, A., & Hooda, Y. (2019). Experimental evaluation on compressive and tensile behavior of concrete utilising GGBS, fly ash and recycled aggregates. *Int J Eng Adv Technol, 8*(5), 2249-8958.

[21] Babu, K. G., & Kumar, V. S. R. (2000). Efficiency of GGBS in concrete. *Cem Concr Res, 30*(7), 1031-1036. [CrossRef]

[22] Sangeetha, S. P., & Joanna, P. S. (2014). Flexural behaviour of reinforced concrete beams with partial replacement of GGBS. *Am J Eng Res, 3*(1), 119-127.

[23] Khatib, J. M., & Hibbert, J. J. (2005). Selected engineering properties of concrete incorporating slag and metakaolin. *Constr Build Mater, 19*(6), 460-472. [CrossRef]

[24] Hawileh, R. A., Abdalla, J. A., Fardmanesh, F., Shahsana, P., & Khalili, A. (2017). Performance of reinforced concrete beams cast with different percentages of GGBS replacement to cement. *Archives of Civil and Mechanical Engineering, 17*, 511-519. [CrossRef]

[25] Hawileh, R. A., Badrawi, H. A., Makahleh, H. Y., Karzad, A. S., & Abdalla, J. A. (2022). Behavior of reinforced concrete beams cast with a proposed geopolymer concrete (GPC) mix. *Int J Appl Sci Eng, 19*(2), 1-11. [CrossRef]

[26] Bai, X., Zhou, H., Bian, X., Chen, X., & Ren, C. (2024). Compressive strength, permeability, and abrasion resistance of pervious concrete incorporating recycled aggregate. *Sustainability, 16*(10), 4063. [CrossRef]

[27] Divsholi, B. S., Lim, T. Y. D., & Teng, S. (2014). Durability properties and microstructure of ground granulated blast furnace slag cement concrete. *Int J Concr Struct Mater, 8*, 157-164. [CrossRef]

[28] Zhang, Z., & Li, H. (2024). Flexural fatigue behavior of prestressed high-performance concrete bridges with double mineral fine powder admixture: An experimental study. *Appl Sci, 14*(17), 7511. [CrossRef]

[29] Gautam, A., & Tung, S. (2024). Advancing sustainability in concrete construction: Enhancing thermal resilience and structural strength with ground granulated blast furnace slag. *Asian J Civ Eng, 25*(8), 6119-6129. [CrossRef]

[30] Parashar, A. K., Kumar, A., Singh, P., & Gupta, N. (2024). Study on the mechanical properties of GGBS-based geopolymer concrete with steel fiber by cluster and regression analysis. *Asian J Civ Eng, 25*(3), 2679-2686. [CrossRef]

[31] Oti, J., Adeleke, B. O., Mudiyanselage, P. R., & Kinuthia, J. (2024). A comprehensive performance evaluation of ggbs-based geopolymer concrete activated by a rice husk ash-synthesised sodium silicate solution and sodium hydroxide. *Recycling, 9*(2), 23. [CrossRef]

[32] Thakur, G., Singh, Y., Singh, R., Prakash, C., Saxena, K. K., Pramanik, A., ... & Subramaniam, S. (2022). Development of GGBS-based geopolymer concrete incorporated with polypropylene fibers as sustainable materials. *Sustainability, 14*(17), 10639. [CrossRef]

[33] Kanagaraj, B., Anand, N., Alengaram, U. J., & Raj, R. S. (2023). Engineering properties, sustainability performance and life cycle assessment of high strength self-compacting geopolymer concrete composites. *Constr Build Mater, 388*, 131613. [CrossRef]

[34] Deepa, K., Murugesan, P., Valliappan, V., & Choudary, S. (2023). Experimental research on pervious concrete performance with partial replacement of foundry sand nano and GGBS. *Materials Today Proceedings, 103*, 534-540. [CrossRef]

[35] Mironovs, V., Broņka, J., Korjakins, A., & Kazjonovs, J. (2011). Possibilities of application iron containing waste materials in manufacturing of heavy concrete. *Civil Engineering '11 - 3rd International Scientific Conference, Proceedings, 3*, 14-19.

[36] Olutoge, F., Onugba, M., & Ocholi, A. (2016). Strength properties of concrete produced with iron filings as sand replacement. *Br J Appl Sci Technol, 18*(3), 1-6. [CrossRef]

[37] Ekop, I. E., Okeke, C. J., & Inyang, E. V. (2022). Comparative study on recycled iron filings and glass particles as a potential fine aggregate in concrete. *Resour Conserv Recycl Adv, 15*, 200093. [CrossRef]

[38] Helmand, P., & Saini, S. (2019). Mechanical properties of concrete in presence of iron filings as complete replacement of fine aggregates. *Materials Today: Proceedings, 15*, 536-545. [CrossRef]

[39] American Concrete Institute. (2008). *Building code requirements for structural concrete (ACI 318-08) and commentary*. ACI 318-08.

J Sustain Const Mater Technol, Vol. 9, Issue. 4, pp. 327–334, December 2024

Journal of Sustainable Construction Materials and Technologies
Web page info: https://jscmt.yildiz.edu.tr
DOI: 10.47481/jscmt.1608352

Research Article

Accelerated alkali-silica reaction after a seven-year ASR-dormancy period

Ahsanollah BEGLARİGALE*

Department of Civil Engineering, İstanbul Okan University, İstanbul, Türkiye

ARTICLE INFO

Article history
Received: 24 May 2024
Revised: 10 November 2024
Accepted: 25 November 2024

Key words:
Alkali silica reaction, cement, durability, supplementary cementitious materials

ABSTRACT

The ongoing alkali-silica reaction (ASR) in concrete can be halted by dryness, which is important for repairing ASR-suffered concrete structures. Drying of the concrete establishes an ASR-dormancy period until the end of the dryness. The residual expansion of such concrete after the ingress of water—the end of the dormancy period—is a significant risk, especially for repair works. In this experimental study, the post-dormancy expansion of various mixtures prepared by eight different Portland cement and three different supplementary cementitious materials (SCM) were tested using an accelerated mortar bar test. After accelerated ASR expansions, an ASR-dormancy period was established by keeping the specimens dry for seven years; the residual ASR expansions of the specimens were tested by the same accelerated method. The effect of pre-dormancy reactions on the residual expansions was discussed through two perspectives. The post-dormancy expansion behavior of mixtures without or with insufficient SCM indicated that expansions were primarily driven by the swelling of old gel, whereas in specimens with sufficient SCM, the dominant mechanism was new gel formation, a result of lower pre-dormancy expansions due to the ASR-mitigating effect of SCMs.

Cite this article as: Beglarigale, A. (2024). Accelerated alkali-silica reaction after a seven-year ASR-dormancy period. *J Sustain Const Mater Technol*, 9(4), 327–334.

1. INTRODUCTION

Alkali silica reaction is one of concrete's significant and commonly seen durability problems; therefore, innumerable studies have been carried out for decades worldwide to understand its nature and overcome its deleterious effects. Since Stanton's paper [1], dealt with the chemistry of ASR, many test methods have been developed to analyze the reactivity of aggregates and to assess the effectiveness of various ASR-mitigation approaches. However, there are still many ASR-suffered structures and many at risk of being suffered. Therefore, the repair and maintenance works—techniques include, but are not limited to, injection of epoxy resins into cracks [2], precast prestressed concrete confinement [3], CFRP sheet bonding [4], surface coating using acrylic and urethane-based continuous fiber sheets, and concrete jacketing [5] as well as novel methods such as applying bacteria-containing grout to the surface of ASR-suffered concrete [6]—have been carried out for many years worldwide and will be executed in the future.

A successful repair must be accompanied either by a waterproofing application or drainage/removal of water in contact with the concrete. In other words, the dryness of the ASR-suffered concrete must be ensured— such as improvement of drainage, sealing surface of the structure to prevent water ingress, and silane treatment of the structure [7]—to halt reactions (ASR-dormancy period) and to avoid swelling of the existing ASR gel. Otherwise, the reaction and the expansion will continue; thus, the deterioration will occur again. Daidai et al. [3] have reported that the water trapped

---

***Corresponding author.**
*E-mail address: ahsan.beglari@okan.edu.tr / ahsan.beglari@gmail.com

Published by Yıldız Technical University Press, İstanbul, Türkiye

Table 1. The additive content of the Portland cement used in this study

Cement type	Additive content
CEMI-1 (CEM I 42,5 R)	None
CEMII-1 (CEM II/B-M (L-W) 42,5 R)	24% fly ash (calcareous) and 6% limestone
CEMI-2 (CEM I 42,5 R)	None
CEMII-2 (CEM II/B-M (L-W) 42,5 R)	22% fly ash (calcareous) and 7.5% limestone
CEMI-3 (CEM I 42,5 R)	None
CEMII-3 (CEM II/A-M (V-LL) 42,5 R)	6.98% fly ash (siliceous) and 5.95% limestone
CEMI-4 (CEM I 42,5 R)	None
CEMII-4 (CEM II/A-LL 42,5 R)	10% limestone

inside the concrete before the injection repair and surface coating works was the main reason behind the continuous expansion of the repaired bridge concrete. They have also emphasized that penetration of the drainage water and deicing salts to the repaired concrete bridge piers accelerated the ASR reactions. The ASR-dormancy period can be maintained as long as the concrete is dry.

The ASR-dormancy period established by preventing water ingress will be over whenever water penetrates any ASR-suffered concrete. To the best of the author's knowledge, only one scientific paper dealt systematically with the post-dormancy (after 14 14-month drying period) ASR expansions [8]. Multon and Toutlemonde [8] have investigated the effect of moisture conditions and transfers on ASR-suffered concrete specimens. They showed that water supply causes new ASR expansions in the ASR-suffered dry concretes. However, there is a lack of information regarding the effects of pre-dormancy expansion levels and supplementary cementitious material usage on post-dormancy expansions. This study endeavored to understand this matter through accelerated reactions and a seven-year ASR-dormancy period (7Y-DP). It can also shed light on using recycled concrete aggregates obtained from ASR-suffered concrete structures.

2. EXPERIMENTAL PROGRAM

2.1. Materials

Two different cement types, Ordinary Portland cement (CEM I 42.5R) and Portland composite/blended cement (CEM II 42.5R), supplied by four different producers, were used in this study. The contents of these eight cements are presented in Table 1. The fly ashes used in this study were Class-F fly ash (FF) and Class-C fly ash, according to the ASTM C618-19 [9]. Moreover, a ground granulated blast furnace slag (S) was used in this study. The chemical compositions of the cement and the SCMs are presented in Table 2.

The reactive aggregate was an andesitic basalt, crushed and quarried from the Aliağa region north of Izmir, Turkey. Its ASR potential, albeit no reported case in structures, has been observed in a few studies up to now [10–14]. The studies conducted by Copuroglu et al. [15] and Yuksel et al. [11], for instance, revealed that the fine fraction of this aggregate caused, respectively, 0.55% and 0.5% expansions (14-day) in accelerated mortar bar test. The mineralogical and microstructural characteristics of the aggregate were studied in detail by Copuroglu et al. [15]. They revealed that the primary source of the observed expansion can be explained by the reactive glassy phase of the basalt matrix having approximately 70% SiO_2 [15].

2.2. Preparation of Specimens

Mortar bars with 25×25×285 mm dimensions were prepared according to ASTM C1260 [16] and ASTM C 1567 [17] with a water-to-binder ratio of 0.47 and a sand-to-binder ratio of 2.25. The replacement ratios of fly ashes were, respectively, 30% and 25% (by cement weight)— the maximum recommended ratios in the TS13515 [18] standard —for the CEMI and CEMII cement. These ratios were 45% and 30% for the Slag.

2.3. Accelerated Mortar Bar Test

The initial lengths of mortar bars were measured immediately after demolding, prior to immersion in 80 °C water for 24h. After that, the lengths of mortar bars immersed in the 80 °C NaOH solution were measured periodically. As the primary purpose of this research was to scrutinize the effects of pre-dormancy expansion levels on the post-dormancy expansions, it was aimed to have different expansion ranges before the 7Y-DP; therefore, various (almost determined randomly) exposure durations were applied—of course, not so divergent (42–59 days). After the last length measurement, the specimens were taken from the solution and dried; then, they were stored in plastic storage boxes. They were kept in the boxes for more than seven years (7Y-DP) until the post-dormancy measurements. A similar measurement procedure was carried out after the 7Y-DP up to 43 days as if the specimens had just been demolded. In other words, each one of the specimens had gone through at least 42 days of accelerated ASR expansion, then a 7-year dormancy period (dried), and again 43 days of accelerated ASR expansion.

3. RESULTS AND DISCUSSION

In the ASTM C 1260 method, aggregate is usually considered reactive if the cement-aggregate combinations (mortar bars) immersed in the 80 °C NaOH solution exhibit expansions greater than 0.10% after 14 days of exposure

Table 2. The chemical compositions of the cement and the SCMs

	SiO_2	Al_2O_3	Fe_2O_3	CaO	MgO	Na_2O	K_2O	Cl	SO_3	Free CaO	Loss on ignition	Total alkali
CEMI-1 (CEM I 42,5 R)	18.48	4.40	3.12	64.13	1.35	0.44	0.78	0.006	3.51	1.34	3.75	0.95
CEMII-1 (CEM II/B-M (L-W) 42,5 R)	23.36	7.98	3.50	54.03	1.81	1.23	0.92	0.073	3.40	2.32	2.85	1.83
CEMI-2 (CEM I 42,5 R)	20.68	6.24	2.34	62.28	1.50	0.23	0.97	0.008	3.12	0.95	2.14	0.87
CEMII-2 (CEM II/B-M (L-W) 42,5 R)	22.11	7.56	2.63	55.92	1.48	0.23	1.03	0.009	3.26	1.55	5.27	0.90
CEMI-3 (CEM I 42,5 R)	19.57	4.65	3.00	63.07	1.55	0.21	0.87	0.010	3.00		4.08	0.78
CEMII-3 (CEM II/A-M (V-LL) 42,5 R)	21.7	6.68	2.92	56.96	2.17	0.37	0.86	0.008	2.60		4.84	0.93
CEMI-4 (CEM I 42,5 R)	19.27	4.78	3.75	63.39	2.16	0.13	0.61	0.0085	2.92	1.81	2.99	0.53
CEMII-4 (CEM II/A-LL 42,5 R)	17.90	4.28	3.15	61.53	3.00	0.12	1.02	0.01	2.82	1.00	6.09	0.79
CF (Class-C fly ash)	41.52	19.52	4.34	22.61	2.26	1.02	1.41		3.11	4.24	0.91	1.94
FF (Class-F fly ash)	52.38	17.14	10.23	<0.00111	4.676	0.197	1.526	0.003	0.444	0.01	0.77	1.20
S (GG-Blast Furnace Slag)	43.58	10.62	1.06	33.19	7.29	0.26	0.77	0.0096	0.40		0.08	0.76

according to ASTM C 1778-20 [19]. In addition, combinations of SCMs and aggregates (ASTM C 1567) [17] that result in an expansion of less than 0.10% after 14 days are considered an "acceptable" level.

As mentioned earlier, the ASR-mitigation ability of SCMs, after all now, is a well-known phenomenon; therefore, this study endeavors to focus on the further expansion of various specimens following a relatively long ASR-dormant period. However, the 14-day expansions should be briefly evaluated. Despite the concerns regarding the severe test conditions of the accelerated mortar bar (AMB) test, Bérubé et al. [20] have emphasized that it can be applied for evaluation of the ASR-mitigation performance of SCMs as long as the test period is restricted to 14 days.

As shown in Figure 1, the performance of the blended cement, type II (CEMII), depends, obviously, on their additive contents. The CEMII-1 and CEMII-2 had significantly lower— of course, they were not below the critical level— expansions compared to those of the CEMs, while the expansions of the 3rd and 4th CEMIIs were almost the same with the CEMIs. Given the contents of the blended cement, these results are expected outcomes; the CEMII-1 and 2 include 22–24% fly ash, but none in the CEMII-4 and only ~7% in the CEMII-3.

The utilization of the FF and S had almost similar effects and could keep the expansion of the mortars, no matter the cement type, below the critical level. However, the CF couldn't do so. In other words, the 30% and 25% replacement ratios were insufficient for the class C fly ash. The relatively poorer performance of class C fly ashes is not an unexpected nor unknown outcome [11, 21].

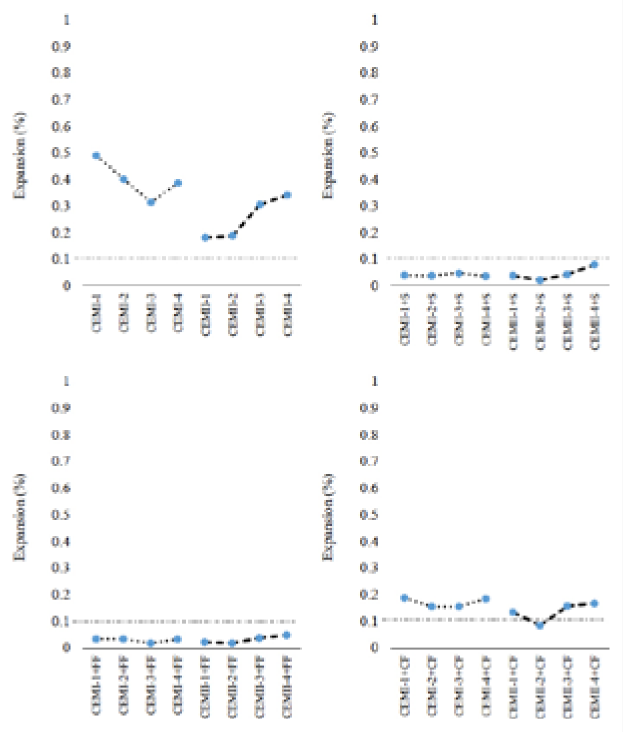

Figure 1. The expansions of the mortar bars before and after the 7Y-DP.

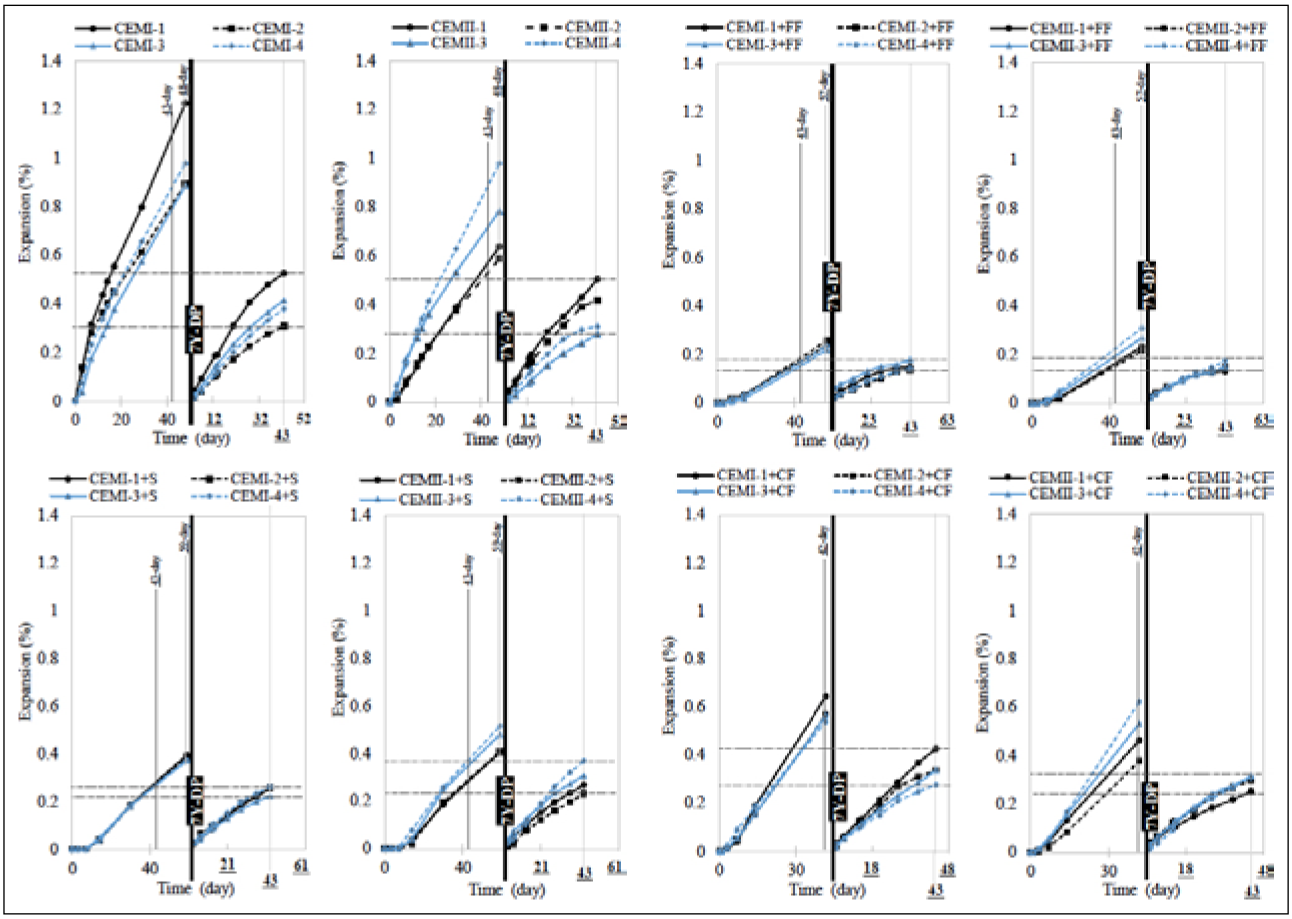

Figure 2. The expansions of the mortar bars before and after the 7Y-DP.

The expansions of the mortar bars after the 7Y-DP will be evaluated through two different types of graphs: 1) Ignoring the expansion values before the 7Y-DP as if the specimen were subjected to the NaOH solution for the first time, 2) Continuous (cumulative expansion) curves; as if there was no a dormancy period.

Figure 2 shows the expansions of the mortar bars before and after the 7Y-DP. It is obvious that the pre-7Y-DP (48 days) reactions considerably reduced the post-7Y-DP expansions of all CEMI mixtures as compared to the pre-7Y-DP's expansions — as pointed out earlier, this 7-year can be considered as a period in which ASR reactions is halted, for example, by preventing water ingress. This behavior is also valid for the plain CEMII mixtures; nevertheless, the extent of the decrement, as expected, is not high for the CEMII-1 and CEMII-2 mixtures—because the pre-7Y-DP expansions were lower than those of the other plain CEMI/CEMII mixtures. It must be mentioned that the CEMII-1 and 2 include 22–24% fly ash, but none in the CEMII-4 and only ~7% in the CEMII-3. Generally speaking, the higher the pre-7Y-DP expansion of a mixture reaches, the lower post-7Y-DP expansion would be—of course, compared to its pre-7Y-DP expansions. This fact is much more apparent in the plain CEMI mixtures with no ASR-mitigation mechanism. In other words, a great extent of the possible accelerated ASR reactions/or expansions—given the severe test condition of the AMB test, it is not necessary to have the same expansion level in the site even up to the end of service life of a real structure—that can be observed in these mixtures within a certain period had already occurred prior to the 7Y-DP.

The source of the post-7Y-DP expansions is the swelling of the old gel (absorption of water by the dry gel) and further ASR reaction, thus forming a new gel. The swelling of the old gel is more likely to be the dominant mechanism in the mixtures with higher pre-7Y-DP expansions, or at least, the contribution ratio of the post-7Y-DP expansions was higher in such mixtures. In other words, the residual available reactive silica would be limited in the mixtures in which there was no or insufficient SCM. Multon and Toutlemonde [8] showed that absorption of water (re-wetting) by old gel at any time of the life of an ASR-damaged structure can cause rapid swelling. This phenomenon was also reported in a few studies that dealt with the ASR reactivity of recycled concrete aggregates (RCA) obtained from ASR-suffered concrete. The expansion of old gel in the RCA is considered one of the contributing factors to the higher expansion (concrete prism test) of the RCA-containing concrete compared to the concrete containing the same virgin reactive aggregate [22, 23]. In addition, one of the reasons behind the lower expansion of the same RCA in AMBT was attributed to the loss of the old gel—that would swell by absorbing the moisture—as a result of further crushing of the coarse RCA to produce sand-size fraction for the test [22, 24].

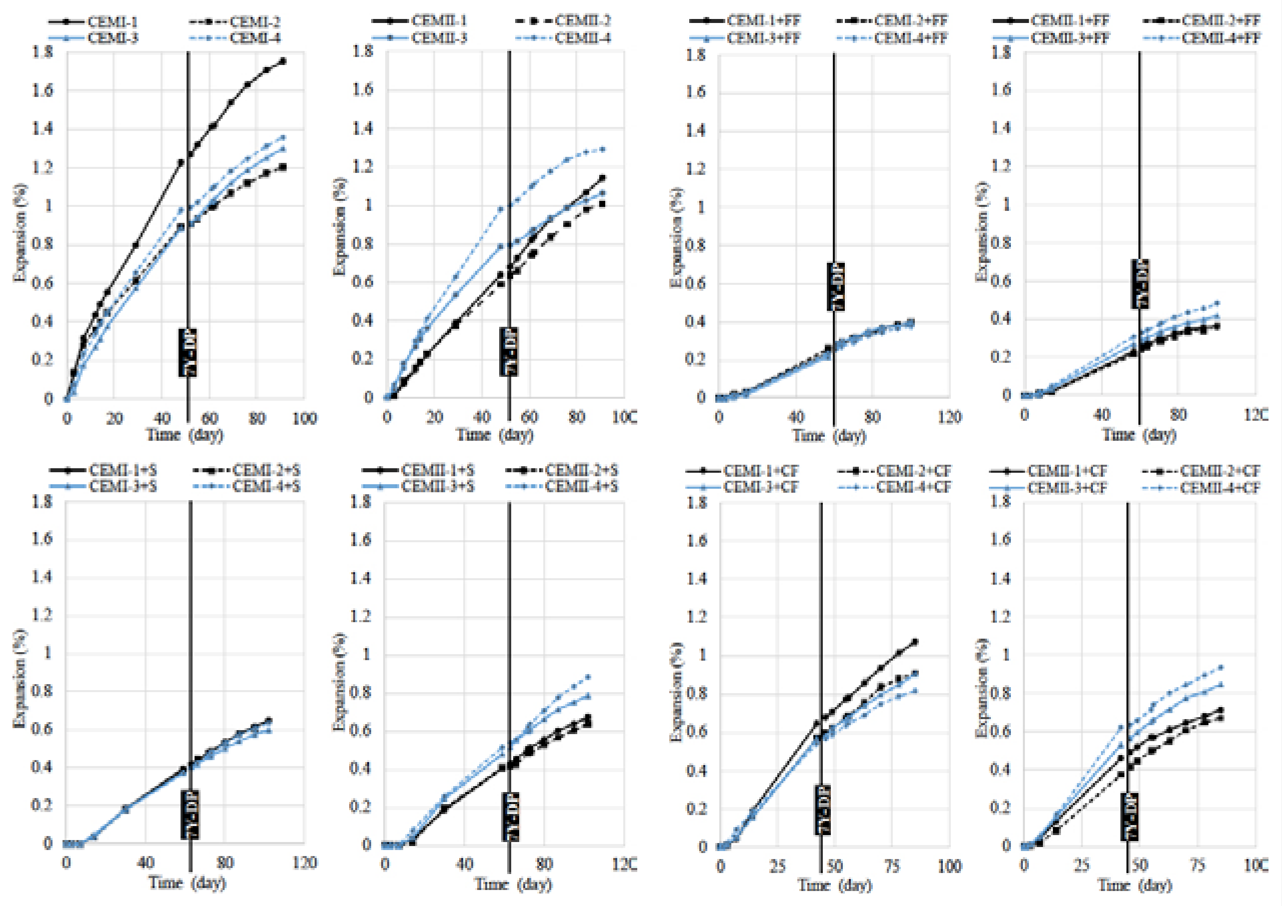

Figure 3. The cumulative expansions of the mortar bars before and after the 7Y-DP.

The post-7Y-DP expansions of S-containing and FF-containing mixtures were almost the same level as those of the pre-7Y-DP (43-day), even though the pre-7Y-DP exposure period (57–59 days) of them was 9–11 days longer than that of plain (48 days) mixtures. This finding shows that a significant amount of the ASR reaction/expansion was delayed owing to the ASR-mitigation effect of the S and FF; therefore, the specimens expanded almost like the pre-7Y-DP —except the first 14 days in which the ASR-mitigation effect of SCMs are much more dominant (it will be discussed later)— as if they were subjected to the NaOH solution for the first time and did not have an ASR history. It can be assumed that the contribution ratio of the new ASR-gel (post-7Y-DP gel) on the expansion was higher in these mixtures. On the other hand, the CF-containing mixtures acted almost like the plain mixtures because of the poorer ASR-mitigation performance of the class C fly ash. In other words, the 30% and 25% CF replacement ratios were not sufficient to delay the ASR reaction of, respectively, the CEMI and CEMII mixtures; therefore, a great extent of the possible accelerated ASR reactions/or expansions that can be observed in these mixtures within a certain period of time had already occurred before the 7Y-DP. It should be noted that the pre-7Y-DP exposure period (42 days) was even one day shorter than that of the post-7Y-DP; it was 15 and 17 days shorter than the post-7Y-DP exposure periods of S-containing and FF-containing mixtures, respectively. The abovementioned behavior would be more evident if the pre-7Y-DP exposure period were extended.

An interesting point comes out when the post-7Y-DP expansions are cumulatively added to the pre-7Y-DP curves as if there was no dormancy period (Fig. 3). Meanwhile, it should be noted that ASR-induced expansion is permanent and cumulative in the presence of water [8]. Multon and Toutlemonde [8] have reported that the shrinkage of ASR-suffered concrete due to drying at 30% RH had perfectly the same kinetics and range— no matter the conditions of ASR-induced damage and the direction of measurements— as for the sound concrete. They have stated that the drying shrinkage cannot balance the expansion; thus, the expansions and cracks are irreversible [8].

As shown in Figure 3, the appearance of the cumulative curves is almost like continuous ASR expansions, as if there were no 7Y-DP—especially S and FF-containing mixtures. Moreover, the increasing rates of the initial portion of the post-7Y-DP expansions almost match the pre-7Y-DP expansion trends. This behavior can be considered solid proof for the finding of Multon and Toutlemonde [8], who showed that water absorption by the dry old gel at any time can cause rapid swelling. If not, the formation of new gel—without the expansion of the old gel— would cause lower expansion rates. This phenomenon is much more critical for the mixtures in which there was no or insufficient SCM. As pointed out earlier, the residual available reactive silica

Table 3. The levene and ANCOVA analysis results

Mixture	Levene (Sig.)	ANCOVA P—T int. (Sig.)	Mixture	Levene (Sig.)	ANCOVA P—T int. (Sig.)
CEMI-1	0.207	0.001	**CEMI-1+S**	0.125	**0.88**>0.05
CEMII-1	0.666	0.003	**CEMII-1+S**	0.134	**0.124**>0.05
CEMI-2	0.126	0.001	**CEMI-2+S**	0.123	**0.108**>0.05
CEMII-2	0.559	0.001	**CEMII-2+S**	0.71	**0.47**>0.05
CEMI-3	0.186	0.001	CEMI-3+S	0.76	0.007
CEMII-3	0.096	0.001	**CEMII-3+S**	0.70	**0.40**>0.05
CEMI-4	0.134	0.001	**CEMI-4+S**	0.142	**0.276**>0.05
CEMII-4	0.070	0.001	**CEMII-4+S**	0.230	**0.916**>0.05
CEMI-1+FF	0.316	0.014	CEMI-1+CF	0.341	0.001
CEMII-1+FF	0.215	0.005	CEMII-1+CF	0.164	0.001
CEMI-2+FF	0.204	0.001	CEMI-2+CF	0.342	0.001
CEMII-2+FF	0.331	**0.37**>0.05	CEMII-2+CF	0.568	0.002
CEMI-3+FF	0.290	0.015	CEMI-3+CF	0.295	0.001
CEMII-3+FF	0.216	0.001	CEMII-3+CF	0.251	0.001
CEMI-4+FF	0.299	0.003	CEMI-4+CF	0.161	0.001
CEMII-4+FF	0.248	0.001	CEMII-4+CF	0.211	0.001

would be limited in these mixtures for the post-7Y-DP period, so the source of such post-7Y-DP expansion rates could not, certainly, be just the formation of a new gel.

As mentioned earlier, a significant amount of the ASR reaction was delayed owing to the ASR-mitigation effect of the S and FF; therefore, it can be assumed that the contribution ratio of the new ASR-gel (post-7Y-DP gel) on the expansion was higher in these mixtures. The reason behind the same increasing rate of the very initial portion of the post-7Y-DP expansions as the very last portion of the pre-7Y-DP expansions can be explained not only by the rapid swelling of the old gel but also by the early formation of new ASR gel—that no longer could be suppressed by the ASR-mitigation effect of SCMs in AMBT (80 °C NaOH solution). It should be remembered that AMBT can be applied to evaluate the ASR-mitigation performance of SCMs as long as the test period is restricted to 14 days [20]. There are vital differences between the ASR mitigation mechanisms of SCMs in the AMBT and those in other test methods. Reduction in the permeability of the matrix due to the pozzolanic reaction of SCMs is the dominant ASR-mitigation mechanism in the AMBT [25] as the solution continually supplies alkali. Therefore, higher impermeability strengthens the cementitious matrix's resistance against the ions' diffusion [25]. Diminution in the alkalinity of the matrix itself is, of course, one of the mechanisms, but it is not the main reason, as in the concrete prism methods [26]. Such a high impermeability was no longer the case beyond 14 days due to the continuous formation of cracks in the very early post-7Y-DP ASR reactions. Thus, the formation of new gel would be almost like that in the mixtures with insufficient SCMs. Although in natural structures and realistic conditions, such high expansion is not likely to occur in the SCM-containing mixtures, these results show that the ASR-mitigation capacity of SCMs would be limited after the repairing work conducted on a structure deteriorates under extreme conditions. But, of course, the primary purpose of using SCMs in this study was to scrutinize the effects of the pre-dormancy expansion levels on the post-dormancy expansions. Beyond 14-day, as mentioned earlier, AMBT is not a suitable test method for analyzing the ASR-mitigation behavior of SCMs; in future studies, the effect of dormancy period on the ASR-mitigation behavior could be investigated in the test methods having more realistic test conditions like concrete prism test.

In addition to assessing the initial increasing rates and the appearance of the curves, a series of statistical analyses were also conducted on each of the 32 mixtures to understand better the overall trends of the pre-7Y-DP and post-7Y-DP expansion curves. The Levene test was applied to measure the homogeneity of variances between the pre-7Y-DP and post-7Y-DP period data. According to the Levene test results, since "p" was less than 0.05 in all mixtures (Table 3), it was proven that the variances of both periods were homogeneous at the 95% significance level. Then, an analysis of covariance (ANCOVA) was applied between both periods.

In the ANCOVA test, the significance of "Period—Time" (P-T) interaction was used to assess whether the effect of time on a dependent variable, ASR expansions, differs across the periods. This interaction term captures any systematic change in the trend or rate between the two periods. If P (significance) is less than 0.05, it suggests that the relationship between time and expansion differed between periods. A significant P-T interaction would indicate that ASR trends changed after the 7Y-DP. In this case, either the dormancy or the pre-7Y-DP expansion/reaction levels —that is more likely to be, as discussed earlier in detail— might have altered the trend of post-7Y-DP expansions relative to that of pre-7Y-DP. On the other hand, no significant P-T interaction ($p \geq 0.05$) suggests that the ASR cumulative expansion curve continued after the 7Y-DP without substantial alteration. In other words, in such mixtures, the ASR reaction was delayed to a great extent —owing to the ASR-mitigation effect of some of the SCMs— so that it could be interpreted that the contribution ratio of the new ASR-gel (post-7Y-DP gel) on the expansion was much higher in these mixtures.

The P-T interaction's Sig. (p) values obtained from ANCOVA analysis of each mixture's data are presented in Table 3. The SCM-containing mixtures highlighted by the black color in the table have no significant P-T interaction ($p>0.05$), implying no statistically meaningful difference in slopes between the periods. In other words, the ASR reaction was delayed to a great extent, so the contribution ratio of the new ASR-gel (post-7Y-DP gel) to the expansion was much higher in these mixtures than in the other SCM-containing mixtures. As can be seen, this phenomenon was dominant only in the GGBFS-containing mixtures.

4. CONCLUSIONS

It can be interpreted from the test results that rapid swelling of old (and dry due to an extended drying/or dormancy period) ASR gel and formation of new gel can cause remarkable expansions again—no matter the mixture type or pre-dormancy period—in an ASR-suffered concrete (in which reactions were halted by dryness) whenever water can continually ingress into it for a long time. The post-dormancy expansion behavior of the mixtures without or with insufficient SCM revealed that the swelling of old gel was the dominant mechanism behind the expansions. On the other hand, the formation of new gel was the dominant reason in the specimens with sufficient SCM, which had lower pre-dormancy expansions due to the ASR-mitigation effect of the SCMs. The mechanisms above should be considered in the repair works of ASR-suffered structures. It can be concluded that an ASR-dormancy period established by water drainage or sealing of concrete, probably accompanied by repair work, will end if water can again ingress into the concrete. The level and rate of the post-dormancy expansions will be highly dependent on the extent of the pre-dormancy reactions, the gel formed, and the post-dormancy conditions. The other important parameters, such as the chemical compositions of old gel and post-dormancy moisture content, should be assessed in future studies.

ETHICS

There are no ethical issues with the publication of this manuscript.

DATA AVAILABILITY STATEMENT

The author confirm that the data that supports the findings of this study are available within the article. Raw data that support the finding of this study are available from the corresponding author, upon reasonable request.

CONFLICT OF INTEREST

The author declare that they have no conflict of interest.

FINANCIAL DISCLOSURE

The author declared that this study has received no financial support.

USE OF AI FOR WRITING ASSISTANCE

Not declared.

PEER-REVIEW

Externally peer-reviewed.

REFERENCES

[1] Stanton, T. E. (1942). Expansion of concrete through reaction between cement and aggregate. *Trans Am Soc Civ Eng, 107*(1), 54-84. [CrossRef]

[2] Daidai, T., Torii, K. (2008). *A proposal for rehabilitation of ASR-affected bridge piers with fractured steel bars*. Proc. of 13th Inter. Conf. on Alkali-aggregate Reaction in Concrete.

[3] Daidai, T., Andrade, O., Torii, K. (2012). *The maintenance and rehabilitation techniques for ASR-affected bridge piers with fracture of steel bars*. Proc. 14th Inter. Conf. on Alkali-aggregate Reaction in Concrete, Austin, Texas.

[4] Torii, K., Prasetia, I., Minato, T., Ishii, K. (2012). *The feature of cracking in prestressed concrete bridge girders deteriorated by alkali-silica reaction*. Proc. 14th Inter. Conf. on Alkali-aggregate Reaction in Concrete, Austin, Texas.

[5] Nomura, M., Komastubara, A., Fujimoto, K., Torii, K. (2013). *Evaluation of maintenance methods for ASR-damaged structures in Hokuriku district, Japan*. Proceedings, Third International Conference on Sustainable Construction Materials and Technologies, Kyoto, Japan.

[6] Luan, Y., Arasawa, T., Mutsuyoshi, H., & Kawana, R. (2021). Repair of alkali-silica reaction-induced cracks using bacteria: Crack recovery and other properties. *ACI Mater J, 118*(4), 133-142. [CrossRef]

[7] Bakker, J. D. (2008). Control of ASR related risks in the Netherlands. In *Proceedings of the 13th International Conference on Alkali-Aggregate Reaction in Concrete, Trondheim, Norway*, (pp. 16-20).

[8] Multon, S., & Toutlemonde, F. (2010). Effect of moisture conditions and transfers on alkali silica reaction damaged structures. *Cement Concr Res, 40*(6), 924-934. [CrossRef]

[9] ASTM International. (2019). *Standard specification for coal fly ash and raw or calcined natural pozzolan for use in concrete*. ASTM-C618.

[10] Yüksel, C., Mardani-Aghabaglou, A., Beglarigale, A., Yazıcı, H., Ramyar, K., & Andiç-Çakır, Ö. (2017). Alkali-silica reaction expansions and the extent of alkali leaching in concretes containing basalt and waste glass as aggregate. *Teknik Derg, 28*(2), 7865-7882. [CrossRef]

[11] Yüksel, C., Mardani-Aghabaglou, A., Beglarigale, A., Yazıcı, H., Ramyar, K., & Andiç-Çakır, Ö. (2016). Influence of water/powder ratio and powder type on alkali-silica reactivity and transport properties of self-consolidating concrete. *Mater Struct, 49*, 289-299. [CrossRef]

[12] Andiç-Çakır, Ö. (2007). *Investigation of test methods on alkali aggregate reaction*, [Doctoral dissertation], Ege University.

[13] Beglarigale, A., Yazıcı, H. (2013). The effect of alkali-silica reaction on steel fiber-matrix bond characteristics of cement based mortars. *Constr Build Mater, 47*, 845-860. [CrossRef]

[14] Beglarigale, A., & Yazici, H. (2014). Mitigation of detrimental effects of alkali-silica reaction in cement-based composites by combination of steel microfibers and ground-granulated blast-furnace slag. *J Mater Civ Engin, 26*(12), 04014091. [CrossRef]

[15] Çopuroğlu, O., Andiç-Çakir, Ö., Broekmans, M. A., & Kühnel, R. (2009). Mineralogy, geochemistry and expansion testing of an alkali-reactive basalt from western Anatolia, Turkey. *Mater Charact, 60*(7), 756-766. [CrossRef]

[16] ASTM International. (2007). *1260 Standard test method for potential alkali reactivity of aggregates (Mortar-Bar Method)*. ASTM C1260-07

[17] ASTM International. (2007). *Standard test method for determining the potential alkali-silica reactivity of combinations of cementitious materials and aggregate (Accelerated Mortar-Bar Method)*. ASTM International. ASTM C1567-07.

[18] Turkish Standards Institution. (2012). *Complementary Turkish Standard for the implementation of TS EN 206*. TS 13515.

[19] ASTM International. (2020). *Standard guide for reducing the risk of deleterious alkali-aggregate reaction in concrete*. ASTM International. ASTM C1778-20.

[20] Bérubé, M. A., Duchesne, J., & Chouinard, D. (1995). Why the accelerated mortar bar method ASTM C 1260 is reliable for evaluating the effectiveness of supplementary cementing materials in suppressing expansion due to alkali-silica reactivity. *Cement Concrete Aggregates, 17*(1), 26-34. [CrossRef]

[21] Shon, C. S., Sarkar, S. L., & Zollinger, D. G. (2004). Testing the effectiveness of Class C and Class F fly ash in controlling expansion due to alkali-silica reaction using modified ASTM C 1260 test method. *J Mater Civ Eng, 16*(1), 20-27. [CrossRef]

[22] Johnson, R., & Shehata, M. H. (2016). The efficacy of accelerated test methods to evaluate alkali silica reactivity of recycled concrete aggregates. *Constr Build Mater, 112*, 518-528. [CrossRef]

[23] Piersanti, M., & Shehata, M. H. (2022). A study into the alkali-silica reactivity of recycled concrete aggregates and the role of the extent of damage in the source structures: Evaluation, accelerated testing, and preventive measures. *Cem Concr Compos, 129*, 104512. [CrossRef]

[24] Piersanti, M. (2015). *Testing recycled concrete aggregate suffering different levels of alkali-silica reaction for use in new structures* [Doctoral dissertation], Toronto Metropolitan University.

[25] Xu, G. J., Watt, D. F., & Hudec, P. P. (1995). Effectiveness of mineral admixtures in reducing ASR expansion. *Cem Concr Res, 25*(6), 1225-1236. [CrossRef]

[26] Kawabata, Y., & Yamada, K. (2015). Evaluation of alkalinity of pore solution based on the phase composition of cement hydrates with supplementary cementitious materials and its relation to suppressing ASR expansion. *J Adv Concr Technol, 13*(11), 538-553. [CrossRef]

J Sustain Const Mater Technol, Vol. 9, Issue. 4, pp. 335–345, December 2024

Journal of Sustainable Construction Materials and Technologies
Web page info: https://jscmt.yildiz.edu.tr
DOI: 10.47481/jscmt.1600562

Journal of Sustainable Construction Materials and Technologies

Research Article

Thermophysical, strength, and electrical properties of clay modified with groundnut shell ash for building purposes

Joseph Bassey EMAH*[1], **Abayomi Ayodeji EDEMA**[2], **Sylvester Andrew EKONG**[1], **David Adeniran OYEGOKE**[3], **Ubong Williams ROBERT**[1], **Funke Olawumi FASUYI**[4]

[1]*Department of Physics, Akwa Ibom State University, Uyo, Nigeria*
[2]*Department of Geological Sciences, Archivers University, Owo, Nigeria*
[3]*Department of Chemistry, Archivers University, Owo, Nigeria*
[4]*Department of Science Laboratory Technology, Osun State College of Technology, Osun State, Nigeria*

ARTICLE INFO

Article history
Received: 03 June 2024
Revised: 04 November 2024
Accepted: 18 November 2024

Key words:
Abrasion, bulk density, electrical resistance, thermal insulation, water absorption coefficient

ABSTRACT

This study investigated the effects of Groundnut Shell Ash (GSA) on clay samples for making sustainable and low-cost building materials. The clay-GSA composites' physical, chemical, thermal, and mechanical properties were evaluated to assess their suitability for construction. The results revealed that the addition of GSA to the clay matrix had a significant impact on various properties of the samples. The physical characterization showed that GSA was finer and lighter than clay, making the composites more flowable. Chemical analysis indicated that clay and GSA were rich in SiO_2, Al_2O_3, and Fe_2O_3, with the clay exhibiting high SiO_2 content suitable for brick manufacturing. The composites had lower electrical resistance and higher conductivity with more GSA, which could enable temperature monitoring. Thermophysical testing demonstrated that the composites had better thermal insulation properties with more GSA, as shown by higher specific heat capacity and lower thermal diffusivity. The composites absorbed more water with more GSA, indicating higher porosity due to finer particles. The composites had similar bulk density to sandcrete blocks, implying adequate load capacity. Mechanical testing revealed lower flexural strength but higher abrasion resistance with more GSA. The optimal GSA content for strength was 10.0%. More GSA resulted in more voids and weaker bonds. The study provided insights for further research and development.

Cite this article as: Emah, J. B., Edema, A. A., Ekong, S. A., Oyegoke, D. A., Robert, U. W., & Fasuyi, F. O. (2024). Thermophysical, strength, and electrical properties of clay modified with groundnut shell ash for building purposes. *J Sustain Const Mater Technol*, 9(4), 335–345.

1. INTRODUCTION

Humans are blessed with various natural resources, including clay soil, which can be used for multiple applications. However, clay soil needs to be stabilized for shelter construction due to its inherent challenges, such as low strength, high volumetric change, and susceptibility to water damage [1]. One way to overcome these drawbacks is through thermal treatment, which involves firing clay bricks at high temperatures in a kiln [2, 3]. Another effective modification technique is chemical treatment using Portland cement [4, 5]. While these methods can improve the physico-mechanical properties of clay bricks, they also come with potential dangers. Thermal treatment requires high energy and emits carbon dioxide, contributing to environmental issues as a greenhouse gas. Cement dependency is uneco-

---

***Corresponding author.**
*E-mail address: josephemah@aksu.edu.ng

Published by Yıldız Technical University Press, İstanbul, Türkiye

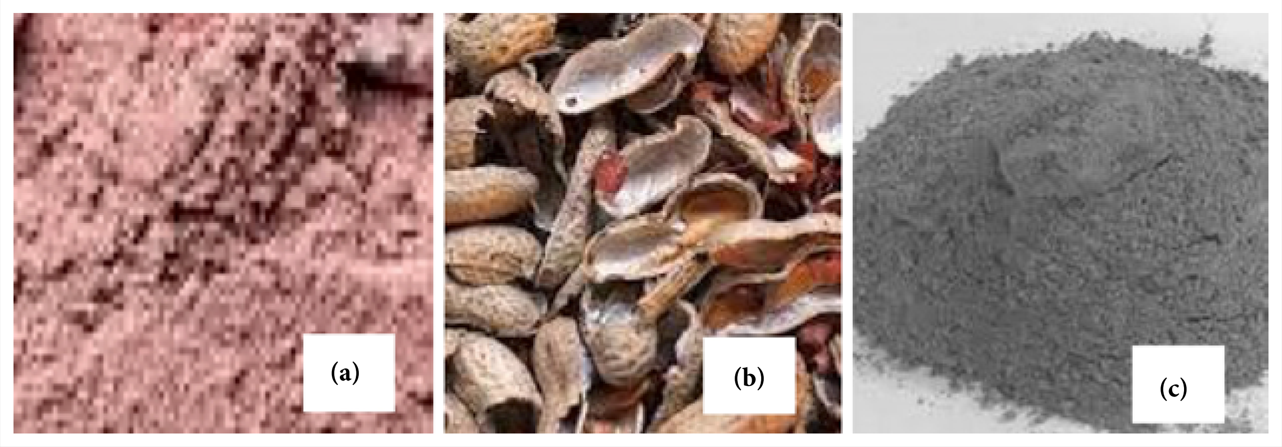

Figure 1. Appearance of **(a)** clay soil, **(b)** groundnut shells, and **(c)** GSA.

nomical due to rising building material costs [6], and the cement industry emits approximately 1.5456 million tons of carbon dioxide into the environment annually [7].

As a result, there has been a growing interest in finding alternative stabilizing agents, mainly focusing on waste valorization for sustainable economic purposes. Realizing that materials with high economic and financial values could be thrown into dustbins [8], man's yearning for the development of industrialization has taken an alarming dimension [9]. Researchers have explored the use of various waste materials, such as textile ash waste [10], rice husk ashes [11], sugarcane bagasse ashes [12], and corn cob ashes [13], which have shown promising potential in improving the properties of clay-based composites compared to cement. Fly ash and slag have also been studied for modifying clay soil with positive results [14–16]. These studies indicate that waste materials can be utilized effectively to enhance clay soil's mechanical and resistance properties for construction.

More so, Ubi et al. [17] treated lateritic soil with groundnut shell ash (GSA) for sub-base material in road construction. They observed that, at 6% content of the GSA, maximum dry density increased from 1.78Mg/m^3 to 2.15Mg/m^3 while the optimum moisture content decreased from 18.5% to 10%. Arthi et al. [18] used GSA to stabilize expansive clay. They found that the investigated properties (maximum dry density, moisture content, and unconfined compression strength) were satisfactory using 10% of the GSA. Sathiparan et al. [19] investigated the density, water absorption rate, compressive, flexural, impact, durability, and thermal characteristics of stabilized earth blocks produced by utilizing GSA. The study's conclusion suggests that the blocks have some promise for significantly reducing the amount of cement needed in the building sector. Sujatha et al. [20] utilized GSA to stabilize locally available highly compressible clay soil and then evaluated consistency limits, compaction characteristics, undrained cohesion, and modulus of elasticity of the soil. They reported that the GSA could be a viable economic alternative in constructing roads and stabilizing soil as a bearing medium.

This study investigates GSA-modified clay materials' thermophysical, strength, and electrical properties to determine their suitability for building purposes. In addition to examining the thermophysical and strength properties, specific electrical properties of the clay-based samples are also evaluated to assess their self-sensing capabilities. Groundnut shells were chosen for this study because they are underutilized and generated in large quantities as waste during groundnut (Arachis hypogaea L.) processing. Ajeigbe et al. [21] noted that groundnut yield could amount to 41.3 million tons from 24.6 million hectares, with China, India, Nigeria, the USA, and Mayaamer as the countries in which it is produced. The shells have been used for various purposes, such as sculpture making [22], biodiesel production [23], heavy metal adsorption [24], and carbon nano-sheet formation [25]. However, improper waste management practices, such as open burning and indiscriminate dumping, have adverse effects on the environment and public health, highlighting the urgent need to address this issue.

2. MATERIALS AND METHODS

2.1. Materials

The primary materials used in this study were groundnut shells, pink clay soil (with a wet and plastic nature), and potable water. These materials were obtained from Uyo Local Government Area of Akwa Ibom State, Nigeria.

2.2. Processing of the Clay and Preparation of Groundnut Shell Ash (GSA)

The clay soil (in small clusters) was spread on a large aluminum tray daily and dried under direct, intense sunlight. Each day, it was weighed after drying, put in a plastic container, and covered correctly. The drying process was discontinued when its weight remained constant for more than five consecutive days of the measurement. The dried clay soil was then crushed using a hammer and screened through a 2-mm sieve. The groundnut shells were soaked in water for 24 hours to remove impurities, followed by complete drying. The dried shells were incinerated in a 20 kW electric furnace at 500 °C for 3 hours to obtain groundnut shell ash (GSA). Figure 1 shows the appearance of the clay soil, groundnut shells, and GSA.

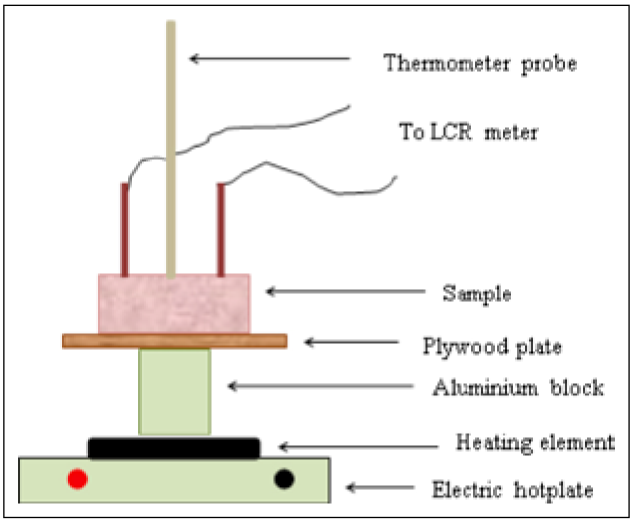

Figure 2. Setup for electrical resistance measurement.

2.3. Analysis of the Processed Materials

The clay and GSA were divided into two portions, with one portion of each material used for analysis. The angle of repose was determined using the fixed funnel method [1]. In this experiment, a material was poured through a plastic funnel onto a predetermined base with known roughness properties. As the material accumulated in a conical shape, the height and radius of the heap were measured within the range of 2.5 cm to 10.0 cm. Seven sets of these measurements were obtained and utilized to create a graph plotting the height against the radius. The angle of repose was then determined by calculating the slope of the graph and applying the inverse tangent rule:

$$\varnothing=\tan^{-1}(S) \quad (1)$$

where $\varnothing$ = angle of repose and S= slope of the graph.

Particle size analysis of the clay was conducted using the hydrometer method of sedimentation according to the standard procedure outlined in [26]. The loose density of the materials was calculated as the ratio of their mass to untapped volume [27]. Using an energy-dispersive X-ray fluorescence spectrometer (Spectro X-lab 2000), the materials were analyzed for chemical composition [28], and their loss on ignition was determined as the decrease in mass during firing [29].

2.4. Sample Fabrication

The remaining portions of each material were used to prepare the samples. Various volume fractions of GSA were considered on an untapped (loose) dry basis. The measured proportions of GSA were added to a fixed clay volume and thoroughly mixed. Moistening of each material mix was carried out using a 1:4 volumetric ratio of water to clay. The resulting mixtures were compacted with a load of 80 kg for 6 hours. Samples for electrical characteristics evaluation were formed into rectangular shapes measuring 50 mm x 28 mm x 15 mm and cured for 18 hours by sprinkling with water for six hours (to keep their surfaces moist) before testing. Two identical copper plates (each with a length of 49 mm and width of 10 mm) were used as electrodes, embedded to a depth of 5 mm and separated by a distance of 35 mm symmetrically from the ends of each sample. Samples for thermophysical property evaluation were developed in circular molds measuring 110 mm in diameter and 7 mm in thickness.

In comparison, samples for strength property examination were formed in molds with dimensions of 220 mm x 33 mm x 14 mm. The samples were fabricated in triplicates for each formulation, and all were dried to constant weight before testing. In this study, the samples were sun-dried for 14 days and then in an electric oven (Model N30C, Genlab) set at 105 °C for about 24 hours. Each sample was weighed before the commencement and at certain intervals during the oven-drying schedule. This oven-drying and weighing process was continuous until no further reduction was noticed in the mass.

2.5. Sample Testing

2.5.1. Electrical Resistance, Temperature Coefficient of Resistance, and Thermal Constant

Figure 2 illustrates this study's setup employed for conducting electrical resistance measurements. A larger thermal insulant, specifically a plywood plate, was utilized to ensure a consistent upward heat flow from the hotplate through the test sample (without heat absorption from the sides). Additionally, an aluminum block (with a height of 80 mm and diameter of 75 mm) was employed to protect the plywood from potential damage caused by direct contact with the heating element.

Before initiating the heating process, the electrodes were adequately insulated with cotton wool. These electrodes were then connected to the probe of an LCR meter (Model No. 9183). Furthermore, a digital thermometer probe was securely clamped to establish firm contact with the top of the sample. The control dial on the hotplate was adjusted to a suitable level for controlling the heat flow.

During the heating process, temperature monitoring and measurement were carried out using the thermometer, and the resistance of the sample was read from the meter at five °C intervals starting from 30 °C. The mean resistance values and their corresponding standard error values were computed for each formulation.

The temperature coefficient of resistance was determined using the following equation:

$$\alpha = \left(\frac{\Delta R}{R_o \Delta T}\right) 100\ \% \quad (2)$$

where α represents the temperature coefficient of resistance, R_o is the electrical resistance at infinity, ΔR is the change in electrical resistance of the sample corresponding to a change in temperature, ΔT.

Furthermore, the value of the thermal constant, β, for each sample was deduced by plotting *ln* R against the inverse of the absolute temperature, T, based on the following relation [30–32]:

$$R = R_o \exp\left[\frac{\beta}{T}\right] \quad (3)$$

where R denotes the mean electrical resistance of the sample.

2.5.2. Water Absorption Coefficient and Bulk Density

The water absorption coefficient of the samples was evaluated using the technique described by Ekong et al. [33]. Figure 3 depicts the experimental setup, where a sample was suspended above water in a transparent vessel using a strong wire. The scale level was adjusted until the sample was submerged approximately 4 mm from its lower end. The timing of water penetration into the sample was initiated, and the mass of the sample was recorded every 15 seconds. At each time interval, the mass of absorbed water (the difference between the dry mass of the sample and the scale reading) was determined. The water absorption coefficient, w, was graphically deduced based on the acquired data using the following relation:

$$w = \frac{M_a}{(A\sqrt{t})} \quad (4)$$

where M_a represents mass of the absorbed water, A is the surface area of the sample through which water vertically penetrates, and t is the duration of water penetration.

Regarding bulk density, a digital weighing scale (S.METTLER - 600 g) was used to measure the mass of each dry sample. The bulk volume was determined using a modified water displacement method [34], and the bulk density was calculated as follows [35, 36]:

$$\rho = \frac{M_s}{V} \quad (5)$$

Where ρ denotes the bulk density of the sample, M_s represents the mass of the sample, and V is the bulk volume of the sample.

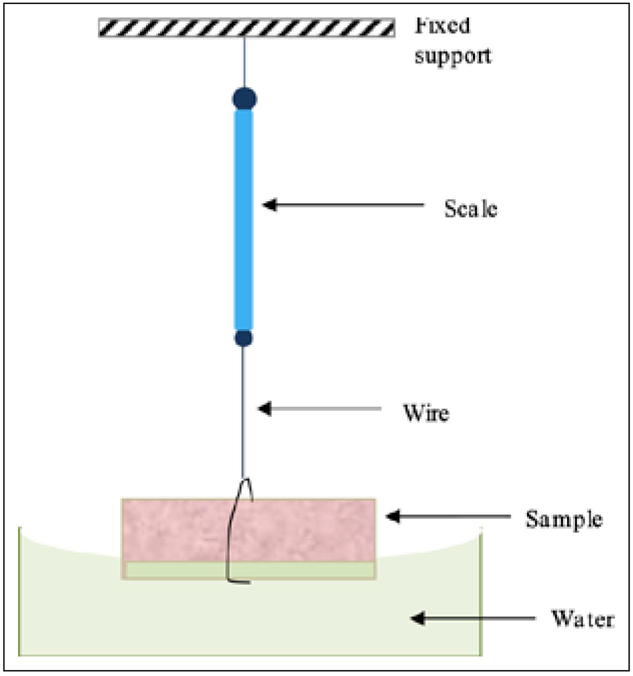

Figure 3. Setup for assessment of water absorption coefficient.

2.5.3. Thermal Conductivity

Each sample's thermal conductivity was assessed using the Modified Lee-Charlton's Disc Apparatus Technique, following the methodology described elsewhere [37]. The experimental setup included two identical discs (with a diameter of 110 mm and thickness of 10 mm) and a cylindrical aluminum block, as reported by Robert et al. [38]. An electric hotplate (Lloytron E4102WH) served as the heat source. Before heating, the sample's thickness was insulated with cotton wool. Temperature measurement was performed using two properly calibrated digital thermometers (Model 305) with type-K probes. During each measurement schedule, the control dial of the hotplate was adjusted to enable the temperature of the lower disc to rise and remain at 100 °C. When the steady state was established, the temperature-time data were taken. Origin Software (Version 2019) was utilized to generate temperature-time models based on the data collected during the steady state. The cooling rate of the disc was then determined, and it was used to calculate the thermal conductivity using the equation:

$$k = \left(\frac{Mcx}{A\Delta\theta}\right)\frac{dT}{dt} \quad (6)$$

where k = thermal conductivity of the sample, M = mass of the disc used, c = specific heat capacity of the disc, x = thickness of the sample under test, A = area of the sample's cross-section, Δθ = difference between the temperature of the upper and lower discs at steady state, and $\frac{dT}{dt}$ = cooling rate of the disc.

2.5.4. Specific Heat Capacity, Thermal Diffusivity, and Thermal Lag

The specific heat capacity of each sample was determined using SEUR's apparatus [39]. For heat exchange, an aluminum plate and a plywood plate with a thickness of 8 mm were employed as accessories. A square cavity with dimensions 60 mm x 60 mm was created in the center for embedding the accessories. The aluminum plate was heated in an electric oven to approximately 65 °C and quickly sandwiched between the plywood and the sample. During heat exchange, the aluminum plate supplied heat to both the sample and plywood plate, and the temperature of each accessory was monitored. Once thermal equilibrium was reached, assuming the conservation of heat energy, the obtained data were utilized to calculate the specific heat capacity as follows [40]:

$$C = \left(\frac{Q_a - Q_p}{M_s \delta T}\right) \quad (7)$$

where C= specific heat capacity of the sample, Q_a = amount of heat lost by the aluminum plate, Q_p = amount of heat gained by the plywood, M_s = mass of the sample, δT = rise in temperature of the sample.

The values obtained for bulk density, thermal conductivity, and specific heat capacity were utilized to compute the corresponding thermal diffusivity using the equation [41–44]:

$$\lambda = \frac{k}{\rho C} \quad (8)$$

where λ = thermal diffusivity of the sample.

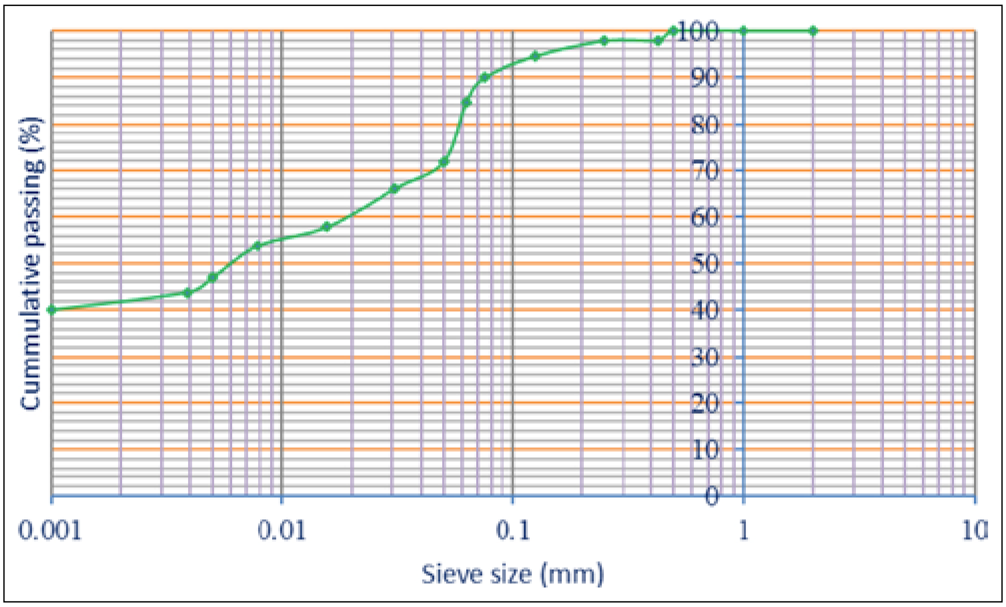

Figure 4. Particle size distribution of the clay soil used.

Table 1. Description of clay and GSA properties

Parameters	Clay	GSA
Loose density (kgm^{-3})	957.1	235.7
Index of plasticity (%)	23.4	–
Static angle of repose (°)	29.2	36.8

GSA: Groundnut shell ash.

Table 2. The chemical composition of the clay and GSA used

Major oxides		Proportion (%)	
Name	Formula	Clay	GSA
Silica	SiO_2	49.79	49.00
Alumina	Al_2O_3	30.68	12.00
Ferric oxide	Fe_2O_3	6.90	8.20
Lime	CaO	0.74	5.00
Magnesium oxide	MgO	0.21	6.74
Potassium oxide	K_2O	1.87	2.04
Sulphate	SO_3	–	6.21
Loss on ignition	LOI	8.61	4.00

GSA: Groundnut shell ash.

Furthermore, the thermal lag was calculated on a 24-hour basis using the formula [45]:

$$T_L = \left(\sqrt{\frac{T_p}{4\pi\lambda}}\right) x \tag{9}$$

where T_L = thermal lag of the sample, and T_p = period of the heating cycle.

2.5.5. Abrasion and Flexural Strength

Since the samples may undergo wear during their utilization as building materials, an abrasion test was conducted to predict their durability. During the test, the mass of each sample was recorded, and both surfaces were cleaned using a lint-free cloth. A hard shoe brush was used to rub against the sample surfaces in forward and backward movements for 50 strokes. A 0.5 kg weight was firmly attached to the top of the brush to ensure uniform pressure. The flaked sample was weighed, and the mass of flaking (decrease in sample mass) was determined. The susceptibility to abrasion, A_s, was calculated using the following formula [46]:

$$A_s = \left(\frac{M_f}{M_o}\right) 100\% \tag{10}$$

where A_s = abrasion, M_f = mass of flaking (decrease in the mass of the sample after being flaked), and M_o = mass of the sample before flaking.

Flexural strength investigation used the three-point bending method outlined in ASTM C67/67M [47]. An Electromechanical Universal Testing Machine (WDW-10) was utilized for the test. Each sample was supported at two points on the flexure arrangement of the machine and loaded at its center until failure occurred. At that point, the maximum load applied, F, and the width of the sample, b, were recorded and used to compute the flexural strength, σ, using the following equation [48]:

$$\sigma = \frac{3FL}{2bx^2} \tag{11}$$

where L = separation of the support points (span length).

For each test, all the samples were evaluated as described in this work, and the mean value for each property was calculated and tabulated along with its corresponding standard error value.

3. RESULTS AND DISCUSSION

Table 1 presents the index properties of the clay and GSA, describing their characteristics. It can be observed that the loose density of GSA is 76.84% lighter than that of the clay. This significant difference suggests that the particles of GSA are smaller compared to those of the clay, as the angle of repose is known to correlate inversely with par-

Table 3. The electrical resistance of the samples at various temperatures

Temperature, T (°C)	Electrical resistance, $R(10^3\ \Omega)$based on the GSA proportion in the samples				
	0.0%	10.0%	20.0%	30.0%	40.0%
30.0	876.0±0.3	94.0±0.2	80.6±0.4	72.8±0.3	59.7±0.2
35.0	512.0±0.2	82.1±0.2	59.1±0.3	56.9±0.3	49.7±0.3
40.0	300.0±0.4	74.9±0.4	50.4±0.3	49.0±0.2	40.6±0.2
45.0	198.0±0.2	68.5±0.3	42.8±0.2	40.3±0.4	34.2±0.3
50.0	143.0±0.4	61.2±0.2	38.7±0.2	35.0±0.4	26.4±0.4
55.0	106.0±0.3	52.9±0.3	34.7±0.4	30.9±0.2	21.5±0.3
60.0	71.0±0.3	46.4±0.2	29.0±0.2	25.3±0.3	15.9±0.2

GSA: Groundnut shell ash.

ticle size [49]. Additionally, based on the interpretation of flowability in terms of the angle of repose [50], the obtained values for both the clay and GSA indicate acceptable flow characteristics for manufacturing purposes.

Figure 4 illustrates the clay's gradation, showcasing the particle size distribution. It can be observed that the fraction of sand particles (2 mm–0.06 mm) is the least, followed by silt particles (0.06 mm–2 μm), and finally, clay-sized particles (<2 μm).

Table 2 presents the chemical compositions of the processed materials, clay, and GSA. In that order, both materials are predominantly composed of SiO_2, Al_2O_3, and Fe_2O_3. The clay contains approximately 50% SiO_2, which aligns with the findings of Velasco et al. [51] that clay used in brick factories typically contains 50% to 60% SiO_2. This indicates that the clay material used in this study is suitable for utilization in such factories. For the GSA, the combined proportions of SiO_2, Al_2O_3, and Fe_2O_3 amount to 69.20%. Additionally, the LOI value of the GSA (4.00%) is below the maximum requirement of 6.0%, and the fraction of SO_3 (6.21%) is slightly above 5%. These characteristics signify that the GSA belongs to the class C pozzolanic material according to ASTM C 618 [52].

Table 3 presents the electrical resistance of the developed samples at various temperatures. It can be observed that the electrical resistance of each sample decreases as the temperature increases. This indicates that the samples become more electrically conductive with rising temperatures. The electrical resistance and temperature relationship follows an exponential decay pattern, typical of a negative temperature coefficient (NTC) thermistor (Fig. 5). Robert et al. [53] proposed that this behavior is attributed to the activation energy associated with electron jumping across interfaces in the samples. This phenomenon can be utilized for effective temperature monitoring.

Furthermore, it is noteworthy that the electrical resistance decreases as the proportion of GSA increases in the sample. The inclusion of GSA at a level of 10.0% initiates a significant reduction in the resistance of the clay. The results demonstrate that the resistance of the control clay sample decreases by approximately 89.27%, 90.79%, 91.69%, and 93.18% when incorporating GSA at 10.0%, 20.0%, 30.0%, and 40.0%, respectively, to produce the studied samples. This observation may be attributed to calcium's higher reactivity than aluminum, as the GSA contains a higher proportion of CaO than the clay. Incorporating GSA as a filler in the clay matrix provides the resulting samples with advantages such as low cost, large sensing volume, and the absence of mechanical property loss. These samples exhibit a desirable response to temperature changes and can be applied as walling elements in building construction.

Table 4 displays the variations in the temperature coefficient of resistance and thermal constant of the samples with different GSA contents. It can be observed that the inclusion of GSA leads to samples with a higher temperature coefficient of resistance compared to the control sample

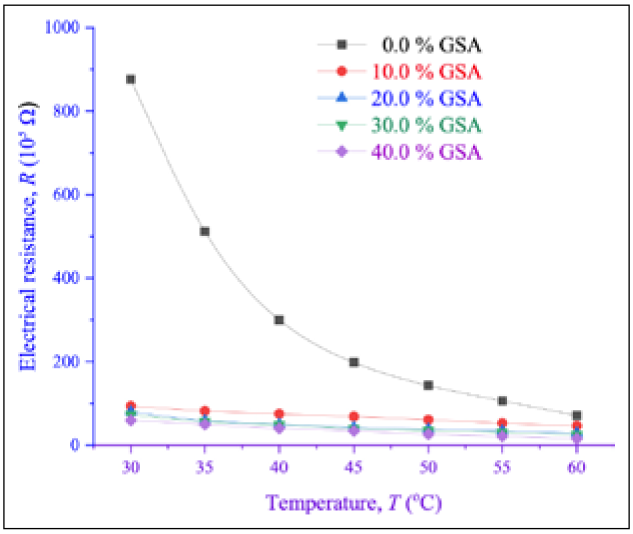

Figure 5. Variation of electrical resistance with temperature of the sample.

Table 4. Temperature coefficient of resistance and Thermal constant of the samples

Proportion of GSA (%)	α (%/°C)	β (K)
0.0	-3.06	8241
10.0	-1.69	2281
20.0	-2.13	3183
30.0	-2.17	3411
40.0	-2.45	4356

GSA: Groundnut shell ash.

Table 5. Thermophysical and strength properties of the samples

Proportion of GSA (%)	w (kg/m^2 h$^{0.5}$)	ρ (10^3 kgm^{-3})	k (Wm^{-1} K^{-1})	C (10^3 Jkg^{-1} K^{-1})	λ (10^{-7} m^2 s^{-1})	T_L (Mins.)	A_S (%)	σ (MPa)
0.0	27.56±0.03	1.662±0.002	0.531±0.004	1.654±0.004	1.93±0.02	22.00±0.09	1.008±0.002	2.894±0.003
10.0	27.14±0.02	1.622±0.004	0.469±0.003	1.671±0.002	1.73±0.01	23.23±0.07	1.024±0.001	2.903±0.002
20.0	28.05±0.04	1.584±0.003	0.436±0.004	1.710±0.004	1.61±0.02	24.14±0.13	1.042±0.002	2.886±0.002
30.0	28.43±0.02	1.568±0.002	0.409±0.006	1.811± 0.002	1.44±0.02	25.49±0.18	1.101±0.002	2.848±0.003
40.0	28.69±0.03	1.549±0.004	0.386±0.005	1.979±0.003	1.26±0.02	27.25±0.18	1.124±0.003	2.799±0.002

GSA: Groundnut shell ash.

(clay sample without GSA content). This indicates an improvement over the control sample, as temperature changes influence a more significant portion of resistance due to incorporating GSA into the clay matrix.

Regarding the values of the thermal constant, it can be inferred that the energy required to enhance electrical conduction is reduced by introducing GSA into the clay matrix. In both cases, the optimal GSA content for achieving the best performance of the samples is 10.0%. With this proportion, the highest temperature coefficient of resistance and the lowest thermal constant values are obtained.

The results of the thermophysical and strength tests conducted on the samples are presented in Table 5. The water absorption coefficient directly correlates with an increasing proportion of GSA. This observation can be attributed to variations in particle sizes between the materials used. Larger particles pack less efficiently, creating larger voids than smaller particles [54]. It has been reported that larger particle sizes result in lower water absorption than smaller ones [55]. These findings lend credence to the water absorption coefficient results in this study, indicating that the GSA particles are finer than those of the clay.

Consequently, as the fraction of GSA increases, the narrowing of the capillary pores is enhanced, thus leading to an increased water absorption coefficient for the samples. However, the value obtained by adding 10% GSA contradicts this assertion, possibly due to the optimal reaction between lime, alumina, and silica in the GSA at that level, enhancing inter-particle packing and micro-aggregation, thereby reducing inter-particle voids. Similar observations were noted in testing clay-based composites containing hydrothermally-calcined waste paper ash materials [1]. Despite the observed variations, all water absorption coefficients obtained in this study fall within the recommended range (20 to 30 kg/m^2 h$^{0.5}$) for solid blocks [33].

The mean bulk density values of the samples exceed the minimum value (1500 kg/m^3) specified for sandcrete blocks made with lightweight aggregates [56] by 3.27% to 10.80%. However, these percentage differences are insignificant, suggesting that the samples could provide a load capacity comparable to that of sandcrete blocks. Samples with 10.0% and 20.0% GSA content exhibit bulk density values similar to those reported for sandcrete blocks with 10% sand partially replaced with untreated coconut husk, cured for 7 days (1575 kg/m^3) and 28 days (1612 kg/m^3) respectively [57]. It is also noteworthy that the thermal conductivity of the samples is slightly lower than the values reported for red clay (0.545 W/mK), white clay (0.559 W/mK), and laterite (0.737 W/mK) recommended for passively cooled building designs [58].

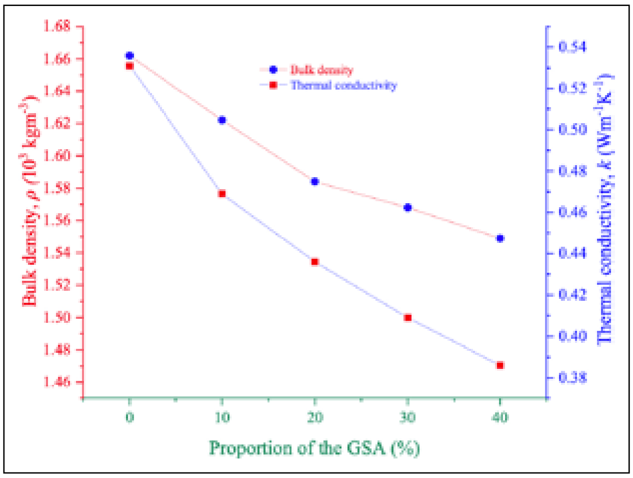

Figure 6. Variation of bulk density and thermal conductivity with proportion of the GSA.

Figure 6 illustrates the inverse trends of bulk density and thermal conductivity with the proportion of GSA used. The characteristics of GSA can explain these tendencies. GSA is lighter than the clay soil used in this study, and therefore, an increased proportion of GSA results in a further reduction in the bulk density of the resulting sample. Additionally, incorporating GSA increases the number of pores/voids in the samples. As the samples are dehydrated, the primary phase for thermal energy transmission is the gaseous phase, predominantly filled with air. Since air is a poor heat conductor, the thermal conductivity of the samples decreases as the fraction of GSA increases due to the presence of more air in the samples. This resonates with the assertion that thermal conductivity is a function of bulk density [59].

The improvement in thermal insulation performance of the samples is evident in the higher values of specific heat capacity as the proportion of GSA is increased. With a higher GSA content, the heat-storing ability of a kilogram of the samples is enhanced before a unit change in temperature. This is supported by the observed reduction in thermal diffusivity values as more GSA is incorporated. Thermal diffusivity is directly related to thermal conductivity but is inversely associated with the samples' bulk density and specific heat capacity. By including GSA, thermal conductivity and bulk density are reduced while specific heat capacity is increased.

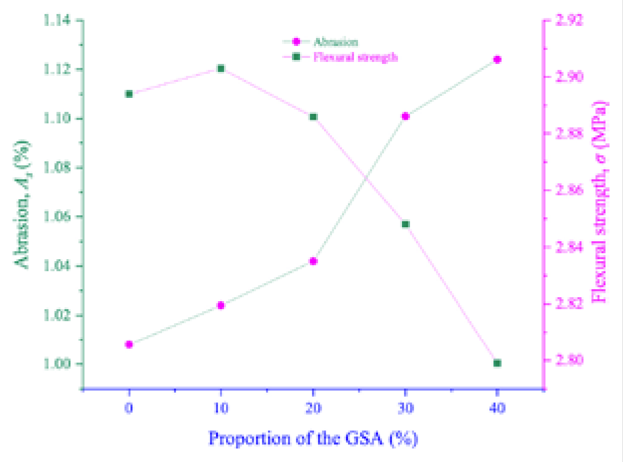

Figure 7. Variation of abrasion and flexural strength with proportion of the GSA.

Consequently, as the proportion of GSA increases, the samples exhibit enhanced resistance to heat transmission and increased demand for heat to effect a change in temperature. This results in a reduced rate of thermal energy diffusion across the thickness of the samples. These tendencies indicate that GSA can improve the thermal insulation of the samples, with a higher proportion of GSA correlating with increased heat-insulating ability. The higher value of thermal lag due to the incorporation of more GSA can be attributed to the trend in thermal diffusivity, suggesting that GSA has the potential to increase the time difference between the maximum temperatures at the outside and inside of the samples when subjected to periodic heating as walling materials in buildings.

The abrasion test results on the samples characterize their flakiness, while the flexural strength values indicate their ability to withstand bending stress during service. A material with a lower abrasion value maintains its original structure and appearance better by resisting mechanical wear [60]. Figure 7 clearly shows that the proportion of GSA influences these properties differently. Abrasion increases with an increasing proportion of GSA as the internal bond between clay particles is weakened by the presence of GSA. However, the effect is not very pronounced, suggesting that the susceptibility to mechanical wear caused by incorporating GSA into the clay matrix may not significantly impact the durability of the clay-modified samples as potential building construction materials.

The chemical composition of GSA highly influences the flexural strength of the samples. During hydration, the chemical phases formed from GSA's calcium, silicates, and aluminate contents play a crucial role in strength development. Specifically, SiO_2 aids in strength development, and in the presence of water, CaO first forms $Ca(OH)_2$, which then yields $CaCO_3$ with the availability of carbon dioxide for hardening and strength development. Flexural strength increases up to a 10% GSA incorporation level, beyond which it progressively declines. This suggests that 10% is the optimum level for achieving maximum strength through the reaction of silica. In other words, as the GSA undergoes a pozzolanic response at a 10% loading level, its silica content dissolves alongside the alumina. It reacts with the calcium hydroxide continuously to form a gel. The presence of water in the process increases the amount of the gel. Since the GSA has finer particles, it is incorporated into the clay matrix as filler. As such, the gel formed can fill the voids in the clay, enhancing particle binding, thereby resulting in a gain of strength by the sample. Further increases in the proportion of GSA lead to excess fractions that are not effectively utilized, resulting in increased void fractions and pores that weaken the inter-particle bonding in the developed composites.

Apart from the fact that the GSA is cheap as a result of being derived from readily available waste material, reliance on GSA for clay stabilization is more economical than dependence on cement. This can be seen in energy consumption (which portrays cost implications if monetary values are considered at a given time). For instance, cement production needs 3.4 GJ of thermal energy (in the wet process) and 110 kWh of electrical power on average, as Afkhami et al. [61] reported. The 20 kW furnace used for 3 hours to prepare the GSA in this study consumes about 216 MJ of electrical energy. It is obvious that even if the production of the GSA is repeated ten times, the total energy consumption would still be less compared to the case with cement.

4. CONCLUSION

In conclusion, this study investigated the properties and performance of clay samples modified with Groundnut Shell Ash (GSA) for potential application as building materials. The key results obtained and deductions drawn from the study can be summarized as follows:

- Physical Properties of the materials: The loose density and angle of repose indicated that the GSA had smaller particle sizes than the clay, making it lighter and more flowable. The particle size distribution of the clay confirmed the presence of sand, silt, and clay-sized particles.
- Chemical Composition: Both the clay and GSA were dominated by SiO_2, Al_2O_3, and Fe_2O_3. The clay contained a high proportion of SiO_2, making it suitable for brick factories. The GSA exhibited pozzolanic properties according to ASTM C 618, making it a potential candidate for construction materials.
- Electrical Resistance: The addition of GSA to the clay matrix significantly reduced electrical resistance. Higher proportions of GSA led to more significant decreases in resistance, with 10.0% GSA content showing the most pronounced effect. This suggests that GSA incorporation can improve electrical conductivity and make the samples suitable for temperature monitoring applications.
- Thermophysical Properties: The thermal insulation performance of the samples improved with increasing proportions of GSA. Specific heat capacity increased while

thermal diffusivity decreased. The highest thermal lag was observed at higher GSA content, indicating a potential for improved energy efficiency and temperature regulation in building applications.

- Water Absorption and Bulk Density: The water absorption coefficient increased with the proportion of GSA, indicating that the GSA particles were finer than the clay. All samples exhibited acceptable water absorption coefficients within the recommended range for solid blocks. Bulk density values were comparable to sandcrete blocks, suggesting that the samples could provide adequate load capacity.
- Flexural Strength and Abrasion Resistance: Flexural strength decreased with increasing GSA content, while abrasion resistance increased. The nature and composition of GSA influenced these properties, with silica playing a crucial role in strength development. Optimum strength was achieved at a 10% GSA incorporation level, beyond which further increases in GSA content weakened the inter-particle bonding and reduced strength.

Based on these results, it can be deduced that adding GSA to clay samples has significant implications for their properties and performance as building materials. The modified samples exhibited improved electrical conductivity, enhanced thermal insulation, and adequate water absorption characteristics. Incorporating GSA also influenced flexural strength and abrasion resistance, with an optimum GSA content of 10.0% yielding the best results.

Overall, this study provides valuable insights into the potential utilization of clay-GSA composites as sustainable and cost-effective materials for construction applications. The findings contribute to understanding their physical, chemical, and thermal properties, paving the way for further research and development in this field.

ETHICS

There are no ethical issues with the publication of this manuscript.

DATA AVAILABILITY STATEMENT

The authors confirm that the data that supports the findings of this study are available within the article. Raw data that support the finding of this study are available from the corresponding author, upon reasonable request.

CONFLICT OF INTEREST

The authors declare that they have no conflict of interest.

FINANCIAL DISCLOSURE

The authors declared that this study has received no financial support.

USE OF AI FOR WRITING ASSISTANCE

Not declared.

PEER-REVIEW

Externally peer-reviewed.

REFERENCES

[1] Robert, U. W., Etuk, S. E., Emah, J. B., Agbasi, O. E., & Iboh, U. A. (2022). Thermophysical and mechanical properties of clay-based composites developed with hydrothermally calcined waste paper ash nanomaterial for building purposes. *Int J Thermophys, 43*(5), 1-20. [CrossRef]

[2] Tsega, E., Mosisa, A., & Fuga, F. (2017). Effects of firing time and temperature on physical properties of fired clay bricks. *Am J Civ Eng, 5*(1), 21-26. [CrossRef]

[3] Rondonane, H. T., Mbeny, J. A., Bayiga, E. C., & Ndjigui, P. D. (2020). Characterization and application tests of kaolinite clays from Aboudeia (Southeastern Chad) in fired bricks making. *Sci Afr, 7*, e00294. [CrossRef]

[4] Garzõn, E., Cano, M., O'Kelly, B. C., & Sãnchez-Soto, P. J. (2015). Phyllite clay-cement composites having improved engineering properties and material applications. *Appl Clay Sci, 114*, 229-233. [CrossRef]

[5] Santos, L. M. A., Neto, J. A. S., & Azerẽdo, A. F. N. (2020). Soil characterisation for adobe mixtures containing Portland cement as a stabiliser. *Revista Matẽria, 25*(1), 1-10. [CrossRef]

[6] Ihuah, P. W. (2015). Building materials costs increases and sustainability in real estate development in Nigeria. *Afr J Econ Sustain Dev, 4*(3), 218-233. [CrossRef]

[7] Dunuweera, S. P., & Rajapakse, R. M. G. (2018). Cement types, composition, uses and advantages of nanocement, environmental impact on cement production, and possible solutions. *Adv Mater Sci Eng, 2018*, 4158682. [CrossRef]

[8] Etuk, S. E., Robert, U. W., Emah, J. B., & Agbasi, O. E. (2021). Dielectric properties of eggshell membrane of some select bird species. *Arab J Sci Eng, 46*, 769-777. [CrossRef]

[9] Etuk, S. E., Agbasi, O. E., Abdulrazzaq, Z. T., & Robert, U. W. (2018). Investigation of thermophysical properties of Alates (swarmers) termites wing as potential raw material for insulation. *Int J Sci World, 6*(1), 1-7. [CrossRef]

[10] Binici, H., Gemci, R., Aksogan, O., & Kaplan, H. (2010). Insulation properties of bricks made with cotton and textile ash wastes. *Int J Mater Res, 101*(7), 894-899. [CrossRef]

[11] Agbede, O., & Joel, M. (2011). Effect of rice husk ash (RHA) on the properties of Ibaji burnt clay bricks. *Am J Sci Ind Res, 2*(4), 674-677. [CrossRef]

[12] Reddy, K. S., Vivek, P. S., & Chambrelin, K. S. (2017). Stabilization of expansive soil using bagasse ash. *Int J Civ Eng Technol, 8*(4), 1730-1736.

[13] Sankar, V. S., Raj, P. D. A., & Raman, S. J. (2019). Stabilization of expansive soil by using agricultural waste. *Int J Eng Adv Technol, 8*(3S), 154-157.

[14] Mandal, S., & Singh, J. P. (2016). Stabilization of soil using ground granulated blast furnace slag and fly ash. *Int J Innov Res Sci Eng Technol, 5*(12), 21121-21126.

[15] Nath, B. D., Molla, M. K. A., & Sarkar, G. (2017). Study on strength behavior of organic soil stabilized with fly ash. *Int Scholarly Res Notices, 2017*, 5786541. [CrossRef]

[16] Dayalan, J. (2016). Comparative study on stabilization of soil with ground granulated blast furnace slag (GGBS) and fly ash. *Int Res J Eng Technol, 3*, 2198-2204. [CrossRef]

[17] Ubi, S. E., Nyak, E. E., & Agbor, R. B. (2022). Enhancement of soil stability with groundnut shell ash. *J Civ Eng Res, 12*(1), 1-7.

[18] Arthi, A. J. J., Aarthi, G., Kumar, V. V., & Vishnuprriya, U. (2023). Stabilization of clay using groundnut shell ash and sugarcane bagasse ash. *Key Eng Mater, 960*(1), 197-204. [CrossRef]

[19] Sathiparan, N., Anburuvel, A., Selvam, V. V., & Vithurshan, P. A. (2023). Potential use of groundnut shell ash in sustainable stabilized earth blocks. *Constr Build Mater, 393*, 132058. [CrossRef]

[20] Sujatha, E. R., Dharini, K., & Bharathi, V. (2016). Influence of groundnut shell ash on strength and durability properties of clay. *Geomech Geoeng, 11*(1), 20-27. [CrossRef]

[21] Ajeigbe, H. A., Waliyar, F., Echekwu, C. A., Ayuba, K., Motagi, B. N., Eniayeju, D., & Inuwa, A. (2014). *A farmer's guide to groundnut production in Nigerian*. International Crops Research Institute for the Semi-Arid Tropics.

[22] Sakoalia, K. D., Adu-Agyem, J., Amenuke, D. A., & Deffor, B. (2019). Groundnut shell (powder) as an alternative sculpture material for fine art: The case of Salaga Senior High School, Ghana. *J Arts Humanit, 8*(4), 30-43.

[23] Udeh, B. A. (2018). Bio-waste transesterification alternative for biodiesel production: A combined manipulation of lipase enzyme action and lignocellulosic fermented ethanol. *Asian J Biotechnol Bioresour Technol, 3*(3), 1-9. [CrossRef]

[24] Sowmya, T. A., Gayavajitha, E., Kanimozhi, R., & Subalakshmi, R. (2018). Removal of toxic metals from industrial wastewater using groundnut shell. *Int J Pure Appl Math, 119*(15), 629-634.

[25] Kanokon, N., Andrea, S., & Peter, B. (2018). Influence of KOH on the carbon nanostructure of peanut shell. *Resol Discov, 3*(2), 29-32. [CrossRef]

[26] ASTM D7928. (2017). *Standard test method for particle-size distribution (gradation) of fine-grained soils using the sedimentation (hydrometer) analysis*. ASTM International.

[27] Robert, U. W., Etuk, S. E., Agbasi, O. E., Okorie, U. S., Abdulrazzaq, Z. T., Anonaba, A. U., & Ojo, O. T. (2021). On the hygrothermal properties of sandcrete blocks produced with sawdust as partial replacement of sand. *J Mech Behav Mater, 30*(1), 144-155. [CrossRef]

[28] Bediako, M., & Amankwah, E. O. (2015). Analysis of chemical composition of cement in Ghana: A key to understand the behaviour of cement. *Adv Mater Sci Eng, 2015*, 1-5. [CrossRef]

[29] Inegbenebor, A. I., Inegbenebor, A. O., Mordi, R. C., Kalada, N., Falomo, A., & Sanyaolu, P. (2016). Determination of the chemical compositions of clay deposits from some part of South West Nigeria for industrial applications. *Int J Appl Sci Biotechnol, 4*(1), 21-26. [CrossRef]

[30] Adeniran, A. O., Akankpo, A. O., Etuk, S. E., Robert, U. W., & Agbasi, O. E. (2022). Comparative study of electrical resistance of disc-shaped compacts fabricated using calcined clam shell, periwinkle shell, and oyster shell nanopowder. *Kragujevac J Sci, 44*, 25-36. [CrossRef]

[31] Robert, U. W., Etuk, S. E., Agbasi, O. E., Iboh, U. A., & Ekpo, S. S. (2020). Temperature-dependent electrical characteristics of disc-shaped compacts fabricated using calcined eggshell nanopowder and dry cassava starch. *Powder Metall Prog, 20*(1), 12-20. [CrossRef]

[32] Munifah, S. S., Wiendartun, W., & Aminudim, A. (2018). Design of temperature measuring instrument using NTC thermistor of Fe_2TiO_5 based on microcontroller ATmega 328. *J Phys Conf Ser, 1280*, 022052. [CrossRef]

[33] Ekong, S. A., Oyegoke, D. A., Edema, A. A., & Robert, U. W. (2022). Density and water absorption coefficient of sandcrete blocks produced with waste paper ash as partial replacement of cement. *Adv Mater Sci, 22*(4), 85-97. [CrossRef]

[34] Robert, U. W., Etuk, S. E., & Agbasi, O. E. (2019). Bulk volume determination by modified water displacement method. *Iraqi J Sci, 60*(8), 1704-1710. [CrossRef]

[35] Ekpenyong, N. E., Ekong, S. A., Nathaniel, E. U., Thomas, J. E., Okorie, U. S., Robert, U. W., Akpabio, I. A., & Ekanem, N. U. (2023). Thermal response and mechanical properties of groundnut shells' composite boards. *Res J Sci Technol, 3*(1), 42-57.

[36] Robert, U. W., Etuk, S. E., Ekong, S. A., Agbasi, O. E., Akpan, S. S., & Inyang, N. J. (2023). Paper-sawdust composites: Fabrication and comparison in terms of heat transfer and strength properties. *Struct Environ, 15*(1), 38-48. [CrossRef]

[37] Robert, U. W., Etuk, S. E., Agbasi, O. E., & Okorie, U. S. (2021). Quick determination of thermal conductivity of thermal insulators using a modified Lee-Charlton's disc apparatus technique. *Int J Thermophys, 42*(8), 1-20. [CrossRef]

[38] Robert, U. W., Etuk, S. E., Agbasi, O. E., Okorie, U. S., Ekpenyong, N. E., & Anonaba, A. U. (2022). On the modification of Lee-Charlton's disc apparatus technique for thermal conductivity determination. *Res J Sci Technol, 2*(3), 1-17.

[39] Etuk, S. E., Robert, U. W., & Agbasi, O. E. (2020). Design and performance evaluation of a device for determination of specific heat capacity of thermal insulators. *Beni-Suef Univ J Basic Appl Sci, 9*(1), 1-7. [CrossRef]

[40] Etuk, S. E., Robert, U. W., & Agbasi, O. E. (2022). Thermophysical properties of oil empty fruit bunch peduncle for use as a mulching material. *J Oil Palm Res, 35*, 448-455. [CrossRef]

[41] Etuk, S. E., Robert, U. W., & Agbasi, O. E. (2021). Investigation of heat transfer and mechanical properties of Saccharum officinarum leaf boards. *Int J Energy Water Resour, 6*(1), 95-102. [CrossRef]

[42] Umoren, G. P., Udo, A. O., & Udo, I. E. (2023). Suitability of Lagenaria breviflora rind-filled plaster of Paris ceilings for building design. *Res J Sci Technol, 3*(2), 1-14.

[43] Etuk, S. E., Robert, U. W., Agbasi, O. E., & Ekpo, S. S. (2022). A study on thermophysical properties of clay from Agbani: Its assessment as potential walling material for naturally-cooled building design. *Epitoanyag-J Silicate Based Compos Mater, 74*(3), 93-96. [CrossRef]

[44] Robert, U. W., Etuk, S. E., Agbasi, O. E., Ekong, S. A., Nathaniel, E. U., Anonaba, A. U., & Nnana, L. A. (2021). Valorisation of waste carton paper, melon seed husks, and groundnut shells to thermal insulation panels for structural applications. *Polytechnica, 4*, 97-106. [CrossRef]

[45] Robert, U. W., Etuk, S. E., Agbasi, O. E., Okorie, U. S., & Lashin, A. (2021). Hygrothermal properties of sandcrete blocks produced with raw and hydrothermally-treated sawdust as partial substitution materials for sand. *J King Saud Univ Eng Sci, 2021*, 10.005. [CrossRef]

[46] Robert, U. W., Etuk, S. E., Iboh, U. A., Umoren, G. P., Agbasi, O. E., & Abdulrazzaq, Z. T. (2020). Thermal and mechanical properties of fabricated plaster of Paris filled with groundnut seed coat and waste newspaper materials for structural application. *Építôanyag-J Silicate Based Compos Mater, 72*(2), 72-78. [CrossRef]

[47] ASTM C67/67M. (2021). *Standard test methods for sampling and testing brick and structural clay tile*. ASTM International.

[48] Robert, U. W., Etuk, S. E., Agbasi, O. E., Ekong, S. A., Abdulrazzaq, Z. T., & Anonaba, A. U. (2021). Investigation of thermal and strength properties of composite panels fabricated with plaster of Paris for insulation in buildings. *Int J Thermophys, 42*(2), 1-18. [CrossRef]

[49] Lu, H., Guo, X., Liu, Y., & Gong, X. (2015). Effects of particle size on flow mode and flow characteristics of pulverised coal. *Kona Powder Part I, 32*, 143-153. [CrossRef]

[50] USP. (2007). Powder flow. In *USP 30-NF 25*. United States Pharmacopeial Convention.

[51] Velasco, P. M., Ortíz, M. P. M., Giró, M. A. M., & Velasco, L. M. (2014). Fired clay bricks manufactured by adding wastes as sustainable construction material - A review. *Constr Build Mater, 63*, 97-107. [CrossRef]

[52] ASTM C618. (2023). *Standard specification for coal fly ash and raw or calcined natural pozzolan for use in concrete*. ASTM International.

[53] Robert, U. W., Etuk, S. E., Ekong, S. A., Agbasi, O. E., Ekpenyong, N. E., Akpan, S. S., & Umana, E. A. (2022). Electrical characteristics of dry cement-based composites modified with coconut husk ash nanomaterial. *Adv Mater Sci, 22*(2), 65-80. [CrossRef]

[54] Alssoun, B. M., Hwang, S., & Khayat, K. H. (2015). Influence of aggregate characteristics on workability of superworkable concrete. *Mater Struct, 49*(1), 597-609. [CrossRef]

[55] Kang, M., & Weibin, L. (2018). Effect of the recycled aggregate concrete. *Adv Mater Sci Eng, 2018*, 2428576. [CrossRef]

[56] British Standards Institution. (1975). *BS 2028: Precast concrete blocks*. London.

[57] Robert, U. W., Etuk, S. E., Agbasi, O. E., & Ekong, S. A. (2020). Properties of sandcrete block produced with coconut husk as partial replacement of sand. *J Build Mater Struct, 7*(1), 95-104. [CrossRef]

[58] Ekpe, S. D., & Akpabio, G. T. (1994). Comparison of the thermal properties of soil sample for passively cooled building design. *Turk J Phys, 18*, 117-122.

[59] Robert, U. W., Etuk, S. E., Agbasi, O. E., Umoren, G. P., Akpan, S. S., & Nnanna, L. A. (2021). Hydrothermally-calcined waste paper ash nanomaterial as an alternative to cement for clay soil modification for building purposes. *Acta Polytechnica, 61*(6), 749-761. [CrossRef]

[60] Robert, U. W., Etuk, S. E., Agbasi, O. E., & Umoren, G. P. (2020). Comparison of clay soils of different colors existing under the same conditions in a location. *Imam J Appl Sci, 5*, 68-73. [CrossRef]

[61] Afkhami, B., Akbarian, B., Beheshti, N., Kalaee, A. H., & Shabani, B. (2015). Energy consumption assessment in a cement production plant. *Sustain Energy Technol, 10*, 84-89. [CrossRef]

J Sustain Const Mater Technol, Vol. 9, Issue. 4, pp. 346–354, December 2024

Journal of Sustainable Construction Materials and Technologies
Web page info: https://jscmt.yildiz.edu.tr
DOI: 10.47481/jscmt.1606833

Journal of Sustainable Construction Materials and Technologies

Research Article

Accelerated microwave curing of hybrid geopolymers with nano-silica for enhanced physico-mechanical properties

Bolat BALAPANOV[1], Sarsenbek MONTAYEV[2], Beyza AYGUN*[3], Mucteba UYSAL[4]

[1]Department of Architecture and Construction, Korkyt Ata Kyzylorda University, Kyzylorda, Kazakhstan
[2]Industrial Technological Institute, Zhangir Khan West-Kazakhstan Agrarian and Technical University, Uralsk, Kazakhstan
[3]Department of Civil Engineering, İstanbul University-Cerrahpaşa, İstanbul, Türkiye
[4]Department of Civil Engineering, Yıldız Technical University, İstanbul, Türkiye

ARTICLE INFO

Article history
Received: 14 November 2024
Revised: 06 December 2024
Accepted: 17 December 2024

Key words:
Curing methods, geopolymers, mechanical properties, microwave curing, physical properties

ABSTRACT

This paper presents the microwave curing method as an alternative to conventional thermal curing of hybrid (fly ash-slag) geopolymer mortars (GMs) to achieve comparable performance with significantly reduced curing times. This study aimed to ascertain the impact of varying nano-silica contents (0.5%, 0.75%, and 1%) on the geopolymer matrix to identify the optimal dosage for enhancing densification and bond improvement phases. Mixture proportions were designed to achieve high mechanical and durability performances. The activator/binder (A/B) ratio was set at 0.71, the sodium silicate to sodium hydroxide ratio at 1.5, and the sand/binder (S/B) ratio at 2.5. This study considered two curing methods: thermal curing at 80 °C for 24 hours and microwave curing at 119 W for 3 minutes. The latter method produces equivalent thermal effects in a significantly shorter time. Physical properties tested after seven days included water absorption, porosity, and mechanical properties related to compressive and flexural strength. The results demonstrated that incorporating NS markedly enhanced the physical and mechanical characteristics. Moreover, microwave curing has been identified as a promising approach for producing hybrid geopolymers, offering a low-energy and high-performance alternative.

Cite this article as: Balapanov, B., Montayev, S., Aygun, B., & Uysal, M. (2024). Accelerated microwave curing of hybrid geopolymers with nano-silica for enhanced physico-mechanical properties. *J Sustain Const Mater Technol*, 9(4), 346–354.

1. INTRODUCTION

Sustainable construction has become the most important focus area of modern research and industrial applications, considering the urgent need to reduce the environmental impacts associated with traditional building materials. Portland cement (PC) remains the backbone of conventional construction. It is well known for its high emission of CO_2 into the environment due to its value chain engagement in intensive energy consumption in its manufacturing process. PC production is estimated to account for about 7% of total CO_2 emissions worldwide, primarily due to the calcination of limestone and high-temperature processes. This ecological footprint and the depletion of non-renewable resources raised the interest in investigating alternative materials with a lower environmental impact. Geopolymer mortars (GMs) synthesized with industrial by-products like fly ash (FA) and ground granulated blast furnace slag (GGBFS) represent a promising class of sustainable construction ma-

---

***Corresponding author.**
*E-mail address: beyza.aygun@ogr.iuc.edu.tr

Published by Yıldız Technical University Press, İstanbul, Türkiye

terials. Such binders efficiently utilize wastes and offer improved mechanical, thermal, and chemical resistances, thus finding applications in variants of infrastructure development. GMs are a type of alkali-activated aluminosilicate material, and the mechanism of their synthesis is based on the dissolution and polycondensation of silica and alumina precursors [1–5]. The resulting three-dimensional framework forms a compact matrix with excellent strength and durability. The three most prevalent parameters influencing the mechanical behavior and durability of GMs are composition, type of activator, and curing conditions. Although the raw materials and their chemical formulations are of utmost importance, the curing techniques stand at the core of determination for all properties of the GMs [6–10]. Hence, traditional thermal curing, if applied, is very effective even for a prolonged time under higher temperatures to increase the rate of geopolymerization. It improves the dissolution of aluminosilicate precursors, allowing for easier gel formation and higher matrix densification, improving mechanical properties like compressive strength and flexural strength. However, high energy demand and long processing times for thermal curing have become quite a big barrier regarding scalability and cost-effectiveness. Newly developed curing methods have recently been among the potential alternatives to traditional thermal curing; microwave curing has received increased interest due to its efficiency in energy use and speed of processing. Unlike heat-curing, which relies on outside heat transfers, microwave curing depends upon heat generated internally through the interaction of microwave radiation with polar molecules in the material. This permits uniform and speedy heating that, in many cases, greatly reduces the curing time and produces comparable material properties or even superior to the best current practices. Indeed, it has been demonstrated that microwave curing can enhance early-age strength in GMs, reduce pores, and increase the matrix's general densification. Besides this, the energy consumption from microwave curing is considerably lower than that of conventional thermal curing, hence meeting the bigger principles underlying sustainability and cost efficiency in construction. The other key factor that influences GMs' performance is including supplementary materials such as nano silica. Nanosilica (NS) possesses a high surface area and reactivity, acting in a dual role on GMs. NS acts as a micro filler to fill up the voids among the matrixes, reducing porosity and increasing their density. This inorganic nanofiller agent acts as an additional source of silicate ions during the geopolymerization reaction, increasing the population of cross-linked aluminosilicate gels and, strengthening the matrix and enhancing mechanical properties. NS incorporation has been found to enhance GMs' compressive and flexural strengths while increasing their resistance to chemical and physical degradation. However, the effectiveness of NS is attached to its dosage and dispersion in the matrix, besides the curing conditions. In this respect, incorporating NS and microwave curing shows several synergistic effects that could be applied to develop high-performance geopolymers at lower energies with improved sustainability. Thus, microwave curing reinforces the interaction of nano silica addition by enhancing material strength by fast activating the GM matrix. This combination has the potential to overcome some of the limitations of the currently used curing methods, with the added advantage of offering improved mechanical and physical properties. Notwithstanding the optimistic test results obtained from the few studies that have been performed, comprehensive research is still sorely needed to optimize the interaction between microwave curing parameters with NS content and GM composition [11–13]. The practical application of GMs in construction requires a profound understanding of their mechanical and durability properties under various curing conditions. Compressive strength, symbolic of a material's axial load-carrying capacity, is one of the most vital parameters in structural applications. Similarly, important is the flexural strength, a representative of the material's resistance to bending forces, which is equally vital for usability assessment in load-bearing and thin-section elements. Apart from mechanical properties, porosity, water absorption, and capillarity are considered some of the most important physical properties concerning GMs' durability and long-term performance under aggressive environmental exposure. The development of GMs with superior performance metrics along these parameters can go a long way toward their widespread use in construction. Microwave curing is such a disruptive technology that can help restructure the production aspects of GMs and overcome their inherent inefficiencies. In this respect, the rapid capability of processing reduces its energy footprint in the curing process, apart from reducing the production times. Microwave radiation thus provided uniform heating and maintained the material properties consistent without thermal gradients that might have resulted in microcracking and other defects [14–19]. Because of the prospects of NS addition, microwave curing signifies a paradigm shift in the studies conducted on sustainable and high-performance construction materials.

This paper studies the effects of microwave curing and nano-silica addition on some physical and mechanical properties of GMs made using locally available materials in Turkey. Microwave curing generally provides considerable energy economy and significantly reduces curing time. At the same time, high internal temperatures with limited performance loss were attained compared to conventional thermal curing. NS may act as a micro-filler and a reactive additive to achieve matrix densification through reducing porosity, with increased silicate ions strengthening the geopolymer gel network. Thus, GMs were prepared with the addition of NS at different levels of 0.5%, 0.75%, and 1%, and their mechanical properties like compressive and flexural strengths along with water absorption and apparent porosity were evaluated under ambient and thermal and microwave curing methods. ANOVA test was conducted to interpret the developed trend in these tests at a 95% confidence level.

Table 1. Chemical compositions of materials

Components (%)	SiO_2	Al_2O_3	Fe_2O_3	TiO_2	CaO	MgO	K_2O	Na_2O	LOI	MnO
GBFS	40.55	12.83	1.10	0.75	35.58	5.87	0.68	0.79	0.03	–
FA	58.75	25.24	5.76	–	1.46	2.22	–	0.60	0.015	–

GBFS: Granulated blast furnace slag; FA: Fly ash.

Table 2. GM mix design (g)

Mixing code	GBFS	FA	Sand	Na_2SiO_3	NaOH	NS
SFA	225	225	1125	255.6	127.8	0
SFA05NS	225	225	1125	255.6	127.8	2.25
SFA075NS	225	225	1125	255.6	127.8	3.375
SFA1NS	225	225	1125	255.6	127.8	4.5

GBFS: Granulated blast furnace slag; FA: Fly ash; NS: Nanosilica.

2. MATERIALS AND METHODS

2.1. Materials

FA was obtained from Zonguldak/Turkey. GGBFS was purchased from Bolu/Turkey, and the chemical properties of both binders are shown in Table 1. The specific gravity of FA and GGBS is 1.96 and 2.91, respectively. The study used sodium hydroxide (NaOH) and sodium silicate (Na_2SiO_3) as chemical activators. NaOH purity value is higher than 99%, Na_2SiO_3 has a percentage of 27.2 SiO_2, 8.2 Na_2O, and its pH value is between 11 and 12.4.

2.2. Mix Design

The binder is composed of an equal proportion of FA and GGBFS, with NaOH and Na_2SiO_3 acting as activators in a 1.5:1 ratio and an A/B ratio of 0.71. This ensures a balance between the workability and strength of the binder. NS is incorporated at 0%, 0.5%, 0.75%, and 1% by binder weight, resulting in enhanced densification, reduced porosity, and augmented mechanical performance. GMs are designated as SFA, SFA05NS, SFA075NS, and SFA1NS, where SFA represents the control series devoid of NS, while the other codes indicate series with 0.5%, 0.75%, and 1% NS by binder weight, respectively (Table 2). Fine aggregates comprise natural sand with a sand-to-binder ratio of 2.5:1, thereby ensuring the production of GM with a consistent texture. The mixture is combined in a Hobart mixer for five minutes to ensure uniformity. GMs are subjected to three curing regimes: microwave, thermal, and ambient. In the case of microwave curing, the specimens are subjected to microwave energy at 119 W for three minutes immediately following their casting [20, 21]. This process induces the reaction kinetics and partial polymerization necessary for the specimens to undergo the desired chemical changes. In the case of thermal curing, the specimens are initially left at room temperature for 24 hours to achieve the initial setting, after which they are exposed to 80°C for a further 24 hours to maximize polymerization. Ambient curing is employed as a control, simulating standard curing conditions without additional heat treatment. Mixture design balances sustainability, advanced curing techniques, and local material utilization, thereby providing a robust framework for evaluating the effects of NS and curing methods on physical and mechanical properties. Furthermore, statistical analyses are employed to quantify these effects, ensuring a comprehensive understanding of the performance of GMs.

2.3. Methods

Unit weight, water absorption, and porosity tests on GMs were carried out according to ASTM C-642 [22] standard. Assesses the workability of GM using the flow table following ASTM C-1437 [23] standards. GMs were produced in 50x50x50 mm cubes, and their CS was applied in an automatic test device per TS EN 12390-3 [24] standard. Three prism samples with dimensions of 40x40x160 mm were used to determine the FSs (TS EN 12390-5 [25]). GMs were loaded from a single point in the automatic testing machine according to the standard, and the tests were carried out on the 28th day (Fig. 1).

3. RESULTS AND DISCUSSION

3.1. Fresh Properties

Figure 2 represents the relation of NS content to flowability for GMs. It exhibits a regular decline in flowability with an increase in the NS content from 0% (SFA) to 1% (SFA1NS). For the SFA series, the flowability without NS was 15 cm, representing the most workable mix in the series. Adding NS by 0.5% resulted in a fall in flow to 14.2 cm, a loss of 5.33%. With further increases up to 0.75% SFA075NS and 1% SFA1NS, the values fall within the range of 13.5 cm and 12.8 cm, respectively, relating to 10% and 14.67%. These represent the reduction in values due to the direct attack of NS on the viscosity and particle mobility of the GM matrix. Declining flowability is attributed to NS's extremely high surface area and reactive nature; these increase water demand and densify the mix. The absorbed free water by NS particles decreases the effective water content available for lubrication between particles. This increases the viscosity of the mix. Besides, the increase in the particle packing density due to NS decreases the free-flowing ability of the matrix. For instance, at 1% NS, SFA1NS develops considerably higher stiffness than the controlled series SFA. This is one of the trade-offs between matrix densification and workability. This behavior characterizes the challenge of maintaining adequate flowability when high nano-silica proportions are used, especially in practical applications involving large-scale casting and placing. A comparison of the impact of NS in the series evidences that the dependence is nonlinear, while the highest dosage of NS results in the most significant reduction of flowability. From 0% NS (SFA) to 0.5% NS (SFA05NS), the reduction of relative

Figure 1. Curing setup and testing of GMs.

values is less compared with the decrease from 0.75% NS (SFA075NS) to 1% NS (SFA1NS). This means that the NS effect on workability becomes more and more evident with its higher dosages; thus, the measures taken to adjust mix proportions or apply some admixtures like superplasticizers should be more substantial. Although these reductions occur, the inherent advantages of NS addition in mechanical and durability enhancement justify its inclusion due to improved compressive strength, flexural strength, and reduced porosity. For example, mixes with higher NS content, even though less workable, function satisfactorily for a long time under durability and heavy loads. Hence, they can be used for structural components where fluidity during placement is not critical. In practice, the adverse effect of loss of flowability is commonly partly offset by optimization of the water-to-binder ratio or activator proportions. When this is not sufficient, needed flow characteristics can be maintained either by modifying the sand-to-binder ratio or using high-range water-reducing admixtures in manners that do not prejudice the integrity of the matrix. These observations confirm the need for a careful balance between the achievement of adequate workability and the exploitation of the performance benefit of nano-silica, especially in applications where facility of placement and high mechanical strength are both required. Also, it was strongly indicated by the observed trends that complete testing is immensely vital in tailoring the GM design to the intended application, especially in immediate workability and long-term performances [26–30].

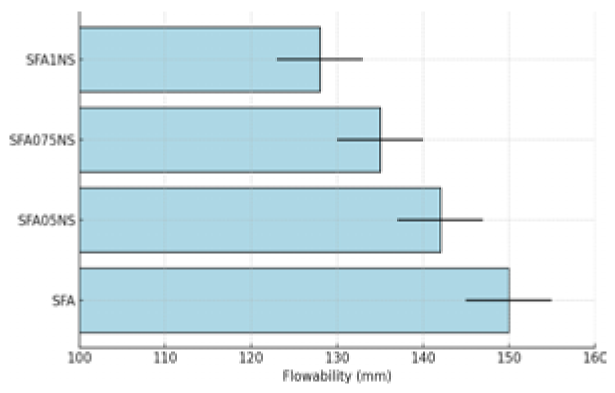

Figure 2. Flowability of GMs under different curing methods.

3.2. Physical Properties

Figure 3 presents the effects of nano-silica content series SFA, SFA05NS, SFA075NS, and SFA1NS on water absorption and porosity for three different curing methods: thermal, microwave, and ambient. Figure 3 illustrates complex

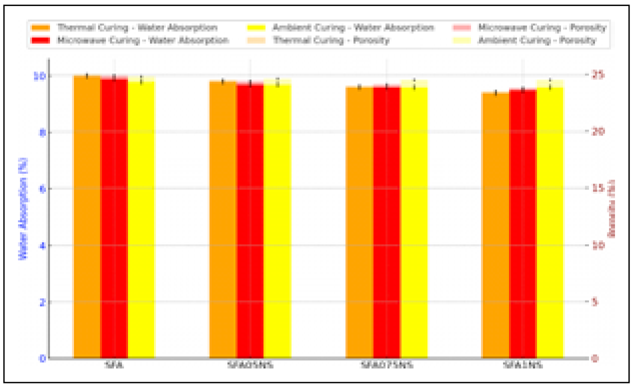

Figure 3. Water absorption and porosity of GMs under different curing methods.

features of the densification and permeability reduction mechanisms. Water absorption trends indicate that thermal curing achieved the maximum reduction from 10.0% for SFA to 9.4% for SFA1NS, constituting a 6% reduction. This trend confirms that long-term high-temperature exposure favorably promotes the dissolution of the aluminosilicate precursors, accelerating geopolymerization and developing a dense, impermeable matrix. Microwave curing shows less effectiveness than thermal curing yet still exhibits a reasonable reduction in water absorption from 9.9% for SFA to 9.5% for SFA1NS, corresponding to a decrease of 4%. This result implied that microwave energy could quickly heat the matrix and promote partial densification, which is nevertheless limited by a three-second curing time compared to thermal curing.

On the other hand, ambient curing presents the least water absorption reduction from 9.8% SFA to 9.6% SFA1NS, only a 2% reduction, because of the slower reaction kinetics and incomplete geopolymerization under room temperature. The porosity trends are also parallel to those of water absorption. Again, thermal curing is performing better when comparing others, as it decreases from 25.0% with SFA to 23.5% for SFA1NS, corresponding to an increase of 6%, showing that superior densification and compactness were achieved via maintained heat exposure. Microwave curing reduces the porosity from 24.9% of SFA to 23.8% of SFA1NS, which accounts for a 4.4% decrease. Though less significant than thermal curing, it reinforces the development of microwave energy use as one of the promising treatment methods, which reduces voids and improves the microstructure. However, when curing by ambient exposition, the porosity decreases only from 24.8% to 24.5%, a very moderate 1.2% reduction, further showing the limited potential of this curing method for achieving significant improvement in densification and structural refinement. Overall, from all the trends, one can notice that with the increase in nano-silica content, higher water resistance and higher porosity reduction are progressively obtained for all curing methods. NS acts as a reactive microfiller, which increases the filler density by reducing the void spaces and provides additional silicate ions to strengthen the gel structure of the GM [26–30]. Among the curing methods, thermal curing offers the best results since it can sustain higher temperatures for longer, aiding complete geopolymerization and densification. Microwave curing is a much more energy-effective treatment that gives results comparable, or near equivalent, to those obtained by thermal curing in much shorter times; further optimizations may ultimately bridge the gap. Ambient curing gave the least effect out of the three methods, but again, this sees improvements with the addition of NS, although less dramatic than microwave curing. The clear evidence of synergy between nano-silica content and advanced curing methods in enhancing durability and the mechanical performance of GMs has shown clear implications for material design and process optimization in different construction applications.

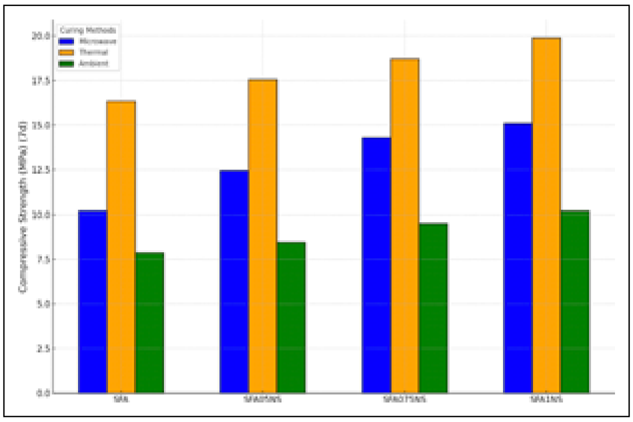

Figure 4. Compressive strength of GMs under different curing methods.

3.3. Mechanical Properties

Results of the compressive strength values of hybrid-GMs were evaluated for different nano-silica ratios and curing methods and are presented in Figure 4. It was indeed found that there was a systematic and progressive increase with increasing NS content, reflecting consistently in the densification of the matrix and mechanical performance. For the baseline mixture, without NS SFA, the thermal curing gave the best result, a value of 16.34 MPa against 10.21 MPa for microwave-cured and 7.88 MPa for ambient-cured samples. These results agree with the performance expected of an unmodified GM under various curing conditions since continuous exposure to a high temperature expedites the reaction kinetics and enhances the consolidation of the GM matrix. Microwave curing reached 62.47% of the strength of thermal curing, testifying to its quickening of geopolymerization reactions even with reduced exposure time. Ambient curing trailed far behind, penalized by the limited response kinetic at room temperature, but it contributed a cost-effective baseline for comparison. All three methods provide increased compressive strength with the addition of SFA05NS, indicating that NS acts catalytically in developing properties for an improved GM matrix. With thermal curing, the improvement was about 7.47%, reaching a value of 17.56 MPa, indicative of NS's ability to enhance gelation and particle packing with long thermal exposure.

On the other hand, microwave curing offered a better improvement of about 21.90%, reaching 12.45 MPa, because NS amplified this method's rapid heat-induced densification characteristics. Ambient curing presented a more modest delivery of 7.23%, reaching 8.45 MPa, indicative of NS's contribution even within low-activation environments. By this stage, the result agrees with values from literature in cases of low NS dosage, as it is common to have incremental improvements in the early stages of NS addition. Increasing the NS addition rate to 0.75% (SFA075NS) induced higher increments; thus, thermal curing attained as high as 18.72 MPa, representing a percentage increase of 14.56% over the control. This result underlines the synergy between high dosage rate and thermal activation, which enhances the development of a more compact and cross-linked-GM matrix. Microwave curing registered a growth of 39.99% at 14.30 MPa, demonstrating the efficiency of such a method in using NS as the accelerator for the consolidation of the matrix. Ambient curing increased by 20.56% to reach 9.50 MPa, which, although far lower than others, constitutes a remarkable enhancement for an ambient condition. These results are within the expected range, though higher values from this dosage of NS for microwave curing could be expected; hence, there may still be room for optimization of either temperature control or curing duration. At 1% NS content, the compressive strength for SFA1NS reached its peak for all methods, having obtained a value through thermal curing of 19.88 MPa, obtaining a cumulative gain of 21.65% over the baseline. This was equal to the highest performance ever reported in NS-reinforced geopolymers with high-temperature curing, as prolonged heat application encourages the complete dissolution of aluminosilicates and maximizes gel formation. Microwave curing, therefore, yielded a compressive strength of 15.10 MPa, an outstanding increase of about 47.87%, and its place was secured as a time-saving, energy-efficient alternative to thermal curing. Ambient curing, while still trailing, chalked up a gain of 29.44% to reach 10.20 MPa, showing the capabilities of NS for mechanical performance improvements even under suboptimal curing conditions.

Although such a set of results follows the trends from GM literature, the values of thermal curing could surpass 20 MPa once the times of heat exposure and activation ratios are optimized, especially at higher dosages of NS—this dual role of NS and a reactive agent-constitutes the backbone for these enhancements. As a micro filler, NS filled the voids in the matrix, which reduced its porosity and increased the density of the GMs. The heat energy supplied under curing thermal and microwave conditions favored dispersion and integration of the NS particles, causing this densification effect to be more evident. NS is an active agent with additional silicate ions that participate in geopolymerization and form strong and interlocked gel structures. Improved integrity of the matrix and reduced micro-defects result in increased compressive strength. The curing by microwave, while shorter, showed the ability to produce properties almost comparable with those of the thermally cured specimens, thus indicating that fast heating was performing its job in accelerating reaction kinetics [26–30].

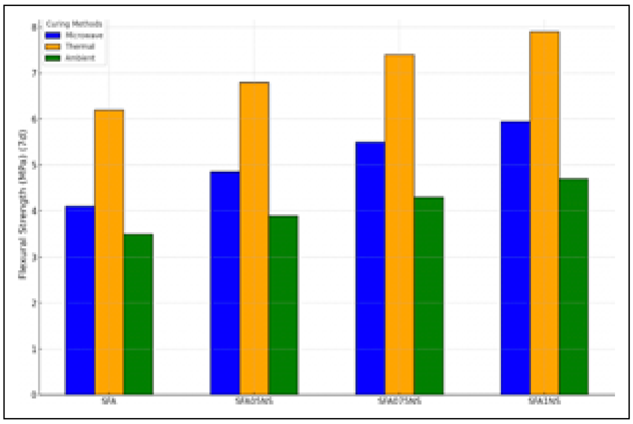

Figure 5. Flexural strength of GMs under different curing methods.

It can be observed from Figure 5 that the flexural strength of hybrid GMs increased significantly and consistently with the gradual addition of NS. Among the various applied curing methods, the highest value of flexural strength for the baseline mixture SFA was recorded through thermal curing at a value of 6.20 MPa, followed by microwave curing at a value of 4.10 MPa, and thirdly, ambient curing method at a value of 3.50 MPa. This result agrees with the expected behavior of the thermally cured geopolymers, which can achieve optimal reaction kinetics conditions with a longer period under high temperatures and improve the tensile bond strength of the aluminosilicate gel. The Microwave curing reached 66.13% of the strength of thermal curing. It showed its capability for rapidly promoting geopolymerization, while the degree of Cure was slightly less than that ofhermal curing. The lowest flexural strength was recorded for the case of ambient curing, naturally due to incomplete tensile-resistant bond formation within the matrix, constrained by the limited reaction rates at room temperature. Adding 0.5% nano-silica produced a detectable improvement in resistance to flexural stresses for all curing methods. In thermal curing, the enhancement was 9.68%, reaching a value of 6.80 MPa, which again evidenced that nano silica could enhance the gel network due to its contribution of reactive silicate species to this strengthening in the tensile integrity of the matrix. On the other hand, microwave curing exhibited a more abrupt enhancement of 18.29% to 4.85 MPa since the accelerated heating mechanism of microwaves amplified nano silica dispersion and interaction within the matrix. Ambient curing exhibited a moderate gain of 11.43% at 3.90 MPa, indicating that nano silica can partly compensate for the slower reaction kinetics under room temperature conditions. At 0.75% nano-silica, the improvement in flexural strengths became more pronounced. Thermal curing recorded a strength of 7.40 MPa, representing an increase of 19.35% over the baseline, reflecting the synergistic effect of higher nano silica content and sustained thermal activation. Microwave curing significantly improved by 34.15% to attain a value of 5.50 MPa since nano silica enhanced the fiber-matrix bonding

Table 3. ANOVA results for physical and mechanical properties of GMs

Property	F-Statistic	p-Value
Water absorption (%)	0.8620639108765783	0.4544251661505388
Porosity (%)	0.003418452169689903	0.9965886774244932
Compressive strength (MPa)	30.847268624182604	9.372489021240787e-05
Flexural strength (MPa)	18.869639794168087	0.0006032845854845374

and reduced microcracking due to the increase in gel cohesion. Ambient curing was better by 22.86%, attaining 4.30 MPa, the lowest among the other two, but still suggesting that nano silica can incrementally enhance tensile properties even under less than ideal cure conditions. Flexural strength reached a maximum in all three curing modes at 1% nano-silica (SFA1NS). The highest, 7.90 MPa, was obtained from thermal curing, representing a cumulative percentage improvement of 27.42% above the baseline. Therefore, thermal curing favors maximum nano silica potential in matrix strengthening through complete gelation and elimination of weak points in tension. The second closest was microwave curing, at 5.95 MPa; very impressively, enhancement of as high as 45.12% was recorded, showing how effective rapid heating is in enhancing tensile properties. Although unimpressive and ineffective, ambient curing was far from an unimpressive improvement ratio of 34.29%, reaching 4.70 MPa and consistently improving tensile performance by nano-silica even in less reactive environments. The improvement in flexural strength with nano silica content is due to its dual role as a microfilter and reactive additive. As a micro filler, it fills up empty spaces in the GM matrix, optimizing its density and reducing the micro defects that can lead to tensile failure. Such an effect is more pronounced under thermal and microwave curing conditions on account of the facilitation provided by heat energy for the uniform incorporation of NS into the gel structure. As a reactive additive, NS provides additional silicate ions that strengthen the aluminosilicate gel, enhancing tensile strength, restricting crack propagation, and improving flexural performance. The reasons behind achieving such high strength by microwave curing can be further elaborated by its ability to cause a heat rise very quickly and, accordingly, assist in developing a more homogeneous matrix. For this reason, microwave curing could be quite feasible as an alternative to thermal curing in those applications where time is of the essence. However, the rather inferior flexural strength concerning the corresponding thermal curing for higher nano silica dosages indicates that full geopolymerization might not have been achieved due to incomplete heat diffusion or insufficient curing time. Ambient curing, though less effective in general, also showed a consistent improvement as nano silica was incorporated, especially at higher dosages. This confirms the trend of nano-silica, adding to improved tensile strength through better gel cohesion and reduced porosity without any fitting external heat. Such improvements make the ambient curing option feasible at low-cost applications where a moderate tensile performance is acceptable [26–30].

3.4. Statistical Properties

ANOVA results provide a comprehensive evaluation of the impact of curing methods on GMs' critical physical and mechanical properties, explicitly focusing on water absorption, porosity, compressive strength, and flexural strength (Table 3). The analysis reveals statistically significant differences for compressive strength (F=30.85, p<0.001) and flexural strength (F=18.87, p<0.001), confirming the crucial role of curing methods in enhancing the mechanical performance of these materials. Thermal curing is the most effective method, consistently delivering the highest compressive and flexural strengths due to its prolonged high-temperature exposure, accelerating geopolymerization, and densifying the matrix. Microwave curing shows intermediate performance, leveraging rapid internal heating to improve mechanical properties within shorter durations, while ambient curing, constrained by limited reaction kinetics, results in the lowest strength values. Conversely, the properties of water absorption (F=0.86, p=0.454) and porosity (F=0.003, p=0.997) exhibit no statistically significant differences across curing methods, indicating that these durability-related parameters are primarily influenced by the incorporation of nano-silica, rather than the curing method itself. NS acts as a micro filler, uniformly reducing porosity and improving water resistance by minimizing voids and increasing matrix compactness, regardless of the curing approach. This consistency across curing methods suggests that the effects of NS on these properties dominate over the thermal or mechanical energy provided by the curing processes.

4. CONCLUSIONS

- Adding NS at an optimum dosage of 1% provides the maximum gains in compressive strength. It was also reported that the highest value reaches as high as 21.65% under thermal curing and as high as 47.87% under microwave curing. It realized relatively increasing trends through remarkable flexural strength values for thermal and microwave curing, reaching 27.42% and 45.12% accordingly, at 1% NS. This evidences their potential to improve tensile integrity or reduce the matrix's micro-defects.
- All the curing methods proved to yield a significant statistical difference from each other statistically since the p-value is below 0.001.
- Durability, mainly determined by water absorption and porosity in water, was related much to the composition itself.

- Several technical and logistical challenges in scalability regarding microwave curing in industrial applications pertain to how one can maintain consistency and uniform heating across more significant volumes of GMs. In addition, managing costs associated with microwave equipment will be required while meeting the need for energy efficiency to maintain sustainability advantages. Uniform heating becomes particularly critical in such a case because the variation in temperature distribution might result in heterogeneous geopolymerization, leading to weak zones or cracks in the matrix. This problem can, however, be minimized if more sophisticated microwave generators that could provide frequency modulation for homogeneous energy distribution within the material can be used. Modulus designs the curing units in batches of building elements-prefabricated panels or blocks manufactured within the current production flow. Besides, energy consumption by microwave curing, though much below that of conventional thermal methods, needs optimization to balance between rapid curing rates and energy efficiency, which could be attained through exposure times and power settings tailored based on the size and composition of the material concerned. In the case of long-term durability, GMs cured by microwaves are found to show adequate resistance against environmental actions like freezing-thawing, sulfate attacks, and thermal variations due to the dense aluminosilicate gel in the matrix. Long-term durability for many varieties in which these materials would be under continuous exposure to UV radiation, constant moisture, or chemical pollutants has been under ongoing research for several decades in an aggressive environment. The existing gap between the actual results from accelerated aging tests and field trials is necessary evidence to confirm the practical viability associated with structural applications. While its relative effectiveness is apparent for early age strength and densification, ambient curing has high potential in low cost and low energy where considerations about mechanical performance are not immediate. On some occasions, the comparably modest reaction kinetics of geopolymerization under ambient conditions have been balanced by NS content optimization or by using an assistant to boost geopolymers' reactivity. NS dispersion is considered an essential role player in such improvements due not only to its microfilming role, which decreases the voids and loosening, but also due to serving as an active additive by providing extra silicate ions to reinforce such a gel structure. The only prerequisites for accurate uniform dispersion are narrowly defined mixing protocols, using mechanical mixers to allow for the avoidance of particle agglomerations, which would impede the density and mechanical integrity of the base matrix. Although some literature has pointed out the synergistic effects of microwave curing and nano-silica addition, this establishment is undoubtedly required as a key design strategy toward high-performance geopolymer systems since higher rates of heating provided by microwaves could fasten the proper integration of NS into the matrix; improved compactness, reduced porosity, and overall increased durability along with mechanical strength could be noticed. While these integrated approaches offer solutions for the scalability of microwave curing, they also position it as a transformational technology to meet the goals of sustainable construction practices.

ETHICS

There are no ethical issues with the publication of this manuscript.

DATA AVAILABILITY STATEMENT

The authors confirm that the data that supports the findings of this study are available within the article. Raw data that support the finding of this study are available from the corresponding author, upon reasonable request.

CONFLICT OF INTEREST

The authors declare that they have no conflict of interest.

FINANCIAL DISCLOSURE

The authors declared that this study has received no financial support.

USE OF AI FOR WRITING ASSISTANCE

Not declared.

PEER-REVIEW

Externally peer-reviewed.

REFERENCES

[1] Asil, M. B., & Ranjbar, M. M. (2022). Hybrid effect of carbon nanotubes and basalt fibers on mechanical, durability, and microstructure properties of lightweight geopolymer concretes. *Constr Build Mater, 357*, 129352. [CrossRef]

[2] Cong, P., & Cheng, Y. (2021). Advances in geopolymer materials: A comprehensive review. *J Traffic Transp Eng (Engl Ed), 8*(3), 283-314. [CrossRef]

[3] Farooq, F., Jin, X., Javed, M. F., Akbar, A., Shah, M. I., Aslam, F., & Alyousef, R. (2021). Geopolymer concrete as sustainable material: A state of the art review. *Constr Build Mater, 306*, 124762. [CrossRef]

[4] Mo, B. H., Zhu, H., Cui, X. M., He, Y., & Gong, S. Y. (2014). Effect of curing temperature on geopolymerization of metakaolin-based geopolymers. *Appl Clay Sci, 99*, 144-148. [CrossRef]

[5] Jindal, B. B. (2019). Investigations on the properties of geopolymer mortar and concrete with mineral admixtures: A review. *Constr Build Mater, 227*, 116644. [CrossRef]

[6] Namitha, S., Nabil, K. M., Rafeeque, N. V. M., Sundhar, R., Raju, T., & Ramaswamy, K. P. (2020). A study on the setting and flow behavior of alkali-activated slag/fly ash composites in ambient condition. *IOP Conf Ser Mater Sci Eng, 989*(1), 012004. [CrossRef]

[7] Kretzer, M. B., Effting, C., Schwaab, S., & Schackow, A. (2021). Hybrid geopolymer-cement coating mortar optimized based on metakaolin, fly ash, and granulated blast furnace slag. *Clean Eng Technol, 4*, 100153. [CrossRef]

[8] Nuaklong, P., Wongsa, A., Boonserm, K., Ngohpok, C., Jongvivatsakul, P., Sata, V., Sukontasukkul, P., & Chindaprasirt, P. (2021). Enhancement of mechanical properties of fly ash geopolymer containing fine recycled concrete aggregate with micro carbon fiber. *J Build Eng, 41*, 102403. [CrossRef]

[9] Bellum, R. R. (2022). Influence of steel and PP fibers on mechanical and microstructural properties of fly ash-GGBFS-based geopolymer composites. *Ceram Int, 48*(5), 6808-6818. [CrossRef]

[10] Bellum, R. R., Al Khazaleh, M., Pilla, R. K., Choudhary, S., & Venkatesh, C. (2022). Effect of slag on strength, durability and microstructural characteristics of fly ash-based geopolymer concrete. *J Build Pathol Rehabil, 7*(1), 25. [CrossRef]

[11] Ramezanianpour, A. A., & Moeini, M. A. (2018). Mechanical and durability properties of alkali-activated slag mortars containing nanosilica and silica fume. *Constr Build Mater, 163*, 611-621. [CrossRef]

[12] Rahmawati, C., Aprilia, S., Saidi, T., Aulia, T. B., & Hadi, A. E. (2021). The effects of nanosilica on mechanical properties and fracture toughness of geopolymer cement. *Polymers, 13*(13), 2178. [CrossRef]

[13] Deb, P. S., Sarker, P. K., & Barbhuiya, S. (2015). Effects of nano-silica on the strength development of geopolymer cured at room temperature. *Constr Build Mater, 101*, 675-683. [CrossRef]

[14] Gultekin, A. (2024). Compressive strength and microstructure of microwave-cured waste brick powder-based geopolymer mortars. *Iran J Sci Technol Trans Civ Eng, 48*, 3119-3133. [CrossRef]

[15] Aschoff, J., Partschefeld, S., Schneider, J., & Osburg, A. (2024). Effect of microwaves on the rapid curing of metakaolin- and aluminum orthophosphate-based geopolymers. *Materials, 17*(2), 463. [CrossRef]

[16] Chindaprasirt, P., Rattanasak, U., & Sompop, T. (2013). Role of microwave radiation in curing the fly ash geopolymer. *Adv Powder Technol, 24*(3), 812-818. [CrossRef]

[17] Khaleel, F., Atiş, C. D., Durak, U., İlkentapar, S., & Karahan, O. (2021). The effect of microwave curing on the strength development of Class-F fly ash-based geopolymer mortar. *Erciyes Univ J Inst Sci Technol, 37*(1), 118-128.

[18] Sun, Y., Zhang, P., Hu, J., et al. (2021). A review on microwave irradiation to the properties of geopolymers: Mechanisms and challenges. *Constr Build Mater, 294*, 123491. [CrossRef]

[19] Gultekin, A., & Ramyar, K. (2023). Investigation of high-temperature resistance of natural pozzolan-based geopolymers produced with oven and microwave curing. *Constr Build Mater, 365*, 130059. [CrossRef]

[20] Guan, X., Luo, W., Liu, S., Hernandez, A. G., Do, H., & Li, B. (2023). Ultra-high early strength fly ash-based geopolymer paste cured by microwave radiation. *Dev Built Environ, 14*, 100139. [CrossRef]

[21] Mangat, P. S., Grigoriadis, K., & Abubakri, S. (2016). Microwave curing parameters of in-situ concrete repairs. *Constr Build Mater, 112*, 856-866. [CrossRef]

[22] ASTM International. (2021). *Standard test method for density, absorption, and voids in hardened concrete*. ASTM C642.

[23] ASTM International. (2020). *Standard test method for flow of hydraulic cement mortar*. ASTM C1437.

[24] Turkish Standards Institution. (2019). *Concrete-Testing hardened concrete-Part 3: Compressive strength of test specimens*. TS EN 12390-3.

[25] Turkish Standards Institution. (2019). *Concrete-Testing hardened concrete-Part 5: Flexural strength of test specimens*. TS EN 12390-5.

[26] Hashemi, A., Mousavi, S. S., Nazarpour, H., & Dehestani, M. (2024). Effect of nano-SiO2 and sulfate solutions curing on bond strength of GGBFS-based geopolymer repairing mortar. *Constr Build Mater, 435*, 136778. [CrossRef]

[27] Chen, K., Wu, D., Chen, H., Zhang, G., Yao, R., Pan, C., &, Zhang, Z. (2021). Development of low-calcium fly ash-based geopolymer mortar using nano-silica and hybrid fibers. *Ceram Int, 47*(15), 21791-21806. [CrossRef]

[28] Al Tawaiha, H., Alhomaidat, F., & Eljufout, T. (2023). A review of the effect of nano-silica on the mechanical and durability properties of cementitious composites. *Infrastructures, 8*, 132. [CrossRef]

[29] Adak, D., Sarkar, M., & Mandal, S. (2014). Effect of nano-silica on strength and durability of fly ash-based geopolymer mortar. *Constr Build Mater, 70*, 453-459. [CrossRef]

[30] Chiranjeevi, K., Abraham, M., Rath, B., & Praveenkumar, T. R. (2023). Enhancing the properties of geopolymer concrete using nano-silica and microstructure assessment: A sustainable approach. *Sci Rep, 13*, 17302. [CrossRef]

J Sustain Const Mater Technol, Vol. 9, Issue. 4, pp. 355–364, December 2024

Journal of Sustainable Construction Materials and Technologies
Web page info: https://jscmt.yildiz.edu.tr
DOI: 10.47481/jscmt.1607472

Journal of Sustainable Construction Materials and Technologies

Research Article

Moderating the soft storey impact in multi-storey buildings: A comparative seismic investigation

Shabla K.*[1], Praseeda K.I[1], Chitaranjan PANY[2]

[1]*Department of Civil Engineering, NSS College of Engineering, Palakkad, India*
[2]*Structural Entity, VSSC, Thiruvananthapuram, India*

ARTICLE INFO

Article history
Received: 23 April 2024
Revised: 05 December 2024
Accepted: 06 December 2024

Key words:
Bracings, response spectrum analysis, shear wall, soft storey, stiffer columns, viscous damper

ABSTRACT

A storey with lateral stiffness less than 70% of the storey above or less than 80% of the average stiffness of the three storeys above is considered a soft storey. Ground-floor open-air buildings are frequently used for parking, particularly in metropolitan settings with considerable space limits. Soft-story buildings with irregular stiffness tend to collapse more than conventional buildings. The study's main goal was to understand better the soft storey effect in multi-storey structures and how to mitigate it using strategies such as adding shear walls, bracings, viscous dampers, and stiffer columns. A G+14 storey building finite element model (FEM) has been established via ETABS software and performed Response Spectrum Analysis at three seismic zones-III, IV and V. To determine the best method for reducing the soft storey effect in buildings, an analysis is conducted taking into account many parameters, including storey shear, stiffness, storey drift, and storey displacement for the entire structure, as well as the responses at the soft storey level for different configurations. According to the findings, adding a shear wall to a soft-storey building increases storey shear while reducing maximum displacement and storey drift. The first floor of the structure (soft storey) exhibits the most significant reduction in displacement (79.29%) and storey drift (79.3%) when shear walls are incorporated at the corners. There is also a 33.11% increase in base shear at the first story level, and the structure's stiffness increases by 6.5 times compared to a soft storey building. Adding a shear wall reduces the soft storey building's maximum displacement and storey drift by 25.27% and 59.28%, respectively. The soft storey building's maximum storey shear rises by 33.38%. Regarding seismic performance, a soft-storey building with a shear wall performs better than other soft-storey mitigation techniques.

Cite this article as: Shabla, K., Praseeda, K. I., & Pany, C. (2024). Moderating the soft storey impact in multi-storey buildings: A comparative seismic investigation. *J Sustain Const Mater Technol*, 9(4), 355–364.

1. INTRODUCTION

Parking is needed, particularly in cities with severe space restrictions. Under these circumstances, buildings' ground floors remain open without the addition of any infill walls to make room for parking. Buildings get stiffness irregularities as a result. The ground floor displacement moves significantly when subjected to seismic force, while the upper stories, which move as one unit, move far less. As seen in Figure 1, this produces a weak point and causes the building to fall entirely [1]. The research aims to study the soft storey effect in multi-storey structures and find ways to address it by using stiffer columns, shear walls, bracings, and viscous dampers, among other methods.

---

*Corresponding author.
*E-mail address: shabla1999@gmail.com

Published by Yıldız Technical University Press, İstanbul, Türkiye

Figure 1. Soft storey building failure during Gujarat Earthquake (2001) in India [1].

Seismic retrofitting has now become a critical problem. Retrofitting aims to improve the structure's strength, resistivity, and lifespan. Recent earthquakes in different regions have emphasized the urgency of repairing inadequate seismic structures. The review paper [2] summarized the solution to seismic strengthening. Seismic study of multi storey building with and without floating column carried out and its effects presented [3]. The wall piers were modeled using a multi-layer shell element based on the composite strength of materials, which was divided into one or more orthotropic reinforcement layers and several concrete layers with equivalent thickness according to the reinforcement situation and actual component size [4].

Shear walls withstand lateral forces like wind and seismic activity and thereby increase lateral stability and safety of the building, usually constructed from materials like reinforced concrete or steel. Shear walls enhance the stiffness of the structure and thereby decrease the displacement of the structure. The incorporation of shear wall at corners increased storey stiffness and reduced displacement, thereby effectively transforming the soft storey into a standard structure and enhancing overall structural stability [5]. Bracing systems, such as V, cross, and diagonal bracing, help to mitigate soft storey effects in multi-storey buildings, distribute seismic forces uniformly to the structure and enhance structural stability. The optimum location of bracings in a building is at the corners. Strengthening ground storey columns effectively addresses soft storey vulnerabilities by increasing stiffness and load-bearing capacity, reducing the risk of structural damage during seismic events. Viscous dampers, strategically placed within the soft storey, dissipate energy and minimize lateral movement, providing cost-effective retrofitting solutions that enhance resilience of building to seismic forces. Strengthening the columns in the ground storey of building is a highly effective strategy for addressing the soft storey issue in open ground storey structures [6-14]. Kannan (2023) evaluated the effects of a soft storey for frames with different column shapes in different earthquake zones and locations along the soft storey's axis, from the first to the top level. Analyses using X bracings and shear walls were conducted. According to findings, shear walls can be employed in seismic danger zones because they lessen lateral displacement and storey drift. For low seismic zones, steel bracing is advised [15]. The impact of a soft storey and its placement on the seismic behavior of a supporting building and non-structural components was investigated by Pesaralanka et al. [16] in 2023.

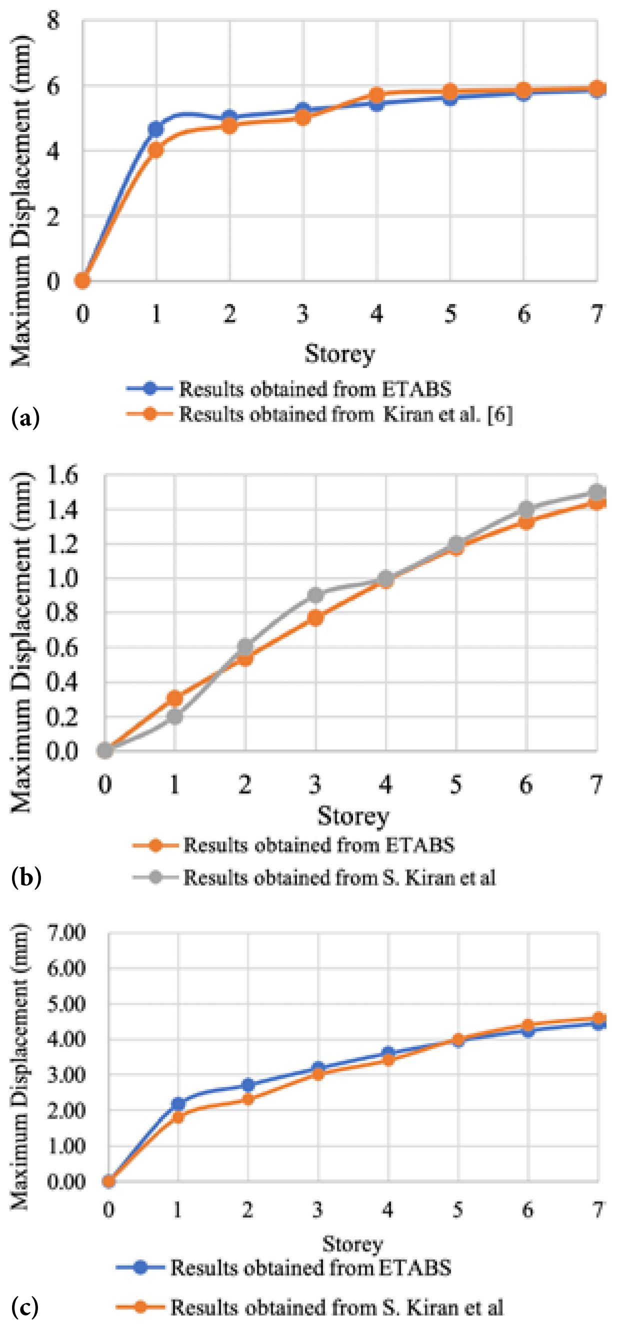

Figure 2. Comparison of displacement of **(a)** soft storey building, **(b)** soft storey building with shear wall and **(c)** soft storey building with bracings.

The models' bottom (ground), middle, and top storey levels retain the soft narrative's placement. According to the study, there is a significant vertical stiffness irregularity in the bottom soft storey, which suggests that the seismic performance of ground-level open-storied buildings has to be investigated [16]. To lessen the effect of soft storeys on the dynamic performance of the structure, Chanumolu and

Table 1. Model description

Description	Specification
No. of stories	G+14
Storey height	3.5 m
Type of soil	Medium (II)
Grade of steel	Fe415
Grade of concrete	M30
Modulus of elasticity of concrete	27386
Modulus of elasticity of steel	2 x 105 N/mm^2
Live load	3.5 kN/m^2
Floor finish	1 kN/m^2
Importance factor	1
Response reduction factor	3
Seismic zone	III, IV and V
Wind Speed	50 m/s
Terrain category	3
Column size	600 mm x 600 mm
Beam size	300 mm x 500 mm
Plinth beam size	400 mm x 600 mm
Thickness of Slab	150 mm
Thickness of brick wall	230 mm
Thickness of shear wall	230 mm
Steel section	ISMB 350
Thickness of stiffer column	600 mm x 800 mm
Viscous damper	FVD500

Anthugari (2020) arranged gap components at beam-column joints to act as a spring in either or both of the beam and column. When compared to the standard models, this aids in lowering storey displacements, inter-storey drift ratios, over-turning moments, and an increase in storey stiffness [17]. Comparative seismic response analysis of the two multi-storey reinforced concrete 3D frames under seismic loads, with and without base isolation, was carried out by Qambrani and Mirza (2023). The analysis findings demonstrate how well base isolators work in Balochistan's high-seismic-risk Zone 4 to lessen displacements, drifts, and shear in multistorey buildings. The building time period, stiffness, and energy dissipation were all successfully extended by LRB isolators [18].

The strategies above contribute to the mitigation of soft storey vulnerabilities in diverse ways, and it is necessary to determine the most effective technique for seismic retrofitting structures. This study aims to evaluate different soft storey mitigation strategies, such as stiffer columns, bracings, dampers, and shear walls, to identify the most efficient method for reducing the soft storey effect in multi-storey buildings. The study technique entails a detailed analysis utilizing ETABS software to model the behavior of structural components in connection with the soft storey effect in multi-storey structures.

2. MODELING AND ANALYSIS OF STRUCTURES

Modeling of a G+6-storey building with a symmetrical floor plan, as presented in [6], was done using ETABS software. Analyzes of a soft-storey bare-frame building with

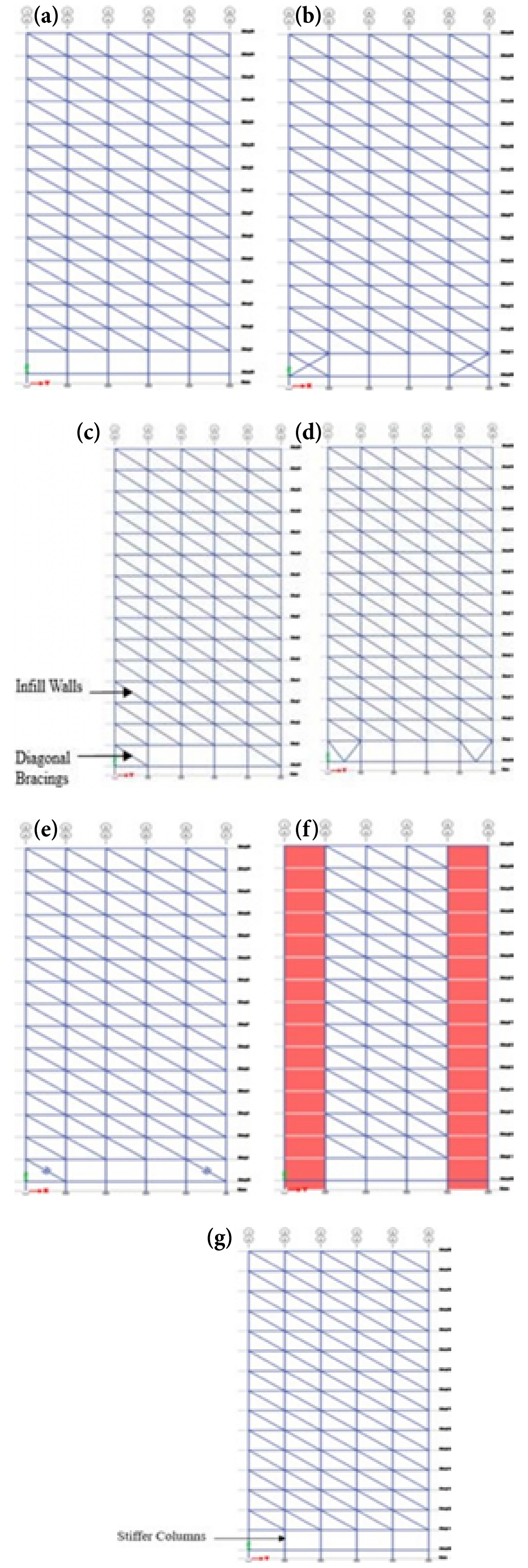

Figure 3. **(a)** Building with ground open storey, Soft storey building with **(b)** cross bracings, **(c)** diagonal bracings, **(d)** V bracings, **(e)** viscous damper, **(f)** shear wall, **(g)** stiffer columns.

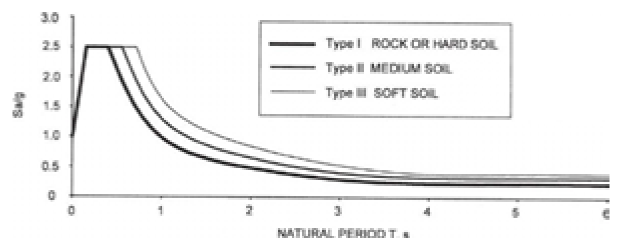

Figure 4. Spectra for response spectrum method [19].

cross bracings and a shear wall were performed, compared with the results in the literature, validating the analytical procedure. The comparison between results obtained from ETABS for the present study and the literature is shown in Figure 2.

The G+14-storey building is modeled as a bare-frame, soft-storey building using ETABS software with cross bracings, diagonal bracings, V-shaped bracings, viscous dampers, shear wall and stiffer columns using ETABS 18.0.2 standard. The beam modeling of infill walls is done using the corresponding method of diagonal bracings given in Part 1 of IS1893 2016.

The dimensions of buildings and parts are described in Table 1. Models of bare frame models, soft floor buildings with cross bracings, diagonal bracings, V- bracings, viscous dampers modeled with ETABS 18.0.2 software, shear wall, and stiffer columns are shown in Figure 3a–g.

A ground-floor open-storey building is modeled by keeping the ground floor unoccupied and adding infill walls to the higher floors, as seen in Figure 3a. According to IS1893 2016 Part 1, the masonry infill wall of the building is modeled using an equivalent diagonal strut approach.

$W_{ds}=0.175(\alpha_h)-0.4L_{ds}$

where $\alpha_h=h\sqrt[4]{(E_m\,t\,sin(2\theta))/(4\,E_f I_c\,h)}$

h=Height of infill panes

Ef=Expected elastic modulus of frame material E_m= Expected elastic modulus of infill material,

$E_m=550 \times f_m$

where f_m is the compressive strength of masonry prism (in MPa) obtained as per IS 1095 or given by expression:

$fm=0.433 x f_b^{0.64} x f_{mo}^{0.36}$

where f_b is the compressive strength of brick in MPa and f_{mo} is the compressive strength of mortar in MPa

I_c=Moment of inertia of column

L_{ds}=Diagonal length of infill panel t=Thickness of infill panel and equivalent strut

θ=Angle whose tangent is the infill height-to-length aspect ratio

L=Length of infill wall

By substituting these values,

α^h=2.0038749 and W_{ds}=583 mm

Response Spectrum Analysis in ETABS software analyzes various models, such as bare frames, soft storey buildings with cross bracings, diagonal bracings, V bracings, viscous dampers, shear walls, and stiffer columns.

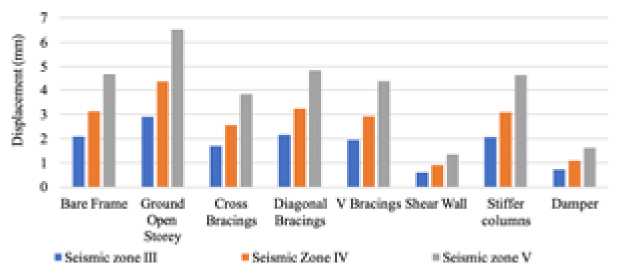

Figure 5. Comparison of displacement in first storey level for different models.

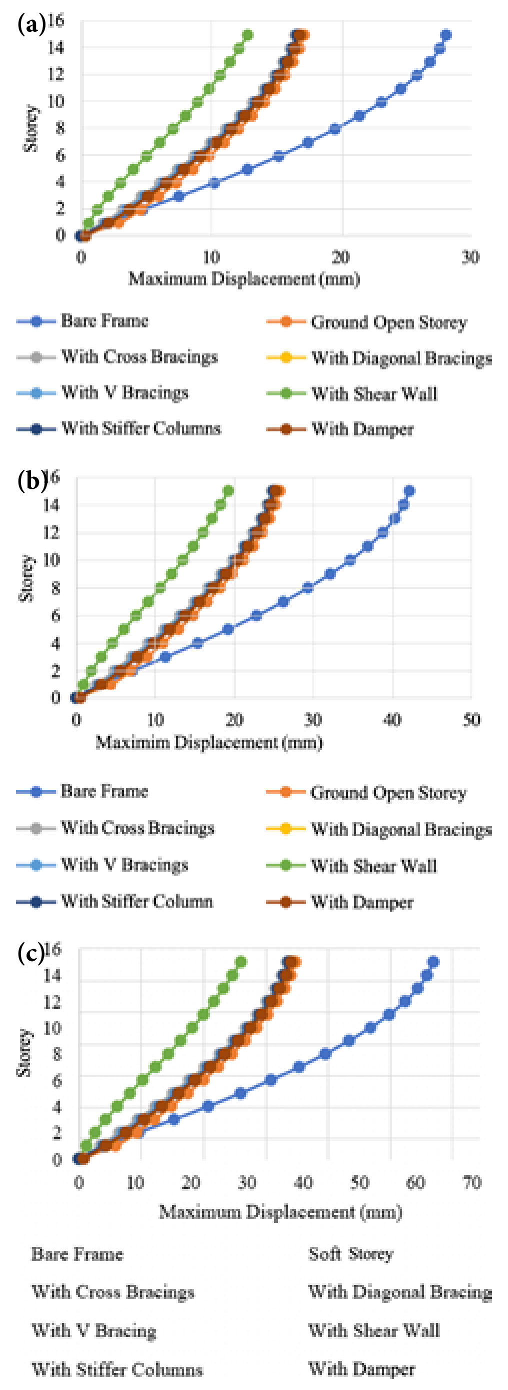

Figure 6. Comparison of different models in **(a)** seismic zoneIII, **(b)** seismic zoneIV and **(c)** seismic zone V.

Table 2. Comparison of displacement at first storey level obtained for different models

Models	Displacement at first storey level in zone III (mm)	Displacement at first storey level in zone IV (mm)	Displacement at first storey level in zone V (mm)	% reduction as compared to soft storey building
Soft storey building	2.901	4.352	6.528	–
Cross bracings	1.7	2.55	3.826	41.4
Diagonal bracings	2.153	3.229	4.843	25.8
V bracings	1.9	2.916	4.374	33.5
Shear wall	0.601	0.901	1.352	79.29
Stiffer columns	2.057	3.085	4.627	29.11
Viscous damper	0.72	1.08	1.62	75.18

Table 3. Comparison of maximum displacement obtained for different models

Models	Maximum displacement in zone III (mm)	Maximum displacement in zone IV (mm)	Maximum displacement in zone V (mm)	% reduction as compared to soft storey building
Soft storey building	17.173	25.759	38.639	–
Cross bracings	16.477	24.715	37.073	4.05
Diagonal bracings	16.838	25.257	37.886	1.95
V bracings	16.637	24.956	37.434	3.12
Shear wall	12.834	19.25	28.876	25.27
Stiffer columns	16.651	24.976	37.464	3.04
Viscous damper	16.838	25.257	37.886	1.95

Table 4. Comparison of storey drift at first storey level obtained for different models

Model	Storey drift at first storey level in seismic zone III (mm)	Storey drift at first storey level in seismic zone IV (mm)	Storey drift at first storey level in seismic zone V (mm)	% reduction as compared to soft storey building
Soft storey building	0.000727	0.000109	0.0001636	–
Cross bracings	0.000415	0.000623	0.000935	42.99
Diagonal bracings	0.000528	0.000792	0.001188	27.52
V bracings	0.000476	0.000714	0.001072	34.64
Shear wall	0.000151	0.000226	0.000339	79.30
Stiffer columns	0.000514	0.000771	0.001156	29.46
Viscous damper	0.000151	0.000227	0.00034	79.25

The spectra for the response spectrum method are shown in Figure 4. The system's maximum acceleration, velocity, and displacement values in response to time-dependent dynamic excitation are displayed graphically in the response spectrum. Maximum displacement, storey drift, storey shear, and stiffness are the basis for the analysis. The response of the entire structure and the reaction on the first floor are considered. While storey drift is the relative horizontal displacement between two neighboring floors or storeys during an earthquake, maximum displacement is the most prominent horizontal movement a specific storey within the structure experiences. In a structure, storey shear is the lateral force that external sources, such as lateral loads, act on a particular level or storey. The resistance to deformation under external loads is measured by stiffness.

3. RESULTS AND DISCUSSIONS

Comparisons are made between the displacement, storey drift, stiffness, and storey shear results for several models in seismic zones III, IV, and V.

3.1. Storey Displacement

Figure 5 compares the displacement at the first storey level for various models. Figures 6a–c show the results for the maximum displacement in the different models for seismic zones III, IV, and V, respectively. Tables 2 and 3 compare displacement at the soft storey level and the maximum displacement of various models, respectively, about the soft storey building.

It is noted that, as illustrated in Figure 5, the soft storey building with shear wall experiences the least displacement at, while the bare soft storey building experiences the high-

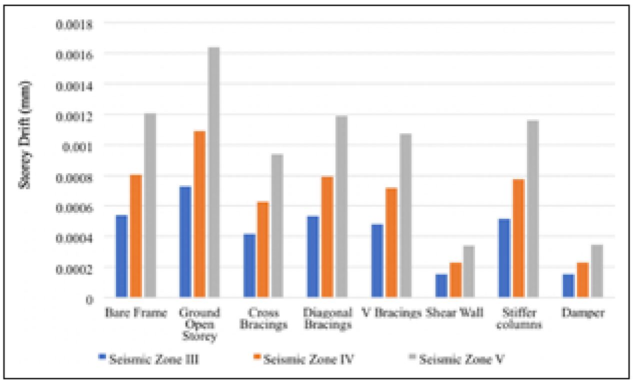

Figure 7. Comparison of storey drift in first storey level for different models.

est displacement. When a soft storey structure incorporates a shear wall, viscous damper, cross bracings, V bracings, stiffer columns, and diagonal bracing, the first storey displacement appears to reduce by 79.29%, 75.18%, 41.4%, 33.5%, 29.11%, and 25.8%, respectively, as shown in Table 2. The maximum displacement of the soft storey building decreases when shear walls, cross bracings, V bracings, stiffer columns, diagonal bracings, viscous dampers, and stiffer columns are incorporated, by amounts of 25.27%, 4.05%, 3.12%, 3.04%, 1.95%, and 1.95%, respectively, as shown in Table 3. It is also clear from Figure 6 that, as one moves into greater seismic zones, lateral displacement increases because of the stronger seismic action. Shear walls, bracings, and stiffer columns all contribute to increased stiffness, which lessens lateral sway and displacement. The addition of a damper causes energy to be absorbed and dispersed, which lowers lateral movement.

3.2. Storey Drift

Figure 7 compares the storey drift at the first storey level for several models. Figure 8a–c show the maximum storey drift for various models for seismic zones III, IV, and V, respectively. Tables 4 and 5 present a comparison of storey drift at the soft storey level and the maximum displacement of various models, respectively, in relation to the soft storey building.

The first floor storey drift is reduced by 79.3%, 79.25%, 42.99%, 34.64%, 29.46%, and 27.52 when shear wall, viscous damper, cross bracings, V-braces, stiffer columns and diagonals bracings respectively as shown in Figure 7 (Table 4). Figure 8–c it is evident that the maximum storey drift of the soft floor building is reduced by 59.28%, 40.85%, 40.3%, 34.52%, 29.29% and 27.37% when the shear wall, cross bracings, viscous dampers and V bracings, stiffer columns and diagonal braces are added, as shown in Table 5. Reduction of storey drift through soft storey mitigation measures due to reduced lateral movement.

3.3. Storey Shear

Variation of storey shear for different models in first storey level is shown in Figure 9. Storey shear for different models for seismic zone III, IV and V are illustrated in Figure 10a–c respectively. Tables 6 and 7 present a comparison of storey shear at the soft storey level and the maximum displacement of various models, respectively, in relation to the soft storey building.

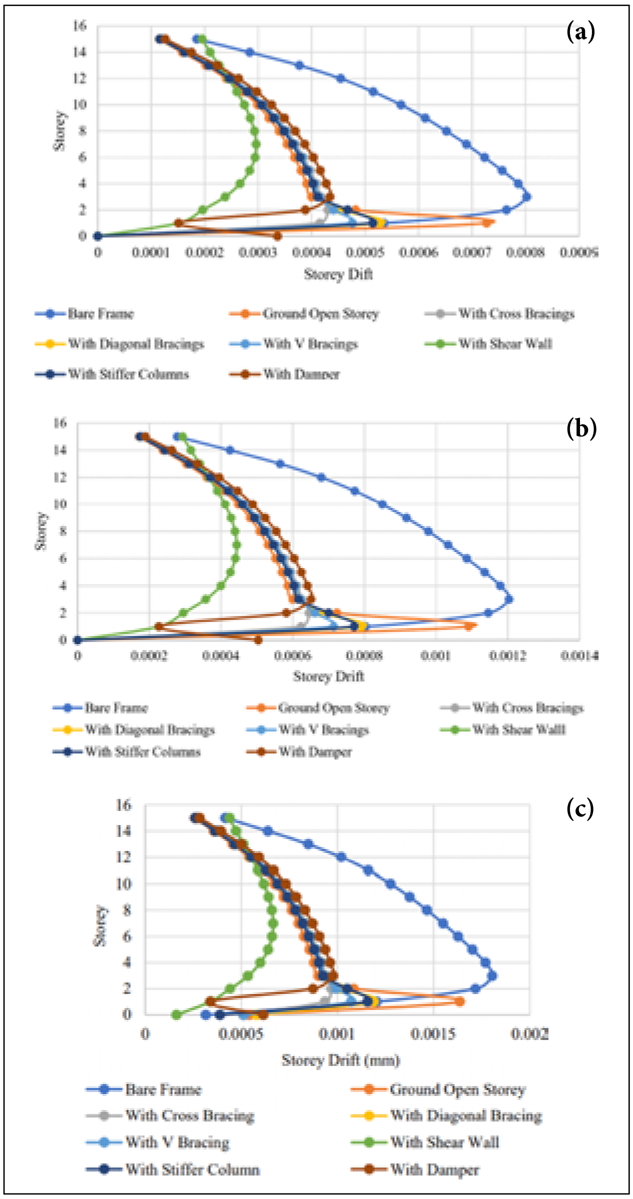

Figure 8. Comparison of storey drift for different models in **(a)** seismic zone III, **(b)** seismic zone IV and **(c)** seismic zone V.

Storey shear is highest for soft storey given with shear wall. Figure 9 demonstrates that base shear (or storey shear in first floor level) increments by 33.11%, 2.92%, 2.58%, 2.39% and 2.05%by the incorporation of shear wall, cross bracings, stiffer columns,V bracings and diagonal bracings separately as shown in Table 6. It is additionally apparent that base shear diminishes by 89.7% with the consolidation of viscos damper due to the adaptability afforded by damper which makes the building less stiffer. From Figure 10 a-c, it is appeared that maximum storey shear of the soft storey building increases by 33.38%, 2.92%,2.76%,2.4%, 2.08% and 2.07% with the addition of shear wall, cross bracings, stiffer columns, V bracings, viscos damper and diagonal bracings,

Table 5. Comparison of maximum soft drift obtained for different models

Models	Maximum storey drift in zone III (mm)	Maximum storey drift in zone IV (mm)	Maximum storey drift in zone V (mm)	% reduction as compared to soft storey building
Soft storey building	0.000727	0.00109	0.001636	–
Cross bracings	0.00043	0.00065	0.000968	40.83
Diagonal bracings	0.000528	0.00079	0.001188	27.38
V bracings	0.000476	0.00071	0.001072	34.47
Shear wall	0.000296	0.00044	0.000666	59.29
Stiffer columns	0.000514	0.00077	0.001156	29.34
Viscous damper	0.000434	0.00065	0.000977	40.28

Table 6. Comparison of base shear obtained for different models

Model	Base shear in seismic zone III (kN)	Base shear in seismic zone IV (kN)	Base shear in seismic zone V (kN)	% increase as compared to soft storey building	% decrease as compared to soft storey building
Soft storey building	2473.90	3710.84	5566.27	–	–
Cross bracings	2546.15	3819.225	5728.837	2.92	–
Diagonal bracings	2525.056	3787.584	5681.375	2.05	–
V bracings	2533.353	3800.03	5700.045	2.39	–
Shear wall	3299.58	4949.37	7424.06	33.11	–
Stiffer columns	2542.161	3813.242	5728.837	2.58	–
Viscous damper	254.76	382.14	573.22	–	88.90

Table 7. Comparison of maximum storey shear obtained for different models

Models	Maximum storey shear in zone III (mm)	Maximum storey shear in zone IV (mm)	Maximum storey shear in zone V (mm)	% reduction as compared to soft storey building
Soft storey building	2473.896	3710.844	5566.265	–
Cross bracings	2546.15	3819.225	5728.837	2.92
Diagonal bracings	2525.056	3787.584	5681.375	2.07
V bracings	2533.353	3800.03	5700.045	2.40
Shear wall	3299.581	4949.371	7424.056	33.38
Stiffer columns	2542.161	3813.242	5719.863	2.76
Viscous damper	2525.374	3788.06	5682.09	2.08

as depicted in Table 7. This trend is due to enhancement of stiffness which improves the effective distribution of lateral force within the structure and hence storey shear at each level increases.

3.4. Storey Stiffness

Variation of stiffness for different models in first storey level in shown in Figure 11. Stiffness for different models for seismic zone III, IV and V are illustrated in Figure 12–c respectively. Table 8 present a comparison of stiffness at the soft storey level of various models, respectively, in relation to the soft storey building.

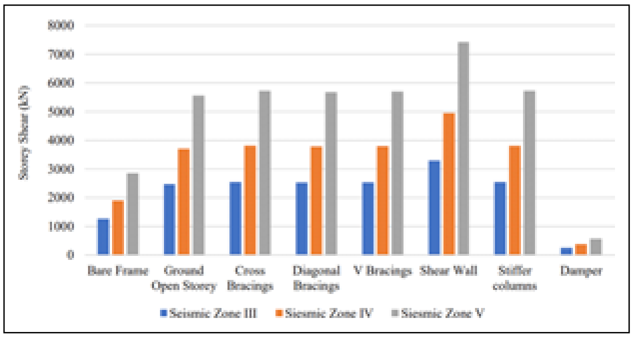

Figure 9. Comparison of storey shear in first storey level for different models.

Since stiffness is not zone-specific, the stiffness of the models is constant throughout the three zones. It is evident from Figure 11 that adding a shear wall, cross bracings, V bracings, stiffer columns, and diagonal bracings increases stiffness at the first storey level by 549.12% (6.5 times), 84.27%, 58.057%, 46.09%, and 45.06%, respectively, as shown in Table 8. This is because these structural components were able to distribute the load effectively. Because

Table 8. Comparison of stiffness obtained for different models

	Stiffness (kN/m)	% increase as compared to soft storey building	% decrease as compared to soft storey building
Soft storey building	997001.33	–	–
Cross bracings	1837228.70	84.27	–
Diagonal bracings	1446308.96	45.06	–
V bracings	1575837.85	58.057	–
Shear wall	6471766.13	549.12	–
Stiffer columns	1456597.07	46.09	–
Viscous damper	726023.72	–	27.18

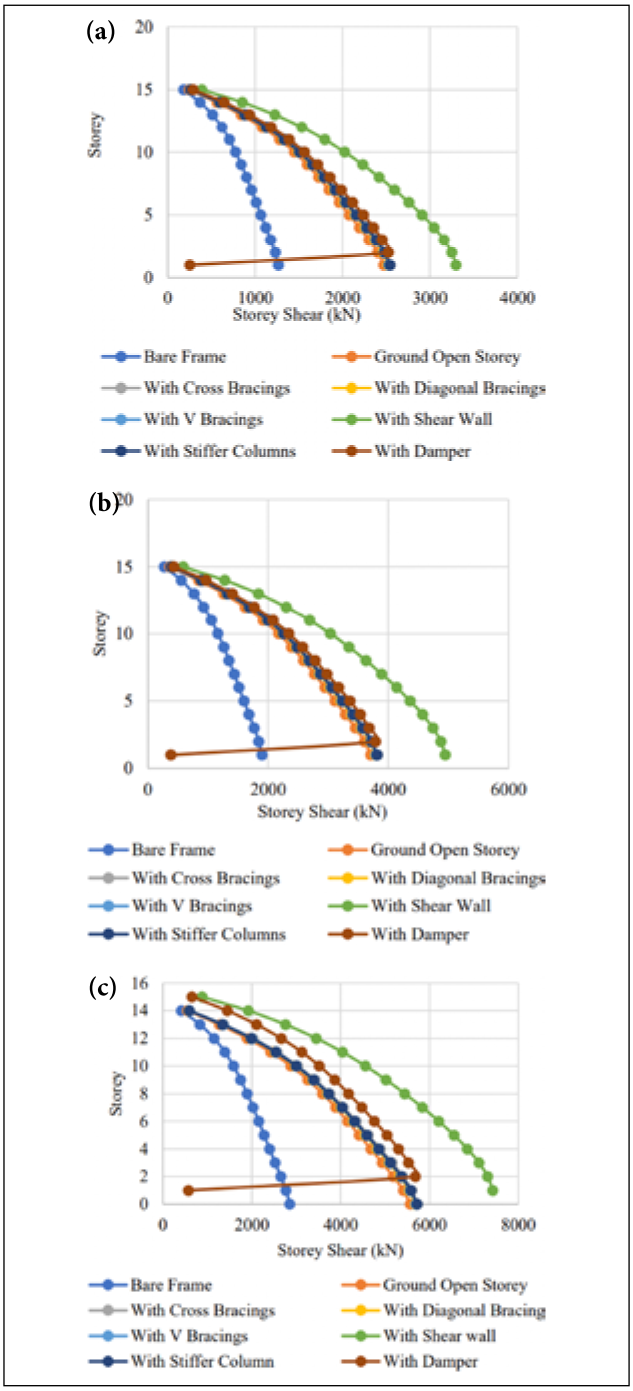

Figure 10. Comparison of storey shear for different models in **(a)** seismic zone III, **(b)** seismic zoneIV and **(c)** seismic zone V.

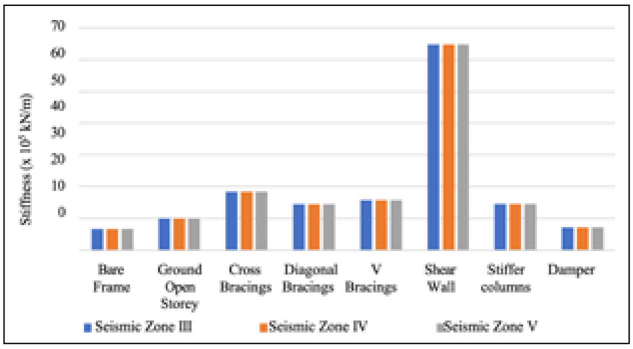

Figure 11. Comparison of stiffness in first storey level for different models.

of the flexibility that the viscous damper adds to the level, the structure's stiffness at the first storey level decreases by a factor of 27.19% when incorporated. Three seismic zones' worth of variations in stiffness for various models are depicted in Figures 12a–c. The percentage increase in the overall stiffness of soft storey buildings resulting from including viscous damper, cross bracings, stiffer columns, and the shear wall is 16.05%, 7.56%, and 1.18%. Including V and diagonal bracings reduces stiffness by 0.14% and 0.05%, respectively.

4. CONCLUSIONS

Because of their irregular stiffness, soft-storey buildings are more likely to collapse after an earthquake. Therefore, buildings must minimize the impact of their soft stories. Comparative seismic analysis is researched to lessen the soft storey impact on structures. Shear walls, cross bracings, diagonal bracings, V bracings, stiffer columns, and viscous dampers approaches are used in the present study to know their effect. The following are the study's main conclusions:

- The addition of different soft storey mitigation techniques improved the seismic performance of the soft storey building.
- The structure's first floor exhibits the most significant reduction in displacement (79.29%) and storey drift (79.3%) when shear walls are incorporated at the corners. There is also a 33.11% increase in base shear, and the structure's stiffness increases by 6.5 times compared to a soft storey building.

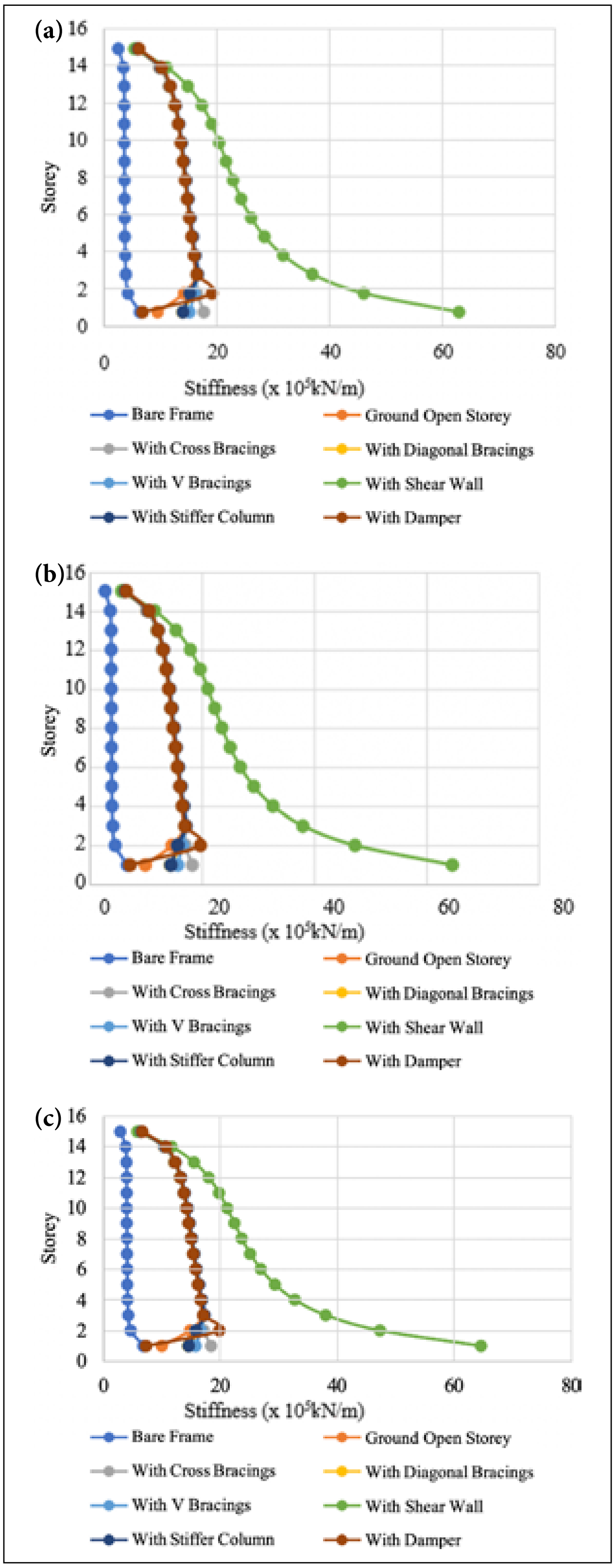

Figure 12. Comparison of stiffness for different models in **(a)** seismic zone III, **(b)** seismic zone IV, and **(c)** seismic zone Vb.

- Adding a shear wall reduces the soft storey building's maximum displacement and storey drift by 25.27% and 59.28%, respectively. The soft storey building's maximum storey shear rises by 33.38%.
- Compared to other soft storey mitigation techniques, the seismic performance of soft-storey buildings with shear walls positioned at corners is superior.

Future research can assess how well these configurations work together to reduce the soft storey effect in buildings. The most cost-effective way to mitigate the soft storey effect in buildings can also be determined by performing a cost analysis of structures integrated with various strategies.

ETHICS

There are no ethical issues with the publication of this manuscript.

DATA AVAILABILITY STATEMENT

The authors confirm that the data that supports the findings of this study are available within the article. Raw data that support the finding of this study are available from the corresponding author, upon reasonable request.

CONFLICT OF INTEREST

The authors declare that they have no conflict of interest.

FINANCIAL DISCLOSURE

The authors declared that this study has received no financial support.

USE OF AI FOR WRITING ASSISTANCE

Not declared.

PEER-REVIEW

Externally peer-reviewed.

REFERENCES

[1] Ahmer, K., & Chouka, S. S. (2020). Seismic performance evaluation of multi-storey building having soft storey with different location of shear walls. Int *J Innov Technol Explor Eng, 9*(11), 50-55. [CrossRef]

[2] Sreadha, A. R., Pany, C., & Varkey, M. V. (2020). A review on seismic retrofit of beam-column joints. *Int J Mod Trends Sci Technol, 6*(9), 80-93. [CrossRef]

[3] Sreadha, A. R., & Pany, C. (2020). Seismic study of multistorey building using floating column. *Int J Emerg Sci Eng, 6*(9), 6-11. [CrossRef]

[4] Lu, X., Xie, L., Guan, H., Huang, Y., & Lu, X. (2015). A shear wall element for nonlinear seismic analysis of super-tall buildings using OpenSees. *Finite Elem Anal Des, 98*, 14-25. [CrossRef]

[5] Khudhair, S.Y. (2019) The suitable location for shearing walls on soft storey in high rise buildings to increase its stiffness. *Int J Civ Eng Technol, 10*(2), 2096-2105.

[6] Kiran, S., Ramtekkar, G. D., & Titiksh, A. (2017). Comparative study for mitigating the soft storey effect in multi storey buildings using different structural arrangements. *Int J Civ Eng Technol, 8*(3), 520-531.

[7] Dheekshith, K., & Naveen K.M.S. (2018). Comparative study on seismic analysis of two RC buildings

with irregularities under varying seismic zones. *Int Res J Eng Technol, 5*(7), 81-88.

[8] Gairola, P., & Dhyani, S. (2019). Seismic analysis of open soft storey building for different models. *Int J Eng Res Technol, 8*(5), 124-132.

[9] Ghate, N.A., & Siddh, S.P. (2018). Seismic demand of soft storey building and it's strengthening for seismic resistance. *Int J Civ Eng Technol, 9*(5), 602-610.

[10] Shaji, A., Binu, A., Divakaran, D. & Sasidharan, A. (2019). Seismic analysis of soft storey buildings. *Int J Sci Eng Res, 8*(3), 10.

[11] Mazza, F., Mazza, M., & Vulcano, A. (2018). Base-isolation systems for the seismic retrofitting of r.c. framed buildings with soft-storey subjected to near-fault earthquakes. *Soil Dyn Earthq Engi, 109*, 209-221. [CrossRef]

[12] Sharma, P., Rajendra, S., & Vanisree, C. N. (2016) Comparative study on effects of regular and irregular structures subjected to lateral loading by equivalent static method and response spectrum method. *Int J Adv Eng Manag Sci, 2*(5), 263-268.

[13] Halde, V. V., & Deshmukh, A. H. (2015). Review on behavior of soft storey in building. *Int Res J Eng Technol, 2*(8), 327-329.

[14] Takeuchi, T., Wada, A., Matsui, R., Sitler, B., Lin, P., Sutcu, F., Sakata, H., & Qu, Z. (2017). *Buckling-restrained braces and applications*. Japan Society of Seismic Isolation.

[15] Kannan, S. S. (2023). *Seismic analysis of soft storey building in earthquake zones*. In IOP Conference Series: Earth and Environmental Science (Vol. 1130, No. 1, p. 012023). IOP Publishing. [CrossRef]

[16] Pesaralanka, V., Challagulla, S. P., Vicencio, F., Chandra Babu, P. S., Hossain, I., Jameel, M., & Ramakrishna, U. (2023). Influence of a soft story on the seismic response of non-structural components. *Sustainability, 15*(4), 2860. [CrossRef]

[17] Chanumolu, M., & Anthugari, V. (2022). Dynamic performance of soft-storey structures with gap elements at beam-column joints. *Mater Today Proc, 52*, 622-631. [CrossRef]

[18] Qambrani, M. M., Mirza, F., & Habib, M. (2023). Comparative seismic response analysis of a multi-storey building with and without base isolators under high magnitude earthquake. *Eng Proceed, 44*(1), 6. [CrossRef]

[19] Bureau of Indian Standards. Criteria for earthquake resistant design of structures. IS 1893: 2016 Part 1

J Sustain Const Mater Technol, Vol. 9, Issue. 4, pp. 365–373, December 2024

Journal of Sustainable Construction Materials and Technologies
Web page info: https://jscmt.yildiz.edu.tr
DOI: 10.47481/jscmt.1607851

Journal of Sustainable Construction Materials and Technologies

Research Article

Effect of sealed water curing and fiber length on compressive strength and fracture energy of fly ash-based geopolymer mortars

Adil GÜLTEKİN*

Department of Civil Engineering, Düzce University Faculty of Engineering, Düzce, Türkiye

ARTICLE INFO

Article history
Received: 05 July 2024
Revised: 13 December 2024
Accepted: 16 December 2024

Key words:
Fracture energy, geopolymer, PVA fiber, sealed curing, water curing

ABSTRACT

In this study, the effect of the curing method and polyvinyl alcohol (PVA) fiber inclusion on some engineering properties of fly ash-based geopolymer mortars was examined. In this context, six fly ash-based mortars were produced using sodium hydroxide and sodium silicate solution. The fracture energy values were determined with notched samples of 50×50×240 mm dimensions, and a clip-on gage was used to measure the crack mouth opening displacements. The notch width and notch height were 3 mm and 10 mm, respectively. Specimens were cured in hot water (80 °C) for 18 hours. Before curing, one series of samples was sealed with three layers of polyvinyl chloride (PVC) cling film and two layers of duct tape, while the other was not. The results showed that sealing the specimens during curing increased the compressive strength, and these increases were 18% for the reference mortar and 18% and 12% for mortars produced with 6 mm and 12 mm PVA fiber, respectively. Sealed curing enhanced fracture energy and peak loads and reduced the rate of capillary water absorption. With fiber inclusion, increases of up to 1508% in fracture energy values were achieved. The results revealed that sealing samples during curing significantly affects the mechanical properties.

Cite this article as: Gültekin, A. (2024). Effect of sealed water curing and fiber length on compressive strength and fracture energy of fly ash-based geopolymer mortars. *J Sustain Const Mater Technol*, 9(4), 365–373.

1. INTRODUCTION

Concrete is the most widely used building material in the world. However, the production of Portland cement consumes significant energy and emits substantial quantities of carbon dioxide. The cement industry is estimated to be responsible for approximately 8% of global carbon dioxide emissions. Alternative materials are required to reduce these drawbacks. One potential alternative to cement is geopolymers [1].

In the production of geopolymers, aluminosilicate powder materials like fly ash and slag are used with the activator solution. This activator is generally produced using sodium hydroxide, sodium silicate, potassium hydroxide, and potassium silicates, and the resulting reaction between aluminosilicate and activator is known as geopolymerization [2]. Geopolymers offer several advantages, including significantly reducing cement-related carbon dioxide emissions, possessing high mechanical properties and good durability, providing the disposal of waste materials, exhibiting low shrinkage, and having good sulfate and corrosion resistance [3].

Although geopolymers have many advantages, these materials are brittle, similar to traditional concrete. Different types of fibers can reinforce geopolymers like fiber-reinforced cement-based concrete, and numerous studies have addressed this subject [4]. Fibers reduce brittleness and microcracking, thereby increasing the fracture tough-

---

***Corresponding author.**
*E-mail address: adilgultekin@duzce.edu.tr

Published by Yıldız Technical University Press, İstanbul, Türkiye

ness of geopolymer concretes. Research has been conducted studies on the use of various fiber types, such as steel, polyvinyl alcohol (PVA), glass, polypropylene, carbon, and natural fibers, in the production of fiber-reinforced geopolymers [5]. Yurt [6] examined the effect of fiber inclusion on the mechanical properties of blast furnace slag-based alkali-activated concretes and reported that flexural strengths increased with adding fibers. In a similar study, Faris et al. [7] investigated the effect of steel fiber geometry on the properties of fly ash-based fiber-reinforced geopolymer concretes. They stated a substantial increase in the flexural strength of the concretes with the addition of fibers, reaching up to 144%. The optimal fiber dosage was found to be 1% in terms of flexural strength, and it was demonstrated that hooked end fibers are particularly advantageous in enhancing flexural behavior. Wang et al. [8] reported that incorporating 0.05% basalt fiber by volume increased the peak load and fracture energy of fly ash-based geopolymer concretes by 37% and 56%, respectively. Deepa et al. [9] explored the influence of steel fiber inclusion on fly ash-based geopolymer concretes. Researchers reported that the first crack load, peak load, fracture toughness, and fracture energy values increased with fiber addition, and the facts were more pronounced with higher fiber content. It was stated that the fracture energy increased by 345% compared to the control sample produced without fiber addition when the fiber content reached 0.75%.

Fracture energy can be summarized as the required energy to create a one-unit crack area and can be determined using notched beam specimens [10]. Parameters like water/cement ratio, quantity of aggregate, aggregate size and strength [11], sample and notch geometry, and the presence of fibers [12], as well as aggregate gradation [13], were reported to affect the fracture energy of concrete significantly. Numerous studies have investigated the fracture energies of both cement-based composites and geopolymer/alkali-activated materials. Kozlowski et al. [14] investigated the effect of foaming agent dosage on the fracture energy of Portland cement-based foam composites. Tang et al. [15] examined the effect of partially replacing coarse aggregate with polystyrene on fracture energy in concrete. Celik and Bingol [16] investigated the effect of dosage of polypropylene, glass, and basalt fiber inclusion on the fracture energy of Portland cement-based self-compacting concrete. Ipek and Aksu [17] studied the effect of fiber type, length, and content on the fracture energy of cement-based SIFCON composites. Similar studies have also been conducted on geopolymer/alkali-activated materials. Ding et al. [18] investigated the effects of alkali concentration, alkali solution modulus, and liquid/binder ratio on the fracture energy of fly ash/slag-based geopolymer concretes cured under ambient conditions. Researchers reported that the fracture energy increased with the increase in alkali concentration, activator modulus, and slag amount, while the opposite was true for the liquid/binder ratio. In a similar study, Gomes et al. [19] examined the effect of steel fiber dosage on the fracture parameters of metakaolin-based geopolymer concretes cured under ambient conditions and reported significant improvements in fracture behavior with fiber addition. Liu et al. [20] conducted a study on the effect of steel fiber and silica fume inclusion on the fracture energy of ultra-high-performance geopolymer concretes and reported that the mechanical properties of these concretes were comparable to those of conventional ultra-high-performance concrete.

Table 1. Chemical composition and some physical properties of fly ash

Compound	(%)	Property	Value
SiO_2	55.9	Specific gravity	2.21
Al_2O_3	23.3	Retained on 32 μm	26.7%
Fe_2O_3	6.3	Retained on 45 μm	20.0%
CaO	5.3	Retained on 90 μm	6.4%
MgO	2.1		
Na_2O	0.6		
K_2O	2.3		
SO_3	0.2		
Loss on ignition	2.0		

While various alternatives like steam and ambient curing are possible in geopolymer production, oven curing is commonly employed [21]. Heat curing can be used to achieve the desired strengths [22], and the curing temperatures are generally below 100 °C [23]. Apart from these, different methods such as microwave curing [24], solar curing [25], water curing, and saline water curing [26] are also used. However, it has been reported that alkalis in the geopolymer can leak into the curing environment during water curing, and it was stated that the mechanical properties could be negatively affected [27]. The number of studies addressing water curing in geopolymer or alkali-activated material production is limited. Moreover, most previous studies have focused on water curing at room temperature. Therefore, further research is needed to explore the effects of water curing at relatively high temperatures and the incorporation of fibers in water-cured geopolymers. This study examined the fracture energies, compressive strengths, and sorptivity properties of hot water-cured fly ash-based geopolymer composites. For this purpose, 50×50×240 mm prism specimens with a notch of 10 mm in height and 3 mm in width were used. Curing was applied in two different ways. One series of geopolymer composites was cured directly in water at 80 °C, while another was covered with (polyvinyl chloride) PVC film and duct tape before curing. This approach can prevent the leaching of alkalis from the geopolymer into the curing water.

2. MATERIALS AND METHOD

2.1. Materials

In this study, low calcium-bearing fly ash, a mixture of sodium silicate and sodium hydroxide, and CEN standard sand conforming to TS EN 196-1 [28] were used as the aluminosilicate, activator solution, and aggregate, respectively. The chemical composition and some physical properties of ash are presented in Table 1. The sodium hydroxide was in pellet form with a minimum purity of 98%, and the sodium silicate solution contained 9.1% Na_2O, 28.6% SiO_2, and 62.3% H_2O. In preparing the activator solution, sodium hydroxide pellets (11.4% by weight) were dissolved in sodium silicate solution (88.6% by weight), and the resulting activator was allowed to rest for 24 hours. To reduce the setting time of mixtures, a CEM I 42.5 R type ordinary Portland cement was used. PVA fibers of 6 mm and 12 mm lengths reinforced the mortars.

2.2. Production of Samples

Mortar mixtures were prepared using a mortar mixer. CEN standard sand, fly ash, cement, activator solution, and water were sequentially placed into the mixer bowl, and the mixer was operated at 62.5 rpm for 90 seconds. Fibers were added to the bowl using the sprinkling method for approximately 30 seconds during this initial mixing stage. After 90 seconds of mixing, materials adhering to the bowl's walls were scraped off with a spoon, and mixing was continued at the same speed for another 90 seconds.

After the mixing process, the flow diameters of the mixtures were determined according to the TS EN 459-2 [29] Standard. The mortars were placed in 50×50×240 mm metal prismatic molds in two layers. Each layer was compacted with 25 jolts using a jolting table. The mortars were allowed to be set under laboratory conditions for six hours. Due to the low CaO content in the used fly ash, the setting time under laboratory conditions was significantly prolonged (approximately one week). To address this issue, portland cement was incorporated to accelerate the setting process. After the setting period, the samples were demoulded. The demoulded samples were divided into two groups. One group of mortars was tightly sealed with three layers of PVC cling film and two layers of duct tape, as shown in Figure 1, while the other group was not sealed.

The samples were cured in tap water at 80 °C for 18 hours. At the end of the curing period, the samples were removed from the water, and once the specimens cooled to room temperature, tests were conducted. The reference mortar and mortars containing short and long fibers are abbreviated as Ref, SF, and LF, respectively. Samples cured with PVC cling film and duct tape were called "Sealed" samples, while the others were designated as "Unsealed." For instance, the sample specified as SF-Sealed represents the series produced using 6 mm PVA fiber and cured after being sealed with PVC and duct tape.

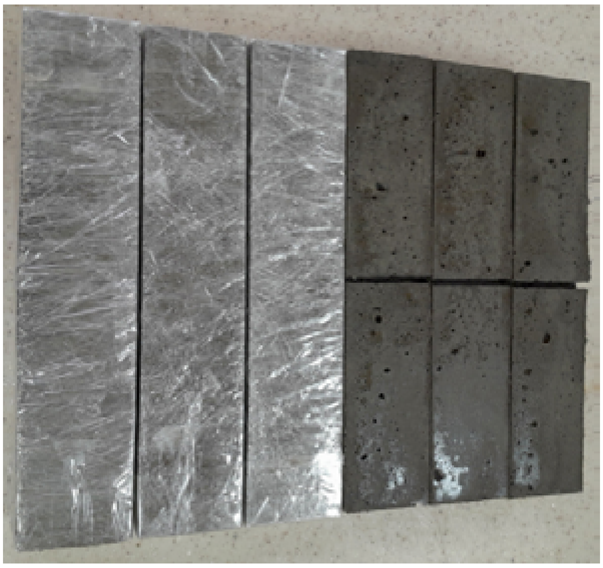

Figure 1. Sealed and unsealed specimens before water curing.

2.3. Tests

Notched samples, as shown in Figure 2, were used for the fracture energy tests. A clip-on gage was used to measure the crack mouth opening displacements (CMOD). For this purpose, two metal blades were fixed to the sample to attach the clip-on gauge. The experiment was conducted using a 3-point bending test setup. A displacement-controlled universal test device was used, and the crack opening rate was set to 0.05 mm/min. The test was automatically stopped for each sample when a 95% reduction in peak load was observed. The load-CMOD graph was plotted, and the area under the curve (W_0) was calculated. Subsequently, Equation 1, suggested by RILEM (1985) [10], was modified and used to calculate the fracture energies. Three samples were tested for each series, and the average fracture energy value was reported.

$$\text{Fracture energy} = (W_0+mg\delta)/A_{lig} \quad (1)$$

In the equation, mg, δ, A_{lig} represent the weight of the specimen between supports, the maximum crack opening displacement, and the fracture area, respectively.

Compressive strength tests were performed by ASTM C349 [30] Standard, with some modifications using six split samples following the fracture energy tests. These tests were conducted with a 500 kN capacity concrete press. The loading rate was set at 0.9 kN/s, and a compression device with a 50x50 mm frame was used, as shown in Figure 3.

Table 2. Mixture proportions and some properties of mixtures

Mix	Ingredient (g)							Flow diameter (mm)	Fresh unit weight (kg/m³)
	Fly ash	Cement	Alkali solution	Sand	Water	PVA fiber			
						6 mm	12 mm		
Ref	405	45	213	1350	40	–	–	144	2212
SF	405	45	213	1350	40	7.2	–	129	2174
LF	405	45	213	1350	40	–	7.2	120	2161

PVA: Polyvinyl alcohol; SF: Short fiber; LF: Long fiber.

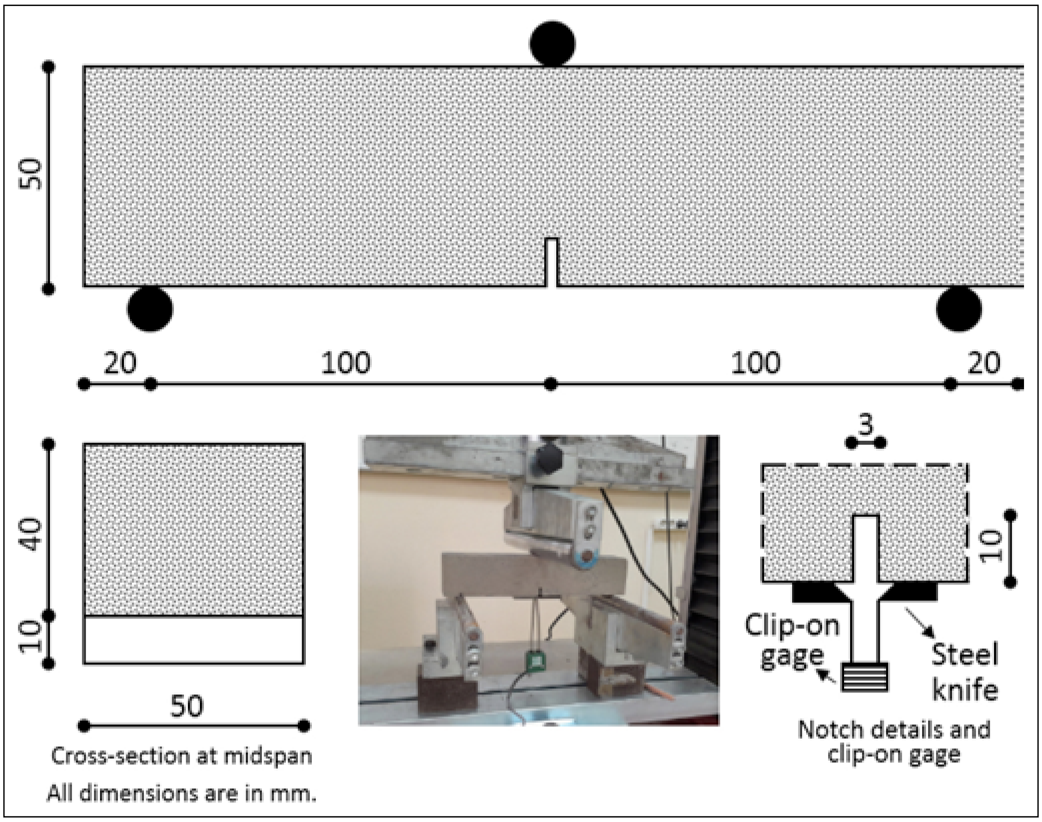

Figure 2. Geometry of specimen, notch details, test set-up, and test photograph.

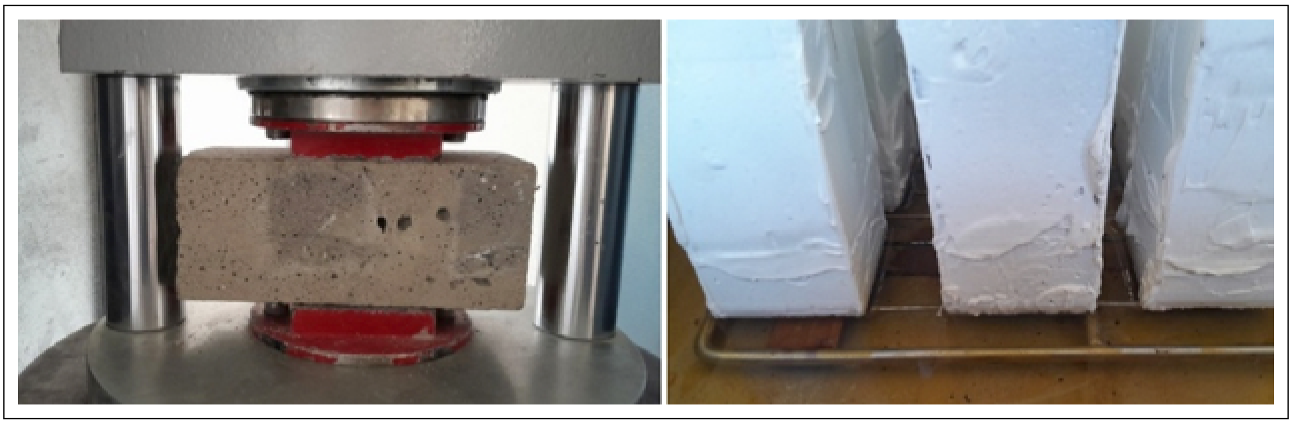

Figure 3. Compressive strength and sorptivity test photographs.

Sorptivity tests were conducted on 50×50×240 mm samples without notches, following the ASTM C1585 [31] Standard with some modifications. After the curing period, the samples were dried in an oven at 50 °C for 72 hours. Subsequently, all parts of the samples except the bottom area (50×50 mm) were covered with a waterproof material. The amount of water absorbed by the samples was measured over 6 hours. The I-$s^{0.5}$ graphs were plotted, and the capillary water absorption rates were determined using the best-fit line passing through these points.

2.4. Mixtures

The amount of ingredients, flow diameters, and fresh unit weight values of the mortars are presented in Table 2. Due to the prolonged setting time of fly ash at room temperature, mixtures were prepared with 10% cement in the total powder content to expedite the setting process. The fiber content was maintained at 0.6% of the total mortar volume. It was noted that adding fiber reduced both the mortars' flow diameters and fresh unit weights.

3. RESULTS AND DISCUSSION

3.1. Compressive Strength

The compressive strengths of the mortars are presented in Figure 4. Among all series, the compressive strength of the sealed samples was higher than that of the unsealed samples. Sealing the samples with PVC cling film increased the compressive strength of the reference mixture by 18%. Similarly, these increments were 18% and 12% for the short and long

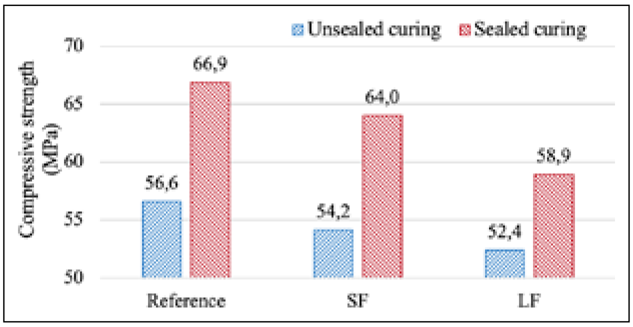

Figure 4. Compressive strength test results.

fibers including mixtures. The difference in strength between sealed and unsealed mortars prepared from the same mix suggests a greater degree of geopolymerization in the sealed samples. Despite limited prior research on sealed water curing, Giasuddin et al. [26] reported that the compressive strengths of fly ash-based geopolymers cured in tap water and two different concentrations of saline water (8% and 15%) were 48, 61 and 65 MPa, respectively. However, the compressive strength of samples sealed with silicone and plastic sheets increased to approximately 90 MPa. Researchers suggested that sealing the samples hindered possible ion transfer between water and the sample, enhancing the compressive strength. In a similar study, Kannangara et al. [32] investigated the effect of curing methods on the compressive strength of fly ash-based geopolymer pastes. Different composite series were produced using various alkaline solution/fly ash ratios and sodium silicate/sodium hydroxide ratios at 60 °C for 24 hours using a climatic test chamber. One series was covered with a polymeric film layer, while the other was left uncovered. It was found that the compressive strengths of the film-covered series were 4% to 179% higher compared to the uncovered samples. The researchers stated that the phenomenon occurred due to the initial dehydration of the matrix in the uncovered series. This dehydration led to deterioration in the matrix structure, and water loss negatively affected the dissolution and gelation processes. It was also emphasized that carbonation may had an impact on the situation.

When the effect of fiber inclusion on compressive strength is examined, it is observed that there was a slight decrease in strength with the addition of fiber. While the reductions in compressive strength for unsealed-cured short and long fiber-reinforced mortars were 4.2% and 7.4%, respectively, in sealed samples, these values were 4.3% and 12%. The negative effect of using long fibers on compressive strength is greater than that of short fiber addition. Many researchers have investigated the mechanical properties of fiber-reinforced geopolymers, and it has been proven that fiber inclusion and fiber dosage can significantly affect mechanical properties. In a similar study, Zhang et al. [33] investigated the effect of PVA fiber addition from 0.2% to 1.0% with 0.2% intervals on the mechanical properties of fly ash/metakaolin-based geopolymer concretes. Researchers reported that low fiber dosages increased the compressive strength, but the strengths gradually decreased with increasing fiber content. Lower compressive strength values were obtained at dosages of 0.8% and 1% compared to the control mixture. In a similar study, Manfaluthy and Ekaputri [34] reported that the addition of 0.3%, 0.5%, and 0.8% PVA fiber by volume increased the compressive strength of fly ash-based geopolymer concrete by 2.4%, 3.7%, and 9.8%, respectively. Zhang et al. [35] stated that using PVA fiber at an appropriate dosage in geopolymer composites increases strength by providing crack control. Still, the use of an inappropriate dosage has a negative effect on the strength by creating pores within the structure. Sukontasukkul et al. [36] highlighted the impact of fiber dosage. They emphasized that using 1% polypropylene fiber in fly ash and silica fume-based geopolymer mortars reduces the compressive strength by 14%.

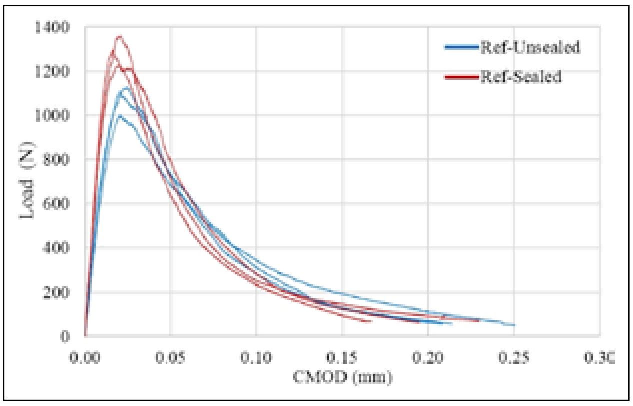

Figure 5. Load-CMOD curves of reference mortars.

CMOD: Crack mouth opening displacement.

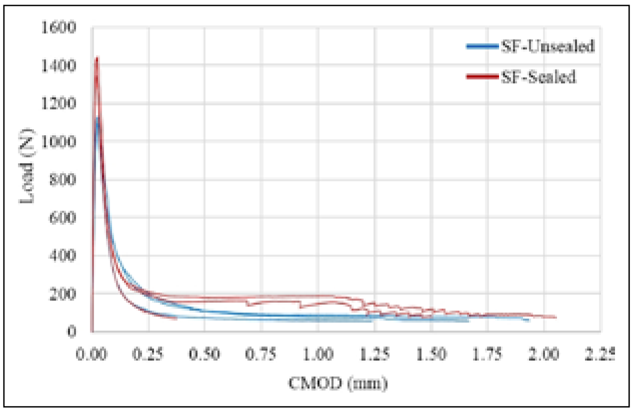

Figure 6. Load-CMOD curves of short fiber-reinforced mortars.

3.2. Fracture Energy

The load-CMOD curves of the three samples from each series after fracture energy tests are presented in Figure 5–7. As expected, the peak load was reached shortly after loading began in all series. After the peak load, the load-carrying capacity of all samples decreased. Due to the absence of fiber reinforcement in the reference samples, the test was finished at low crack openings. However, the ultimate CMOD values were significantly higher in the fiber-reinforced series than in the reference samples. The fracture behavior was more ductile when short fibers were used, and the toughness value increased significantly. With the use of long fibers, these values increased further. Figure 8 illustrates the bridging ability of the fibers.

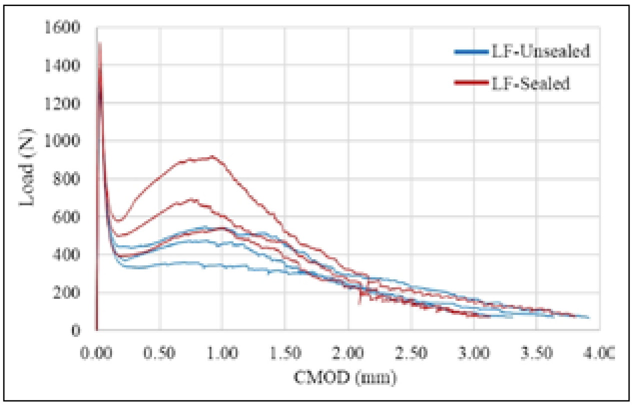

Figure 7. Load-CMOD curves of long fiber-reinforced mortars.

The peak loads and fracture energy values of the mortars are presented in Figure 9 and Figure 10, respectively. The average peak loads of sealed specimens, regardless of fiber inclusion or fiber length, were higher than those of the unsealed series. This increase was 20% in the reference sample, 27% and 8% in the series produced with short and long fiber inclusion, respectively. This situation was attributed to the higher strength of the matrix in the sealed samples. In addition, the possible increase in fiber-matrix bond is also thought to affect the situation. When the effect of fiber usage on peak loads was examined, it was observed that peak loads increased due to fibers' ability to bridge stresses, as expected. This increase was recorded as 3% and 22% in the short- and long fiber-reinforced series produced without sealing, respectively, while it was recorded as 9% and 10% in the sealed-cured series. In this context, long fibers provided higher peak loads than short fibers. Previous studies on similar topics have proved the contribution of fiber inclusion and curing regimes. The effects of fiber addition and curing regime on the mechanical properties of geopolymer composites have been the subject of numerous studies, yielding similar results. Nath and Sarker [37] investigated the effect of curing time on the mechanical properties of geopolymer composites. They stated that the fracture energy and peak loads increased as the curing duration increased from 28 days to 90 days in fly ash-based geopolymer concretes produced by ambient curing and activated with sodium silicate and sodium hydroxide. In a similar study, Wang et al. [8] investigated the effect of basalt fiber addition on the fracture energy of fly ash-based geopolymer concrete. The researchers reported that the peak loads achieved in the fiber-reinforced series were 17–37% higher than the control series due to the effect of basalt fiber addition on crack propagation. It was also reported that fracture energies increased with the addition of basalt fibers, with the highest increase observed being 56% at 0.05% fiber addition [8]. It was reported that using fiber in appropriate dosages improves fracture behavior and increases fracture energy in geopolymer composites due to mechanisms such as bridging, fiber fracture, and fiber pull-out [38]. Cai et al. [39] investigated the effect of PVA fiber and PVA powder on fly ash-based geopolymer composites and obtained SEM images illustrating the three aforementioned fiber working mechanisms.

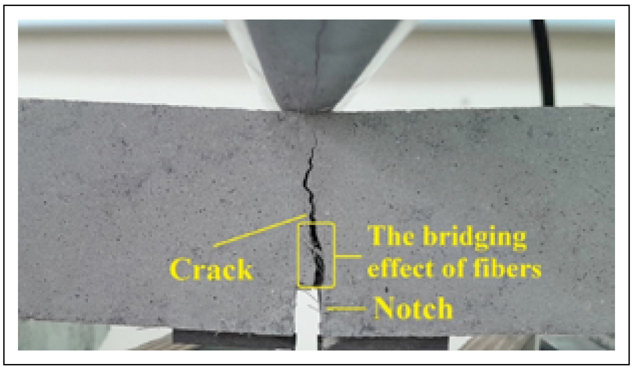

Figure 8. Fracture energy test and bridging effect of fibers.

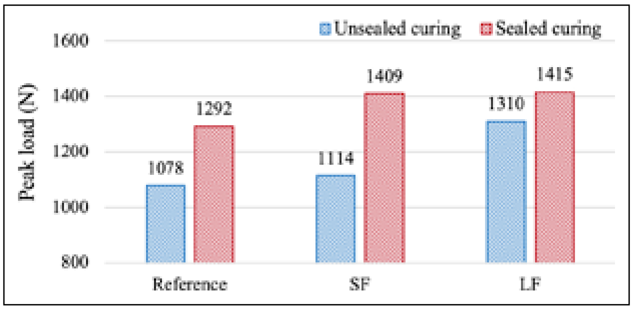

Figure 9. Average peak loads in the fracture energy test.

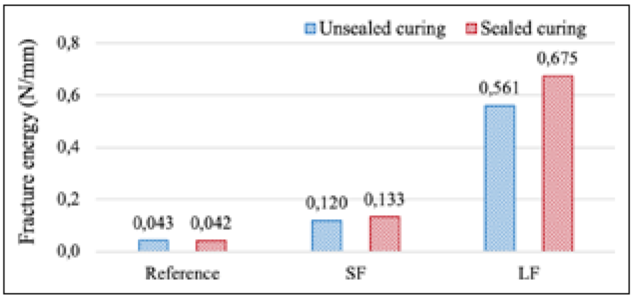

Figure 10. Average fracture energy values in the fracture energy test.

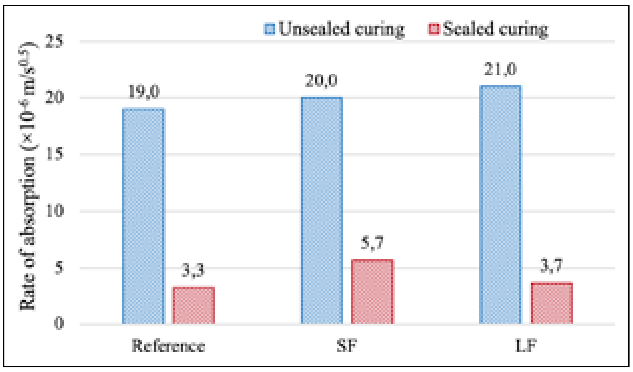

Figure 11. Initial rate of water absorption values.

3.3. Sorptivity

The rate of initial water absorption values of the mortars is presented comparatively in Figure 11. It is observed that the values for both the reference mortar and the fiber-reinforced mortars were very close to each other. Although there was no significant difference between the values, considerable variations were evident between the sealed and unsealed samples. Specifically, the initial rate of water absorption value of unsealed reference mortar, 19×10^{-6} m/s$^{0.5}$, decreased by 83% to 3.3×10^{-6} m/s$^{0.5}$ in the sealed series. Similarly, 72% and 82% reductions were observed in the short and long fibers series, respectively. Thokchom et al. [40] investigated the effect of Na_2O amount on the properties of fly ash-based geopolymer mortars. The researchers observed that increasing the Na_2O ratio enhanced geopolymerization, resulting in a denser internal structure, increased compressive strength, and reduced water sorptivity. In a similar study, Shaikh [41] examined the effect of sodium hydroxide concentration (14 and 16 M) and the sodium silicate/sodium hydroxide ratio (2.5, 3.0, and 3.5) on the sorptivity properties of fly ash-based geopolymer concretes. The researcher reported that higher concentrations of sodium hydroxide or an increase in the sodium silicate/sodium hydroxide ratio led to decreased sorptivity, which was attributed to denser sodium aluminosilicate gel formation. In this study, it is thought that the significantly lower rate of absorption values observed in the sealed samples resulted from increased geopolymerization reactions. The observed increase in compressive strength supports this hypothesis.

4. CONCLUSIONS

This study investigated the effect of the curing method, fiber inclusion, and fiber length (6 and 12 mm PVA fiber) on fly ash-based geopolymer mortars' compressive strength and fracture energy. One series of samples was cured in water at 80 °C in direct contact with water, while another was first sealed with PVC cling film and duct tape and then cured in the same medium. Considering the materials used and the experiments conducted, the following results can be drawn:

- The curing method has significant effects on the mechanical properties. The compressive strengths and peak loads in the fracture energy test of the sealed-cured mortars are higher than those of the unsealed-cured series. Sealed curing increased compressive strength from 12% to 18% in this context. Furthermore, the peak load and fracture energy increased by up to 27% and 20%, respectively, due to sealing.
- With the addition of fibers, peak load, and fracture energy values increased; however, compressive strength values decreased. It was observed that long fibers had a more significant positive effect on peak load and fracture energy in both sealed and unsealed curing conditions. Specifically, long fibers provided 368% and 408% higher fracture energy values than short fibers under unsealed and sealed curing conditions. This improvement is attributed to the better bridging capacity of long fibers.
- It was determined that the fiber inclusion did not contribute positively to compressive strength and, in fact, decreased compressive strength by up to 7% and 12% under unsealed and sealed curing conditions, respectively. In this context, it was also observed that the negative effect was more pronounced when long fibers were used. One of the reasons for this situation is the reduced workability, as also provided in the flow-diameter test.
- The water absorption rate at the sorptivity test of the sealed-cured series is significantly lower than that of the unsealed series. The reduction rates were 83%, 72%, and 82% in the fiber-free reference mixture, short and long fiber, respectively.

ETHICS

There are no ethical issues with the publication of this manuscript.

DATA AVAILABILITY STATEMENT

The author confirm that the data that supports the findings of this study are available within the article. Raw data that support the finding of this study are available from the corresponding author, upon reasonable request.

CONFLICT OF INTEREST

The author declares that he has no conflict of interest.

FINANCIAL DISCLOSURE

The author declared that this study has received no financial support.

USE OF AI FOR WRITING ASSISTANCE

Not declared.

PEER-REVIEW

Externally peer-reviewed.

REFERENCES

[1] Verma, M., Dev, N., Rahman, I., Nigam, M., Mohd, A., & Mallick, J. (2022). Geopolymer concrete: A material for sustainable development in Indian construction industries. *Crystals, 12*(4), 514. [CrossRef]

[2] Mamatha, B. S., Sujatha, D., Uday, D. N., & Kiran, M. C. (2023). Properties of fly ash-based wood geopolymer composite. *Low-Carbon Mater Green Constr, 1*(1), 29. [CrossRef]

[3] Zerfu, K., & Ekaputri, J. J. (2016). Review on alkali-activated fly ash based geopolymer concrete. *Mater Sci Forum, 841*, 162-169. [CrossRef]

[4] Chen, P., Li, Y., Yin, L., & Wang, Z. (2024). Review on mechanical properties of fiber-reinforced geopolymer concrete after high-temperature exposure. *Iran J Sci Technol Trans Civil Eng, 48*, 3829-3851. [CrossRef]

[5] Kaya, M. (2022). Effect of steel fiber additive on high temperature resistance in geopolymer mortars. *Iran J Sci Technol Trans Civil Eng, 46*(3), 1949-1967. [CrossRef]

[6] Yurt, Ü. (2022). Effect of curing temperature on fracture properties of alkali-activated fiber concrete. *Osmaniye Korkut Ata Uni J Inst Sci Technol, 5*(1), 176-188. [CrossRef]

[7] Faris, M. A., Abdullah, M. M. A. B., Muniandy, R., Abu Hashim, M. F., Błoch, K., Jeż, B., Garus, S., Palutkiewicz, P., Mohd Mortar, N. A., & Ghazali, M. F. (2021). Comparison of hook and straight steel fibers addition on malaysian fly ash-based geopolymer concrete on the slump, density, water absorption and mechanical properties. *Materials, 14*(5), 1310. [CrossRef]

[8] Wang, Y., Hu, S., & Sun, X. (2022). Experimental investigation on the elastic modulus and fracture properties of basalt fiber-reinforced fly ash geopolymer concrete. *Constr Build Mater, 338*, 127570. [CrossRef]

[9] Deepa, R. S., Ruby, A., Ganesan, N., & Divya, S. (2013). Fracture properties of fibre reinforced geopolymer concrete. *Int Conf Innov Civ Eng, 4*(5), 75-80.

[10] RILEM (50-FMC) (1985). Determination of the fracture energy of mortar and concrete by means of three-point bend tests on notched beams. *Mater Struct, 18*(4), 287-290. [CrossRef]

[11] Wang, X., Saifullah, H. A., Nishikawa, H., & Nakarai, K. (2020). Effect of water-cement ratio, aggregate type, and curing temperature on the fracture energy of concrete. *Constr Build Mater, 259*, 119646. [CrossRef]

[12] Xu, P., Ma, J., Ding, Y., & Zhang, M. (2021). Influences of steel fiber content on size effect of the fracture energy of high-strength concrete. *KSCE J Civ Eng, 25*(3), 948-959. [CrossRef]

[13] Fidi, F., Muin, R. B., & Patty, A. H. (2020). The effect of aggregate gradation on concrete fracture energy using the work of fracture method. *IOP Conf Series Mater Sci Eng, 830*(2), 022061. [CrossRef]

[14] Kozłowski, M., Kadela, M., & Kukiełka, A. (2015). Fracture energy of foamed concrete based on three-point bending test on notched beams. *Procedia Engineering, 108*, 349-354. [CrossRef]

[15] Tang, W., Cui, H., & Tahmasbi, S. (2016). Fracture properties of polystyrene aggregate concrete after exposure to high temperatures. *Materials, 9(8), 630*. [CrossRef]

[16] Celik, Z., & Bingol, A. F. (2020). Fracture properties and impact resistance of self-compacting fiber reinforced concrete (SCFRC). *Mater Struct, 53*(3), 50. [CrossRef]

[17] Ipek, M., & Aksu, M. (2019). The effect of different types of fiber on flexure strength and fracture toughness in SIFCON. *Constr Build Mater, 214*, 207-218. [CrossRef]

[18] Ding, Y., Shi, C. J., & Li, N. (2018). Fracture properties of slag/fly ash-based geopolymer concrete cured in ambient temperature. *Constr Build Mater, 190*, 787-795. [CrossRef]

[19] Gomes, R. F., Dias, D. P., & Silva, F. D. A. (2020). Determination of the fracture parameters of steel fiber-reinforced geopolymer concrete. *Theor Appl Fract Mec, 107*, 102568. [CrossRef]

[20] Liu, Y., Shi, C., Zhang, Z., Li, N., & Shi, D. (2020). Mechanical and fracture properties of ultra-high performance geopolymer concrete: Effects of steel fiber and silica fume. *Cement Concr Comp, 112*, 103665. [CrossRef]

[21] Nurruddin, M. F., Haruna, S., Mohammed, B. S., & Shaaban, I. G., (2018). Methods of curing geopolymer concrete: A review. *Int J Adv Appl Sci, 5*(1), 31-36. [CrossRef]

[22] Rekha, Y., Suriya, S., & Hamedul Irshad, H. M. (2022). Comparative study on oven curing of Geo-polymer concrete over conventional concrete. *Mater Today Procs, 55*, 462-469. [CrossRef]

[23] Davidovits, J. (2017). Geopolymers: Ceramic-like inorganic polymers. *J Ceram Sci Technol, 8*(3), 335-350.

[24] Yilmazer Polat, B. (2023). The influence of microwave curing on the strength of silica fume-added fly ash-based geopolymer mortars. *J Sustain Constr Mater Technol, 8*(3), 207-215. [CrossRef]

[25] Dong, M., Feng, W., Elchalakani, M., Li, K. G., Karrech, A., & May, E. F. (2017). Development of a high strength geopolymer by novel solar curing. *Ceram Int, 43*(14), 11233-11243. [CrossRef]

[26] Giasuddin, H. M., Sanjayan, J. G., & Ranjith, P. G. (2013). Strength of geopolymer cured in saline water in ambient conditions. *Fuel, 107*, 34-39. [CrossRef]

[27] Saludung, A., Azeyanagi, T., Ogawa, Y., & Kawai, K. (2023). Mechanical and microstructural evolutions of fly ash/slag-based geopolymer at high temperatures: Effect of curing conditions. *Ceram Int, 49*(2), 2091-2101. [CrossRef]

[28] Turkish Standarts Institution. (2016). *Methods of testing cement - Part 1: Determination of strength, Ankara*. TS EN 196-1.

[29] Turkish Standarts Institution. (2021). *Building lime - Part 2: Test methods, Ankara*. TS EN 459-2

[30] ASTM International. (2018). *Standard test method for compressive strength of hydraulic-cement mortars (using portions of prisms broken in flexure), USA*. ASTM C349.

[31] ASTM International. (2020). *Standard Test Method for Measurement of Rate of Absorption of Water by Hydraulic-Cement Concretes, USA*. ASTM C1585.

[32] Kannangara, T., Guerrieri, M., Fragomeni, S., & Joseph, P. (2022). Effects of initial surface evaporation on the performance of fly ash-based geopolymer paste at elevated temperatures. *Appl Sci, 12*(1), 364. [CrossRef]

[33] Zhang, P., Han, X., Zheng, Y., Wan, J., & Hui, D. (2021). Effect of PVA fiber on mechanical properties of fly ash-based geopolymer concrete. *Rev Adv Mater Sci, 60*(1), 418-437. [CrossRef]

[34] Manfaluthy, M. L., & Ekaputri, J. J. (2017). The application of PVA fiber to improve the mechanical properties of geopolymer concrete. *MATEC Web Conf, 138*, 01020. [CrossRef]

[35] Zhang, P., Feng, Z., Yuan, W., Hu, S., & Yuan, P. (2024). Effect of PVA fiber on properties of geopolymer composites: A comprehensive review. *J Mater Res Technol, 29*, 4086-4101. [CrossRef]

[36] Sukontasukkul, P., Pongsopha, P., Chindaprasirt, P., & Songpiriyakij, S. (2018). Flexural performance and toughness of hybrid steel and polypropylene fibre reinforced geopolymer. *Constr Build Mater, 161*, 37-44. [CrossRef]

[37] Nath, P., & Sarker, P. K. (2017). Fracture properties of GGBFS-blended fly ash geopolymer concrete cured in ambient temperature. *Mater Struct, 50*(1), 32. [CrossRef]

[38] Wang, T., Fan, X., Gao, C., Qu, C., Liu, J., & Yu, G. (2023). The influence of fiber on the mechanical properties of geopolymer concrete: A review. *Polymers, 15*(4), 827. [CrossRef]

[39] Cai, J., Jiang, J., Gao, X., & Ding, M. (2022). Improving the mechanical properties of fly ash-based geopolymer composites with PVA fiber and powder. *Materials, 15*(7), 2363. [CrossRef]

[40] Thokchom, S., Ghosh, P., & Ghosh, S. (2009). Effect of water absorption, porosity and sorptivity on durability of geopolymer mortars. *ARPN J Eng Appl Sci, 4*(7), 28-32.

[41] Shaikh, F. U. A. (2014). Effects of alkali solutions on corrosion durability of geopolymer concrete. *Adv Concr Constr, 2*(2), 109-123. [CrossRef]

Journal of Sustainable Construction Materials and Technologies
Web page info: https://jscmt.yildiz.edu.tr
DOI: 10.47481/jscmt.1607846

Journal of Sustainable Construction
Materials and Technologies

Research Article

Strength and durability performance of hybrid alkaline clay brick waste – Coconut shell ash cement

Festus Musyimi NGUI[*1], **Victor Kiptoo MUTAI**[2], **Najya MUHAMMED**[1], **Fredrick Mulei MUTUNGA**[1], **Joseph Mwiti MARANGU**[3], **Mike OTIENO**[4]

[1]*Department of Chemistry, Pwani University, Kilifi, Kenya*
[2]*Department of Geoscience, University of Padova, Padova, Italy*
[3]*Department of Physical Sciences, Meru University of Science and Technology, Meru, Kenya*
[4]*School of Civil and Environmental Engineering, University of the Witwatersrand, Johannesburg, South Africa*

ARTICLE INFO

Article history
Received: 04 June 2024
Revised: 27 September 2024
Accepted: 04 October 2024

Key words:
Alkali activator, clay brick waste, coconut shell ash, durability, hybrid alkaline mortar, sodium sulphate

ABSTRACT

Hybrid Alkaline Cement (HAC) has the potential to reduce carbon dioxide (CO_2) and improve concrete structure. The durability of a hybrid alkaline mortar made from a mixture of calcined clay brick waste (CBW) and coconut shell ash (CSA) was compared with that of ordinary Portland cement (OPC) and pozzolanic Portland cement (PPC), which are the two common types of Portland cement. In an open furnace, CSA was obtained by burning coconut shells collected from Kilifi County, Kenya. At the same time, CBW was sampled from brick production and construction sites in Kibwezi sub-county, Kenya, and ground using a laboratory ball mill. Various cement blends were prepared by mixing different mass ratios of OPC:CSA: CBW and activated with 0.5 M and 2 M Sodium sulfate solutions, maintaining a solution-to-cement ratio of 0.5. Control mortar prisms were cast using distilled water and cured in distilled water. Principle Component Analysis (PCA) was used for correlation analysis. Compressive strength development, water sorptivity, Porosity, oxygen permeability index, and thermal resistance were investigated for durability properties. Accelerated chloride ingress and chloride ion diffusion coefficients were determined. Results show that alkali-activated samples exhibited lower sorptivity, Porosity, chloride ingress, and higher compressive strength, oxygen permeability index, and thermal resistance than the cement mix prepared with water. The mix designs 5-1-4, 5-4-1, 3-1-6, and 3-6-1 demonstrated a decreasing optimum performance comparable to OPC in that order. The formulation 5-1-4, prepared with 2 M Sodium sulfate, showed the highest durability in all tests. Moreover, mortar durability was highly influenced by the amount of cement substituted, the kind of precursor, and the concentration of alkali activator.

Cite this article as: Ngui, F. M., Mutai, V. K., Muhammed, N., Mutunga, F. M., Marangu, J. M., & Otieno, M. (2024). Strength and durability performance of hybrid alkaline clay brick waste – Coconut shell ash cement. *J Sustain Const Mater Technol*, 9(4), 374–390.

1. INTRODUCTION

The cement manufacturing industry accounts for roughly 6–8% of global CO_2 emissions annually [1]. We must reduce CO_2 emissions from cement production to mitigate this environmental impact. Using alternative materials, mainly agricultural and industrial waste that would otherwise end up in landfills, presents a viable solution. Hybrid-activated cement (HAC) is emerging as a potential long-term substitutes for traditional Portland cement concrete (PCC) [2].

---

*__Corresponding author.__
*E-mail address: festongu@gmail.com

Published by Yıldız Technical University Press, İstanbul, Türkiye

Producing such cement involves substituting the main clinker component. Replacing PCC with HAC has the potential to reduce carbon emissions by 9% to 80% [1, 3]. Several factors, including the chemistry of the alkaline activator, fuel prices, raw material availability, and the efficiency of the clinkering operation in a given region, affect the degree to which emissions can be reduced. However, the durability of the concrete structure is of great importance as CO_2 reduction is achieved.

The durability of concrete structures made with Ordinary Portland Cement (OPC) depends on the quality of the cement and raw materials used. Climate changes, acidic conditions, and carbonationally threaten concrete durability. Exposure to high temperatures causes several chemical and physical transformations in cementitious materials, resulting in internal pore pressure, different thermal expansion rates of components, and decomposition of cement compounds [4]. Once hardened, the cement paste is the least stable component. Due to the degradation of calcium hydroxide (CH) and calcium silicate hydrate (C-S-H), OPC is physically and chemically degraded at high temperatures [5].

In contrast, HAC structures exhibit resilient performance under adverse conditions. They are characterized by low CH and C-S-H content, forming a stable three-dimensional Sodium Alumino-Silicate Hydrate (N-A-S-H) gel formed by connecting SiO_4 and AlO_4 tetrahedra with O atoms in alternating cycles [6, 7]. This results in HAC blends with thermal conductivity typically less than 1 W/m.C, making them an excellent thermal insulator [8]. Aggregate Porosity and mineralogy also influence degradation severity [9]. Concrete deterioration often allows external aggressive chemicals, such as chloride ions, water, and oxygen, to penetrate the concrete matrix through pores and microscopic fissures. The main pathways for ingress into the system are permeability, capillary absorption, and diffusion [10]. Permeability, or the combination of pore structure and proportion of capillary pores, determines how well concrete resists aggressive chemicals. The binder's formulation is the most critical component that affects the permeability of concrete. Binders made from alkali-activated well-blended OPC exhibit denser microstructures than those made from the OPC system, contributing to HAC's enhanced performance potential.

Despite the long history of alkaline activation of aluminosilicates [11, 12], hybrid alkali-activated agricultural and industrial binders have only recently gained recognition as acceptable substitutes for Portland cement [13, 14]. However, the long-term durability of HAC remains to be definitively demonstrated, especially concerning properties related to aggressive ion permeability and thermal resistance.

Thus, further research is needed to enhance engineers' and concrete practitioners' understanding of HAC as an alternative to conventional concrete. This study aims to address critical challenges related to the permeability of aggressive agents and the fire resistance of novel binder construction materials. Specifically, a focus on hybrid alkaline blend materials to investigate changes in sorptivity and chloride ion permeability as OPC replacement, alkali activator concentration, and CBW: CSA ratio are adjusted. Thermal resistance is also evaluated as an essential attribute.

Table 1. Relative percentages of binder type for mortar (w/c=0.5, 28 days curing)

Binder	OPC	CSA	CBW
OPC	100	0	0
5-1-4*	50	10	40
5-4-1*	50	40	10
3-1-6*	30	10	60
3-6-1*	30	60	10

*: Label based on the mix mass ratio of PC-to-CSA-to-CBW. OPC: Ordinary portland cement; CSA: Coconut shell ash; CBW: Clay brick waste.

2. MATERIALS AND METHODS

2.1. Blaine test and Preparation of Mortar Prisms

The specific surface area of the binders was determined according to the Blaine test protocol outlined in the K S EAS 148:-6:1 (2000) standard. Mortar prisms were prepared for Testing by KS EAS 148: 1 [15] using 1,350 g of standard sand complying with EN 196. A mixture of 450 g of test cement and standard sand was prepared using a PAN Analytica mixer machine for 1 minute. Subsequently, an alkaline solution of 0.5 M or 2 M Na_2SO_4, was added to achieve the desired consistency. The mixture was trowel-mixed for another 4 minutes to ensure uniformity in the cement mortar. The resulting slurry was then transferred into a three-pong mold, measuring 40×40×160 mm for compressive strength tests and 100×100×100 mm for durability studies.

The molds were clamped onto a vibrating machine for 2 minutes to compact the mortar. Upon removal from vibration, the mortar prisms were immediately identified by their casting date and the type of cement used, denoted as 5-1-4, 5-4-1, 3-1-6, and 3-6-1, representing the mix mass ratio of OPC:CSA: CBW as detailed in Table 1.

To safeguard against moisture loss caused by evaporation, a polythene sheet that was impermeable and flat was used to cover the prisms. These prisms were then placed in a temperature-controlled room with relative humidity exceeding 90% for 24 hours±30 minutes, after which they were demolded and air-cured for 28 days. Similarly, PC specimens were also prepared for reference purposes, but potable water was used as the mixing liquid, and they were cured in water for 28 days.

2.2. Compressive Strength Testing

The 28-day compressive strength was determined using an automatic compression testing machine (model YAW-300) housed at Mombasa Cement Limited, a prominent cement manufacturing company in Kilifi County, Kenya. The testing procedure strictly followed the protocol outlined in KS EAS 148: 1 (2000).

2.3. Differential Thermogravimetric Analysis (DTA)

A Stanton Redcroft STA-781 device was used for the thermal analysis of raw clay, coconut shell powder, and hydrated cement. 25 g each of the clay, coconut shell powder, and hardened cement were placed in a platinum crucible and the thermal analyzer. The measurements were between

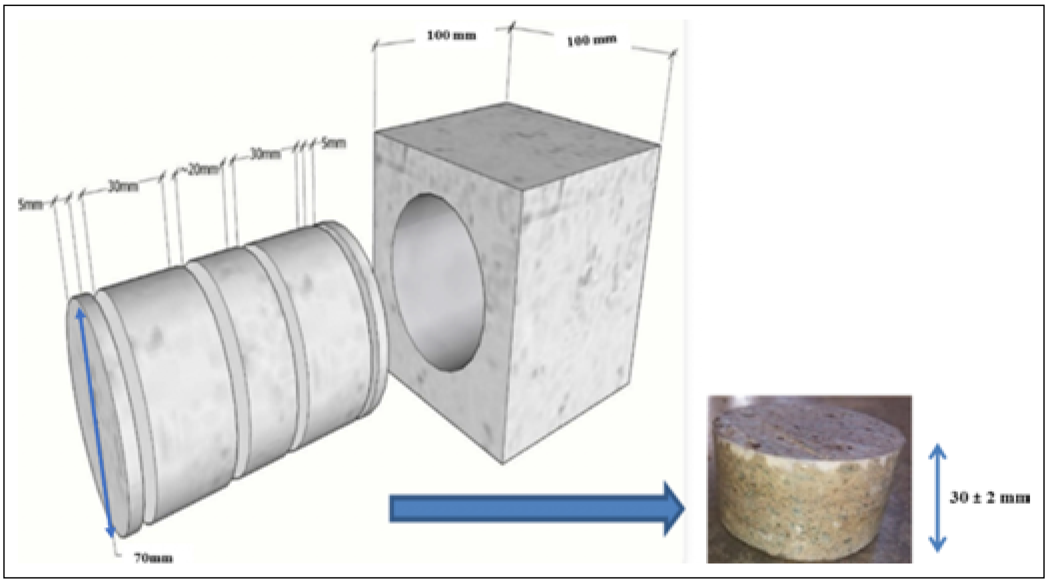

Figure 1. Preparation of specimens from the cube [16].

25 °C and 1000 °C, and the heating rate was set to 10 °C per minute. Thermal analysis of clay and powder samples was performed under atmospheric air conditions, whereas measurements for hydrated cement samples were conducted under a nitrogen atmosphere.

2.4. Durability Test

The experimental materials' permeability, sorptivity, Porosity, and durability were assessed by following the durability testing manual recommended by [16]. Two methods are available to evaluate the level of connectivity of pores in a concrete matrix: oxygen permeability index (OPI) and sorptivity [17]. The durability properties' quantification involves measuring the flow rate derived from Darcy's formula for laminar flow through a porous medium.

2.4.1. Preparation of Specimens for Durability Test

Durability tests were conducted following the protocol outlined by Alexander and coworkers [16]. Cement blocks of dimensions 100 millimeters that were allowed to harden for 28 days were bored perpendicular to the pouring direction and divided into slices, as illustrated in Figure 1, to obtain two specimens, each with a diameter of 70±2 millimeters and a depth of 30±2 millimeters.

The samples were labeled with an identifying number on their exterior using a permanent ink marker. Before experimentation, the labeled samples were permitted to dehydrate for seven days in a drying chamber regulated to 50 °C. After the samples were extracted from the drying chamber, they were cooled in an airtight container for 120 minutes until achieving a regulated indoor temperature of ±23 °C.

2.4.2. Oxygen Permeability Index Test

The South African standard [18], which prescribes the use of the oxygen permeability index (OPI), was used to assess oxygen permeability. The test setup consisted of a 70 mm diameter core fixed in a rubber sleeve and attached to a permeability cell, with a 30 mm thick piece as a cover concrete. The aim was to observe the oxygen pressure drop in this section. The method involved measuring the pressure decay of oxygen passed through a 30 mm thick slice (representing the cover concrete) of a 70 mm diameter core placed in a rubber collar secured on top of a permeability cell. Then, the permeability cells were placed in the test apparatus.

The cell was prepared for insulation by exposing it to an oxygen pressure of 100±5 kPa. The pressure and time factors were then recorded accordingly. The test was terminated 6 hours ±15 minutes after the start, or at a pressure of approximately 50 kPa, with pressure lags recorded at intervals of approximately 5 kPa. Using Equation 1, we calculated the Darcy permeability coefficient, K, in meters per second.

$$K = \frac{\omega V g}{RA}\frac{[d]}{[\theta.t]}\ln\frac{[Po]}{[P]} \tag{1}$$

Where K is the permeability coefficient in m/s; ω is the molecular mass of oxygen, 32 g/mol; V is the volume of oxygen under pressure in permeameter (m^3), g is the gravitational acceleration whose value is 9.81 m/s^2, R is the universal gas constant, 8.313 Nm/Kmol. A is the superficial cross-sectional area of the sample (m^3), d is the average sample thickness (m), **θ** is the absolute temperature (K), t is time (s) for pressure to decrease from Po to P, Po is the pressure at the beginning of the test (kPa), and P is the pressure at the end of the test.

Subsequently, the oxygen permeability index (OPI) was determined as in Equation 2.

$$\text{Oxygen permeability index} = -\log(k) \tag{2}$$

2.5.3. Testing for Sorptivity and Porosity

The disc samples were subjected to permeability and water sorptivity tests according to the protocols described in the durability handbook [16]. Samples were tapped up to 5 mm above the test surface to ensure the unidirectional flow of the caliper. They were then placed in a dish of calcium hydroxide solution, ensuring that the solution level was just above the edge of the sample. The samples were weighed at 3, 5, 7, 9, 12, 16, 20 and 25 minutes, respectively.

This was followed by vacuum saturation of specimens by applying 75 kPa suction. Finally, the specimens were submerged in water saturated with $Ca(OH)_2$ for 18 hours and fifteen minutes. The samples were re-weighed, and their Porosity was calculated using Equation 3.

$$n = \frac{M_{SV}-M_{SO}}{A.d.p_w} \tag{3}$$

Where: M_{sv} is the vacuum saturated mass of the samples to the nearest 0.01; M_{so} is the initial mass of the specimen to the nearest 0.01 g at a time to; A is the cross-sectional area of the specimens to the nearest 0.02 m^2; d is the average specimens' thickness to the nearest 0.02 mm; Pw is the density of water, 10^{-3} g/mm^3.

The mass of the water absorbed at each weighing period is calculated using Equation 4:

$$M_{wt}=M_{st} - M_{so} \tag{4}$$

Where: M_{st} is the mass to the nearest 0.01 g of the specimen at time t. Sorptivity was calculated from the slope of the graph of water absorbed (M_{wt}) versus the square root of time (an hour) using Equation 5.

$$S = \frac{F.d}{M_{SW} - M_{SO}} \tag{5}$$

Where: F is the slope of the best-of-fit line obtained by plotting M_{wt} against t½; S is sorptivity

2.5. Correlation Analysis for Permeability Test Parameters

The intercorrelations between the results of the permeability tests were compared with the compressive strength performances for all cement mixes produced. The factors correlating permeability included oxygen permeability index (OPI), Porosity, and sorptivity. Principal component analysis (PCA) was used to determine the correlation. A scree plot for the eigenvalues was plotted to determine the number of significant components. The "elbow" for the eigenvalues (Fig. 2) falls on eigenvalue 2, indicating two principal components. The first two factors explain a variance of 94.82%. The selected principal components were used to plot the loading, biplots, and score plots and analyze the existing correlations. Chemometrics Agile Tool (CAT) was used to perform the PCA, which works with the programming language R and the algorithm NAPLES (Nonlinear Algorithm for Partial Least Squares).

2.6. Migration Test

Following the procedures described in ASTM C1202-97 (2001), three samples of the 50% OPC replacement and the reference cement were allowed to cure in water for 28 days before being tested for accelerated chloride ion migration.

In an electrochemical test setup, 500 cm^3 of a 3.5% NaCl solution was added to the cathode compartment, while an equal volume of a 0.3 M NaOH solution was added to the anode compartment. Epoxy-coated mortar prisms were positioned in the test cell for each cement category. Stainless steel electrodes were attached, and the arrangement was clamped in place. A potential difference of 12±0.1 V was applied for 36 hours, and the current was monitored every 30 minutes. The containers were covered with polyethylene paper to prevent evaporation, and glass rods were used to shake the solutions continuously. After exposure, the prisms were removed, the surfaces abraded, and cut into layers. Depending on the distance from the aggressive media, the samples were dried, pulverized, and packaged before being subjected to chloride analysis.

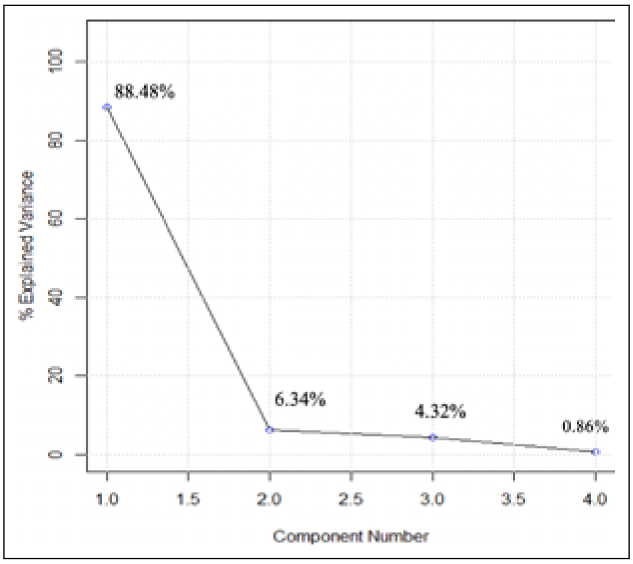

Figure 2. Scree plot for the eigenvalues.

2.6.1. Chloride Analysis

10 g of ground samples were mixed with 75 ml of deionized water for one hour using a shaker. After a settling time of 30 minutes, the sample was treated with 25 ml of strong nitric acid to dissolve the cement lumps. The mixture was stirred, rinsed into a beaker, and allowed to stand for 4 minutes. The filtrate was heated and filtered. It was then poured into a volumetric flask. A sodium hydrogen carbonate solution was introduced, and water was added until the total volume reached 100 ml. The resulting solution was split into three equal parts, each titrated with a 0.1 M silver nitrate solution. This titration was performed three times on each part.

A chloride-free $CaCO_3$ blank was run through the same procedure. Using Equation 6, the concentration of chloride ions in the original sample was determined based on the titration results.

$$[Cl^-] = \frac{(V1-V2)\ X\ 35.46\ X\ M}{V} \tag{6}$$

Where V_1 is the final volume of the extract, V_2 is the volume of the blank, V is the volume of silver nitrate, and M is the molarity of silver nitrate used.

2.6.2. Determination of Diffusion Coefficients

The standard procedures outlined in Kenyan standards [19] were adopted to determine the chloride concentration in the tested samples. These results were represented in chloride profiles. From the graphs, chloride diffusion

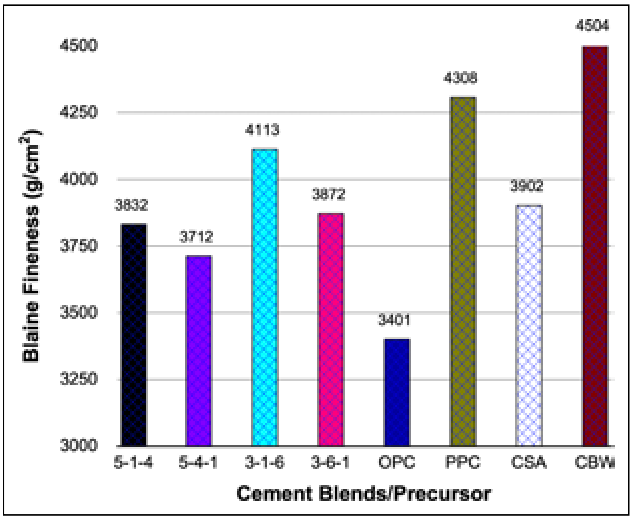

Figure 3. Binders mix blain fineness results.

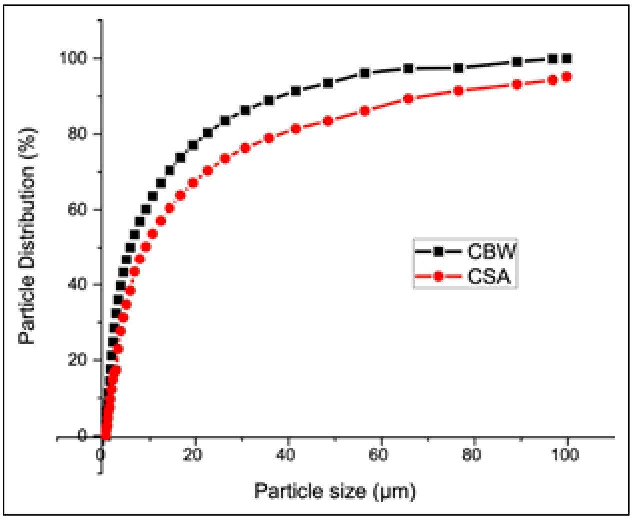

Figure 4. Particle size distribution results for CBW and CSA.

coefficients, D_{mig}, were derived from error fitting curves in Equation (7) using the method of least squares [20, 21].

$$\frac{\delta C}{\delta t} = D\frac{\delta^2 C}{\delta x^2} \tag{7}$$

C is the concentration of the Cl^- ions at a depth x, and at the moment, t and D are the diffusion coefficients.

The diffusion of chloride ions in concrete is approximated from the solution to Fick's second law equation [22] under non-steady-state conditions assuming boundary conditions boundaries $C_{(x,\ t)}=0$ at t=0, $0 < x < \infty$ and $C_{(x,\ t)}=Cs$ at X= 0, $0 < t < \infty$, constant ion interactions, linear chloride binding, and one-dimensional diffusion into a semi-infinite solid. Crank's solution to Fick's second law of diffusion is given by Equation 8.

$$C_{(x,\ t)}\text{-}C_{(s)}[1\text{-erf}(\frac{x}{(2\sqrt{D_{mig}\,t})})] \tag{8}$$

The surface concentration ($C_{(S)}$), migration diffusion coefficient (D_{mig}), and the chloride ion concentration ($C_{(x,t)}$) at any depth (x) within the mortar bulk at time t constitute the equation. The Gaussian error function is obtained in computer spreadsheets as the error correction function, abbreviated as erf. Apparent diffusion coefficients, D_{app}, are calculated from the following equation [20, 21].

$$D_{app}=\frac{RT}{Z_iF}D_{mig}\frac{\mathrm{Int}^2}{\Delta E} \tag{9}$$

In this context, R stands for the gas constant, F represents the Faraday constant, T indicates the electrolyte temperature measured in Kelvin, Zi denotes the valency of the ion ΔE refers to the effective applied voltage measured in volts, and t represents the duration of the test or exposure measured in seconds.

2.7. Determination of Thermal Resistance

The prepared mortar prisms (40 mm x 40 mm x 160 mm) of 5-1-4 and OPC cement paste were cured for 28 days and pressure tested after exposure to an electric furnace at 5.0 °C per minute. To maintain thermal stability for 60 minutes at the desired temperature, two thermocouples were used to measure the surface and internal temperature differentials. After allowing the samples to cool, they were weighed, and the thermal expansion was measured with a vernier caliper. Mass loss due to the high temperatures was measured with an electronic scale. The residual compressive strength was documented, and the thermal resistivity was calculated using Equations 10 and 11, considering both weight loss and strength loss as a measure of thermal stress.

$$W_L = \frac{W_1-W_2}{W_1}\ X\ 100 \tag{10}$$

W_1 and W_2 are the specimen weights before and after heating, respectively, and W_L is the loss in weight.

$$C_L = \frac{C_1-C_2}{C_1}X100 \tag{11}$$

C_L is the loss of strength, while C_1 and C_2 are the compressive strength of the mortar before and after heating, respectively.

3. RESULTS AND DISCUSSION

3.1. Blaine Test of the Precursor Materials, Blended and Commercial Types of Cement

The specific surface area (SSA) is an essential factor in determining the reactivity of binders. Figure 3 represents the SSA for the binders. In this figure, the particles' specific surface area (in g/cm^2) of the test materials is displayed as measured by the Blaine air permeability analysis

All the blended cement had higher SSA values above the minimum 3401 cm^2/g of the standard OPC. The mechanically activated precursor (CSA/CBW) materials show high SSA of 3902 and 4504 cm^2/g and are responsible for the overall high SSA in the binders.

Increased CBW substitution resulted in a higher surface area on the blended cement than the addition of CSA. As it reacts, a layer of hydration product forms around the outside of the particle, separating the unreacted core of the particle from the surrounding water. As this layer grows

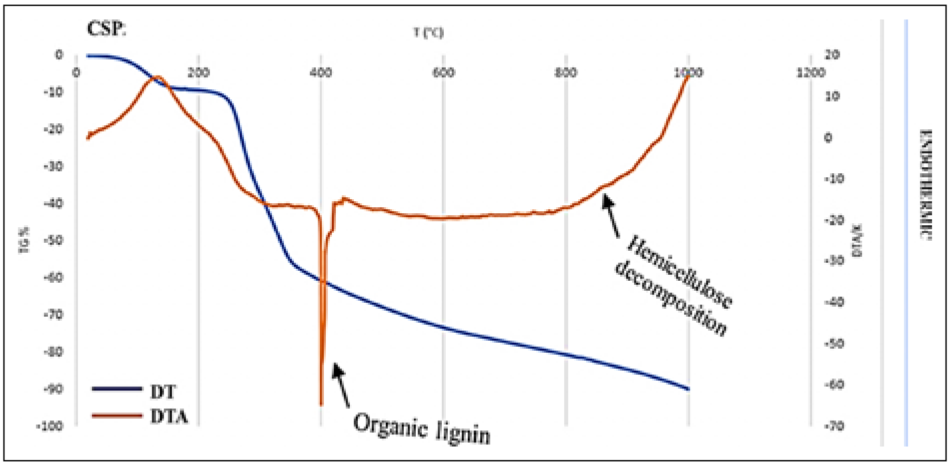

Figure 5. TG-DTA analysis for coconut shell powder.

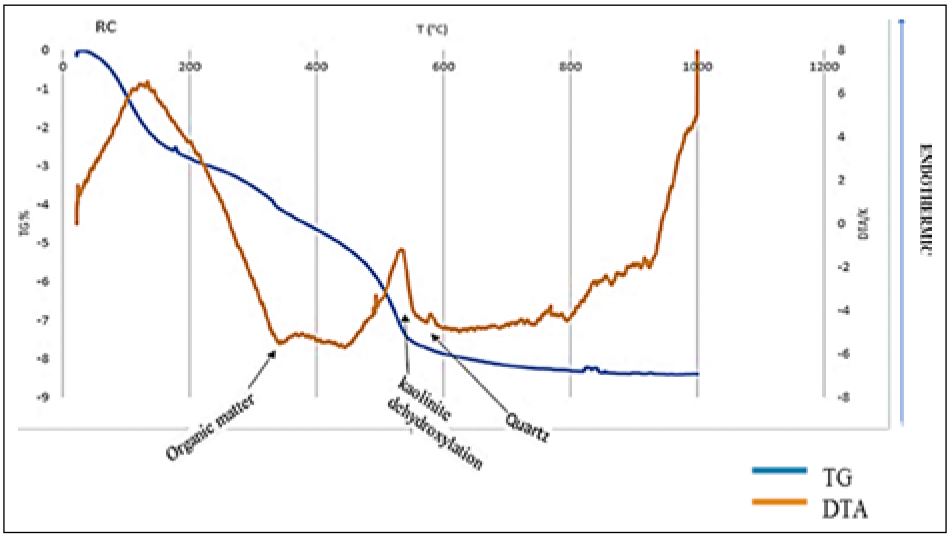

Figure 6. TG-DTA analysis for the raw clay sample.

thicker, the rate of hydration slows down [23]. This implies that a small particle will react faster than a large particle. Thus, CBW is mechanically more reactive than CSA.

3.2. Particle Size Distribution of the Precursor Materials

The particle size distribution of the mechanically activated CSA and CBW are represented in Figure 4. The particle size distribution of any cementitious material significantly affects its performance. The graph provides a detailed visual representation of the granular composition of these materials after mechanical activation. The particle size distribution of any cementitious material significantly affects its performance.

The CBW had a slightly higher particle size distribution compared to CSA, with more than 90% of its particles being below 45 microns in size, as shown in Figure 4. Thus, the CSA contains larger particles compared to CBW. This could result from the unburned carbon particles as heat in the furnace was not controlled. It is known that the material passing the sieve 45 µm is more reactive [24]. This indicates that both precursor materials are potentially mechanically reactive [25]. The reaction rate of the active precursor materials/cement particles primarily depends on their sizes. [26] worked on the microstructural and physical characterization of different solid wastes from clay bricks for reuse with cement. They observed that the clay brick waste sample particle with a small radius (large surface area) was more pozzolanic. Smaller particles hydrate more quickly in water than larger particles [27]. Typically, particles with a diameter of 1 µm react entirely in about one day, while one with a diameter of 10 µm reacts completely in about one month. It is assumed that one with a diameter larger than 50 µm never becomes fully reacted, even in the presence of a sufficient water source [27]. Arslan [28], in their study on the dissolution kinetics of iron oxide leaching from clays by oxalic acid, reported that small powdered particles [29] had a high dissolution.

3.3. Thermal analysis of the precursor

The thermal analysis carried out on the precursors used in this study is shown in Figures 5 and 6.

The graphs represent the various phase transformations that occur when coconut shell powder and raw clay are heated at different temperatures.

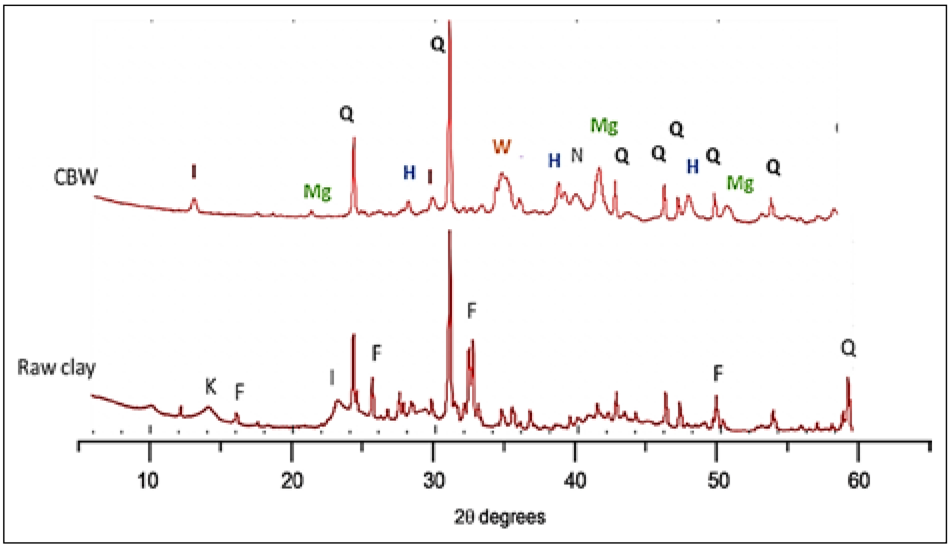

Figure 7. Comparison of the XRD pattern for the raw clay (top) and CBW (bottom) clay.

I: Illite; Mg: Magnetite; Q: Quartz; H: Hematite; W: Wollastonite; N: Nepheline; K: Kaolinite; F: Feldpar.

The TG/DTA analysis of the raw coconut shell powder shows a smaller region of mass loss at lower temperatures (below 250 °C), accompanied by an endothermic peak up to a temperature of about 150 °C. It could be associated with evaporation of the moisture [30]. This is preceded by a region of thermal decomposition and mass loss, followed by a sharp exothermic peak near 400 °C, further associated with the formation of coconut shell activated charcoal [31]. Additionally, it could be related to the combustion of the organic lignin/cellulose fraction. A broad endothermic peak with gradual mass loss is observed at temperatures above 800 °C. This was related to the thermal decomposition of hemicellulose. These findings agree well with previous work reported by [30], who obtained 38.44% and 47.54% mass loss between 200–280 °C and 280–365 °C, which was linked to the decomposition of cellulose and hemicellulose.

The TG-DTA graph of the clay sample is represented in Figure 6. An endothermic peak below 200°C is observed. This peak is associated with the thermal loss of physisorbed water within the clay interlayer, which is often mobile and loosely bound. At temperatures between 250 °C and 450 °C, an endothermic peak representing the dissolution of water molecules in the interlayer ions' initial strongly bonded coordination sphere is observed. This could further result from the hydroxylation of the functional groups connected to the clay minerals being removed at this temperature range [32]. According to Arslan [28], the condensation and dehydration of structural hydroxyl groups are indicated by an exothermic peak at 450–470 °C in the DTA curve.

An endothermic peak related to removing hydroxyl groups from kaolinite is observed at 550 °C. Similarly, at approximately 573 °C, a smaller peak is observed, indicating a transition from quartz-α to quartz-β [33]. The results also show a broad endothermic peak spanning from 600 °C to almost 940 °C, which is attributed to the dehydroxylation of the silica-alumina content present in illite, forming an amorphous substance. At temperatures above 950 °C, a sharp exothermic peak is detected, indicating the formation of crystalline silica-alumina phases. These findings suggest that the optimal temperature for calcination of kaolinite clays should be below this threshold [34].

3.4. Mineralogical Analysis of CBW and CSA

The mineralogical analysis of the precursor materials of the blend cements is shown in Figures 7 and 8. The figures show various minerals present in raw and calcined clays.

The XRD pattern for the raw and CBW clay (Fig. 7) reveals the presence of various minerals, including illite, magnetite, quartz, hematite, wollastonite, nepheline, kaolinite, and feldspars. The calcined clay brick waste shows the disappearance of the kaolinite upon thermal treatment, whereas illite loss of crystallinity is evident. Furthermore, a collapse of the illite interlayer is observed, with the basal peak shifting to a higher 2θ value. Additionally, hematite and magnetite (Fe oxides) formation is noted, along with the disappearance of feldspars and the emergence of wollastonite and nepheline.

The results in Figure 8 show an XRD analysis of the CSA, revealing a series of peaks associated with crystalline SiO_2 (quartz). These features may indicate burning temperatures exceeding 700 °C [35]. Peaks related to K-chlorate, a phase previously observed in vegetable ashes burned at temperatures above 400 °C, are also identified [36]. The two broad scattering haloes observed around 20° and 27° 2θ angles are related to an unburned organic fraction [37].

Figures 7 and 8 show silica-alumina minerals' presence in the two precursors. Calcined clay, with its high alumina and silica content, promotes the formation of calcium-silicate-hydrate (C-S-H) and calcium-aluminate-silicate-hydrate (C-A-S-H) gels, enhancing the mechanical properties and durability of HACs. The mineralogical compositions of pozzolanic precursor materials, such as CBW and CSA, play a pivotal role in the hydration process and microstructure development in hybrid alkaline cement [38]. Rich in silica, the ash from coconut shells aids in the creation of C-S-H and refines the pore structure, creating a matrix that

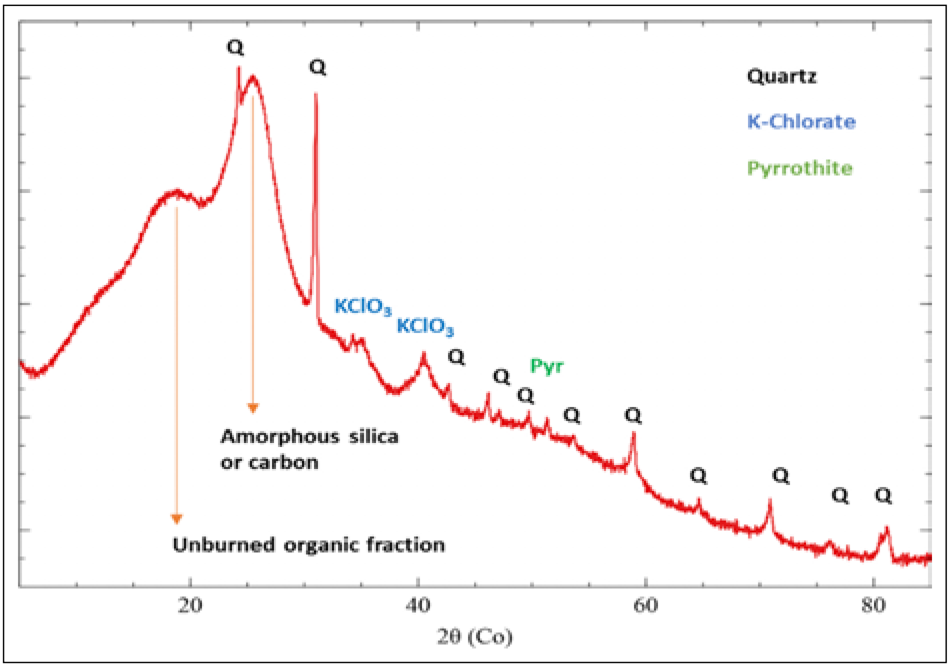

Figure 8. XRD pattern of coconut shell ash (CSA).

is more robust and compact [39]. Recent studies further highlight the importance of understanding the mineralogical properties of these precursors to optimize the performance of hybrid alkaline cement [40, 41].

3.5. Compressive Strength Test for Cement Mortars

The compressive strengths development of the binders (3-6-1, 3-1-6, 5-4-1, and 5-1-4) activated by different concentrations of Na_2SO_4-alkaline activators (0.0, 0.5, and 2 M) and different OPC:CSA:CBW ratio at 28 days of curing are shown in Figure 9. They are compared to conventional cement.

Generally, all blended cement prepared using water exhibited low compressive strength compared to alkali-activated blends and OPC (Fig. 9) after 28 days. This could be attributed to the slow strength development due to the incorporated pozzolana's slow reaction nature. The OPC substitution effect is demonstrated by decreased compressive strength across all the blends with OPC substitution from 50% to 70%. The strength of OPC was almost double that of 70% replacement, with 3-6-1 giving the lowest strength. This can be explained by more proportionate unreacted filler materials (CSA/CBW), hence weak bonding among them [42].

The results show that each formulation (50 and 70 OPC replacement) with high CBW replacement exhibited high compressive strength. Fine particles of calcined clay can explain this and are bound to fill the pores more effectively, resulting in a denser and stronger matrix. Grinding calcined clay brick waste reduced accumulation and decreased the average particle diameter, improving its reactivity and performance in the cement matrix. The optimal particle size distribution ensures better packing density and enhances the mechanical properties of the cement, particularly its compressive strength [43].

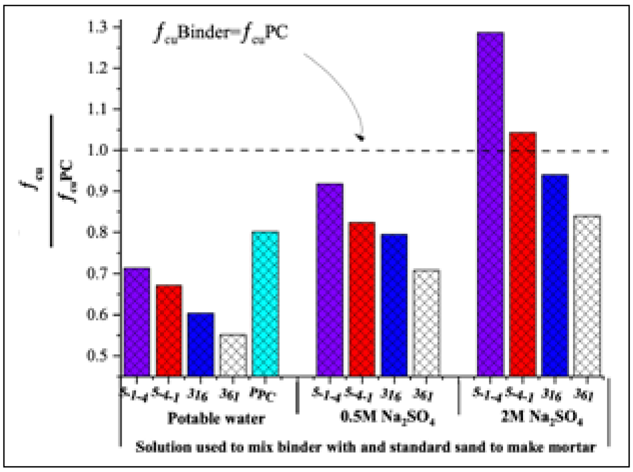

Figure 9. 28-day compressive strength (fcu) results for 0.5 w/c binder mortars compared to Portland cement.

The compressive strength of the activated blended cement achieved about 30% and 50% increase with the addition of the 0.5 M and 2 M Na_2SO_4 in each blend. A considerably significant increase in compressive strength with alkali activation addition in $H_2O<0.5$ M<2 M across all blends is observed. The 50% OPC replacement blends displayed better compressive strength performance than OPC at 2 M Na_2SO_4, with 5-1-4 having the highest compressive strength. The presence of SO_4^{2-} ions in the activator solutions within the cement mortar matrix may explain why chemically activated mortars achieve greater compressive strength values. The amount of alkaline activation products (gels) formed is responsible for the mechanical development of the alkaline hybrid binders [44].

3.6. Durability Index (DI) Test Results

Based on the details provided by Bakera and Alexander [45], this is a synopsis of the findings of the DI tests for oxygen permeability and water sorptivity using CBW and

Table 2. Judgement criteria for the quality of concrete durability index (DI) tests

Qualitative description	Oxygen Permeability Index (OPI) log scale	Water Sorptivity Index (WSI) mm/h$^{0.5}$
Excellent	>10	<6
Good	9.5–10	6–10
Poor	9.0–9.5	10–15
Very poor	<9	>15

CSA. The quality of the concrete was evaluated using the standards laid out in Table 2.

Sorptivity measures the rate of fluid movement through the concrete under capillary suction, while OPI measures the degree of interconnectivity of the pores in the matrix. The Porosity of the cement mortar and the sorptivity are influenced by the degree of hydration and the ratio of weight to cement [46]. The permeability of the sample decreases with increasing OPI value and vice versa. Conversely, high sorptivity/porosity values of cement matrix indicate high permeability. Permeability determines how easily liquids can penetrate and flow through the concrete when exposed to a pressure gradient.

3.6.1. Binder Oxygen Permeability Index

The oxygen permeability test results for different binder types cured for 28 days are given in Figure 10. The figure illustrates the variation in permeability based on precursor content and alkali concentration. The values provide a quantitative measure of the concrete's resistance to oxygen ingress, with higher OPI indicating lower permeability and enhanced durability.

The results, based on Durability Index (DI) judgment criteria in Table 2, show that all blended cement mortars prepared using water had OPI values below 9.5 (log scale), signifying "poor" quality. This value was lower compared to PPC and OPC mortar. As can be observed in Figure 10, there was a notable decrease in OPI in blended cement in the order 5-1-4>5-4-1>3-1-6>3-6-1. This order was replicated for the blends prepared with the activator at the two different concentrations. Hybrid alkali-activated mortars exhibited higher OPI compared to the respective non-activated mortars. They had values above 9.5 (log scale), which signifies "good" quality. There was also an increasing trend in OPI values with an increase in the concentration of Na_2SO_4, the alkali activator, for each cement mix. The 2 M Na_2SO_4 HAC showed higher OPI values than those of 0.5 M Na_2SO_4, with all having OPI values above 10 (log scale), which signifies "excellent" quality. This could be attributed to the presence of SO_4^{2-} ions in the activator solutions in the cement mortar matrix. SO_4^{2-} in mortars has been reported to form ettringite crystals, which fill the hardened cement mortar cracks and pores, lowering the permeability [47]. The ettringite formation is as shown in Equation 12.

$$6Ca^{2+}+2[Al(OH)_4]^{-}+3SO_4^{2-}+26H_2O \rightarrow Ca_6Al_2(SO_4)_3(OH)_{12}.26H_2O \quad (12)$$

The formation of this product in the early days of curing causes densification of the hardened cement matrix.

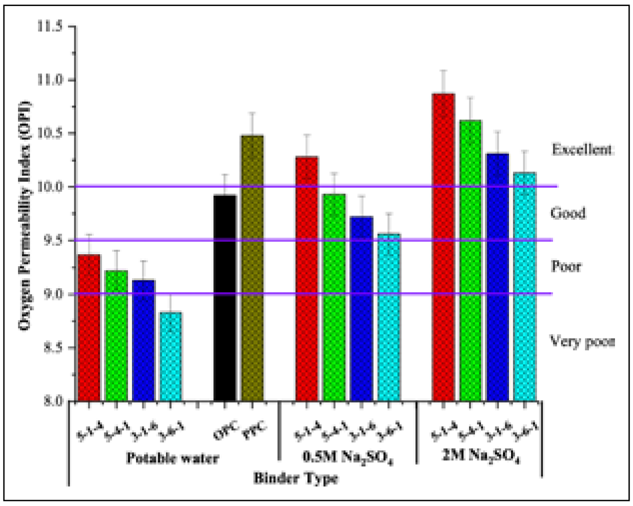

Figure 10. Oxygen permeability index (OPI) results for 0.5 w/c binder mortars cured for 28 days.

It was clear that the substitution effect was a significant factor in the development of the cement matrix. A negative OPI response was pronounced on the increased substitution of CSA compared to that of CBW. This could be linked to the powder's particle size distribution, which is not uniform. The pozzolana "micro-filler effect," in the fine and ultrafine size range in combination with Portland cement, can also enable higher packing densities of the mortar or cement mixture [48]. Heterogeneous nucleation can also be attributed to this effect as a second physical phenomenon that could be significantly related to small particle size distribution. The pozzolana fine particles settle between the clinker crystals, lowering the energy barrier to allow hydrates to form on foreign fine particles. The finer the particles, the faster the reaction. This aspect could contribute positively to the quality of permeability property of 5-1-4 compared to 5-4-1 and 3-1-6 compared to 3-6-1 mortar cement.

Generally, all the HAC blends offered reduced permeability. This could be linked to refined pore structure and the ability to bind chloride ions chemically, limiting chloride ingress and protecting the concrete. Additionally, their high alkalinity maintains a protective passive layer on the steel. These properties make hybrid alkaline cements particularly durable in chloride-rich environments like marine settings and roads treated with de-icing salts [49]. After 28 days of curing, hybrid alkaline cement blends exhibit superior resistance to chloride ion penetration compared to traditional Portland cement, highlighting their enhanced durability in aggressive environments [50]. Continuous curing after 28 days [51] reported significantly improved flexural strength, compressive strength, and resistance to chloride penetration of alkali-activated slag mortar with 2–3% alkali contents.

3.6.2. Porosity of Different Mortars Tested

The Porosity of the different mortars tested is given in Figure 11. The graph with a high porosity indicates a high chance of fluid penetration into the mortar matrix. This highlights the variation in Porosity across the samples,

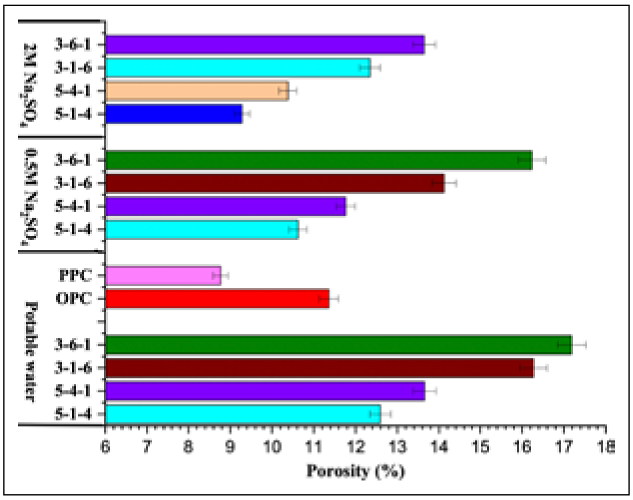

Figure 11. Porosity (%) results for 0.5 w/c binder mortars cured for 28 days.

which directly impacts their mechanical and structural properties and, thus, their performance under different aggressive environments.

All the blended binders in water exhibited higher Porosity compared with OPC mortars (Fig. 11). This trend is more pronounced at a higher precursor replacement of 70%. The blend containing 60% CSA displayed the highest Porosity of 51% higher than the standard OPC mortar. Based on these findings, it appears that the pore structure of the OPC mortar is more complex and intricate than that of mortars made with pozzolana cement. The presence of more visibly enlarged macropores in the pozzolana mortar during its early curing stages could be the reason behind this [52]. The reaction of pozzolanic precursor materials with $Ca(OH)_2$ is a slow process, forming calcium-silica-alumina (C-S-A) gel, an insoluble cementitious material [47]. The formed insoluble crystalline particles may fill the pores of the hardening concrete, making it dense with refined pores at a later age.

Compared to non-activated mortars, alkali-activated hybrid mortars reduced Porosity by more than 10% in all cement categories. The 5-1-4 hybrid mixture of 0.5 M and 2 M Na_2SO_4 showed the highest reduction in Porosity at 19% and 36%, respectively, while the 3-6-1 mixture showed the lowest reduction at 6% and 26%, respectively. Increasing the dosage of Na_2SO_4, an alkali activator, also showed a similar trend. The corresponding 2 M Na_2SO_4 HAC showed lower Porosity than 0.5 M Na_2SO_4 HAC. This could be due to the low water absorption in the OPC hybrid copolymer due to the presence of chemical activators that increase the dissolution and gel formation of silica and alumina, resulting in the formation of more C-S-H gels and AFm-type phases as well as C–A–S–H with longer chains. The dense C-S-H gels formed by the chemical activation of aluminosilicate materials such as calcined clay brick waste/coconut shell ash lead to reduced Porosity in the properties of the chemically activated materials [51]. The C-S-H gels formed during the dissolution and gelation of silica and alumina are structurally similar to those formed during the hydration of cement [53].

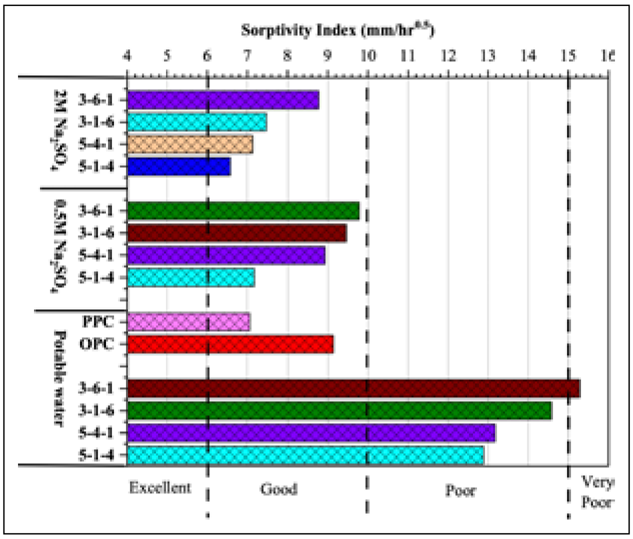

Figure 12. Sorptivity results for 0.5 w/c binder mortars cured for 28 days.

According to Angulo-Ramírez et al. [54], the low Porosity of HB mortar indicates that the pores have been refined and the pore network in this system has become more tortuous. Compared to OPC, hybrid cement mixtures exhibit exceptional pore refinement [55]. This behavior can be associated with the potential of the blended cement structure to reduce Porosity and compactness, which were caused by the existence and production of a strongly cross-linked gel (C-A-S-H) with longer chains than the C-S-H gel commonly seen in Portland cement. The good behavior of alkali-activated CBW- CSA mortar is generally explained by the coexistence of aluminosilicate gels, such as C-A-S-H.

3.6.3. Water Sorptivity Test of Different Mortars Tested

The water sorptivity test results for various binder types, all cured for 28 days, are given in Figure 12. The different binders include OPC, PPC, and CSA/CBW blended cement prepared in water and activated with alkali. This highlights differences in water absorption rates, directly influencing the material's durability and long-term performance. The results provide the suitability of each binder type for use in environments where moisture exposure is a concern.

Hybrid cement prepared with 2 M Na_2SO_4 had lower sorption capacity than those prepared with 0.5 M Na_2SO_4, suggesting that the Porosity of the chemically activated cement decreases with increasing Na_2SO_4 concentration. In alkali-activated cement, chemical activators promote the dissolution of silica and alumina, which favors C-A-S-H gel formation; this could be the reason for the low water absorption of the cement. Since aluminosilicate materials such as CBW-CSA form dense C-A-S-H gels, chemically activated cement has a lower sorption capacity [56]. The architectures of the C-A-S-H gels are similar when the cement is hydrated or activated with alkali [53]. An alkali activator ranging from 0 M to 4 M NaOH was used by [57] to activate phosphogypsum binders and ground granulated blast furnace slag. Their data showed that low molarity was the most porosity-promoting factor.

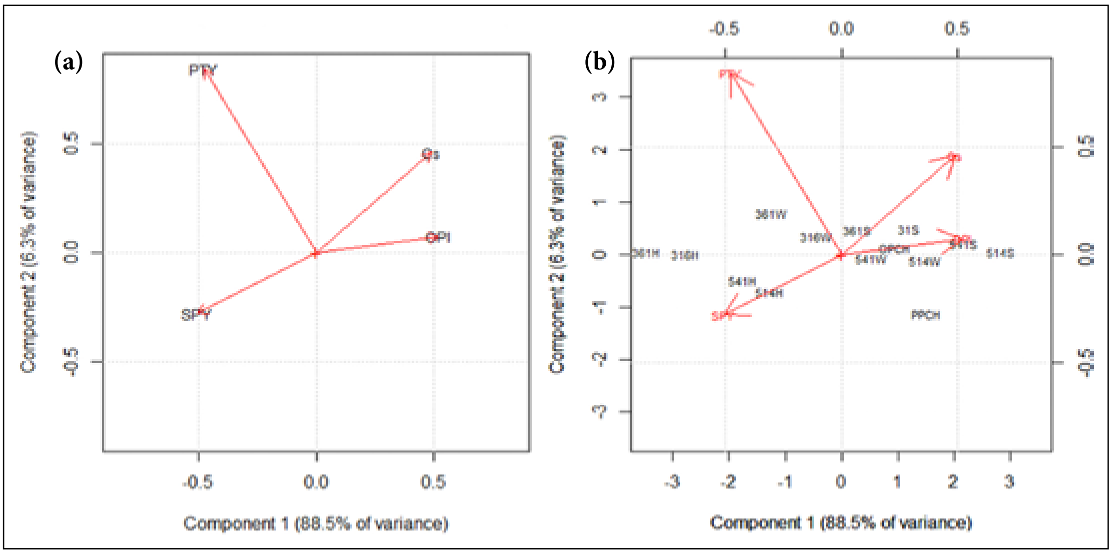

Figure 13. 2D factors loading plots and biplots. **(a)** Loading plot (94.8% of total variance). **(b)**Biplot (94.8% of total variance).

OPI: Oxygen Permeability Index; Cs: Compressive strength; PTY: Porosity; SPY: Sorptivity; 361H, 316H, 541H, and 514H are blends prepared with water, 361W, 316W, 541W, and 514W are blends with 0.5M Na_2SO_4 and 361S, 316S, 541S, and 514S are blended with 2M Na_2SO_4.

In this study, sorptivity reduced as the CBW/CSA ratio increased, according to experiments with varying ratios (1:4 to 4:1). Sample 5-1-4 showed decreased sorptivity independent of the alkali concentration. This could be associated with the high specific surface area of CBW (Fig. 3) in hybrid-blend cement that has been found to enhance its durability significantly. Nano-sized particles, such as nano-silica, improve cement's mechanical properties and durability by filling micro-pores and refining the pore structure. This optimization leads to a denser microstructure, which enhances resistance to water and chloride ingress, ultimately increasing the lifespan of the cement. Additionally, these nanoparticles promote secondary hydration reactions, further contributing to improved durability by creating additional C-S-H gels, which are crucial for the structural integrity of the cement [58]. The activation conditions and precursor characteristics significantly affect the hybrid binder's effectiveness, as stated by Balun and Karataş [59]. The results obtained by Bernal and colleagues [60] from their investigation into the engineering and durability properties of a combination of slag and alkali-activated metakaolin were similar. The results showed that water absorption and permeability were reduced when activator concentrations were increased and metakaolin was substituted within a specific range.

According to several researchers, chemically activated cements have shown mixed results in water absorption and permeability compared to OPC concretes. While using slag as the precursor, Mithun and Narasimhan [61] found that an alkali-activated binder had lower total Porosity, less water absorption, and less chloride ion penetration than an OPC. Air permeability and sorptivity are two areas where AACs made of slag typically underperform regular concrete for a given strength grade [62]. Similarly, Albitar et al. [63] noted that compared to geopolymer concrete, OPC concrete exhibited reduced sorptivity and water absorption. Precursors, activators, specimen maturity, and testing procedures are potential causes of the observed discrepancy between hybrid binders and OPC [64].

3.6.4. Correlation Analysis for the Permeability Test Results

The PCA projection of the factors in the 2D-factor loading space is shown in Figure 13a. The 2D loading plot for the factors is consistent with the previous observations in the literature.

The compressive strength (Cs) and the oxygen permeability (OPI) are projected in the same direction, signifying that they are strongly correlated. This implies that blends with high compressive strength have high OPI and vice versa. On the other hand, the Porosity and sorptivity are projected in the same direction, opposite to compressive strength and OPI, demonstrating the existing inverse relationship between these factors. The biplot, Figure 13, associates cement blends with 2 M Na_2SO_4 activator (361S, 316S, 541S, and 514S) and OPC with a significant correlation with compressive strength and OPI. It can be concluded that these blends performed better and attained higher OPI and compressive strength due to lower Porosity and sorptivity and, thus, lower permeability.

The blends prepared with water only are all projected to the left, correlating strongly with sorptivity and Porosity. It can be concluded that these blends had lower performance in terms of compressive strength and higher permeability. Meanwhile, the blends with 0.5 M Na_2SO_4 activator lie between the two distinct later observations. Thus, intermediate permeability performance.

The compressive strengths for the cement mixes projected in the 2D score plot Figure 14a–d are consistent with the predictions in the loading plots and biplots. Blends prepared with 2 M Na_2SO_4 activator (361S, 316S, 541S, and 514S) and

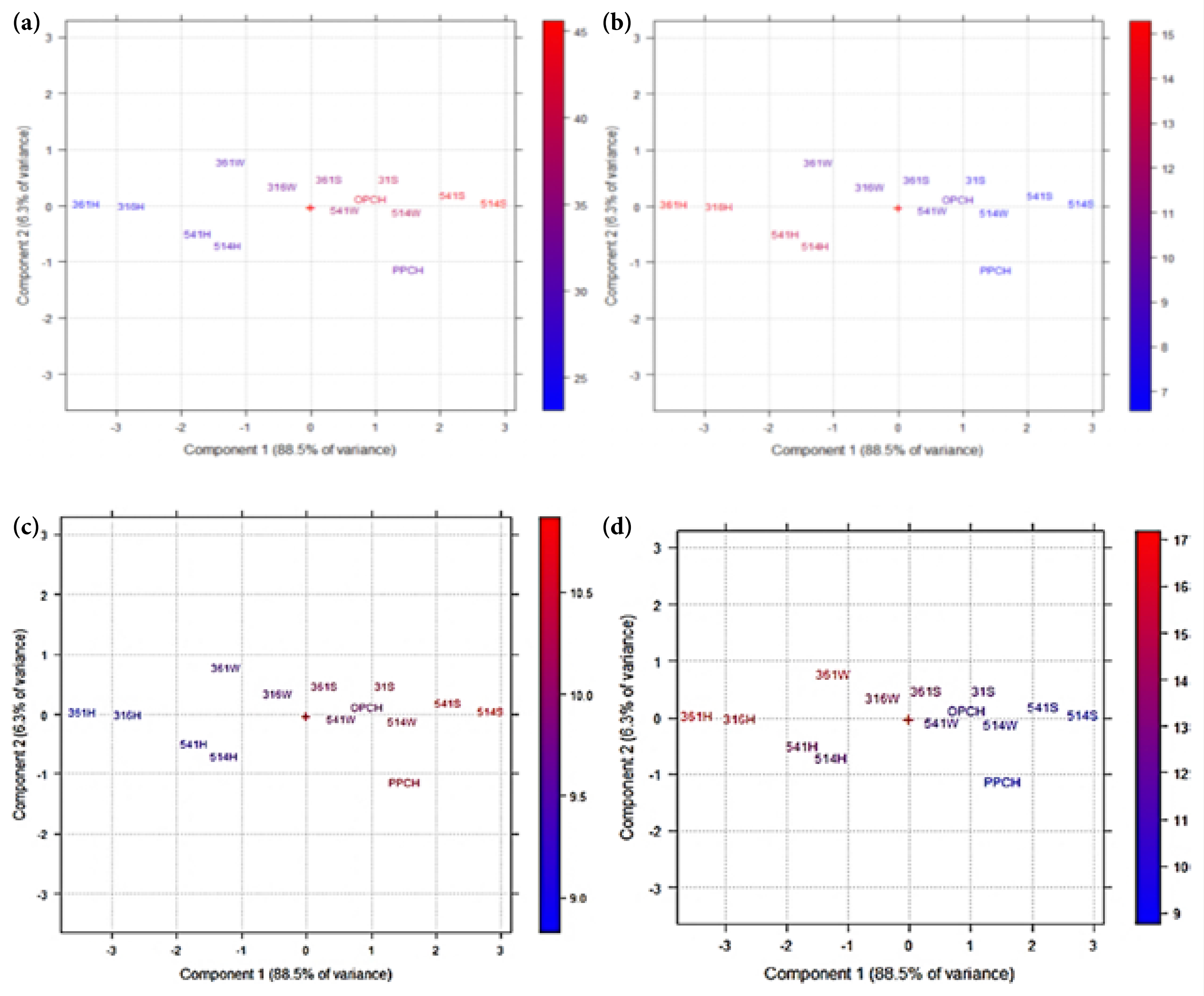

Figure 14. Color score plots for the projected factors. **(a)** Score plot (94.8% of total variance) color scale: Cs. **(b)** Score plot (94.8% of total variance) color scale: SPY. **(c)** Score plot (94.8% of total variance) color scale: OPI. **(d)** Score plot (94.8% of total variance) color scale: PTY.

361H, 316H, 541H, and 514H are blends prepared with water, 361W, 316W, 541W, and 514W are blended with 0.5M Na_2SO_4 and 361S, 316S, 541S, and 514S are blended with 2 M Na_2SO_4.

OPC demonstrate the highest compressive strength, OPI, and lowest Porosity and sorptivity. This is also the case with OPC. Blends prepared with water only are associated with the weakest strengths and OPI and higher Porosity. Blends with 0.5 M activator show average performance between -1 and +1 of component 1, which correlates with intermediate performance. The PCA, therefore, clearly categorizes the different blends into distinct performances about permeability, with 2 M Na_2SO_4 activator blends showing the best performance.

3.7. Chloride Ingress

3.7.1. Chloride Profiling

The chloride profiles against the depth of cover of each category of the mortar cubes are shown in Figure 15. These involved determining the concentration of the chloride ions ($\times 10^{-10}$ g/g) at different depths of the test binders' mortar bulk at 0.5 w/c ratios.

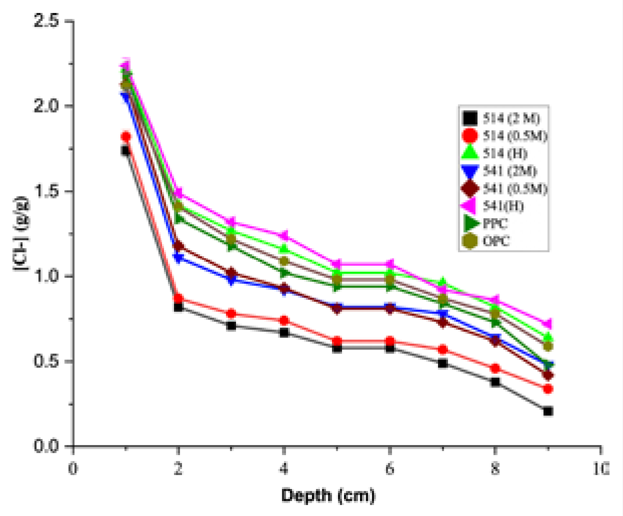

Figure 15. Chloride ions concentration at different depths of penetration for 0.5 w/c binder mortars cured for 28 days.

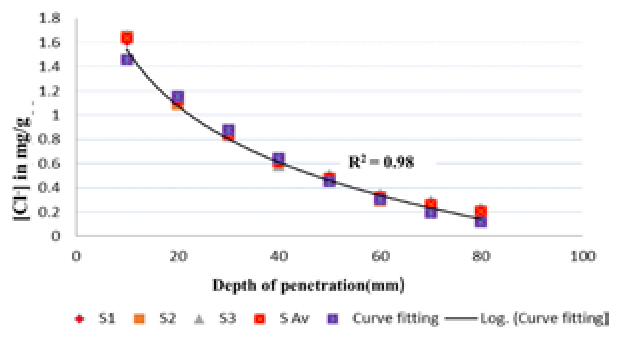

Figure 16. Chloride error function fitting for 5-1-4 (2 M).

D_{app}=4.20 x 10^{-10} m^2/s, and Cs=1.89% (R^2=0.98).

3.7.2. Apparent Diffusion Coefficients for Chloride Ions

Figure 16 displays the error fitting curve for calculating the apparent chloride diffusion coefficient (D_{app}) for the test binder, 514 (2 M) mortar. The chloride apparent diffusion coefficients for each binder category were found using similar error-fitting curves. Table 3 also shows the D_{app} statistics for each binder group.

As the penetration depth increased, the total chloride was observed to be reduced across all binder types (Fig. 15). The alkali-activated blends, blended with more calcined clay brick waste, compared to coconut shell ash, showed an increased reduction in chloride penetration. The chloride concentration in all binders drops drastically at a depth of less than 2 cm. The exposed surface's proximity to the aggressive medium may explain this. Every form of cement binds a certain amount of chloride. Chloride binding slows the chloride's diffusion into the binder's bulk. As observed by Ngui et al. [65] this can be explained by the cement mortar's chloride ion binding capability and diffusivity penetrating the cement mix.

According to the profiles, PPC had less chloride infiltration and a lower D_{app} than OPC (Fig. 15 and Table 3). Moderately substituted pozzolana cements have been found by other researchers to have a lower diffusion coefficient [66]. The pore solution of mixed cement contains less CH than that of OPC, which could explain this. According to Wang et al. [67] blended cement has a low CH content because of a pozzolanic reaction source, the source primary OH and -source; a reduction in OH-concentration reduces the pore water's ability to exchange OH for chlorides [68]. Blended cement is particularly effective in lowering chloride-induced corrosion due to higher aluminate contents than plain Portland cement. Al_2O_3 is known to bind Cl- ions, forming Friedel's salt. This enhances the chloride binding capacity, decreasing the free chlorides resulting in lower chloride ingress. Tang et al. [69] noted that the C-S-H gels, particularly in blended cement with a low calcium-to-silicon ratio, react with chloride salt, producing Friedel's salt. This salt can seal the interior pores, improve the distribution of pore sizes, and make the material more resistant to corrosion caused by chloride ions.

The results (Fig. 15 and Table 3) showed that increasing CBW from 1 to 4 decreased the D_{app} at all mixing liquids. The converse was true of D_{app} on increasing CSA. Thus, the blended cement's D_{app} was 5-1-4<5-4-1 at all mixing liquids.

Table 3. D_{app}, R^2, and Cs (%) values for different cement mortars

Binder type	D_{app} (x 10^{-10} m^2/s)	R^2- Value	Cs (%)
5-1-4 (2 M)	4.20	0.99	1.89
5-1-4 (0.5 M)	4.91	0.98	1.92
5-1-4 (H)	7.37	0.97	2.34
5-4-1 (2 M)	5.83	0.98	2.23
5-4-1 (0.5 M)	6.32	0.97	2.21
5-4-1 (H)	8.66	0.96	2.37
OPC	6.65	0.97	1.92
PPC	6.48	0.97	2.37

OPC: Ordinary portland cement; PPC: Pozzolanic portland cement.

This supports the argument in 3.3 of CBW's superior mineralogical properties compared to CSA Figures 7 and 8. This contributed positively to the mortar microstructural development [24, 70]. Alkali-activated blend cement offered greater resistance to chloride ingress than OPC at any given alkali concentration. There was an increasing trend of D_{app} with the increase of alkali-activator concentration as well as the increase of CSA from 1-4 as [5-4-1(H) < 5-1-4(H) < PPC] < OPC < [5-4-1(0.5 M) < 5-4-1(2 M) < 5-1-4 (0.5 M) <5-1-4 (2 M)]. The introduction of an alkali activator increases the rate of alumina-silicate dissolution. As a result, the concrete becomes denser, attains higher resistivity, and reduces chloride diffusivity due to the greater cementitious material produced by the more pozzolanic reaction. The cementitious material can be produced via alkali-activated cement with increased time [71]. According to Abdulkareem et al. [72], this causes the final mortar or concrete to have less permeability. Chemical activation at an 80% BFS replacement level with a high dose of 10.17 kg/m³ KOH was able to speed up hydration and portlandite consumption, according to [72].

3.8. Thermal Resistance

After exposure to various thermal loads, quantitative evaluation of the hardened paste behavior was determined by measuring their residual strengths following heat exposure. Heat strength profiles of 5-1-4 and OPC pastes binders after being heated to 100, 300, 500, 700, and 800 °C are displayed in Figure 17.

On exposure of cement paste to temperatures ranging from 25 to 100 °C, OPC's compressive strength dropped sharply while 5-1-4 blends increased marginally (Fig. 4). According to Zivica et al. [73], crystalline products can be formed in the structural pores of pozzolana blend and alkali-activated paste when the reaction rate of the unreacted materials is increased by raising the temperature. A possible explanation for OPC's weakening at 0 to 100 °C could be pore water evaporation. At temperatures between 100 and 300 °C, the compressive strength of 5-1-4 blends rapidly decreased. The loss of water content in the specimens is likely to cause this. Free and chemically bonded water within specimens swiftly migrates to the surface and evaporates as the external temperature rises from ambient to 300 °C. This leads to a quick loss of strength in the 100–300 °C range and harms the specimens' internal microstructure [74]. Once the temperature reaches 300 °C, the strength of 5-1-4 blends gradually de-

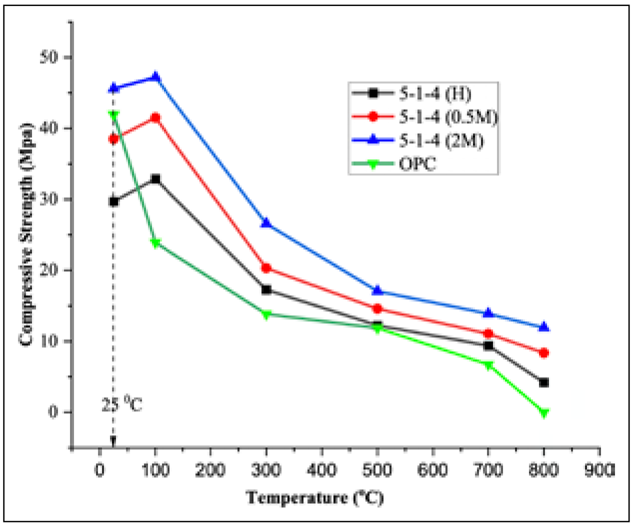

Figure 17. Results of the effect of heat on 5-1-4 blends compared to OPC.

creases in the order of 5-1-4 (2M) < 5-1-4 (0.5M) < 5-1-4(H), indicating a small impact of temperature on strength deterioration in that order. Deterioration in strength also slows down about 300 °C because water evaporation decreases.

OPC at temperatures beyond 300 °C continued to show a relatively steady decrease in compressive strength to total failure at 800 °C. This could be associated with the deterioration of the CSH and Ca(OH), the principal binding phases of the hydrated OPC mortar. OPC has previously indicated an irreversible loss of strength at a temperature above 200 °C [75]. Jeon et al. [76] reported that the main cause of OPC strength reduction on exposure to high temperature was mainly due to the expansion of lime after chilling and that the breakdown of $Ca(OH)_2$ had minimal impact. The OPC system was found to degrade at elevated temperatures up to 600 °C, while Rashad [77] found that Na_2SO_4-activated slag exhibited superior resistance. Their research showed that a higher concentration of Na_2SO_4 and finer slag resulted in superior heat resistance.

Figure 17 shows that at room temperature and after exposure to high temperatures, the compressive strength of CBW-CSA-blend pozzolana and alkali-activated-based paste is greater than that of OPC mortar. Because of this, structural components made with CBW-CSA blend alkali-activated-based mortar can offer the same or even greater fire resistance, and there are many other environmental benefits, including reduced energy consumption and carbon dioxide emissions.

4. CONCLUSION

The described study examined the effects of thermal stability and aggressive media on a cement blend of activated clay brick waste and coconut shell ash. The current findings demonstrate that CSA and CBW, when added to alkali-activated cement mortar, considerably enhance its prospective durability about thermal resistance, compressive strength development, and penetrability (sorptivity, permeability, conductivity, and diffusion). The results show that blend alkali-activated cement mortar can be made of higher quality using CSA and CBW. In most cases, a 5:1:4 ratio of OPC to CSA to CBW and a concentration of alkali activator up to 2 M Na_2SO_4 yield better results. This is because CSA and CBW can change the chemical and physical microstructure of the mortar that has been activated with alkali. It is important to take note of the following findings from the tests.

1. All blended cement had high Blaine values compared to the standard. The Blaine values, which were directly proportional to the particle size distribution of the precursor materials, gave high reactivity, which is seen to be contributed by an increase in CBW content. The formulation of 5-1-4 with a high composition of CBW gave an improved compressive strength at all concentrations compared to the corresponding samples of 5-4-1. In potable water, the compressive strength 5-1-4 was almost double that of 5-4-1.
2. When the concentration of the alkali activator was increased by using 0.5 M and 2M, the outstanding 5-1-4 HAC blend exhibited a compressive strength growth of 30% and 50% concerning the water-prepared blends. Compared to non-activated mortars, alkali-activated blend mortars showed more than 10 percent decreased sorptivity, Porosity, and OPI across all cement categories.
3. Regarding the DI test results, CBW properly mixed with CSA generally produced an excellent binder, which improved with a higher content of CBW than CSA and at a higher alkali concentration. 5-1-4 blends showed an improved DI trend of 19-36 percent against the lowest 3-6-1 blends at 6-26 percent. This is confirmed by the correlation analysis of the permeability test results
4. The chloride ion penetration and chloride diffusion coefficient decreased as the CBW content increased from 1 to 4, the alkali concentration decreased from 0 to 2M, and the CSA content decreased from 4 to 1. Its capacity to bind chlorides and alter the concrete microstructure is probably to blame for this effect. (However, the present investigation did not directly evaluate the HAC chloride binding capacity).
5. In comparison to regular Portland cement, 5-1-4 (2 M) holds up better in hotter environments. The harmful expansion that occurs at high temperatures is caused by the limited lime in 5-1-4 blends. Compared to OPC, the 5-1-4 (2 M) system is the superior fire-resistant binder. So, it's clear that CBW-CSA based on alkali activation can be made for building purposes; these materials show much promise for fire resistance.

ACKNOWLEDGMENTS

The authors gratefully acknowledge MAPRONANO ACE, Uganda and the World Bank for the PhD research scholarship. Access to the scholarly repository and library materials at Pwani University, Kenya is appreciated. Thanks to the University of the Witwatersrand, South Africa, and Mombasa Cement Company, Kenya, for allowing access to their cement laboratory. Special thanks to Prof. Luca Valentini of the University of Padova, Italy, for allowing part of the research in their laboratories and for great input and advice in analyzing the results.

ETHICS

There are no ethical issues with the publication of this manuscript.

DATA AVAILABILITY STATEMENT

The authors confirm that the data that supports the findings of this study are available within the article. Raw data that support the finding of this study are available from the corresponding author, upon reasonable request.

CONFLICT OF INTEREST

The authors declare that they have no conflict of interest.

USE OF AI FOR WRITING ASSISTANCE

Not declared.

PEER-REVIEW

Externally peer-reviewed.

REFERENCES

[1] Andrew, R. M. (2020). A comparison of estimates of global carbon dioxide emissions from fossil carbon sources. *Earth Syst Sci Data, 12*(2), 1437–1465. [CrossRef]

[2] Amer, I., Kohail, M., El-Feky, M. S., Rashad, A., & Khalaf, M. A. (2021). Characterization of alkali-activated hybrid slag/cement concrete. *Ain Shams Eng J, 12*(1), 135–144. [CrossRef]

[3] Provis, J. L. (2014). Green concrete or red herring? Future of alkali-activated materials. *Adv Appl Ceram, 113*(8), 472–477. [CrossRef]

[4] Rashad, A. M., Bai, Y., Basheer, P. M., Collier, N. C., & Milestone, N. B. (2012). Chemical and mechanical stability of sodium sulfate activated slag after exposure to elevated temperature. *Cem Concr Res, 42*(2), 333–343. [CrossRef]

[5] Bahafid, S., Ghabezloo, S., Duc, M., Faure, P., & Sulem, J. (2017). Effect of the hydration temperature on the microstructure of Class G cement: CSH composition and density. *Cem Concr Res, 95*, 270–281. [CrossRef]

[6] Ma, H., Zhu, H., Yi, C., Fan, J., Chen, H., Xu, X., & Wang, T. (2019). Preparation and reaction mechanism characterization of alkali-activated coal gangue-slag materials. *Materials, 12*(14), 2250. [CrossRef]

[7] Zhang, H. Y., Kodur, V., Wu, B., Cao, L., & Wang, F. (2016). Thermal behavior and mechanical properties of geopolymer mortar after exposure to elevated temperatures. *Constr Build Mater, 109*, 17–24. [CrossRef]

[8] Marie, I. (2017). Thermal conductivity of hybrid recycled aggregate-Rubberized concrete. *Constr Build Mater, 133*, 516–524. [CrossRef]

[9] Ullattil, S. G., & Ramakrishnan, R. M. (2018). Defect-rich brown TiO2-x porous flower aggregates: Selective photocatalytic reversibility for organic dye degradation. *ACS Appl Nano Mater, 1*(8), 4045–4052. [CrossRef]

[10] Real, S., & Bogas, J. A. (2017). Oxygen permeability of structural lightweight aggregate concrete. *Constr Build Mater, 137*, 21–34. [CrossRef]

[11] Davidovits, J., & Sawyer, J. L. (1985). *Early high-strength mineral polymer*. US4509985A.

[12] Kuehl, H. (1908). *Slag cement and process of making the same*. US900939A.

[13] Rivera, J., Castro, F., Fernández-Jiménez, A., & Cristelo, N. (2021). Alkali-activated cements from urban, mining and agro-industrial waste: State-of-the-art and opportunities. *Waste and Biomass Valorization, 12*, 2665–2683. [CrossRef]

[14] Al-Kutti, W., Nasir, M., Johari, M. A. M., Islam, A. S., Manda, A. A., & Blaisi, N. I. (2018). An overview and experimental study on hybrid binders containing date palm ash, fly ash, OPC and activator composites. *Constr Build Mater, 159*, 567–577. [CrossRef]

[15] EAS, K. (2000). Kenya standard test method for determination of cement strength.

[16] Alexander, M. G., Ballim, Y., & Mackechnie J. (2018). Durability index testing procedure manual version 4.5.1. https://tinyurl.com/evkvcakb

[17] Moore, A. J., Bakera, A. T., & Alexander, M. G. (2020). Water sorptivity and porosity testing of concrete. *Concrete Beton Technical Note, 162*, 13–16.

[18] University of Cape Town. (2015). *Concrete durability index testing - Oxygen permeability test*. SANS 3001-CO3-2.

[19] Kenya Bureau of Standards. (2017). *Kenya's standard test method for oxide specification of hydraulic cement*. KS EAS 18-1.

[20] Samson, E., Marchand, J., & Snyder, K. A. (2003). Calculation of ionic diffusion coefficients on the basis of migration test results. *Materials and Structures, 36*, 156–165. [CrossRef]

[21] Castellote, M., Andrade, C., & Alonso, C. (2000). Phenomenological mass-balance-based model of migration tests in stationary conditions: Application to non-steady-state tests. *Cem Concr Res, 30*(12), 1885–1893. [CrossRef]

[22] Crank, J. (1975). *The mathematics of diffusion*. Clarendon Press.

[23] Monteiro, P. J., Geng, G., Marchon, D., Li, J., Alapati, P., Kurtis, K. E., & Qomi, M. J. A. (2019). Advances in characterizing and understanding the microstructure of cementitious materials. *Cem Concr Res, 124*, 105806. [CrossRef]

[24] Abdellatief, M., Elemam, W. E., Alanazi, H., & Tahwia, A. M. (2023). Production and optimization of sustainable cement brick incorporating clay brick wastes using response surface method. *Ceram Int, 49*(6), 9395–9411. [CrossRef]

[25] Assi, L. N., Deaver, E. E., & Ziehl, P. (2018). Effect of source and particle size distribution on the mechanical and microstructural properties of fly Ash-Based geopolymer concrete. *Constr Build Mater, 167*, 372–380. [CrossRef]

[26] Schackow, A., Correia, S. L., & Effting, C. (2020). Microstructural and physical characterization of solid wastes from clay bricks for reuse with cement. *Environ Eng Manag J, 19*(4), 565–576. [CrossRef]

[27] Zhou, H., Chen, Y., Li, H., Xu, Z., Dong, H., & Wang, W. (2022). Effect of particles micro characteristics destroyed by ball milling on fly ash electrostatic separation. *Advanced Powder Technology, 33*(3), 103449. [CrossRef]

[28] Arslan, V. (2021). A study on the dissolution kinetics of iron oxide leaching from clays by oxalic acid. *Physicochemical Problems of Mineral Processing, 57*(3), 97–111. [CrossRef]

[29] Hou, P., Kawashima, S., Kong, D., Corr, D. J., Qian, J., & Shah, S. P. (2013). Modification effects of colloidal nanoSiO2 on cement hydration and its gel property. *Composites Part B Engineering, 45*(1), 440–448. [CrossRef]

[30] Anuar, M. F., Fen, Y. W., Zaid, M. H. M., Matori, K. A., & Khaidir, R. E. M. (2020). The physical and optical studies of crystalline silica derived from the green synthesis of coconut husk ash. *Appl Sci, 10*(6), 2128. [CrossRef]

[31] Tayade, R. A., & Kanojiya, M. A. C. (2022) The case study of isothermal adsorption of phenol, O-cresol on natural charcoal's and applications. *Int J Res Appl Sci Eng Technol, 10*(12), 1718–1731. [CrossRef]

[32] Onwona-Agyeman, B., Lyczko, N., Minh, D. P., Nzihou, A., & Yaya, A. (2020). Characterization of some selected Ghanaian clay minerals for potential industrial applications. *J Ceram Process Res, 21*(1), 35–41. [CrossRef]

[33] de Sousa, L. L., Salomão, R., & Arantes, V. L. (2017). Development and characterization of porous moldable refractory structures of the alumina-mullite-quartz system. *Ceram Int, 43*(1), 1362–1370. [CrossRef]

[34] Garg, N., & Skibsted, J. (2016). Pozzolanic reactivity of a calcined interstratified illite/smectite (70/30) clay. *Cem Concr Res, 79*, 101–111. [CrossRef]

[35] Kang, S. H., Hong, S. G., & Moon, J. (2019). The use of rice husk ash as reactive filler in ultra-high performance concrete. *Cem Concr Res, 115*, 389–400. [CrossRef]

[36] Opálková Šišková, A., Dvorák, T., Šimonová Baranyaiová, T., Šimon, E., Eckstein Andicsová, A., Švajdlenková, H., ... & Nosko, M. (2020). Simple and eco-friendly route from agro-food waste to water pollutants removal. *Materials, 13*(23), 5424. [CrossRef]

[37] Park, S., Baker, J. O., Himmel, M. E., Parilla, P. A., & Johnson, D. K. (2010). Cellulose crystallinity index: Measurement techniques and their impact on interpreting cellulase performance. *Biotechnol Biofuels, 3*, 1–10. [CrossRef]

[38] Scrivener, K. L., & Nonat, A. (2011). Hydration of cementitious materials, present and future. *Cem Concr Res, 41*(7), 651–665. [CrossRef]

[39] Khushnood, R. A. O. & Arsalan, R. (2015). *High performance self-compacting cementitious materials using nano/micro carbonaceous inerts* [Doctoral thesis], Politecnico di Torino.

[40] Barboza-Chavez, A. C., Gómez-Zamorano, L. Y., & Acevedo-Dávila, J. L. (2020). Synthesis and characterization of a hybrid cement based on fly ash, metakaolin and portland cement clinker. *Materials, 13*(5), 1084. [CrossRef]

[41] Samarakoon, M. H., Ranjith, P. G., Rathnaweera, T. D., & Perera, M. S. A. (2019). Recent advances in alkaline cement binders: A review. *J Clean Prod, 227*, 70–87. [CrossRef]

[42] Musyimi, N.F., Karanja, T.J., Wachira, M.J., & Mulwa, M.O. (2016). Pozzolanicity and compressive strength performance of kibwezi bricks based cement. *IOSR J Appl Chem, 9*(2), 28–32.

[43] Hanein, T., Thienel, K. C., Zunino, F., Marsh, A. T., Maier, M., Wang, B., ... & Martirena-Hernandez, F. (2022). Clay calcination technology: State-of-the-art review by the RILEM TC 282-CCL. *Mater Struct, 55*(1), 3. [CrossRef]

[44] Chernyshova, N., Lesovik, V., Fediuk, R., & Timokhin, R. (2020). Enhancement of fresh properties and performances of the eco-friendly gypsum-cement composite (EGCC). *Constr Build Mater, 260*, 120462. [CrossRef]

[45] Bakera, A. T., & Alexander, M. G. (2018). *Properties of Western Cape concretes with metakaolin*. In MATEC Web of Conferences (Vol. 199, p. 11011). EDP Sciences. [CrossRef]

[46] Kearsley, E. P., & Wainwright, P. J. (2001). Porosity and permeability of foamed concrete. *Cem Concr Res, 31*(5), 805–812. [CrossRef]

[47] Marangu, J. M., Thiong'o, J. K., & Wachira, J. M. (2019). Review of carbonation resistance in hydrated cement based materials. *J Chem, 2019*(1), 8489671. [CrossRef]

[48] Cordeiro, G. C., Toledo Filho, R. D., Tavares, L. M., & Fairbairn, E. D. M. R. (2009). Ultrafine grinding of sugar cane bagasse ash for application as pozzolanic admixture in concrete. *Cem Concr Res, 39*(2), 110–115. [CrossRef]

[49] van Deventer, J. S., San Nicolas, R., Ismail, I., Bernal, S. A., Brice, D. G., & Provis, J. L. (2015). Microstructure and durability of alkali-activated materials as key parameters for standardization. *J Sustain Cem Mater, 4*(2), 116–128. [CrossRef]

[50] Nath, P., & Sarker, P. K. (2014). Effect of GGBFS on setting, workability and early strength properties of fly ash geopolymer concrete cured in ambient condition. *Constr Build Mater, 66*, 163–171. [CrossRef]

[51] Fang, S., Lam, E. S. S., Li, B., & Wu, B. (2020). Effect of alkali contents, moduli and curing time on engineering properties of alkali activated slag. *Constr Build Mater, 249*, 118799. [CrossRef]

[52] Monticelli, C., Natali, M. E., Balbo, A., Chiavari, C., Zanotto, F., Manzi, S., & Bignozzi, M. C. (2016). Corrosion behavior of steel in alkali-activated fly ash mortars in the light of their microstructural, mechanical and chemical characterization. *Cem Concr Res, 80*, 60–68. [CrossRef]

[53] Palomo, A., Krivenko, P., Garcia-Lodeiro, I., Kavalerova, E., Maltseva, O., & Fernández-Jiménez, A. (2014). A review on alkaline activation: New analytical perspectives. *Mater Constr, 64*(315),

e022. [CrossRef]
[54] Angulo-Ramírez, D. E., Valencia-Saavedra, W. G., & Mejía de Gutiérrez, R. (2020). Alkali-activated concretes based on fly ash and blast furnace slag: Compressive strength, water absorption and chloride permeability. *Ing Investig, 40*(2), 72–80. [CrossRef]
[55] Puertas, F., Palacios, M., Manzano, H., Dolado, J. S., Rico, A., & Rodríguez, J. (2011). A model for the CASH gel formed in alkali-activated slag cements. *J Eur Ceram Soc, 31*(12), 2043–2056. [CrossRef]
[56] Embong, R., Kusbiantoro, A., Shafiq, N., & Nuruddin, M. F. (2016). Strength and microstructural properties of fly ash based geopolymer concrete containing high-calcium and water-absorptive aggregate. *J Clean Prod, 112*, 816–822. [CrossRef]
[57] Gijbels, K., Pontikes, Y., Samyn, P., Schreurs, S., & Schroeyers, W. (2020). Effect of NaOH content on hydration, mineralogy, porosity and strength in alkali/sulfate-activated binders from ground granulated blast furnace slag and phosphogypsum. *Cem Concr Res, 132*, 106054. [CrossRef]
[58] Verma, P., Chowdhury, R., & Chakrabarti, A. (2021). Role of graphene-based materials (GO) in improving physicochemical properties of cementitious nano-composites: A review. *J Mater Sci, 56*(35), 19329–19358. [CrossRef]
[59] Balun, B., & Karataş, M. (2021). Influence of curing conditions on pumice-based alkali activated composites incorporating Portland cement. *J Build Eng, 43*, 102605. [CrossRef]
[60] Bernal, S. A., San Nicolas, R., Myers, R. J., de Gutiérrez, R. M., Puertas, F., van Deventer, J. S., & Provis, J. L. (2014). MgO content of slag controls phase evolution and structural changes induced by accelerated carbonation in alkali-activated binders. *Cem Concr Res, 57*, 33–43. [CrossRef]
[61] Mithun, B. M., & Narasimhan, M. C. (2016). Performance of alkali activated slag concrete mixes incorporating copper slag as fine aggregate. *J Clean Prod, 112*, 837–844. [CrossRef]
[62] Yang, K., Yang, C., Magee, B., Nanukuttan, S., & Ye, J. (2016). Establishment of a preconditioning regime for air permeability and sorptivity of alkali-activated slag concrete. *Cem Concr Res, 73*, 19–28. [CrossRef]
[63] Albitar, M., Ali, M. M., Visintin, P., & Drechsler, M. (2017). Durability evaluation of geopolymer and conventional concretes. *Constr Build Mater, 136*, 374–385. [CrossRef]
[64] Ismail, I., Bernal, S. A., Provis, J. L., San Nicolas, R., Hamdan, S., & van Deventer, J. S. (2014). Modification of phase evolution in alkali-activated blast furnace slag by the incorporation of fly ash. *Cem Concr Compos, 45*, 125–135. [CrossRef]
[65] Ngui Musyimi, F., Wachira, J. M., Thiong'o, J. K., & Marangu, J. M. (2019). Performance of ground clay brick mortars in simulated chloride and sulphate media. *J Eng, 2019*(1), 6430868. [CrossRef]
[66] Mutitu, D. K., Karanja, J. K., Wachira, J. M. (2014). Diffusivity of chloride and sulphate ions into mortar cubes made using ordinary Portland and Portland Pozzolana cements. *IOSR J Appl Chem, 7*(2), 67–73. [CrossRef]
[67] Wang, J., Basheer, P. M., Nanukuttan, S. V., & Bai, Y. (2014). *Influence of compressive loading on chloride ingress through concrete.* In Civil Engineering Research Association of Ireland (CERAI) Proceedings. CERI 2014, Spain.
[68] Marangu, J. M., Thiong'o, J. K., & Wachira, J. M. (2018). Chloride ingress in chemically activated calcined clay-based cement. *J Chem, 2018*(1), 1595230. [CrossRef]
[69] Tang, S., Wang, Y., Geng, Z., Xu, X., Yu, W., & Chen, J. (2021). Structure, fractality, mechanics and durability of calcium silicate hydrates. *Fractal and Fractional, 5*(2), 47. [CrossRef]
[70] Zhang, H., He, B., Zhao, B., & Monteiro, P. J. (2023). Using diatomite as a partial replacement of cement for improving the performance of recycled aggregate concrete (RAC)-Effects and mechanism. *Constr Build Mater, 385*, 131518. [CrossRef]
[71] Juenger, M. C., & Siddique, R. (2015). Recent advances in understanding the role of supplementary cementitious materials in concrete. *Cem Concr Res, 78*, 71–80. [CrossRef]
[72] Abdulkareem, O. M., Fraj, A. B., Bouasker, M., Khouchaf, L., & Khelidj, A. (2021). Microstructural investigation of slag-blended UHPC: The effects of slag content and chemical/thermal activation. *Constr Build Mater, 292*, 123455. [CrossRef]
[73] Živica, V., Palou, M. T., & Križma, M. (2015). Geopolymer cements and their properties: A review. *Build Res J, 61*(2), 85–100. [CrossRef]
[74] Zhang, Z., Provis, J. L., Reid, A., & Wang, H. (2014). Geopolymer foam concrete: An emerging material for sustainable construction. *Constr Build Mater, 56*, 113–127. [CrossRef]
[75] Lin, W., Zhou, F., Luo, W., & You, L. (2021). Recycling the waste dolomite powder with excellent consolidation properties: Sample synthesis, mechanical evaluation, and consolidation mechanism analysis. *Constr Build Mater, 290*, 123198. [CrossRef]
[76] Jeon, D., Yum, W. S., Song, H., Sim, S., & Oh, J. E. (2018). The temperature-dependent action of sugar in the retardation and strength improvement of Ca (OH) 2-Na2CO3-activated fly ash systems through calcium complexation. *Constr Build Mater, 190*, 918–928. [CrossRef]
[77] Rashad, A. M. (2015). Influence of different additives on the properties of sodium sulfate activated slag. *Constr Build Mater, 79*, 379-389. [CrossRef]

J Sustain Const Mater Technol, Vol. 9, Issue. 4, pp. 391–401, December 2024

Journal of Sustainable Construction Materials and Technologies
Web page info: https://jscmt.yildiz.edu.tr
DOI: 10.47481/jscmt.1607828

Journal of Sustainable Construction Materials and Technologies

Research Article

One-part alkali-activated mortars based on clay brick waste, natural pozzolan waste, and marble powder waste

Kübra EKİZ BARIŞ*

Department of Architecture, Kocaeli University Faculty of Architecture and Design, Kocaeli, Türkiye

ARTICLE INFO

Article history
Received: 21 November 2024
Revised: 18 December 2024
Accepted: 18 December 2024

Key words:
Clay brick waste, marble powder waste, natural pozzolan waste, one-part alkali-activated mortar

ABSTRACT

In Türkiye, waste clay bricks (WCB) comprise significant construction and demolition waste. Most research is based on producing WCB-based two-part alkali-activated materials (AAM). Compared to their conventional, two-part alkali-activated counterparts, one-part AAM offers several advantages, such as being more practical, safe, and easy to use. Thus, they may be an excellent choice for commercial construction applications and on-site casting. However, research data on producing WCB-based one-part alkali-activated mortars is limited. The relatively low reactivity of WCB can be increased by replacing WCB with ground granulated blast-furnace slag (GGBS) and fly ash (FA). Unlike these by-products, Nevşehir pozzolan (NP) and marble powder (MP), which are produced as wastes during the stone-cutting process, may be evaluated to produce AAM. This study aims to assess the production possibilities of WCB-based one-part alkali-activated mortar, determine the optimum substitution ratios with NP and MP to improve the mechanical properties, and determine the effects of the curing period up to 365 days. Results showed that the optimum NP substitution ratio was 50%, which increased reaction development, microstructure compactness, and mechanical properties. The highest CS (UV) (3.70 km/s) and compressive strength (CS) (21.58 MPa) were obtained in 25WCB:75MP-containing samples. The increase in properties with the curing period was especially high in the first 28 days.

Cite this article as: Ekiz Barış, K. (2024). One-part alkali-activated mortars based on clay brick waste, natural pozzolan waste, and marble powder waste. *J Sustain Const Mater Technol*, 9(4), 391–401.

1. INTRODUCTION

AAM are energy- and resource-efficient alternatives to traditional Portland cement. The reaction of amorphous alumina and silica-rich solid aluminosilicate sources with high alkali activators produces these binders. The alkali activator ensures the solid raw material's dissolution by increasing the reaction medium's pH. The dissolved components were rearranged and then condensed by polycondensation, forming a three-dimensional amorphous aluminosilicate network structure [1]. Industrial by-products such as FA, GGBS, and silica fume (SF) are often used as aluminosilicate precursors to produce AAM. However, while the continuous supply of these by-products is relatively easy in some countries, it remains limited in others [2]. Therefore, research identifying alternative sources of raw materials to produce the AAM is essential.

During the production of fired clay-based bricks and tiles, which are frequently used in the construction industry, the calcination process occurs at 850–950 °C. At these high calcination temperatures, the bound water in the clay minerals evaporates, the crystalline structure of clay col-

---

***Corresponding author.**
*E-mail address: kubra.ekizbaris@kocaeli.edu.tr

Published by Yıldız Technical University Press, İstanbul, Türkiye

lapses, and irregular amorphous SiO_2 and Al_2O_3 phases are formed [3], which ensures its reactivity [4]. Furthermore, the existence of these amorphous phases in the structure of WCB makes it a low-cost and environmentally friendly alternative aluminosilicate precursor [2]. The material is of most interest because of the abundant availability of WCB and 25–93 MPa strength [5]. A large number of WCB is produced every year on a global scale, both during brick production and construction and demolition activities. With the Transformation of Areas Under Disaster Risk in Türkiye coming into force, the increase in urban transformation practices has further increased the amount of WCB. The majority of WCB is stored in landfills. However, according to the Regulation on the Control of Excavation Soil, Construction, and Demolition Waste, these wastes should be recycled and reused as structure and building materials [6]. Using WCB in AAM is an environmentally and economically viable option as it provides a solution to solid waste management and reduces the carbon footprint in the construction sector [2].

In the research on activating WCB with a mixture of sodium hydroxide (NaOH) and sodium silicate (Na_2SiO_3=SS), Komnitsas et al. [7] investigated the effect of particle size, NaOH molarity (8–14 M), and different curing temperatures (60–90 °C). The highest CS (49.5 MPa) was determined in samples activated with 8 M NaOH and cured at 90 °C. Rakhimova and Rakhimov [8] mixed GGBS and WCB in different proportions (0:100, 20:80, 40:60, 60:40, 80:20, 100:0, by wt.) and activated them with SS or sodium carbonate (SC). The CS of the binder containing only GGBS was 97 MPa for the SS-activated binder and 61 MPa for the SC-activated binder. The CS of the sample with a GGBS: WCB ratio of 60:40 was determined to be the highest (120 MPa). In another study, Zawrah et al. [9] replaced GGBS with WCB at 20%, 40%, 60%, and 80% percentages. They found that a 60% replacement ratio gave the highest CS (64 and 83 MPa at the 7th and 90th days, respectively). The positive effects of using GGBS and WCB together were parallel with the results of Rakhimova and Rakhimov [8].

The potential to produce AAM from a combination of FA and WCB was assessed by Rovnanik et al. [10]. FA: WCB was used in the ratios of 4:0, 3:1, 1:1, and 0:4 by wt. The samples were cured for 7, 28, and 90 days under environmental conditions of 21 °C and 50% RH. According to the study results, samples containing FA and WCB had lower CS than those based only on FA. This result contradicted the findings of Rakhimova et al. [8] and Zawrah et al. [9]. Tuyan et al. [11] studied the influence of alkali activator concentration and curing conditions on the properties of WCB-based AAM. The optimum activator concentration was determined as a SiO_2/Na_2O ratio of 1.6 and a Na_2O ratio of 10%. The maximum CS of 36.2 MPa was reached after 5 days of curing at 90 °C and 40% RH. Increasing the Na_2O ratio from 4% to 10% enhanced the CS by increasing the alkalinity of the mixture and allowing more Si^{4+} and Al^{3+} ions to dissolve. Silva et al. [12] conducted an experimental study in which WCB and natural pozzolan were activated with a combination of NaOH and SS. The optimum alkali activator ratio was 0.60, the Na_2O ratio was 8%, and the water/binder ratio was 0.27. It was determined that a 7-day curing period between 65 and 80 °C resulted in the highest mechanical properties. The 7-day CS of WCB and natural pozzolan-based materials was determined to be 37 and 26 MPa, respectively. Ulugöl et al. [13] reported the effects of different curing temperatures (50–125 °C), curing periods (24–72 h), and NaOH concentrations (10–15%) on the properties of AAM produced from brick, tile, and glass-based construction and demolition waste. Using WCB and 12% NaOH, a CS of more than 45 MPa was achieved after a 24-hour curing period at 115 °C. The larger particle sizes in the glass explained the lower CS of glass-based materials. Another study [14] produced AAM by replacing NaOH-activated GGBS with 10–50% WCB. As the WCB ratio in the mixture increased, the mechanical properties decreased. However, the CS of the samples with a 10–50% WCB ratio (approximately 25–45 MPa) was sufficient and acceptable for many applications.

In recent years, Pommer et al. [15] determined that decreasing the particle size of the WCB resulted in an increased geopolymerization rate and improved mechanical properties. On the other hand, the coarser particles led to an increase in porosity, which influenced the physical properties of the AAM. As a precursor, WCB was substituted for FA by Liang et al. [16], who found pastes containing WCB set faster than the reference paste. The energy used to produce AAM decreased with the addition of WCB. Compared to a reference sample, the total energy savings of the 40 wt% WCB-containing sample were approximately 55%. The effects of alkali activator concentration (8–12 M), alkali solution ratio (1.5–2.5), and curing temperatures (40–60 °C) on the mechanical and durability properties of WCB-based geopolymer bricks were researched by Maaze et al. [17]. The results showed that the optimum molarity, alkali solution ratio, and curing temperature were 10 M, 2.5, and 60 °C, respectively. The samples were considered suitable for high-temperature use because of their thermal stability. Their CS reduced only 3.1–5.8% after exposure to 400 °C and 7.1–8% after exposure to 1000 °C. In another study, Roy et al. [18] replaced GGBS with WCB at 5%, 10%, 15%, and 20% ratios. They found that a 10% replacement ratio with a 6 M alkali concentration gave the maximum CS of 27 MPa. Wang et al. [19] produced an eco-friendly engineered geopolymer composite by using GGBS, FA, and WCB precursors. Three WCB proportions of 20%, 50%, and 80% were used in the precursors. 18 mm polyethylene fibers were included in the samples to increase the ductility. 80% WCB incorporation resulted in the highest values of CS (approximately 50 MPa), tensile strength (higher than 4 MPa), and tensile ductility (4%). Furthermore, 80% WCB incorporation decreased the material's embodied energy, carbon, and cost by 40%, 30%, and 30%, respectively. In another research project conducted by Borçato et al. [20], 25%, 50%, and 75% of the metakaolin (MK) were replaced by WCB. 5% calcium hydroxide was incorporated in some samples because the CaO content of MK and WCB is low. Calcium hydroxide increased the CS from 12.3 MPa to 31.6 MPa on the 28th day. This increasing trend of CS originated

Table 1. Chemical composition of the raw materials (WCB, NP, and MP) by X-ray fluorescence spectroscopy

Oxide content (% wt.)	Raw materials		
	WCB	NP	MP
SiO_2	61.11	77.29	0.22
Al_2O_3	14.05	18.48	0.10
Fe_2O_3	6.11	1.71	–
CaO	8.76	0.33	55.70
MgO	1.72	1.29	0.21
K_2O	2.24	0.30	–
SO_3	0.21	0.10	–
Loss on ignition	5.80	0.50	43.77
Sum of SiO_2, Al_2O_3, and Fe_2O_3 necessary for alkali activation (>70%)	81.27	97.48	0.32

WCB: Waste clay bricks; NP: Nevşehir pozzolan; MP: Marble powder.

from the coexistence of C-A-S-H gel and N-A-S-H gel in the AAM structure. In addition, the CS was higher in the samples with higher WCB content.

Literature data show that WCB enables the production of AAM. In the studies mentioned above, the alkali activator is used in solution (in two parts). Aqueous alkali activators producing conventional two-part AAM are highly corrosive, viscous, and hazardous. Therefore, their use on an industrial scale can be problematic. In contrast, one-part AAM is produced by adding solid alkali activators to the aluminosilicate precursor. Similar to Portland cement, these binders require mixing with water before use. Therefore, using a one-part AAM is more practical and user-friendly than a conventional AAM [21]. However, research data on the production of WCB-based one-part AAM are limited. In addition, it is known that only WCB-based AAM may have poor mechanical properties because WCB has a relatively low pozzolanic activity [8, 10]. Migunthanna et al. [21] studied the production possibilities of a WCB-based one-part AAM. WCB was mixed with FA or GGBS at 20%, 40%, 60%, and 80% wt to obtain higher mechanical properties. The mechanical properties of WCB+GGBS-based samples were higher than those of WCB-based and WCB+FA-based samples. The highest CS (81.8 MPa) was obtained from 40% WCB and 60% GGBS.

In research on the production of both one-part and two-part AAM, WCB is replaced with industrial by-products such as FA and GGBS to improve the relatively low reactivity of WCB and produce materials with higher mechanical properties. Unlike these by-products, both Nevşehir natural pozzolan (NP) of Türkiye and marble powder (MP), which are made wastes during the sunstone-cutting cess, may be used in M. Therefore, this research aims to (i) evaluate the production possibilities of WCB-based one-part alkali-activated mortar; (ii) determine the optimum substitution ratios with NP and MP wastes to improve the mechanical properties of the mortar; and (iii) determine the effects of the curing time, both in the early period and up to 365 days, on the properties of the mortar.

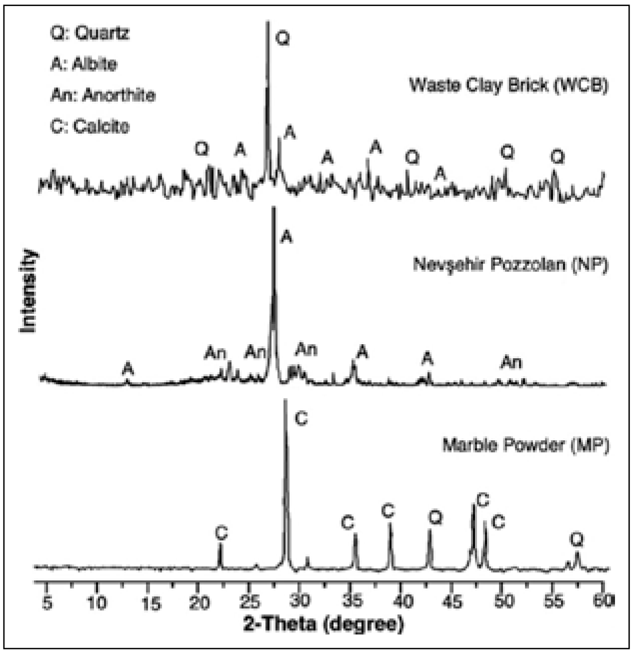

Figure 1. Mineralogical composition of the raw materials (WCB, NP, and MP) by X-ray diffraction (XRD) analysis.

WCB: Waste clay bricks; NP: Nevşehir pozzolan; MP: Marble powder.

2. METHODS

2.1. Raw Materials

WCB, an urban transformation waste, was the aluminosilicate precursor for producing one-part alkali-activated mortar. WCB, with a specific gravity of 2.40, was first broken into small pieces and then dried in an oven at 90 °C for 48 hours until it reached a constant weight. Then, it was ground in a ball mill to a maximum particle size of 90 µm. The mineralogical composition of WCB consists of kaolinite, muscovite, quartz, gypsum, and carbonates. Calcination is applied at 850–950 °C for the production of bricks. While kaolinite and gypsum disappear at these calcination temperatures, quartz and muscovite continue to exist in the structure in a stable state [2]. The mineralogical composition of the raw materials was determined by X-ray diffraction (XRD) analysis using a Shimadzu XRD-6000 energy dispersive diffractometer (Fig. 1). According to the XRD analysis, the main mineralogical composition of WCB consisted of quartz and albite.

The chemical composition of the raw materials was obtained by X-ray fluorescence spectroscopy using a Philips 71 PW-2404 Spectrometer (Table 1). WCB had a high content of SiO_2 (61.11%), as well as 14.05% Al_2O_3. During the calcination stage of the clay, the bound water in the clay minerals evaporates, the crystalline structure of the clay breaks down, and irregular amorphous phases of SiO_2 and Al_2O_3 are formed [22]. These amorphous phases increase the pozzolanic activity of the material [23]. The flexural and compressive strength results (1.12 MPa and 4.56 MPa, respectively) from the pozzolanic activity test carried out according to TS 25 [24] showed that WCB has pozzolanic activity.

Figure 2. Raw materials of the study: **(a)** WCB; **(b)** NP; **(c)** MP; **(d)** NaOH; **(e)** SS; **(f)** SK.

WCB: Waste clay bricks; NP: Nevşehir pozzolan; MP: Marble powder; SS: Sodium silicate; SK: Standart Sand.

Table 2. Mix design for WCB-based one-part alkali-activated mortars

Sample code	WCB (g)	NP (g)	MP (g)	SK (g)	NaOH (g)	SS (g)	Alkali activator: aluminosilicate precursor (wt.%)	NaOH: SS (wt.%)	Binder: SK (wt.%)	Water: binder (wt.%)
100WCB	400	–	–	1200	33.6	66.6	1:4	1:2	1:3	0.65: 1
75WCB:25NP	300	100	–							
50WCB:50NP	200	200	–							
25WCB:75NP	100	300	–							
75WCB:25MP	300	–	100							
50WCB:50MP	200	–	200							
25WCB:75MP	100	–	300							

WCB: Waste clay bricks; NP: Nevşehir pozzolan; MP: Marble powder; SS: Sodium silicate; SK: Standart sand.

WCB (Fig. 2a) was substituted by two various natural stone wastes with low- and high-calcium contents to prevent strength losses due to the relatively low reactivity of WCB in environmental conditions and to produce mortar with higher mechanical properties. NP (Fig. 2b) was waste obtained from the waste storage area of a volcanic quarry in the Cappadocia Region (Nevşehir) of Türkiye. The specific gravity of NP was 2.55, the maximum particle size was 90 µm, and the specific surface area determined according to TS EN 196–6 [25] was 7648 cm^2/g. As shown in Table 1, the sum of SiO_2, Al_2O_3, and Fe_2O_3 contents was more than 70%, revealing that NP could satisfy the chemical requirements for its use in alkali activation. In addition, NP was a low-calcium source because its CaO content (0.33%) was less than 10%. Albite and anorthite, found in NP (Fig. 1), were additional indicators of its pozzolanic activity. Following the pozzolanic activity test [24], NP exhibited pozzolanic activity, as shown by its flexural and compressive strength results (1.86 and 6.81 MPa, respectively).

MP was supplied from a marble-cutting factory in Izmit (Fig. 2c). The bright white MP was dried in an oven at 90 °C for 48 h until it reached a constant weight. Then, it was ground in a ball mill to a maximum particle size of 90 µm. With 55.7% CaO content, MP was a high-calcium source. The mineralogical composition of MP mainly consisted of calcite and a small amount of quartz (Fig. 1).

In the production of AAM, an alkali activator should be used to increase the pH of the reaction medium to ensure the dissolution of the aluminosilicate precursor and the development of subsequent polycondensation reactions [26]. As alkali activators, solid sodium hydroxide (NaOH) with 98% purity (Fig. 2d) and anhydrous sodium metasilicate (Na_2SiO_3=SS) with 50–52% SiO_2 and 50–48% Na_2O ratios (Fig. 2e) were supplied by Sigma-Aldrich. Standard sand

(SK) with a specific gravity of 2.58 and a maximum particle size of 2 mm (Fig. 2f) in compliance with TS EN 196-1 [27] was used as the aggregate.

2.2. Mixing Ratios

The mixture produced only from WCB (100WCB) was accepted as the reference sample. The study attempted to determine the optimum NP and MP substitution ratios to increase the mechanical properties of WCB-based one-part alkali-activated mortar. In this context, the amount of WCB was gradually replaced by NP or MP in proportions of 25%, 50%, and 75% wt. The total alkali activator: aluminosilicate precursor, NaOH: SS, and binder: SK ratios remained constant at 1:4, 1:2, and 1:3, by wt., respectively (Table 2). No chemical additives were used in the mixtures to prevent possible interactions with the alkali solution.

The optimum water: binder ratio that allows producing a workable mortar was determined through trials during the preliminary testing process. The optimum water: binder ratio of WCB-based two-part alkali-activated mortars should be 0.4–0.5 [28, 29], and lower water: binder ratio causes low workability [30]. However, in this study, the optimum water: binder ratio that ensures the workability of WCB-based one-part alkali-activated mortar was determined to be 0.65:1. It is possible that the increased water needs results from solid-state alkali activators, which raise mixing temperatures as soon as they come into contact with water and continue to do so throughout the dissolution process. The resulting heat caused a more significant amount of water to evaporate during mixing, thereby increasing the need for mixing water. On the other hand, in two-part alkali-activated mortars, mixing alkali activators with water for 24 hours before adding them to the mixture does not cause an increase in temperature, so there is no need for more water during mixing.

2.3. Production and Curing Conditions

WCB, NP/MP, solid alkali activators (NaOH and SS), and SK were mixed in dry form for 3 min using the one-part mixing method (Fig. 3a). Then, deionized water was gradually incorporated into the mixture and mixed for another 5 min (Fig. 3b). The fresh mixture was placed into two layers in prismatic molds measuring 40x40x160 mm (Fig. 3c). After half of the mixture was slowly poured into the mold, mechanical vibration was applied for 30 seconds to eliminate air bubbles and ensure complete settling into the mold. Then, the remaining mixture was poured into the mold, and vibration was applied again. The polyethylene-coated samples were kept in the mold at 23 °C for 24 h. The samples removed from the molds after 24 h were cured under ambient conditions of 23 °C and 55% RH for 7, 28, 90, 180, and 365 days (Fig. 3d).

2.4. Experimental Process

A dynamic UV test was applied to the samples by TS EN 14579 [31]. The UV (in km/s) is calculated using the following Eq. (1):

$$UV = l / t \tag{1}$$

Where (l) is the length of the sample and (t) is the time the pulse takes to transverse that length.

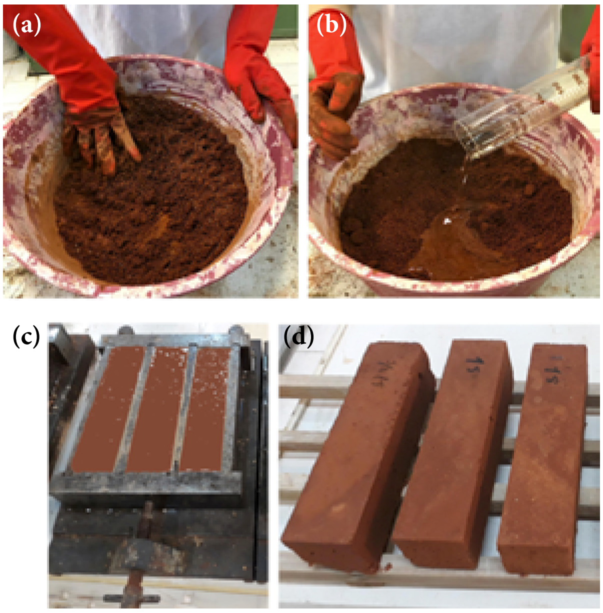

Figure 3. Production stages of WCB-based one-part alkali-activated mortars: **(a)** mixing of dry raw materials; **(b)** incorporation of deionized water to the dry mixture; **(c)** molding the fresh mixture; **(d)** curing the samples under ambient conditions of 23 °C and 55% RH up to 365 days.

WCB: Waste clay bricks.

The CS test was performed using an MFL 100 kN machine at a constant speed of 0.5 N/mm^2 according to TS EN 196-1 [27]. The CS (in MPa) was calculated using the following Eq. (2):

$$CS = F_c / A \tag{2}$$

Where (Fc) is the maximum load at fracture (in N), and (A) is the cross-section of the area of the sample resisting the load (in mm^2).

In an experiment with N measurements, one or more may deviate significantly from the others. These "bad data" may be easily discarded if an error in the experimental procedure or an unrelated effect can be found. A statistical criterion should be applied to determine which results can be rejected. Chauvenet's Criterion is an approach that establishes an acceptable statistical scattering about the mean value of a given sample of "N" measurements. According to the Criterion, every data point that falls in a range around the mean representing a probability of 1-1/(2N) ought to be kept. Data points may be rejected when the data point's deviation from the mean is smaller than 1/(2N) [32]. The current study conducted six measurements using UV and CS tests. The arithmetic means, and standard deviations of the first results were calculated. Then, "Chauvenet's Criterion table" was considered to determine whether any data point should be rejected. According to Chauvenet's Criterion for eliminating a data point, the maximum acceptable deviation was 1.73 for six measurements. All measurement results that deviate more than this value (1.73) were eliminated. Afterward, the arithmetic mean of the remaining results was calculated again [33] and declared the "test result."

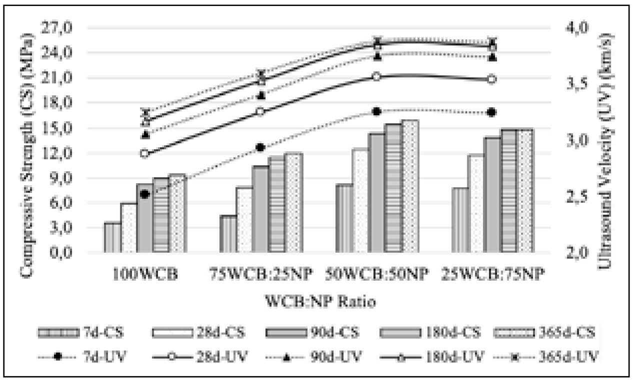

Figure 4. Effect of the WCB: NP ratio on the UV and CS of the samples.

WCB: Waste clay bricks; NP: Nevşehir pozzolan; UV: Ultrasound velocity; CS: Compressive strength.

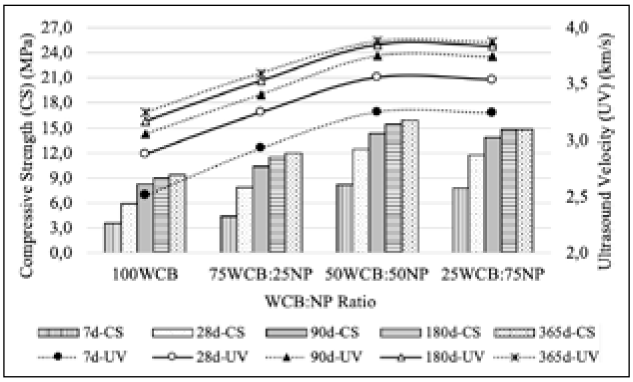

Figure 5. Effect of the WCB: MP ratio on the UV and CS of the samples.

3. RESULTS AND DISCUSSION

3.1. Effect of Mixing Ratios on Mechanical Properties

The effects of the change in the WCB: NP ratio on the UV and CS of the samples are shown in Figure 4.

The reference sample's 7- and 28-day UVs (100WCB) were 2.51 and 2.88 km/s, and the CSs were 3.61 and 5.92 MPa, respectively. The mechanical properties increased as the curing period increased. However, the effect of the long-term curing period on the properties was discussed in the next section. The lower CS of the reference sample at 7 and 28 days revealed that the reference sample was not sufficient to provide high strength when cured at room temperature. Similar to this finding, Migunthanna et al. [21] found the 7- and 28-day CSs of WCB-based mortar activated with only solid SS to be 3.3 and 5.4 MPa, respectively. Although the same aluminosilicate precursor (WCB) type was used, the CS was lower than the values obtained in this study. This may be due to the use of NaOH in addition to SS as an alkali activator. Similarly, Zawrah et al. [9], Tuyan et al. [11], and Robayo-Salazar et al. [34] found that WCB-based two-part alkali-activated mortars activated with SS and NaOH had low CS in the early period under ambient conditions. Because of the low degree of reaction of WCB under ambient conditions [11], the limitations in mechanical properties may be addressed by increasing the curing temperature [12]. However, in this study, only ambient curing was applied, considering that curing at high temperatures increases energy consumption in the production process.

By adding NP to the reference sample, enhanced mechanical properties were obtained in the early period. According to Figure 4, due to substituting WCB with 25% NP, the 7- and 28-day UVs increased to 1.17 and 1.13 times their original value, and the CSs increased to 1.21 and 1.33 times their original value, respectively. The highest mechanical properties were achieved at 50% NP substitution. The 7- and 28-day UVs of the 50WCB:50NP sample increased by 1.29 and 1.23 times compared to the reference sample, reaching 3.25 and 3.56 km/s, respectively. The same samples' 7- and 28-day CS increased by 2.27 and 2.10 times, reaching 8.21 and 12.43 MPa, respectively. For alkali activation to occur to a high degree, the SiO_2, Al_2O_3, Fe_2O_3, and CaO content in the reaction medium must be sufficient. In particular, SiO_2 and Al_2O_3 are primary components that affect the formation of the three-dimensional amorphous network. Mixtures containing high amounts of amorphous SiO_2 and Al_2O_3 allow relatively higher mechanical properties because of the more complete alkali activation reactions consisting of three stages (dissolution, rearrangement, and polycondensation) [35]. The NP's total SiO_2 and Al_2O_3 content (95.77%) was higher than that of the WCB (75.16%). This means that when NP was added to the mixture, it increased the amounts of reactive components and made it easier for the reactions to progress. Thus, higher mechanical properties were achieved. On the other hand, the effect of increasing the NP ratio by more than 50% on strength development was negligible. Similarly, in the literature, when the FA content was more than 40% in WCB+FA-based one-part alkali-activated mortars [21] and more than 50% in two-part alkali-activated mortars [10], the strengths did not increase. Considering that NP has chemical composition properties similar to FA, these results are consistent with the findings of this study.

The effects of the change in the WCB: MP ratio on the UV and CS of the samples are shown in Figure 5.

Adding MP to the reference sample obtained the highest mechanical properties early. As a result of substituting WCB with 25% MP, the 7- and 28-day UVs increased by 1.24 and 1.16 times, and the CSs increased by 2.49 and 2.33 times, respectively. Gradually increasing the MP ratio to 50% and 75% increased mechanical properties. The highest mechanical properties were detected in the 25WCB:75MP sample. This sample's 7- and 28-day UVs increased by 1.37 and 1.28 times, compared with the reference sample's, reaching 3.44 and 3.70 km/s, respectively. The same sample's 7- and 28-day CSs increased by 4.12 and 3.64 times, reaching 14.88 and 21.58 MPa, respectively. In addition, the mechanical properties of WCB+MP-based samples were higher than those of WCB+NP-based samples at the same curing period. This result might be due to the high calcium-containing components in the MP. As shown in Table 1, WCB and NP contain only 8.76% and 0.33% CaO, respectively. MP, which includes 55.7% CaO, is a calcium-rich raw material. A three-dimensional amorphous sodium aluminosilicate hydrate (N-A-S-H) gel forms during alkali activation [1], and this gel gives the mortar its main properties. In this study, the SiO_2 and Al_2O_3 components required for forming

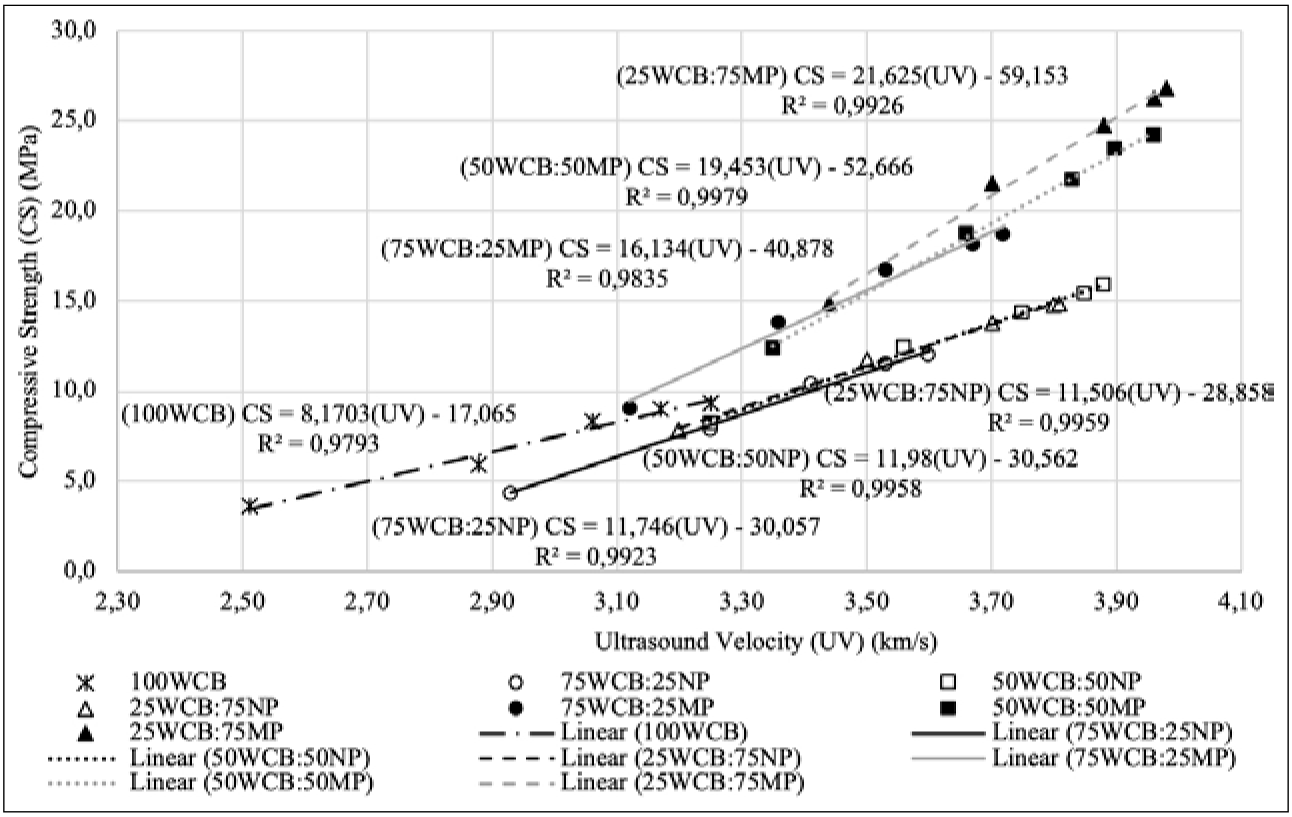

Figure 6. CS of WCB-based one-part alkali-activated mortars as a function of UV.

WCB: Waste clay bricks; NP: Nevşehir pozzolan; UV: Ultrasound velocity; CS: Compressive strength.

the N-A-S-H gel in WCB+MP-based samples were primarily supplied by WCB. During the polycondensation process, when calcium-rich components from MP were added to the reaction medium, Na+ ions in the N-A-S-H gel and dissolved Ca^{+2} ions were replaced, and a solid (N, C)-A-S-H gel was formed. In addition, a calcium silicate hydrate (C-S-H) gel was formed, similar to that in Portland cement. The coexistence of these gels within the aluminosilicate network resulted in higher strength development [9, 36, 37].

By measuring the UV of a material, the early reaction stages, the microstructure development, improvement of rheological properties, setting, hardening, strength development, and even durability properties can be successfully determined [38–40]. It is possible to state that materials with higher UV have a more compact microstructure, as no gaps, cracks, or damage would prevent sound from propagating through the material [41]. A more compact microstructure allows the production of materials with higher mechanical properties. Therefore, regardless of the curing period, the CS-UV relationship of the samples is shown in Figure 6. The lowest CS was determined in the reference sample, whereas the highest was in the 25WCB:75MP sample. All samples showed a similar trend in terms of the CS-UV relationship. The CS changed in direct proportion to the UV. Because the regression lines' correlation coefficients (R^2) were in the range of 0.97–0.99, the relationship between CS and UV was strong, indicating that CS of the one-part alkali-activated mortars could be estimated through UV. The Eq. (3) below represented the linear relationship between CS and UV:

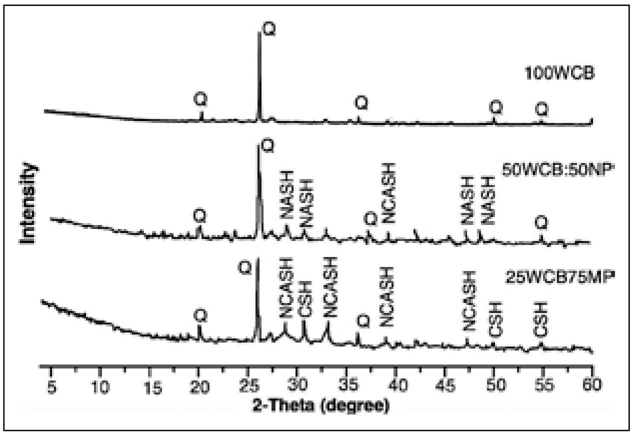

Figure 7. XRD results of one-part alkali-activated mortars.

XRD: X-Ray diffraction.

$$CS = a \times UV + b \tag{3}$$

The slope of the regression lines is referred to as the value "a."

The CS-UV relationship of the samples at each mixture ratio was expressed according to the following Eqs. (4–10):

$$(100WCB)\ CS = 8.17 \times UV - 17.06 \tag{4}$$

$$(75WCB{:}25NP)\ CS = 11.74 \times UV - 30.05 \tag{5}$$

$$(50WCB{:}50NP)\ CS = 11.98 \times UV - 30.56 \tag{6}$$

$$(25WCB{:}75NP)\ CS = 11.50 \times UV - 28.85 \tag{7}$$

$$(75WCB{:}25MP)\ CS = 16.13 \times UV - 40.87 \tag{8}$$

$$(50WCB{:}50MP)\ CS = 19.45 \times UV - 52.66 \tag{9}$$

$$(25WCB{:}75MP)\ CS = 21.62 \times UV - 59.15 \tag{10}$$

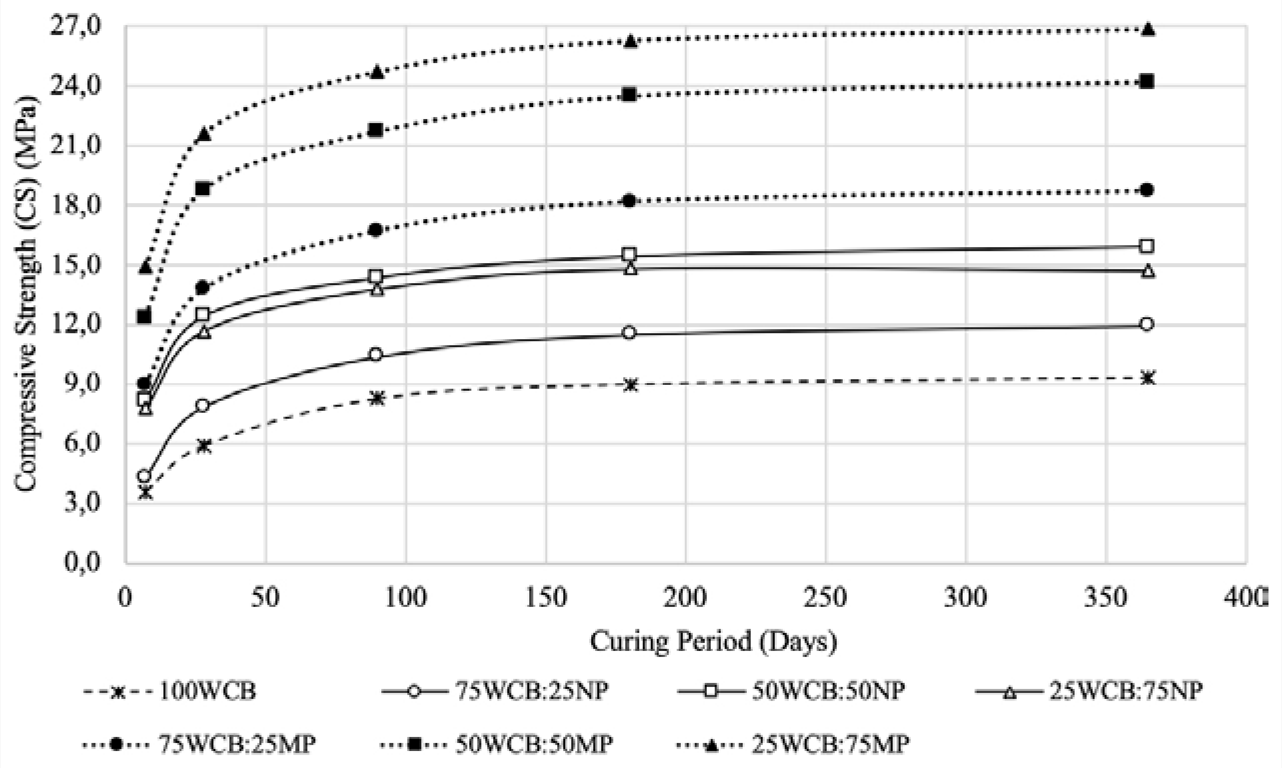

Figure 8. Effects of the curing period on the CS of the samples.

WCB: Waste clay bricks; NP: Nevşehir pozzolan; UV: Ultrasound velocity; CS: Compressive strength.

3.2. Effect of Mixing Ratios on Mineralogical Properties

Figure 7 shows the XRD results of the reference sample and the samples containing NP/MP with the highest mechanical properties (50WCB:50NP and 25WCB:75MP) after ambient curing for 28 days. Quartz mineral (Q) was the main crystalline phase in the reference sample. After alkali activation reactions, no new phase formation was observed. This might be because WCB had a relatively low reactivity, i.e., a low amorphous character, and the reactions could not develop sufficiently under ambient conditions. The low amorphous character of WCB was due to the bricks being allowed to cool slowly after calcination [11]. This finding obtained from the XRD analysis was parallel to the low mechanical properties exhibited by the reference sample after a 28-day curing period under ambient conditions.

The XRD pattern of geopolymer mortars containing various amounts of NP and MP had a similar XRD pattern to the reference sample; however, new amorphous and semi-crystalline phases were present. After the alkali activation of 50WCB:50NP, a mixture high in SiO_2 and Al_2O_3 formed an alkali three-dimensional amorphous aluminosilicate (N-A-S-H) gel called geopolymer gel. In addition, a sodium calcium aluminosilicate hydrate ((N, C)-A-S-H) phase at 2θ=39.8° was present in the mortar. These newly formed gel types provide a better-developed internal structure and, therefore, higher mechanical properties than the reference sample. On the other hand, hydration products in the 25WCB:75MP sample are composed of semi-crystalline phases of calcium silicate hydrate (C-S-H), which have intense peaks centered around 2θ=32.2°, 50.1°, and 55.1°, and (N, C)-A-S-H in amorphous geopolymer structure. This semi-crystalline phase improved the mechanical properties of the mortar by serving as nucleation sites for the development and accumulation of the amorphous geopolymer products [37]. In other words, the coexistence of both gel phases within the same network structure promoted alkali activation and ensured the internal structure development with higher CS of the mortar.

3.3. Effect of Curing Period

The effects of the curing period on the CS of the samples are given in Figure 8.

A tendency to increase in the CS of all samples was observed as the curing period increased. The highest slope of the curve, between 7 and 28 days, indicated that the mortar structure developed rapidly during the early period. During the early curing period, reactions occurred rapidly because the raw materials, water, and sufficient ambient temperature required for alkali activation were present in the mortar. The three-dimensional amorphous network structure produced as a result of the reactions enabled the filling of the voids in the mortar, the development of a more compact internal structure, and thus a rapid increase in mechanical properties [42]. The slope of the CS-curing period curve of the reference sample was relatively low, leading to slower strength development. The fastest strength development in the early period was detected in samples containing WCB and MP. The 25WCB:75MP samples showed the highest UV (3.44 km/s) and

CS (14.88 MPa) after 7 days. These properties improved quickly over time; therefore, the samples retained their highest mechanical properties during the subsequent curing periods. In other words, the development of alkali activation in the first 7 days later contributed to the material's performance.

On the other hand, regardless of the mixing ratio, the increase in CS of all samples decreased gradually starting from the 90th day and tended to remain constant, especially after the 180th day. In particular, the rate of increase between 90 and 365 days was negligible compared with the growth rate between 7 and 90 days. This finding could be attributed to the fact that the reaction products (both the (N, C)-A-S-H and C-S-H gels) that occurred during the early curing period have already filled the voids of the one-part alkali-activated mortar structure, causing the mortar structure to become more compact. The tendency for mechanical properties to remain constant in the later curing period is also compatible with the results of other experimental research in the literature. The strength increment of FA-based one-part AAM between 180 and 365 days was also stated as "negligible" by Haruna et al. [42].

The production of geopolymers from WCB, NP, and MP wastes would lower the cost of storing these wastes, the land demand required for storage, and the requirement for raw materials. Lowering the demand for raw materials would help to decrease greenhouse gas emissions and energy requirements. In addition, using these wastes to synthesize one-part alkali-activated mortars makes them a more environmentally friendly alternative to the traditional ones. The results of this experimental study demonstrate that WCB, NP, and MP wastes can be efficiently used to produce one-part alkali-activated mortars at the laboratory scale. However, the potential challenges for large-scale implementation should be identified to make the one-part alkali-activated mortars available in real-world industrial applications. For instance, the continuity of the waste raw material sources must be ensured. With the use of raw materials on an industrial scale, there might be a shortage of these sources in the foreseeable future. Since the chemical composition of raw materials (SiO_2, Al_2O_3, Fe_2O_3, and CaO contents) significantly influences the development of geopolymerization reactions and the properties of the resulting product in both fresh and hardened states, raw materials with constant chemical composition should be used. It should be considered that the greater transportation distances of the source materials would reduce the environmental benefits of the one-part alkali-activated mortars. In addition, in laboratory-scale applications, mixture preparation, molding, and curing can be easily implemented. However, for this production process to be carried out on an industrial scale, equipment and labor requirements should be defined correctly, and practical application methods should be developed. The production cost of the material on an industrial scale could be another challenge due to the higher cost of alkali activators. Therefore, a detailed cost analysis of WCB-based one-part alkali-activated mortars is required.

4. CONCLUSION

It is possible to draw the following conclusions from the results:

- WCB, obtained as construction and demolition waste, is an aluminosilicate precursor that can produce one-part alkali-activated mortar.
- Solid sodium hydroxide and sodium metasilicate are activator types that can activate WCB-based one-part alkali-activated mortars.
- The early low strength of the WCB-based mortar can be increased by substituting SiO_2- and Al_2O_3-rich NP waste or CaO-rich MP waste with the mortar composition.
- The optimum NP substitution content is 50%, which enhances the development of the reaction, allows the production of mortar with a more compact microstructure, and thus provides higher mechanical properties. Adding NP above this content is insufficient to enhance the properties.
- The highest mechanical properties are obtained in the mortar containing 25% WCB and 75% MP, possibly because this mortar is rich in SiO_2, Al_2O_3, and CaO components.
- WCB+NP-based samples have a three-dimensional amorphous sodium aluminosilicate hydrate gel structure. In addition to this gel structure, calcium silicate hydrate gel in the WCB+MP-based samples enables higher mechanical properties.
- The CS and the UV of WCB-based one-part alkali-activated mortars exhibit a directly proportional relationship.
- The mechanical properties of the samples increase with the curing period. The rate of increase is exceptionally high in the first 28-day curing period. However, the growth rate between 90 and 365 days is negligible compared to that in the early period.
- One-part alkali-activated mortar composed of WCB, NP, and MP may assist in overcoming the waste problem that occurs during urban transformation by making cost-effective use of existing raw materials and minimizing environmental damage.
- Although experimental study findings provide promising data on the production of WCB-based one-part alkali-activated mortars at the laboratory scale, the potential challenges for industrial-scale production, such as the continuity of these wastes, the consistency of chemical composition of the raw materials, greater transportation distances, higher costs of alkali materials, and the stages of mixture preparation, molding, and curing, should be taken into consideration.
- Apart from the WCB, NP, and MP used in this research, the possibility of using other waste types with similar chemical compositions to produce one-part alkali-activated mortar should be explored. Additionally, the durability properties of the material, such as under freezing-thawing, wetting-drying, and high-temperature effects, should be determined in future studies. In addition, detailed economic analyses should be carried out to develop practical solutions for mixing and curing conditions for industrial-scale applications and to use the material economically under Turkish conditions.

ACKNOWLEDGMENTS

The author expresses her gratitude to Akçansa Çimento A.S. for grinding raw materials and Ytong Sanayi A.S. for the supply of standard sand.

ETHICS

There are no ethical issues with the publication of this manuscript.

DATA AVAILABILITY STATEMENT

The author confirm that the data that supports the findings of this study are available within the article. Raw data that support the finding of this study are available from the corresponding author, upon reasonable request.

CONFLICT OF INTEREST

The author declare that they have no conflict of interest.

FINANCIAL DISCLOSURE

The author declared that this study has received no financial support.

USE OF AI FOR WRITING ASSISTANCE

Not declared.

PEER-REVIEW

Externally peer-reviewed.

REFERENCES

[1] Garcia-Lodeiro, I., Palomo, A., & Fernández-Jiménez, A. (2015). An overview of the chemistry of alkali-activated cement-based binders. In Labrincha, J. A., Leonelli, C., Palomo, A., & Chindaprasirt, P. (Eds.), *Handbook of Alkali-Activated Cements, Mortars, and Concretes*, Pacheco-Torgal, F. Woodhead Publishing Limited. [CrossRef]

[2] Migunthanna, J., Rajeev, P., & Sanjayan, J. (2022). Waste clay bricks as a geopolymer binder for pavement construction. *Sustainability, 14*, 6456. [CrossRef]

[3] Baronio, G., & Binda, L. (1997). Study of the pozzolanicity of some bricks and clays. *Constr Build Mater, 11*(1), 41-46. [CrossRef]

[4] Yang, Y., Lu, P., Shao, R., Zhao, Q., Yang, T., & Wu, C. (2024). A comprehensive review of multisource solid wastes in sustainable concrete: From material properties to engineering application. *Constr Build Mater, 435*, 136775. [CrossRef]

[5] Kravchenko, E., Lazorenko, G., Jiang, X., & Leng, Z. (2024). Alkali-activated materials made of construction and demolition waste as precursors: A review. *Sustain Mater Technol, 39*, e00829. [CrossRef]

[6] Resmî Gazete. Hafriyat toprağı, inşaat ve yıkıntı atıklarının kontrolü yönetmeliği. https://www.mevzuat.gov.tr/mevzuat?MevzuatNo=5401&MevzuatTur=7&MevzuatTertip=5

[7] Komnitsas, K., Zaharaki, D., Vlachou, A., Bartzas, G., & Galetakis, M. (2015). Effect of synthesis parameters on the quality of construction and demolition wastes (CDW) geopolymers. *Adv Powder Technol, 26*(2), 368-376. [CrossRef]

[8] Rakhimova, N. R., & Rakhimov, R. Z. (2015). Alkali-activated cements and mortars based on blast furnace slag and red clay brick waste. *Mater Des, 85*, 324-331. [CrossRef]

[9] Zawrah, M. F., Feltin, N., Docourtieux, S., & Gado, R. (2016). Recycling and utilization assessment of waste fired clay bricks (Grog) with granulated blast-furnace slag for geopolymer production. *Process Saf Environ Prot, 103*(A), 237-251. [CrossRef]

[10] Rovnaník, P., Řezník, B., & Rovnaníková, P. (2016). Blended alkali-activated fly ash / brick powder materials. *Procedia Eng, 151*, 108-113. [CrossRef]

[11] Tuyan, M., Andiç-Çakir, O., & Ramyar, K. (2018). Effect of alkali activator concentration and curing condition on strength and microstructure of waste clay brick powder-based geopolymer. *Compos Part B Eng, 135*, 242-252. [CrossRef]

[12] Silva, G., Castaneda, D., Kim, S., Castaneda, A., Bertolotti, B., Ortega-San-Martin, L., Nakamatsu, J., & Aguilar, R. (2019). Analysis of the production conditions of geopolymer matrices from natural pozzolana and fired clay brick wastes. *Constr Build Mater, 215*, 633-643. [CrossRef]

[13] Ulugöl, H., Kul, A., Gurkan, Y., Şahmaran, M., Aldemir, A., Figueira, D., & Ashour., A. (2021). Mechanical and microstructural characterization of geopolymers from assorted construction and demolition waste-based masonry and glass. *J Clean Prod, 280*(1), 124358. [CrossRef]

[14] Alakara, E. H. (2022). İnşaat yıkıntı atıklarından elde edilen atık tuğlaların geopolimer harçlarda kullanımının incelenmesi. *Gaziosmanpaşa Bilim Araşt Derg, 11*(3), 251-259.

[15] Pommer, V., Cerny, R., Keppert, M., & Vejmelkova, E. (2021). Alkali-activated waste ceramics: Importance of precursor particle size distribution. *Ceram Int, 47*(22), 31574-31582. [CrossRef]

[16] Liang, G., Luo, L., & Yao, W. (2022). Reusing waste red brick powder as partial mineral precursor in eco-friendly binders: Reaction kinetics, microstructure and life-cycle assessment. *Resour Conserv Recycl, 185*, 106523. [CrossRef]

[17] Maaze, M. R., & Shrivastava, S. (2024). Development and performance evaluation of recycled brick waste-based geopolymer brick for improved physcio-mechanical, brick-bond and durability properties. *J Build Eng, 97*, 110701. [CrossRef]

[18] Roy, A., & Sadiqul Islam, G. M. (2024). Geopolymer using different size fractions of recycled brick-based mixed demolition waste. *Cleaner Mater, 11*, 100224. [CrossRef]

[19] Wang, F., Zhai, J., Kan, E., Norkulov, B., Ding, Y., Yu., J., & Yu. K. (2024). Value-added recycling of waste brick powder and waste sand to develop eco-friendly engineered geopolymer composite. *Case Stud Constr Mater, 21*, e03590. [CrossRef]

[20] Borçato, A. G., Meeiros Jr, R. A., Thiesen, M. (2024). Incorporation of clay brick wastes and calcium hy-

droxide into geopolymers: Compressive strength, microstructure, and efflorescence. *J Build Eng, 88*, 109259. [CrossRef]

[21] Migunthanna, J., Rajeev, P., & Sanjayan, J. (2021). Investigation of waste clay brick as partial replacement of geopolymer binders for rigid pavement application. *Constr Build Mater, 305*, 124787. [CrossRef]

[22] Reig, L. (2013). Properties and microstructure of alkali-activated red clay brick waste. *Constr Build Mater, 43*, 98-106. [CrossRef]

[23] Pereira-de-Oliveira, L. A., Castro-Gomes, J. P., & Santos, P. M. S. (2012). The potential pozzolanic activity of glass and red-clay ceramic waste as cement mortars components. *Constr Build Mater, 31*, 197-203. [CrossRef]

[24] Turkish Standard Institution. (2008). *Tras, Ankara, Türkiye*. TS 25.

[25] Turkish Standard Institution. (2010). *Methods of Testing Cement - Part 6: Determination of Fineness, Ankara, Türkiye*. TS EN 196-6.

[26] Firdous, R., Stephan, D., & Djobo, J. N. Y. (2018). Natural pozzolan based geopolymers: A review on mechanical, microstructural and durability characteristics. *Constr Build Mater, 190*, 1251-1263. [CrossRef]

[27] Turkish Standard Institution. (2009). *Methods of Testing Cement - Part 1: Determination of Strength, Ankara, Türkiye*. TS EN 196-1.

[28] Liew, Y. M., Heah, C. Y., Mustafa, A. B. M., & Kamarudin, H. (2016). Structure and properties of clay-based geopolymer cements: A review. *Prog Mater Sci, 83*, 595-629. [CrossRef]

[29] Lahoti, M., Narang, P., Tan, K. H., & Yang, E. H. (2017). Mix design factors and strength prediction of metakaolin-based geopolymer. *Ceram Int, 43*(14), 11433-11441. [CrossRef]

[30] Sun, Z., & Vollpracht, A. (2018). Isothermal calorimetry and in-situ XRD study of the NaOH activated fly ash, metakaolin and slag. *Cem Concr Res, 103*, 110-122. [CrossRef]

[31] Turkish Standard Institution. (2009). *Natural Stone Test Methods - Determination of Sound Speed Propagation, Ankara, Türkiye*. TS EN 14579

[32] Bayless, D. (2016). *Statistical rejection of "bad" data-Chauvenet's Criterion*. Word Press.

[33] Akman, S. (1978). *Deney ve Ölçme Tekniğine Giriş, 1st Ed.*, ITU İnşaat Fakültesi Matbaası.

[34] Robayo-Salazar, R. A., Rivera, J. F., & Mejía de Gutiérrez, R. (2017). Alkali-activated building materials made with recycled construction and demolition wastes. *Constr Build Mater, 149*, 130-138. [CrossRef]

[35] Tchadjie, L. N., & Ekolu, S. O. (2018). Enhancing the reactivity of aluminosilicate materials toward geopolymer synthesis. *J Mater Sci, 53*, 4709-4733. [CrossRef]

[36] Nath, P., & Sarker, P. K. (2014). Effect of GGBFS on setting, workability and early strength properties of fly ash geopolymer concrete cured in ambient condition. *Constr Build Mater, 66*, 163-171. [CrossRef]

[37] Yip, C. K., Lukey, G. C., Provis, J. L., & van Deventer, J. S. J. (2008). Effect of calcium silicate sources on geopolymerization. *Cem Concr Res, 38*(4), 554-564. [CrossRef]

[38] Chen, W., Li, Y., Shen, P., & Shui, Z. (2013). Microstructural development of hydrating Portland cement paste at early ages investigated with non-destructive methods and numerical simulation. *J Nondestruct Eval, 32*, 228-237. [CrossRef]

[39] Azarsa, P., & Gupta, R. (2017). Electrical resistivity of concrete for durability evaluation: A review. *Adv Mater Sci Eng, 2017*, 8453095. [CrossRef]

[40] Dai, X., Aydin, S., Yardimci, M. Y., Lesage, K., & Schutter, G. (2022). Early age reaction, rheological properties and pore solution chemistry of NaOH-activated slag mixtures. *Cem Concr Compos, 133*, 104715. [CrossRef]

[41] Postacığlu, B. (1981). *Cisimlerin Yapısı ve Özellikleri: İç Yapı ve Mekanik Özellikler. 1st Ed.* ITU İnşaat Fakültesi Matbaası.

[42] Haruna, S., Mohammed, B. S., Wahab, M. M. A., Kankia, M. U., Amran, M., & Gora, A. M. (2021). Long-term strength development of fly ash-based one-part alkali-activated binders. *Mater, 14*(15), 4160. [CrossRef]

J Sustain Const Mater Technol, Vol. 9, Issue. 4, pp. 402–411, December 2024

Journal of Sustainable Construction Materials and Technologies
Web page info: https://jscmt.yildiz.edu.tr
DOI: 10.47481/jscmt.1607515

Journal of Sustainable Construction Materials and Technologies

Research Article

Clustering analysis of compressive strength of structural recycled aggregate concrete

Hasan DİLBAS[1], Mehmet Şamil GÜNEŞ*[2]

[1]*Department of Civil Engineering, Yüzüncü Yıl University Faculty of Engineering, Van, Türkiye*
[2]*Department of Statistics, Yıldız Technical University Faculty of Arts and Sciences, İstanbul, Türkiye*

ARTICLE INFO

Article history
Received: 31 May 2024
Revised: 17 December 2024
Accepted: 20 December 2024

Key words:
Absolute volume method, clustering, equivalent mortar volume method, recycled aggregate, silica fume

ABSTRACT

Clustering analysis primarily highlights the inhomogeneity of data and can be utilized in structural engineering to demonstrate strength irregularity. It is well-known that strength irregularity between neighboring floors within a structure or among structural elements can lead to non-holistic behavior. Therefore, the clustering of compressive strength holds significant importance. Despite the relevance, only a few studies have addressed the clustering of compressive strength in recycled aggregate concrete (RAC) and proposed potential solutions for clustering issues. This paper aims to investigate the clustering of compressive strength in RAC and explore viable solutions. In this experimental study, four concrete groups were produced under standard conditions. The first group included natural aggregate concretes (NAC) designed with the Absolute Volume Method (AVM) as control concretes. The second group, comprised of RAC, was designed with the equivalent mortar volume method (EVM) as the control RAC. The third group consisted of RAC treated with silica fume (SF) and designed using AVM, while the fourth group included RAC designed with EVM. Statistical analyses were conducted on the 28-day compressive strength test results. The results indicated that the strength class of compressive strength clusters varied among the four groups. The clustering of test results was influenced by the type of concrete components used and the design method employed. Additionally, using silica fume and adopting the Absolute Volume Method reduced strength fluctuation and regulated the strength class of clusters by bringing them closer together. In contrast, the Equivalent Mortar Volume Method resulted in a greater dispersion of strength classes. The clustering effect of recycled aggregate (RA) was more pronounced than that of natural aggregate (NA). Given these findings, it is essential to implement measures when utilizing RAC in sustainable structures to address potential clustering issues.

Cite this article as: Dilbas, H., & Güneş, M. Ş. (2024). Clustering analysis of compressive strength of structural recycled aggregate concrete. *J Sustain Const Mater Technol*, 9(4), 402–411.

1. INTRODUCTION

Evaluation of experimental results is a crucial aspect of engineering structures, with guidelines for evaluation typically well-defined in relevant codes and regulations [1–4]. Material quality control is essential for structural integrity, particularly for large structures such as dams, reinforced concrete buildings, and airport aprons. Quality control must be conducted for each unit of concrete production, as mandated by codes, and it is imperative to evaluate all data for each structural unit statistically. This approach, required by standards such as TS EN 206-1, minimizes human er-

---

***Corresponding author.**
*E-mail address: msgunes@yildiz.edu.tr

Published by Yıldız Technical University Press, İstanbul, Türkiye

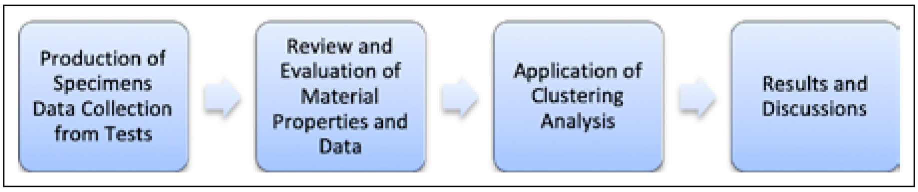

Figure 1. Flowchart of the study.

rors and enhances societal safety. The statistical evaluation of concrete compressive strength is a well-documented subject in the literature [5–8], with many studies employing main statistical parameters (mean, standard deviation, etc.) and distribution functions [6, 7, 9]. The normal distribution function is commonly used and deemed suitable for assessing concrete compressive strength [6, 7, 10, 11]. Typically, statistical evaluations are based on compressive strength test data, observing population behavior through fitting distribution functions. However, clustering within test results can also occur, even when population properties are consistent across groups. Therefore, it is essential to evaluate both the overall data properties and the cluster-specific properties within the big data set.

Clustering analysis is a statistical method that highlights data inhomogeneity and can be a valuable tool in structural engineering for assessing strength irregularity in experimental data. Strength irregularity between neighboring floors or structural elements can lead to non-holistic behavior, affecting soft-story irregularity in concrete structures controlled by national codes. Consequently, the clustering of compressive strength impacts both material and structural behavior, making it a critical area of study. While research on the clustering of experimental results in conventional concrete (NAC) exists [12], this subject has not been extensively studied for recycled aggregate concrete (RAC). For instance, Kılınçarslan et al. [12] investigated the clustering of strengths in concrete with various aggregate types, finding different clustering behaviors across aggregate types, with compressive strengths ranging from 40 to 55 MPa and specific mean strengths for each cluster. The findings highlighted the relationship between aggregate mechanical strength and the clustering behavior of concrete properties. In structural engineering, all concrete or reinforced concrete structure elements are desired to exhibit uniform strength classes. Structural element strength variation can lead to inadequate load-bearing capacity and issues such as soft floors, adversely affecting structural performance under lateral loads like earthquakes. Therefore, it is essential to consider clustering in compressive strength data alongside comprehensive statistical analysis when constructing buildings with concrete of the same strength class. The reuse and recycling of materials, including RAC, are encouraged within the sustainability concept. However, proper clustering analysis is necessary to address potential soft floor issues due to strength fluctuation in RAC structures, and possible solutions must be evaluated. Sustainable buildings incorporating RAC are gaining attention, with green buildings expected to become more prevalent globally.

Table 1. Properties of binders

Contents	SF	Cement
Fe_2O_3 (%)	1.66	3.4
Al_2O_3 (%)	0.72	4.8
SiO_2 (%)	91.42	18.9
SO_3 (%)	0.37	3.42
CaO (%)	0.52	64.7
K_2O (%)	1.21	0.4
MgO (%)	0.92	1.4
Na_2O (%)	0.38	0.7
Density (g/cm^3)	0.642	3.11
Loss on ignition (%)	1.72	1.82
Chlorine ratio (%)	0.04	0.0241
Activity index (%)	118	–
Specific surface area (m^2/kg)	21290	3840

SF: Silica fume.

This paper aims to investigate RAC behavior and the implications of its use. Few studies have focused on the clustering of concrete compressive strength and potential clustering problems. Clustering compressive strength data in concrete with various components can result in soft floors and fluctuating strength distribution in reinforced concrete structures. Typically, concrete structures are assumed to have uniform properties, but research indicates that various factors influence compressive strength and clustering. This study investigated clustering in RAC and potential solutions, producing four concrete groups under standard laboratory conditions. Each group consisted of 30 specimens, cured in water at standard temperature and subjected to compressive strength testing at 28 days, yielding 120 test results. Statistical analyses were performed on the data.

2. MATERIALS AND METHODS

This paper employed different concrete components and mixing methods to support the paper's hypothesis. The general methodological flow of the study is given in Figure 1. The production of the specimens and data collection from the conducted compressive strength tests was the first stage of the study. Materials were prepared to mix, and workability regulations of the concretes were made. Then, the tests were conducted. The data collected from the experiments were reviewed and evaluated. In this stage, the data were corrected and assessed using the literature. This stage can be named as validation part of this paper. Then,

Table 2. Aggregate types and their properties

Notation	Size, mm	LA abrasion value, %	Residual content, %	Density, g/cm^3	Water absorption, %
Sand	0–4	–	–	2.81	1.31
NA	11.2–22.4	24	–	2.70	0.75
	4–11.2	–	–	2.73	0.72
RA	11.2–22.4	55	52.5	2.00	8.95
	4–11.2	–	39.2	2.06	8.80

RA: Recycled aggregate; NA: Natural aggregate; LA abrasion: Los Angeles abrasion test.

the data was used in clustering analysis, and the clusters of the compressive strengths of four concrete groups were obtained. In the last stage of the paper, the results were figured out, presented, and discussed.

2.1. Materials

CEM I 42.5R cement, which conforms to the specifications of TS EN 197-1 (2012), was utilized in the mixtures for general purposes. The characteristics of the binders employed in this study, including silica fume (SF) and cement, are presented in Table 1. CEM I cement was selected primarily due to its widespread usage and high regional prevalence. Consequently, a commonly utilized cement was chosen over a material with more specific applications.

The concrete mixes employed two coarse aggregates: natural gravel and recycled coarse aggregate. The granulometry of the aggregates remained unchanged and was consistent across all concrete mixtures. Calcareous natural aggregate and sand were used in the fresh mixes, as detailed in Table 2. A superplasticizer (SP) with a polycarboxylate ether base was incorporated to enhance the flowability of the concretes, thereby improving low workability, as outlined in Table 3. The S2 slump class, by TS EN 206-1 (2002), was utilized for all mixes to facilitate ease of production and mold placement. It is well-known that plasticizers reduce the pore content in fresh concrete, resulting in a more compact medium. The recycled aggregate originated from concrete waste, precisely elements of reinforced concrete structures. The compressive strength of the recycled aggregate source was less than 20 MPa, classifying it as low strength.

2.2. Concrete Design Method, Mixing, Curation and Testing

In the laboratory, fresh concrete mixes were prepared using a constant cement dosage and water-to-binder ratio, aiming for a target strength of C30/37 (Table 4). The mixing methods employed were the Equivalent Mortar Volume Method (EVM) and the Absolute Volume Method (AVM) by TS 802 (Table 5). The AVM is a widely adopted method recognized in concrete standards such as TS 802, ACI 211, and IS 10262. Additionally, the EVM, a mix design procedure proposed in the literature on recycled aggregate concrete, has demonstrated satisfactory results. Therefore, this study compares these methods and examines their performance.

Table 3. The properties of SP

Content	SP
Structure of material	Polycarboxylic ether
Alkaline ratio (%)	<3
Chlorine ratio (%)	<0.1
Density (kg/l)	1.08–1.14
Color	Amber

SP: Superplasticizer.

Table 4. Components of concrete series

Components	NAC	RAC	RAC.SF	RAC.EVM
Water, kg/m^3	163	163	163	123
Cement, kg/m^3	340	340	323	255
SP, %	0.75	0.85	0.95	1.55
SF, kg/m^3	–	–	17	–
Sand, kg/m^3	806	806	806	608
NA (11–22.4 mm), kg/m^3	775	–	–	–
NA (4–11.2 mm), kg/m^3	392	–	–	–
RA (11–22.4 mm), kg/m^3	–	574	574	774
RA (4–11.2) mm), kg/m^3	–	296	296	368

NAC: Natural aggregate concrete; RAC: Recycled aggregate concrete; SF: Silica fume; EVM: Equivalent mortar volume.

Table 5. Compressive strength results in concrete

Components	RAC.EVM	RAC	RAC.SF	NAC
Average compressive strength	51.89	39.20	42.44	44.12
Std. deviation of compressive strength	3.95	2.52	1.49	2.63
Minimum compressive strength	45.55	28.37	34.48	36.55

NAC: Natural aggregate concrete; RAC: Recycled aggregate concrete; SF: Silica fume; EVM: Equivalent mortar volume.

The AVM requires that a unit volume of concrete includes concrete components in specific proportions for each strength class, as described in Equation 1. The primary components of concrete are cement, water, and aggregate, among others [13].

$$V_1 m^3 = V_{agg} + V_{cem} + V_w + V_{ch} + V_{air} \tag{1}$$

Here, V_{ch} is the volume of chemicals, V_{cem} is the volume of cement, V_{agg} is the volume of aggregate, V_w is the volume of water, and V_{air} is the volume of air in concrete.

In the Absolute Volume Method (AVM), as defined by TS 802, the initial step involves determining the quantity of binding materials. During this stage, parameters such as water and water-to-binder ratios are established. Typically, the material content that occupies one cubic meter of volume is calculated as the unit volume of concrete. Subsequently, the determined material volumes (e.g., cement, water) are subtracted through a reverse calculation process from the unit volume (1 m^3).

Conversely, the Equivalent Mortar Volume Method (EVM) requires that recycled aggregate concrete (RAC) and natural aggregate concrete (NAC) maintain a specific proportion of total mortar volume to natural gravel. The objective is to achieve a consistent aggregate volume in the mixture for both RAC and NAC. The amount of mortar present in recycled aggregate (RA) is a critical factor and must be quantified [14, 15] (Table 2). The mortar content in RA is dissolved using a 0.1 M HCl solution, leaving behind coarse natural aggregate. Consequently, the mortar volume is incorporated into the new mortar content of the fresh mixture, and the remaining portion is considered part of the aggregate volume. Thus, a portion of the calculated mortar and aggregate volumes in the mix is supplied by RA, with the remaining volume being added to the mixtures.

EVM required the constant volume of aggregate, and the volume was calculated as (Eq.3) [16]:

$$V_{RCA}^{RCA-concrete} = \frac{V_{NA}^{NAC} \times (1-R)}{(1-RMC) \times \frac{SG_b^{RCA}}{SG_b^{OVA}}} \tag{2}$$

Here, RMC is the residual mortar content of RA, V_{NA}^{NAC} is the volume ratio of fresh NA in control concrete, $V_{RCA}^{RCA\text{-}concrete}$ is the volume ratio of coarse aggregate in RAC, SG_b^{OVA} and SG_b^{RCA} is original virgin aggregate, and the bulk specific gravity of RA, respectively, and R is the volume fraction of fresh NA content of RAC to fresh NA content of control concrete.

Fresh concrete was cast properly and molded (ASTM C192/C192M–13a (2013)). The vibration was also employed to settle the fresh concrete into the molds. 15 cm cube specimens were produced. The total number of specimens for each series was 30, cured in 22 ∓ 2 °C water. The curing process was applied to the specimens for 28 days. The concrete specimens (28 days old) were applied to the tests, and a 3000 kN compression machine was used to perform the compressive strength test according to TS EN 12390-3 (2010) (Table 5).

According to TS 500 (Requirements for design and construction of reinforced concrete structures), the compressive strength of concrete was determined by a 90% confidence interval. However, in this research, the opposite of TS 500, a 95% confidence interval, was considered to increase the accuracy. The strength class is NAC, RAC, and RAC.SF and RAC.EVM was found by using Eq. 3-4 (TS EN 206):

$$f_{c,\,avg} \geq f_{ck} + 1.96\,\sigma \tag{3}$$
$$f_{c,\,min} \geq f_{ck} - 4.0 \tag{4}$$

Here, $f_{c,\,min}$, and σ are the min. comp. Strength (MPa) and standard deviation, respectively, $f_{c\ avg}$ and f_{ck} are the mean and characteristic compressive strengths (MPa).

2.3. Evaluation of Test Data by Statistical Methods

This study investigated the natural cluster structure of various concrete types using Hierarchical Cluster Analysis (HCA). The clusters were naturally determined, and their accuracy was verified with k-means clustering. Cluster analysis revealed the topography of the measured data, allowing the identification of possible scatter in the strength waves of the concrete clusters. Consequently, changes in the strength class within the measured data of the clusters can be readily calculated—notably, NAC, RAC, and RAC. SF was naturally divided into two clusters each, while RAC. EMV was split into three clusters. The movement of concrete units between clusters was determined using diagonal dendrograms, and the data structure was examined by visualizing the clustering results with dendrograms, which also illustrated the branches of the clusters. The statistical significance of the relationships between clusters obtained from HCA results was assessed using the Chi-square test, providing an overview of the study data's general characteristics. This approach offers insights into the similarity of concrete components concerning strength classes.

Additionally, a structure called a tanglegram, using mutual dendrograms was discussed and employed as a method of classification and comparison. Therefore, the classification and comparison of the results were performed using tanglegrams. The primary advantage of this system is the cross-examination of movements between concrete units, which form the characteristics of the strength classes. Comparisons with the control indicated the direction in which the strength classes moved across different concrete types. One critical factor influenced by this method was the sample size; increasing the number of samples allows for a more detailed examination of the strength class movements. Clustering methods were applied to concrete groups based on their general structure, while Chi-square analysis was used to measure the statistical significance of these groups. All statistical analyses were conducted using R statistical software [17].

2.3.1. Hierarchical Cluster Analysis

Hierarchical Cluster Analysis (HCA) is a statistical method used to partition data into clusters based on the similarities among data points. The primary objective of cluster analysis is to ensure heterogeneity between clusters and homogeneity within clusters. The cluster analysis results are visualized using dendrograms, illustrating the hierarchical relationships among objects [18]. This study's data set was segmented into clusters using the centroid linkage algorithm and Euclidean distance. The centroid linkage method, one of the algorithms in HCA, relies on the means of observations that form the cluster [19]. In addition to HCA, k-means clustering analysis was performed, and the resulting groupings were consistent with those obtained through HCA. Euclidean distance (d):

$$d_{ij} = \sqrt{\sum_{m=1}^{M} (X_{im} - X_{jm})^2} \tag{5}$$

where the sum is extended over the M variables which characterize each pair of objects i and j. The central concept of the centroid linkage technique is to consider the distance between the centroids of the data points in clusters. The equation for the centroid-based linkage approach is below (Centroid of a finite set of k points x1, x2, x3, …, xn).

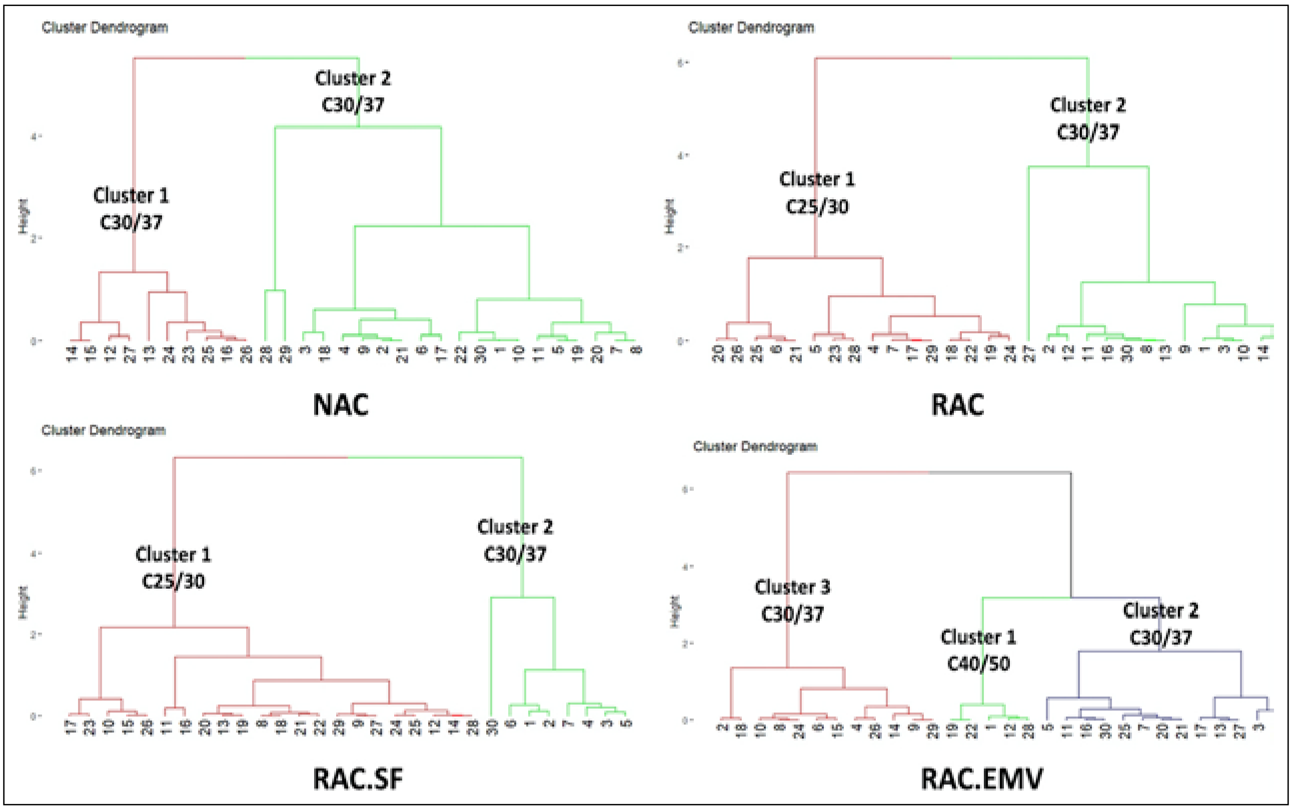

Figure 2. Hierarchical cluster analysis results (dendrograms).

$$C = \frac{x1 + x2 + x3 + \ldots\ldots X_n}{k} \tag{6}$$

2.3.2. Chi-Square Analysis

The Chi-square test was one of the most widely used tests among nonparametric tests in different application areas. The two most commonly used chi-square methods were tests of independence and tests of goodness. The Chi-square independence test was used to examine the relationship between categorical variables in the study. The chi-square distribution was often used to test two independent qualitative criteria. The null hypothesis (H0) states that the two criteria were independent; the research (alternate) hypothesis (HA) stated that there was a relationship between the two criteria [20].

3. RESULTS AND DISCUSSIONS

3.1. Compressive Strength Class of Concretes

The results showed that C30/37 was achieved for RAC.SF and only (Table 6). RAC.EVM has C35/45, and the result of RAC was determined as C25/30. The results presented the influence of the components and considered mixing methods. RA's weak properties (i.e., high water absorption ratio) affected the properties of concrete, decreasing the strengths (i.e., compressive strength) [21–27]. RA adhered to an old mortar (AOM) part in its body, and AOM was the key to opening the negative impact door in concrete. Hence, AOM decreased compressive strength. A question that comes to mind is: How is AOM affected? AOM with a porous structure was the response [28]. However, considering a mineral addition (i.e., SF) in the mix design may treat the strengths, increasing the compressive strength. The treatment steps of SF may be causing an additional C-S-H gel, reducing free calcium hydroxide content and filling/closing pores [29-30]. Besides, EMV responded significantly to the strengths and increased the strength and the strength class [14]. Here, the improvement of EMV may be caused by considering the aggregate concentration for RAC, which should be similar to that of NAC.

Table 6. Strength class of concretes

	RAC	NAC	RAC.SF	RAC.EVM
Strength class	C25/30	C30/37	C30/37	C35/45

NAC: Natural aggregate concrete; RAC: Recycled aggregate concrete; SF: Silica fume; EVM: Equivalent mortar volume.

3.2. Compressive Strength Class of Concretes

In this study, hierarchical cluster analysis (HCA) was applied to examine the natural structure of concretes, with visual results presented in Figure 2. This approach illustrated the strength class mapping of the measured data as clusters, facilitating comparing cluster results. Consequently, changes or constancies in strength classes could be observed, revealing the data's topology. Variations in strength within clusters can affect structural behavior under loads, particularly lateral loads such as those from earthquakes. Therefore, a detailed examination of the measured data was conducted to investigate the behavior of the concretes considered in this paper.

Table 7. Compression test results of concrete clusters

Concrete types	Cluster number	Mean of cluster
NAC	Cluster 1	42.829
	Cluster 2	46.691
RAC	Cluster 1	36.509
	Cluster 2	41.552
RAC.SF	Cluster 1	38.629
	Cluster 2	43.643
RAC.EMV	Cluster 1	57.77
	Cluster 2	53.235
	Cluster 3	47.987

NAC: Natural aggregate concrete; RAC: Recycled aggregate concrete; SF: Silica fume; EVM: Equivalent mortar volume.

Concrete strengths were classified into four groups. According to the cluster analysis results, NAC, RAC, and RAC.SF was naturally divided into two clusters each, while RAC.EMV was split into three clusters. Considering the homogeneity of bulk data, clustering data into subgroups may pose challenges. Ideally, a higher number of clusters would ensure a homogeneous distribution of units within the clusters, thereby achieving overall homogeneity in the data structure. The accuracy of the identified clusters was tested with k-means clustering, and the cluster means are provided in Table 7.

In the literature, Kılınçarslan et al. [12] conducted research on concrete with various aggregate types (trachybasalt (TB), sand and gravel (SG), limestone (L), recrystallized limestone (RL), dolomite (DO), and tephra–phonolite) to investigate clustering of strengths such as compressive strength, splitting tensile strength, and bending strength. They found that R-, L-, and SG-based concretes formed one cluster, DO- and TB-based concretes formed three clusters, and TB-based concrete formed two clusters in the test results [12]. It was reported that concretes with compressive strengths ranging from 40 to 55 MPa were obtained, with L-based concrete exhibiting a mean compressive strength of 44.26 MPa within one cluster [12]. Furthermore, the mechanical strength of aggregate and the clustering behavior of concrete properties (e.g., compressive strength) were correlated [12]. Thus, it can be inferred that RA, with lower properties than NA, may alter clustering, as evidenced by the test results. The concrete mixing process was another factor influencing clustering (Table 7).

Based on the analysis results from hierarchical cluster analysis and descriptive statistical analysis, the strength classes of the concretes were determined and categorized as lower (<20 MPa), medium (20-40 MPa), and high (>40 MPa). According to the dendrograms (Fig. 2), the clusters of concretes generally fell within the medium strength class (C30/37). However, each group exhibited distinct strength classes due to mixing method and mineral treatment variations. For instance, RAC was divided into two clusters, each corresponding to C25/30 and C30/37 strength classes, highlighting the dominant effect of RA when compared to NAC. A similar behavior was observed for RAC.SF, with each cluster also corresponding to C25/30 and C30/37 strength classes. Conversely, RAC.EMV exhibited a unique structure, where the first cluster fell within the high-strength class, and the remaining clusters were within the medium-strength class. These results suggest extensive data on the compressive strength of RAC.SF, and RAC.EMV should be thoroughly analyzed. Furthermore, the findings indicate that clustering may induce a soft floor in reinforced concrete structures and create structural elements with fluctuating strength distributions if concrete designed with RA is used.

Tanglegrams (Fig. 3) were employed to visualize the cluster structure of concretes. The graphs in Figure 3 were constructed based on the displacement of concrete units between clusters. A Tanglegram consists of a pair of dendrograms on the same set of lines, with corresponding lines in the two dendrograms connected by an edge. This allows a visual comparison of dendrograms obtained from different algorithms or experiments by linking data labels with edges. In Figure 3, the displacement of concrete units within the strength classes was analyzed. For example, upon comparison, concrete units 28 and 29, initially in cluster 2 of NAC, were found in cluster 1 of RAC. It was observed that these units shifted from the C30/37 strength class (NAC, Cluster 1) to the C25/30 strength class (RAC, Cluster 1), suggesting that the use of RA contributed to the reduction in strength class results. Another comparison involved NAC and RAC.SF. A significant shift in concrete units' location within cluster and strength classes was noted. The decrease in strength class was anticipated due to the presence of RA in RAC.SF, while the increase in strength class was attributed to adding SF.

When comparing NAC and RAC.EMV tanglegrams, it was notable that most concrete units shifted from the medium strength class (C30/37) to the high strength class (C40/50). Concrete units 28, 1, and 22, initially in NAC (Cluster 2) within the medium strength class (C30/37), moved to the high strength class when compared with RAC.EMV. This shift can be explained by the EMV design, which aims to maintain a consistent NA ratio in the total volume of RAC, providing strength through NA, which serves as a framework in concrete [8]. As a result, the decreases in strength observed in RAC were not present.EMV. However, the natural aggregate structure in RA is believed to play a role in the strength increase [28].

This study clustered concrete strengths using Euclidean distance and the central neighborhood algorithm. The accuracy of the hierarchical cluster analysis results was verified using k-means clustering. Based on the tanglegram results, a high cluster and strength class shift rate was observed between the control group (NAC) and other concrete groups (RAC, RAC.SF, and RAC.EMV).

The null hypothesis (H0) stated that the two criteria were independent. In this paper, all relationships were significant for the Chi-square hypothesis (Table 8). The significance of cluster changes was assessed using the Chi-

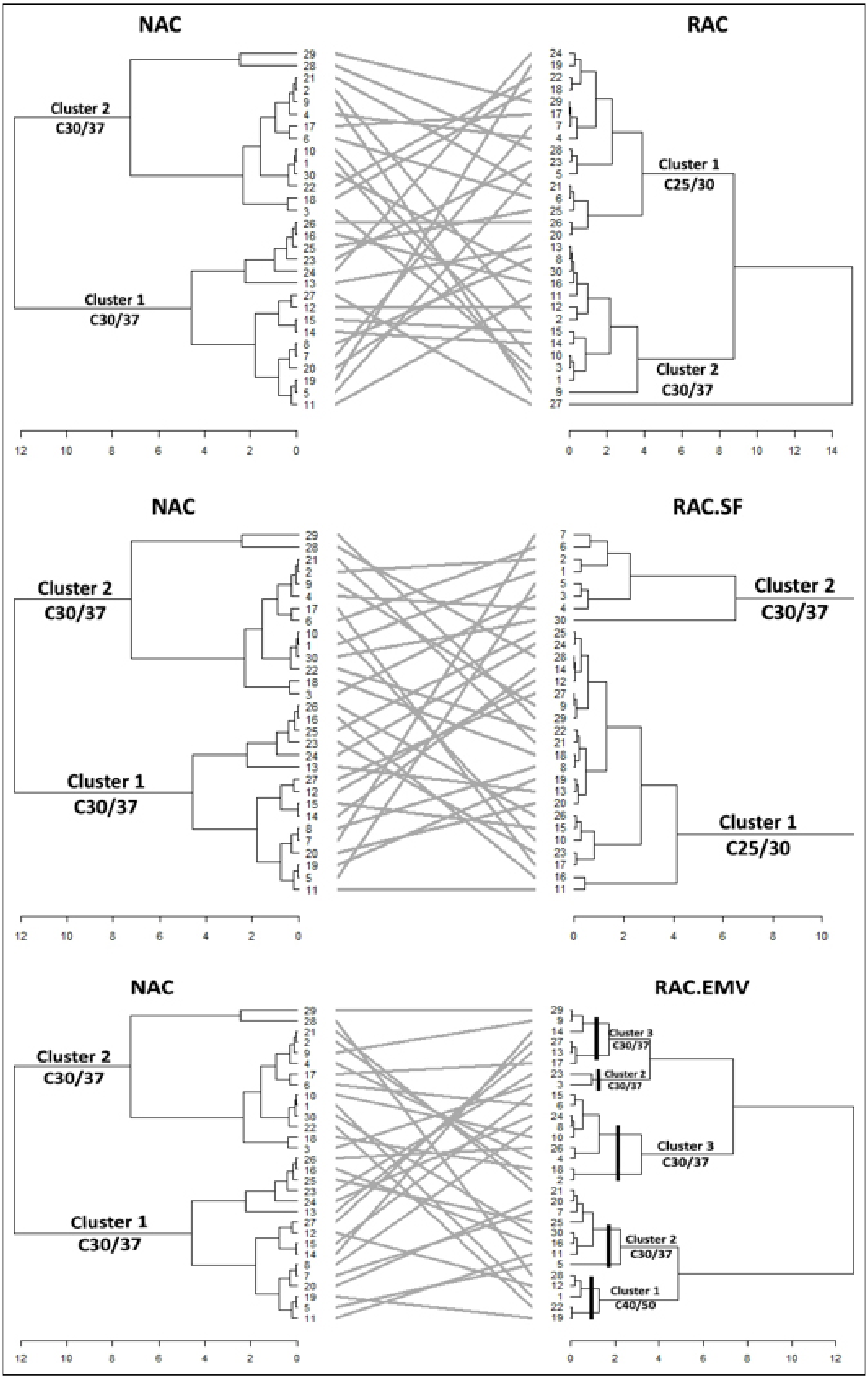

Figure 3. Comparisons of Hierarchical Cluster Analysis results with tanglegrams.

Table 8. Chi-square analysis results according to hierarchical cluster analysis

Variable relationships	Value	df	AS (2-sided)	Results
NAC and RAC	13.125	1	0.000	NAC and RAC have a statistically significant relationship (reject at α=0.05 level).
NAC and RAC.SF	6.429	1	0.011	There is a statistically significant relationship between NAC and RAC.SF (reject at α=0.05 level).
NAC and RAC.EMV	19.165	2	0.000	There is a statistically significant relationship between NAC and RAC.EMV (reject at α=0.05 level).

AS: Asymptotic significance; NAC: Natural aggregate concrete; RAC: Recycled aggregate concrete; SF: Silica fume; EVM: Equivalent mortar volume.

square test (Table 8). The variables (clusters) used in the analysis were derived from hierarchical and k-means clustering. According to the results, the Chi-square tests for all compressive strength groups were significant at the 95% significance level.

3.3. Statistical Parameters of Clusters

In the analysis of the 'Compressive Strength Class of Concretes,' the strength class of the concretes was examined individually (Table 6) and within the context of clusters (Table 7). This approach facilitates the comparison of the overall data and clustering effects on the strength class. According to the results, the targeted strength class of C30/37 was achieved for RAC—SF and NAC. However, the strength class of NAC clusters was observed to be C30/37, consistent with the overall data. This consistency did not extend to the other concretes, as their clusters exhibited different and scattered strength classes. It can be stated that the use of RA in concrete caused a decrease in compressive strength, increased scatter, and standard deviation, resulting in clusters. RA was more dominant than NA—for instance, clusters of RAC.SF included C25/30 and C30/37 strength classes, whereas the overall data for RAC. SF showed a strength class of C30/37. The use of RA in RAC appeared to introduce heterogeneity in the compressive strength data, with the clustering effect of RA being more pronounced than that of NA.

Examining the standard deviation (SD) of clusters revealed that RA increased the SD of compressive strength in clusters, while SF and EMV decreased it. The coefficient of variation (CV), defined as the standard deviation divided by the mean, assessed changes between strength classes. A low CV indicates minimal variation in the data. For NAC, the CV was 6%, with cluster 1 showing a CV of 5% and cluster 2 a CV of 2%. This indicates more significant variability in the first cluster of NAC concrete units with a medium strength class (C30/37). For RAC, the overall CV was 8%, with cluster CVs of 7% and 3%, respectively. Significant shifts were observed in the first cluster of RAC, resulting in differing strength classes: C25/30 for the first cluster and C30/37 for the second cluster.

RAC.SF exhibited some of the lowest CV values at the main (6%) and cluster levels (6% for the first cluster and 2% for the second cluster)—the first cluster of RAC.SF showed a strength class of C25/30 with higher variability, while the second cluster showed a strength class of C30/37 among the three clusters formed from RAC.EMV, low variability was a notable feature, with each sub-cluster exhibiting different strength classes. Cluster 1 had the lowest variability and a high strength class (C40/50), while clusters 2 and 3 had the same CV but different strength classes: C35/45 and C30/37, respectively.

4. CONCLUSIONS

This study aimed to investigate the clustering of the compressive strength of recycled aggregate concrete (RAC). Four concrete groups were produced under standard conditions for this experimental study. The first group included natural aggregate concretes (NAC) designed using the Absolute Volume Method (AVM) as control concretes. The second group comprised RACs designed using the Equivalent Mortar Volume Method (EVM), serving as the control for RAC. The third group consisted of RACs treated with silica fume (SF) and designed using AVM, while the fourth group comprised RACs designed with EVM. Statistical analyses were performed on the test results, including Hierarchical Cluster Analysis (HCA), strength class determination, and Chi-Square Analysis.

The introduction of recycled aggregate (RA) in RAC resulted in more significant heterogeneity in compressive strength data, increased scatter, and higher standard deviation than natural aggregate (NA). Specifically, clusters of RAC showed a broader variation in strength classes (C25/30 and C30/37) compared to NAC, which maintained a consistent strength class of C30/37. This indicates that the clustering effect of RA is more dominant than NA's. Consequently, this heterogeneity may lead to clusters in the compressive strength of concrete and variability in the measured data, potentially creating a soft floor effect in reinforced concrete structures and structural elements with fluctuating strength distributions if RAC is used.

EVM showed potential as a preferred method over mineral addition treatment for enhancing RAC. However, further investigations are warranted to explore additional concrete parameters, such as cement dosage and water-to-binder ratio, which may influence RAC's overall performance and consistency. This critical study area warrants further exploration to enhance RAC's understanding and practical application.

AUTHOR CONTRIBUTIONS

The authors contributed equally to the study.

ETHICS

There are no ethical issues with the publication of this manuscript.

DATA AVAILABILITY STATEMENT

The authors confirm that the data that supports the findings of this study are available within the article. Raw data that support the finding of this study are available from the corresponding author, upon reasonable request.

CONFLICT OF INTEREST

The authors declare that they have no conflict of interest.

FINANCIAL DISCLOSURE

The authors declared that this study has received no financial support.

USE OF AI FOR WRITING ASSISTANCE

English check is made by Microsoft Copilot AI at revision stage.

PEER-REVIEW

Externally peer-reviewed.

REFERENCES

[1] Turkish Standards Institution. (2010). *Testing hardened concrete - Part 3: Compressive strength of test specimens, Ankara, Türkiye*. TS EN 12390-3.

[2] ASTM. (2014). *Standard test method for static modulus of elasticity and poisson's ratio of concrete in compression, Pennsylvania, United States*. ASTM C469.

[3] Turkish Standards Institution. (2010). *Testing hardened concrete - Part 6: Tensile splitting strength of test specimens, Ankara, Türkiye*. TS EN 12390-6.

[4] European Committee for Standardization. (2014). *Design of Concrete Structures - Part 1-1: General Rules for Buildings, Brussels, Belgium*. EN 1992-1-1.

[5] Borhan, T. M. (2012). Properties of glass concrete reinforced with short basalt fiber. *Mater Des, 42*, 265-271. [CrossRef]

[6] Dilbas, H., Erkılıç, E., Saraylı, S., & Haktanır, T. (2011). Beton Mukavemet Deneyleri Değerlendirmesi için Bir İstatistiksel Çalışma. *Yapı Dünya Derg, 178*, 25-31.

[7] Almeida, F. M., Barragán, B.E., Casas, J.R., & El Debs, H.C. (2010). Hardened properties of self-compacting concrete - a statistical approach. *Constr Build Mater, 24*(9), 1608-1615. [CrossRef]

[8] Zhou, C., Li, K., & Ma, F. (2014). Numerical and statistical analysis of elastic modulus of concrete as a three-phase heterogeneous composite. *Comp Struct, 139*, 33-42. [CrossRef]

[9] Brito, J., & Saikia, N. (2014). Recycled Aggregate in Concrete, Springer London, UK.

[10] Xiao, J., Li, W., Fan, Y., & Huang X. (2012). An overview of study on recycled aggregate concrete in China (1996-2011). *Constr Build Mater, 31*, 364-383. [CrossRef]

[11] Xiao, J., Li, W., & Poon C. (2012). Recent studies on mechanical properties of recycled aggregate concrete in China-A review. *Sci China Technol Sci, 55*(6), 1463-1480. [CrossRef]

[12] Kılınçarslan, Ş., İnce, EY., Tuncay, EB., & Yağmurlu F. (2018). Clustering analysis of normal strength concretes produced with different aggregate types. *Open Chem, 16*(1), 918-922. [CrossRef]

[13] Turkish Standards Institution. (2016). *Design of concrete mixes, Ankara, Türkiye*. TS 802.

[14] Abbas, A., Fathifazl, G., Isgor, O. B., Razaqpur, A. G., Fournier, B., & Foo, S. (2009). Durability of recycled aggregate concrete designed with equivalent mortar volume method. *Cement Concr Comp, 31*(8), 555-563. [CrossRef]

[15] Dilbas, H., Çakır, Ö., & Atiş, C. D. (2019). Experimental investigation on properties of recycled aggregate concrete with optimized Ball Milling Method. *Constr Build Mater, 212*, 716-726. [CrossRef]

[16] Kim, J., & Sadowski, Ł. (2019). The equivalent mortar volume method in the manufacturing of recycled aggregate concrete. *Tech Trans, 116*(11), 121-138. [CrossRef]

[17] R Core Team. (2020). *R: A language and environment for statistical computing, R Foundation for Statistical Computing, Vienna, Austria*. https://www.r-project.org/

[18] Everit, B. S., Landau, S., Leese, M., & Stahl, D. (2011) *Cluster analysis. 5th ed.* Wiley. [CrossRef]

[19] Fernández, A., & Gómez, S. (2008). Solving non-uniqueness in agglomerative hierarchical clustering using multidendrograms. *J Classif, 25*(1), 43-65. [CrossRef]

[20] Agresti, A. (2012). *Categorical data analysis (Vol. 792)*. John Wiley & Sons.

[21] Dilbas, H., & Çakır, Ö. (2015). Fracture and failure of recycled aggregate concrete (RAC) - A Review. *Int J Concr Technol, 1*(1), 31-48.

[22] Dilbas, H. (2014). *An examination on mechanical behaviour of a cantilever beam produced with recycled aggregate concrete*. Graduate School of Natural and Applied Science, Yildiz Technical University.

[23] Duan, Z. H., & Poon, C. S. (2014). Properties of recycled aggregate concrete made with recycled aggregates with different amounts of old adhered mortars. *Mater Des, 58*, 19-29. [CrossRef]

[24] Matias, D., De Brito, J., Rosa, A., & Pedro, D. (2013). Mechanical properties of concrete produced with recycled coarse aggregates-Influence of the use of superplasticizers. *Constr Build Mater, 44*, 101-109. [CrossRef]

[25] Dilbas, H., Şimşek, M., & Çakır, Ö. (2014). An investigation on mechanical and physical properties of recycled aggregate concrete (RAC) with and without silica fume. *Constr Build Mater, 61*, 50-59. [CrossRef]

[26] Dilbas, H., Çakır, Ö., & Şimşek, M. (2017). Recycled aggregate concretes (RACs) for structural use: An evaluation on elasticity modulus and energy capacities. *Int J Civil Eng, 15*, 247-261. [CrossRef]

[27] Cantero, B., del Bosque, I. S., Matías, A., & Medina, C. (2018). Statistically significant effects of mixed recycled aggregate on the physical-mechanical properties of structural concretes. *Constr Build Mater, 185*, 93-101. [CrossRef]

[28] Wardeh, G., & Ghorbel, E. (2014, 11-12 August). *Mechanical properties of recycled aggregates concrete: An analytical study*. In International Symposium on Eco-Crete. Reykjavik, Iceland.

[29] De Brito, J., & Saikia, N. (2012). *Recycled aggregate in concrete: Use of industrial, construction and demolition waste*. Springer. [CrossRef]

[30] Çakır, Ö., & Dilbas, H. (2018). A comparative analysis of elasticity modulus of recycled aggregate concrete with silica fume. *Pamukkale Uni Müh Bilim Derg, 24*(6), 1069-1078. [CrossRef]

J Sustain Const Mater Technol, Vol. 9, Issue. 4, pp. 412–420, December 2024

Journal of Sustainable Construction Materials and Technologies
Web page info: https://jscmt.yildiz.edu.tr
DOI: 10.47481/jscmt.1607813

Research Article

The effect of recycled pervious concrete aggregate substitution on properties of pervious concrete

Demet YAVUZ*

Department of Civil Engineering, Van Yüzüncü Yıl University Faculty of Engineering, Van, Türkiye

ARTICLE INFO

Article history
Received: 11 June 2024
Revised: 23 December 2024
Accepted: 24 December 2024

Key words:
Freeze-thaw resistance, mechanical properties, pervious concrete, porosity, recycled aggregate

ABSTRACT

Sustainability has gained significant importance in civil engineering and other areas in recent years. Numerous studies have been conducted on using recycled aggregates to demolish various structures in this context. However, almost all these studies have focused on recycled aggregates from traditional concrete. This study investigated the usability of recycled aggregates obtained from pervious concrete produced in a laboratory environment for use in pervious concrete production. Natural aggregate was substituted with recycled pervious concrete aggregate at weight ratios of 20%, 40%, 60%, 80%, and 100%. The concrete series' compressive, flexural, and splitting tensile strengths, water permeability coefficient, porosity values, and freeze-thaw resistance were examined. Additionally, the microstructure before and after the freeze-thaw effect was analyzed using scanning electron microscopy. The results showed that recycled aggregates increased the water permeability coefficient and porosity but negatively affected the mechanical properties.

Cite this article as: Yavuz, D. (2024). The effect of recycled pervious concrete aggregate substitution on properties of pervious concrete. *J Sustain Const Mater Technol*, 9(4), 412–420.

1. INTRODUCTION

Constructing pedestrian pathways, sidewalks, and roads with impermeable coverings like concrete and asphalt causes various adverse effects due to harsh climate transitions and climate change. As a habit or necessity inherited from past applications, impermeable coverings from impermeable materials occupy a significant area in cities. This leads to undesirable situations such as water accumulation on the surface, water pollution, interruption of the connection between air and soil, and delayed water transfer to the ground. These conditions increase the risk of flooding and disrupt traffic flow safety. Constructing pedestrian pathways, sidewalks, and highways from permeable materials like pervious concrete will facilitate rapid water transmission to the ground, preventing water accumulation on the surface. This will contribute to ensuring traffic safety, facilitating groundwater replenishment, and supporting the partial purification of water due to the retention of polluting particles by concrete [1–4].

Pervious concrete is a special type made from coarse aggregate and cement, without or with low amounts of fine aggregate. Although the porosity of pervious concrete varies in different ranges, it is generally reported to be 15–25% [5]. According to ACI 522-R [6], the porosity of pervious concrete is recommended to be between 15% and 35%. Due to the absence of fine aggregate or its use in only around 10%, the voids in pervious concrete are relatively large and interconnected. However, this structure has significantly lower strengths than previous concrete compared to traditional concrete, which limits its usage [6]. Although the strength ranges vary widely, the compressive strengths of

---

***Corresponding author.**
*E-mail address: demetyavuz@yyu.edu.tr

Published by Yıldız Technical University Press, İstanbul, Türkiye

pervious concrete are reported to be between 2.8–28 MPa, and flexural strengths range from 1.5–3.2 MPa. The mechanical properties of pervious concrete are influenced by various factors such as water-to-cement ratio, compaction degree, binder volume, and aggregate gradation [7].

One of the critical issues recently discussed in the construction sector is earthquakes and the existing building stock. As a result of the increasing need for shelter and recent natural disasters like the Kahramanmaraş earthquake, a significant amount of demolition waste is produced. The demolition caused by the Kahramanmaraş earthquake highlights the importance of the issue, with an estimated amount of waste ranging from 350 to 580 million tons [8]. Reusing these difficult-to-store wastes in new concrete production will add value to the economy and eliminate or reduce the need for landfilling. While countries like France and Japan have specific guidelines for the reuse of waste concrete, numerous researchers worldwide are conducting studies on recycling [9–13]. There are also environmental advantages to using RAs as aggregates in concrete mixtures. Normally, unused RAs are sent to landfills for storage. However, due to increasing urbanization and reconstruction, storage areas are insufficient, and new regions are needed. Therefore, the need for additional storage areas is reduced by re-evaluating RAs. In addition, RAs, which can be produced on-site, can be produced cheaper than virgin aggregates. Thus, it is possible to reduce the cost of aggregate production.

Recycled aggregate (RA) is produced by crushing, sieving, and sorting old concrete into specific sizes. One of the significant challenges encountered when using RA in new concrete production is the presence of old cement paste and mortar adhering to the aggregate particles. This paste and mortar increase RA's water absorption capacity and porosity, decreasing strength properties [14–17]. There are numerous studies on using coarse, fine, or powdered recycled aggregate in different building materials. Hosseinnezhad et al. [18] examined the effect of recycled coarse aggregate substitution on the properties of roller-compacted concrete. Alghader et al. [19] investigated the usability of recycled aggregate in self-compacting concrete production. Kanagaraj et al. [20] studied the properties of geopolymers produced using recycled aggregate, while Tan et al. [21] examined the use of ground recycled aggregate powder as a binder in geopolymer production. Gültekin [22] explored the feasibility of using recycled aggregate in cement-based SIFCON composites, while Eryılmaz et al. [23] investigated using recycled geopolymer concrete aggregate in geopolymer production. Numerous studies have also been conducted on using RA in previous concrete outputs.

Zaetang et al. [10] examined the effect of RA usage on the properties of previous concrete. They reported that 60% RA instead of natural aggregate provided a reasonable compressive strength of 15 MPa. Sriravindrarajah et al. [24] stated that using RA to produce pervious concrete at constant porosity harms compressive strength. Nazari et al. [25] studied the use of recycled aggregates obtained from different types of bricks in pervious concrete. They noted that the increase in RA quantity led to a gradual increase in porosity and a gradual decrease in density, likely due to the porosity of RA. Similarly, Brasileiro et al. [26] reported a 10% increase in water permeability in pervious concrete with 50% RA usage but a 56% loss in compressive strength. Barnhouse et al. [27] examined the effects of RA usage on compressive strength and modulus of elasticity. There have been numerous studies on using recycled aggregate in various building materials, such as aggregate, filler, and even binder. However, most of these studies used recycled aggregate from traditional concrete. Therefore, there is a need for research on the use of recycled aggregate derived from pervious concrete in building material production.

In this study, the effect of recycled pervious concrete aggregate substitution on pervious concrete properties was investigated. In this context, 150x150x150 mm cube pervious concrete samples were produced in the laboratory using limestone aggregate. After determining the compressive strengths of these pervious concretes, they were crushed in a jaw crusher and sieved to obtain recycled pervious concrete aggregates in the range of 5–15 mm. The investigation of the effects of the thickness and properties of the mortar/paste layer adhering to the aggregate on the properties of pervious concrete, which may differ from those of recycled aggregates produced from traditional concrete, constitutes the original aspect of the study. Accordingly, six different series of pervious concrete were made, one containing only crushed limestone and the others containing 20%, 40%, 60%, 80%, and 100% recycled aggregates to replace limestone by weight. The compressive, splitting tensile, and flexural strengths, porosity values, water permeability coefficients, and freeze-thaw resistance of concretes were determined. Additionally, a scanning electron microscopy (SEM) examination was conducted to observe the changes in the internal structure caused by freeze-thaw cycles.

2. EXPERIMENTAL STUDY

2.1. Materials

The study used CEM I 42.5 R type Portland cement conforming to TS EN 197-1 [28] as the binder and crushed limestone in the 5–15 mm size fraction as the aggregate. Tap water was also utilized. The crushed limestone was obtained from a local ready-mix concrete plant. The recycled aggregate was produced under laboratory conditions using limestone and obtained from cement-based pervious concrete with compressive strength ranging from 10 to 15 MPa. After determining the compressive strength of the pervious concrete samples, they were crushed with a jaw crusher and sieved through sieves to obtain recycled aggregate in the 5–15 mm size fraction. Photographs and some physical properties of the aggregates are presented in Figure 1 and Table 1, respectively. The mortar/paste thickness around the recycled aggregate in pervious concrete differs from that in traditional concrete. This resulted in the specific gravity of the recycled aggregate being close to that of crushed limestone aggregate. However, it is observed that the water absorption capacity of the recycled aggregate is significantly higher than that of crushed limestone. To in-

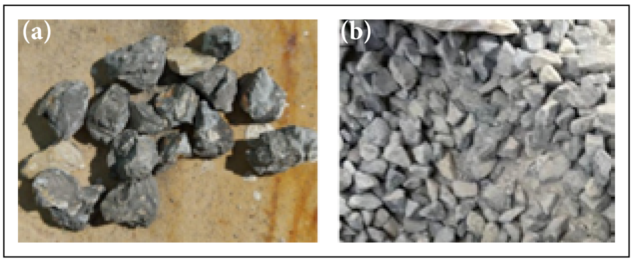

Figure 1. Aggregates **(a)** Recycled aggregate, **(b)** Limestone aggregate.

crease the fluidity of the paste phase, superplasticizer was used in varying proportions ranging from 0.1% to 0.8% of the cement weight, and silica fume was used at a rate of 5% of the total binder weight to increase both the paste volume and contribute to the mechanical properties.

Due to the old cement paste layer in RAs, their specific gravity is lower than natural aggregates (Table 1).

2.2. Concrete Production

The mixtures were prepared using a laboratory-type concrete mixer with a capacity of 40 dm^3. In all mixtures, the binder dosage was set as 400 kg/m^3, the water/binder ratio was fixed as 0.32, and concretes with a target porosity value of 15% were produced. First, cement, silica fume, and aggregates were dry-mixed for 2 minutes. Superplasticizer and water were mixed and added to the mixer in approximately 30 seconds, and the mixer was operated for 2 minutes. At the end of this period, the mixer was stopped, particles adhering to the bowl's walls were scraped off with a trowel, and the mixer was operated for another 2 minutes. At the end of the time, the consistency and homogeneity of the mixture were visually inspected, and the placement process was initiated.

The placement process was carried out in 3 layers, and each layer was compacted with 25 strokes with a tamping rod. The top surfaces of the samples were levelled with a trowel and left to cure under ambient conditions for 1 day. Afterward, specimens were de-molded and subjected to standard water curing for 27 days in lime-saturated water. Cubic specimens with dimensions of 150 mm for compressive strength, prism specimens of 100x100x400 mm for flexural strength, and cylindrical specimens with a diameter of 100 mm and a height of 200 mm for splitting tensile strength were prepared. Porosity and water permeability coefficient tests were also conducted using cylindrical specimens. Three specimens from each series were used for each test, and the average of the three was reported.

2.3. Mixtures

Within the scope of the study, six different concrete series were produced: one control mixture containing only limestone aggregate, one mixture containing entirely recycled aggregate, and four mixtures containing 20%, 40%, 60%, and 80% by weight of recycled aggregate substitution for limestone. Due to the loss of workability with recycled aggregate, superplasticizer was added in proportions ranging from 0.1% to 0.8% of the cement weight (Table 2).

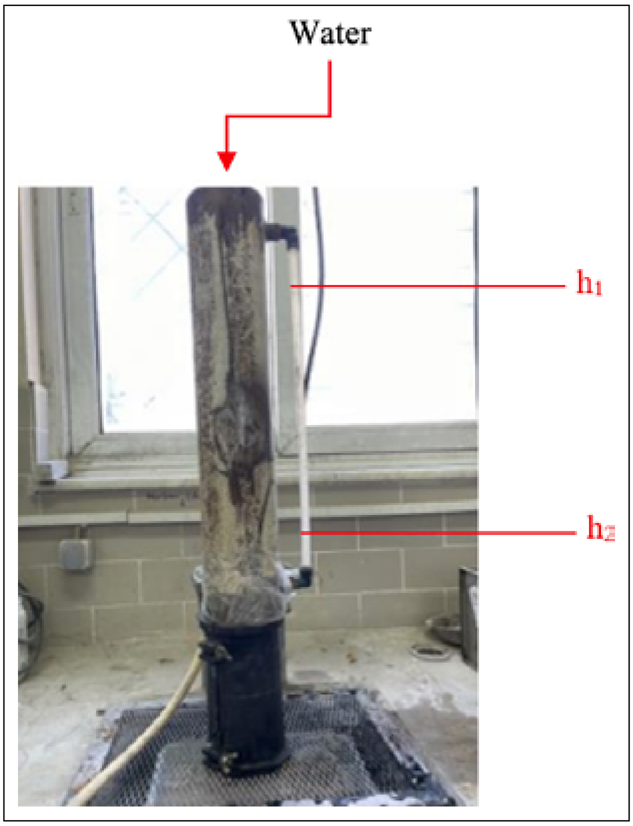

Figure 2. Water permeability coefficient test setup .

Table 1. Physical properties of aggregates

Physical property	Limestone aggregate (LA)	Recycled aggregate (RA)
Specific gravity	2.67	2.63
Water absorption (%)	0.30	8.95

2.4. Tests

Compressive, flexural, and splitting tensile strength tests were conducted following TS EN 12390-3 [29], TS EN 12390-5 [30], and TS EN 12390-6 [31] Standards, respectively.

Porosity values were determined by measuring the weights of the samples after being kept in air and submerged in water for 24 hours. Subsequently, porosity values were calculated using Equation 1.

$$P = \left[1 - \frac{m_h - m_s}{\rho_s \, x \, V}\right] \tag{1}$$

Here, m_h represents the weight of the specimen in the air (g); m_s represents the weight of the specimen in water (g); or(g);ρ_s represents the density of water (g/cm^3); V represents the volume of the sample (cm^3); and P represents the porosity (%).

The water permeability coefficient test was conducted using a decreasing water level test setup, as shown in Figure 2. Firstly, the side surfaces of the sample were sealed with a waterproof insulation material, and the sample was placed in the test setup. Water was supplied from the top,

Table 2. Theoretical material quantities for 1 m^3 of pervious concrete

Code	Materials (kg)					
	Cement	Silica fume	Water	Aggregate		Plasticizer
				LA	RA	
Ref	380	20	128	1590	–	–
RA20	380	20	128	1272	318	0.04
RA40	380	20	128	954	636	0.06
RA60	380	20	128	636	954	0.08
RA80	380	20	128	318	1272	0.18
RA100	380	20	128	–	1590	0.32

LA: Limestone aggregate; RA: Recycled aggregate.

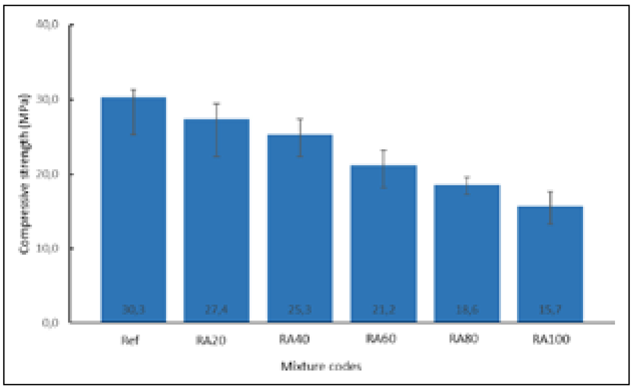

Figure 3. 28-day compressive strength test results.

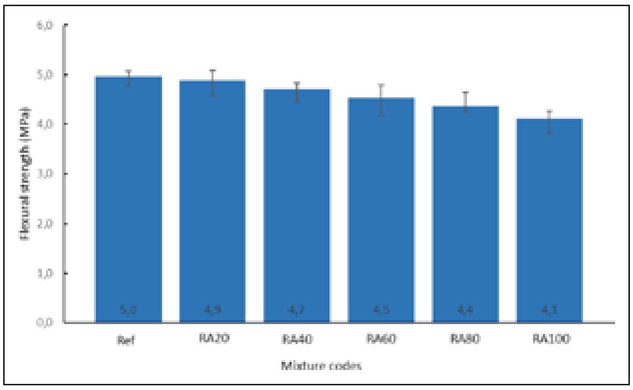

Figure 4. 28-day flexural strength test results.

and the total flow time was measured using a stopwatch. Based on the obtained data, the water permeability coefficient was determined using Equation 2. In the equation, k represents the water permeability coefficient in units of cm/s, a represents the cross-sectional area of the pipe in units of cm^2, l represents the length of the sample in units of mm, A represents the cross-sectional area of the sample in units of cm^2, and t represents the flow time of water in seconds. h_1 and h_2 values indicate the pipe's initial and final water heights in cm, respectively.

$$k = \frac{a\,x\,l}{A\,x\,t}\,In\,\frac{h_1}{h_2} \tag{2}$$

Freeze-thaw resistance tests were conducted following the GB/T 50082-2009 [32] Standard, with freezing at -18±2 °C for two hours followed by thawing at 5±2 °C for two hours. Weight losses were determined after 30, 60, 120, and 180 cycles.

3. RESULTS AND DISCUSSION

3.1. Compressive Strength

The compressive strengths of the series produced within the scope of the study are presented in Figure 3. The negative effect of using RA on the compressive strength of pervious concrete is evident in Figure 3. While the compressive strength of the concrete containing only limestone aggregate is 30.3 MPa, the strengths gradually decrease with the substitution of RA, reaching 15.7 MPa in the series produced entirely with RA, representing a 48% decrease. The highest compressive strength is obtained from the control sample without RA, and as the RA content increases gradually, the compressive strength decreases. Since the water absorption value of RA is higher than that of limestone aggregate, these aggregates absorb some of the mixing water, reducing the water-to-cement ratio in mixtures where RA is used. Additionally, due to the lower compressive strengths of RA compared to limestone aggregates, the fact also negatively affects the compressive strength of pervious concrete.

In a similar study, Yang et al. [33] reported that pervious concrete produced with 60% RA compressive strength was 31% to 32.5% lower than the control mixture. Nazeer et al. [34] investigated the effect of RA usage on the mechanical properties of pervious concrete. They noted that substituting natural aggregate with 50% and 100% RA reduced compressive strengths by 21% and 32%, respectively. Li et al. [35] also determined sharp decreases in the compressive strength of pervious concrete when RA substitution exceeded 40%.

3.2. Flexural and Splitting Tensile Strength

The flexural and split tensile strengths of concrete series produced with different proportions of RA substitution are presented in Figure 4 and Figure 5, respectively. Like compressive strength, the flexural and split tensile strengths decreased with RA substitution, and the reductions continued as the substitution ratio increased. The flexural and splitting tensile strengths of the control sample without RA, which

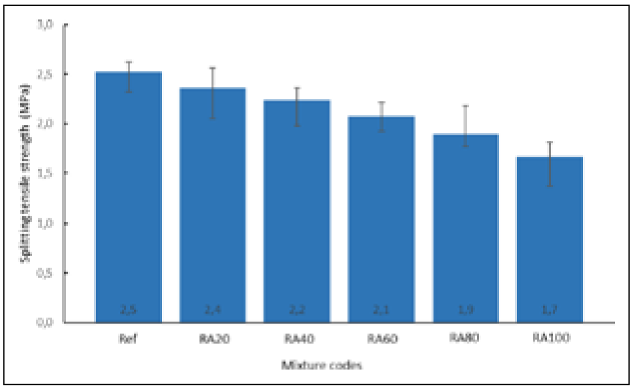

Figure 5. 28-day splitting tensile strength test results.

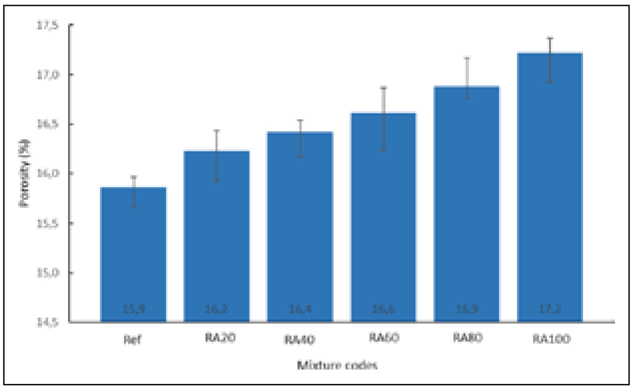

Figure 6. 28-day porosity test results.

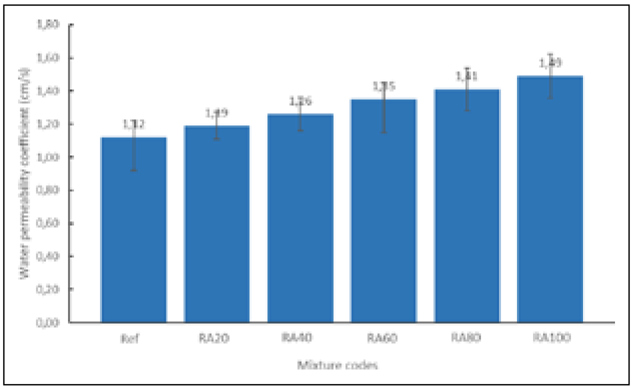

Figure 7. 28-day water permeability test results.

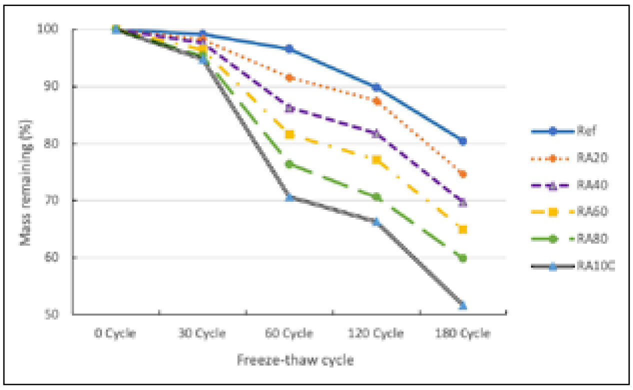

Figure 8. Mass remaining after 0, 30, 60, 120 and 180 freeze-thaw cycles.

were 5.0 MPa and 2.5 MPa, decreased to 4.1 MPa and 1.7 MPa, respectively, with 100% RA substitution, representing reductions of 18% and 32%, respectively. The cutbacks in splitting tensile strength were higher than those of the losses in flexural strength at all substitution ratios. Yang et al. [33] reported losses in flexural strength ranged from 18% to 26% as RA usage increased from 0% to 60% in pervious concrete. In a similar study, Nazeer et al. [34] noted a 13% loss in flexural strength with 50% RA usage, which increased to 41% when RA was used entirely.

3.3. Porosity

The porosity values of the pervious concrete produced in the study are presented in Figure 6. The mixture with the lowest porosity value, at 15.9%, is the reference mixture, while, as expected, porosity values increased gradually with RA usage, reaching 17.2% with an 8% increase at a 100% substitution ratio. Consistent with previous studies on RA usage, contrary to the results in mechanical properties, an increase in porosity values is observed with RA usage. This is primarily attributed to a more significant number of relatively larger voids in coarse aggregates due to the effect of the previous mortar layer adhering to the aggregates [15, 36, 37]. Similar results to those obtained with RA produced from traditional concrete were also obtained in this study. Nazeer et al. [34] reported increased porosity from 19.4% in pervious concrete without RA to 19.8% with 50% RA substitution. Similar studies by El-Hassan et al. [38], Tuan et al. [39], and Malayali et al. [36] have reported increases in porosity values with RA usage.

3.4. Water Permeability Coefficient

The water permeability coefficients of the concrete produced in the study are presented in Figure 7. Similar to the trends in porosity values, it is observed that the permeability coefficient increases with RA usage. The coefficient, which was 1.12 cm/s in the reference series, increased by 33% to 1.49 cm/s with 100% RA substitution. The voids in the aggregate are believed to contribute to this increase and enhance permeability. In previous studies on this matter, Nazeer et al. [34] and Lyu et al. [40] reached similar conclusions to this study, while Yang et al. [33] reported opposite findings, suggesting that although RA usage may increase the permeability of pervious concrete, the decrease in connected voids and practical porosity values might be the cause.

3.5. Freeze-Thaw Resistance

The changes in the weights of the concrete series after 30, 60, 90, 120, and 180 cycles of freeze-thaw are in Figure 8. It is observed that as the RA usage rate increases, the remaining weight after freeze-thaw cycles decreases. It was previously mentioned that, compared to limestone aggregates, RAs have higher water absorption values and thus absorb some mixing water. Therefore, the water present in their structure freezes as the temperature drops and melts as it rises. With repeated occurrences of this process, the cement paste structure is estimated to deteriorate more

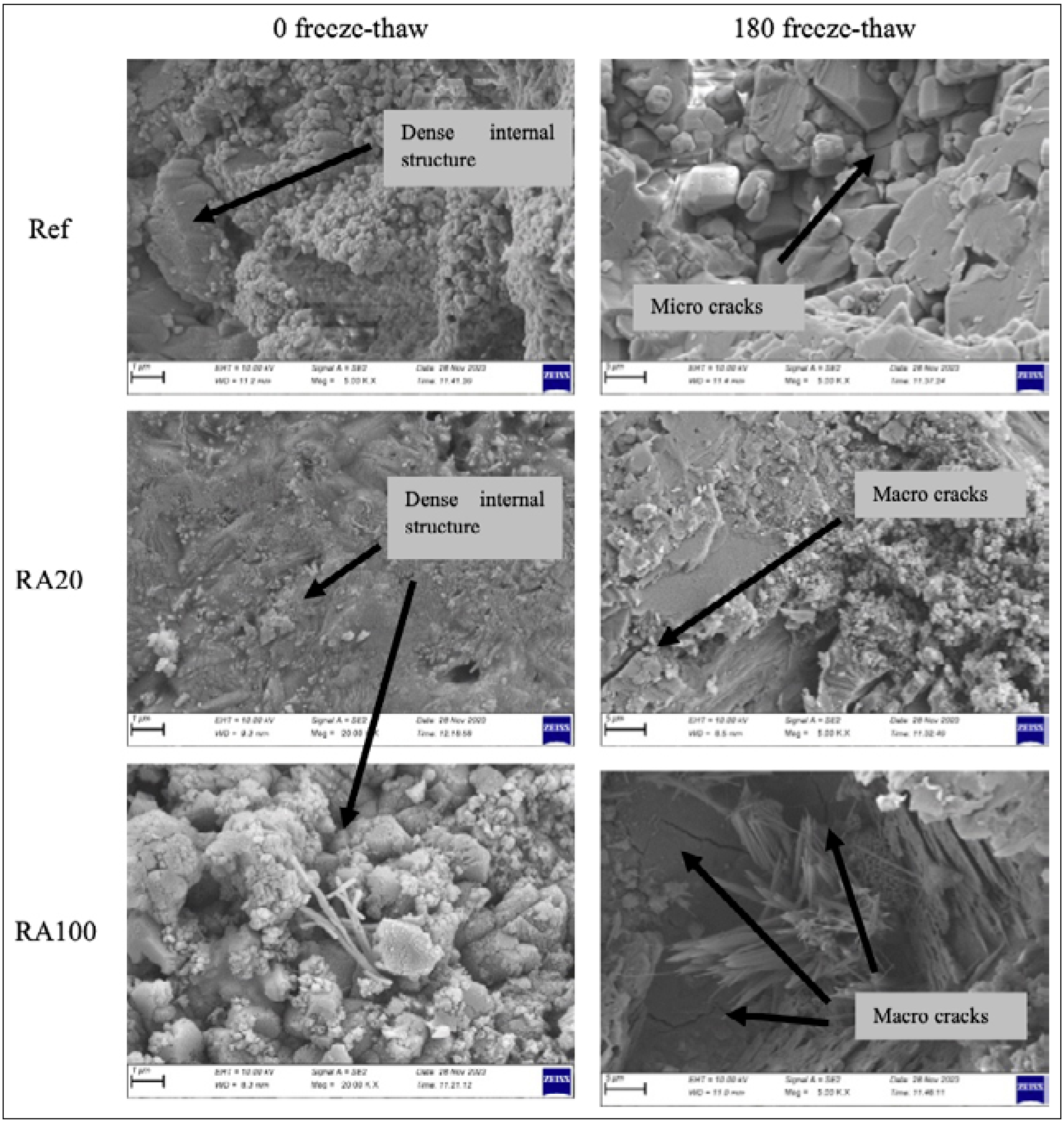

Figure 9. Internal structures of selected samples after 0 and 180 freeze-thaw cycles.

rapidly than the concrete produced with limestone, leading to lower freeze-thaw performance. The weaker interfacial transition zone in concrete produced with RAs has also contributed to this behavior.

Results show that mass losses increase in all samples with successive freeze-thaw cycles. As freeze-thaw continues, the water in the large and wide pores of PCs freezes and then melts. When water changes from liquid to solid, it expands and stresses the pore boundaries. The cement paste structure deteriorates with each cycle, losing its adhesive properties between aggregates. In this study, it is noted that initially, mass losses in the samples during the first freeze-thaw cycles were relatively low. Still, as freeze-thaw continued, mass loss increased cumulatively. The increased ratio of RA usage adversely affected the freeze-thaw behavior of PCs. It is known that concretes with lower mechanical behavior also exhibit relatively lower freeze-thaw performance. Therefore, mixtures containing RAs are expected to show lower freeze-thaw resistance. After 180 cycles, the mass loss in the control sample was 80.46%, while for RA20, RA40, RA60, RA80, and RA100 samples, these values were 74.65%, 69.74%, 64.88%, 59.87%, and 51.68%, respectively. Considering that the samples lost approximately half of their mass after 180 cycles, the effect of freeze-thaw damage becomes evident.

Liu et al. [41] produced pervious concretes by substituting RA for natural aggregates at ratios of 0%, 25%, 50%, 75%, and 100%, and reported that as the RA usage ratio increased, the freeze-thaw resistance of these concretes decreased significantly. Wu et al. [42] stated that among the RA-containing pervious concretes they produced at ratios of 0%, 30%, 50%, 70%, and 100%, the mixture with RA% had the worst freeze-thaw resistance. They mentioned that this mixture lost its strength before reaching 100 cycles. Still, by adding sufficient amounts of fly ash and air-entraining admixture to the same mix, the freeze-thaw performance could be extended up to 150 cycles. Yan et al. [43] replaced natural aggregates with RA at 0%, 30%, 70%, and 100% ratios and examined their effects on pervious concrete. It was noted that the compressive strength after freeze-thaw cycles decreased gradually with increasing RA ratio and cycle duration.

Figure 9 presents SEM images of the control, RA20, and RA100 specimens after 0 and 180 freeze-thaw cycles. Upon examining the SEM images, it can be observed that the internal structures of the specimens not subjected to freeze-thaw cycles are denser and undamaged. At the same time, deep cracks are formed in the internal structures of the pervious concretes after 180 cycles.

4. CONCLUSIONS AND RECOMMENDATIONS

In this study, recycled aggregates obtained from pervious concrete were used by replacing specific proportions of limestone, and the compressive, flexural, and splitting tensile strengths, porosity, and water permeability coefficient, as well as freeze-thaw performance of the produced pervious concretes, were investigated. Considering the materials used and the experimental methods applied, it is possible to state the following results:

- Substituting recycled aggregate resulted in decreases in compressive, flexural, and splitting tensile strengths, with reductions intensifying as the substitution rate increased. Specifically, at a 100% substitution rate, the decrease in compressive strength was 48%, while the losses in flexural and splitting tensile strengths were 17% and 34%, respectively.
- Both porosity and permeability coefficients increased gradually with recycled aggregate and an increase in substitution rate. The lowest water permeability value was obtained in the reference mixture at 1.12 cm/s, while the highest value of 1.49 cm/s was observed at 100% recycled aggregate substitution.
- As the freeze-thaw cycles increased, the mass loss observed in pervious concrete also increased. Additionally, the usage rate of recycled aggregate negatively impacted the freeze-thaw performance. The control mixture, produced solely with limestone aggregate without recycled aggregate, exhibited the best freeze-thaw performance, while the mixture with 100% recycled aggregate showed the lowest performance.
- When SEM images taken before and after freeze-thaw cycles were examined, it was observed that there were no micro or macro cracks in the internal structure of the cement paste before the cycles. With an increase in the number of cycles, it was determined that microcracks appeared partially at low replacement rates, while at high replacement rates, larger cracks accompanied the microcracks.

ACKNOWLEDGMENTS

This study was supported by the Scientific Research Projects Coordination Unit of Van Yüzüncü Yıl University under project number FYD-2023-10731.

ETHICS

There are no ethical issues with the publication of this manuscript.

DATA AVAILABILITY STATEMENT

The author confirm that the data that supports the findings of this study are available within the article. Raw data that support the finding of this study are available from the corresponding author, upon reasonable request.

CONFLICT OF INTEREST

The author declares that she has no conflict of interest.

USE OF AI FOR WRITING ASSISTANCE

Not declared.

PEER-REVIEW

Externally peer-reviewed.

REFERENCES

[1] Kováč, M., & Sičáková, A. (2017, 27-28 April). *Pervious concrete as a sustainable solution for pavements in urban areas*. In Proceedings of the International Conference on Environmental Engineering, ICEE, Vilnius Gediminas Technical University, Lithuania. [CrossRef]

[2] Lorenzi, A., Haselbach, L., Silva Filho, L. C. P. D., Pessutto, Â. S., & Bidinotto, G. B. (2018). Thermal profiles in pervious concrete during summer rain simulations. *Matéria Rio de Janeiro, 23*, e12170. [CrossRef]

[3] Schwartz, S. S. (2010). Effective curve number and hydrologic design of pervious concrete storm-water systems. *J Hydrol Eng, 15*(6), 465-474. [CrossRef]

[4] Shu, X., Huang, B., Wu, H., Dong, Q., & Burdette, E. G. (2011). Performance comparison of laboratory and field produced pervious concrete mixtures. *Constr Build Mater, 25*(8), 3187-3192. [CrossRef]

[5] Xie, H. Z., Li, L. G., Ng, P. L., & Liu, F. (2023). Effects of solid waste reutilization on performance of pervious concrete: A review. *Sustainability, 15*(7), 6105. [CrossRef]

[6] American Concrete Institute. (2010). *Report on Pervious Concrete*. ACI 522R-10.

[7] Ferić, K., Sathish Kumar, V., Romić, A., & Gotovac, H. (2023). Effect of aggregate size and compaction on the strength and hydraulic properties of pervious concrete. *Sustainability, 15*(2), 1146. [CrossRef]

[8] Doğdu, G., & Alkan, S. N. (2023). Deprem sonrası oluşan inşaat ve yıkıntı atıklarının değerlendirilmesi: 6 Şubat 2023 Kahramanmaraş depremleri. *Artvin Çoruh Üniv Müh Fen Bilim Derg, 1*(1), 38-50.

[9] Yan, H. D., & Huang, G. H. (2005). Study on pervious road brick prepared by recycled aggregate concrete. *Key Eng Mater, 302*, 321-328. [CrossRef]

[10] Zaetang, Y., Sata, V., Wongsa, A., & Chindaprasirt, P. (2016). Properties of pervious concrete containing recycled concrete block aggregate and recycled concrete aggregate. *Constr Build Mater, 111*, 15-21. [CrossRef]

[11] Zhu, X., Chen, X., Shen, N., Tian, H., Fan, X., & Lu, J. (2018). Mechanical properties of pervious concrete with recycled aggregate. *Comput Concr, 21*(6), 623-635.

[12] Ulloa-Mayorga, V. A., Uribe-Garcés, M. A., Paz-Gómez, D. P., Alvarado, Y. A., Torres, B., & Gasch, I. (2018). Performance of pervious concrete containing combined recycled aggregates. *Ingeniería e Invest, 38*(2), 34-41. [CrossRef]

[13] Strieder, H. L., Dutra, V. F. P., Graeff, Â. G., Núñez, W. P., & Merten, F. R. M. (2022). Performance evaluation of pervious concrete pavements with recycled concrete aggregate. *Constr Build Mater, 315*, 125384. [CrossRef]

[14] Yao, Y. (2018). Blending ratio of recycled aggregate on the performance of pervious concrete. *Fract Struct Integr, 46*(2018), 343-351. [CrossRef]

[15] Liu, W., Zhang, H., Chen, Z., Tao, J., Zhang, X., & Zhao, B. (2024). Performance of pervious concrete influenced by typical properties of recycled concrete aggregate and suggestions for practical use. *Road Mater Pave Des, 25*(5), 1090-1111. [CrossRef]

[16] Mikami, R. J., Kummer, A. C. B., & Döll, M. M. R. (2020). Leaching of pervious concrete produced using mixed recycled aggregates. *Braz Arch Biol Technol, 63*, e20180408. [CrossRef]

[17] Li, J., & Liu, Z. (2011). Microanalysis of recycled coarse aggregate and properties of no-fines pervious recycled concrete. *J Test Eval, 39*(5), 766-772. [CrossRef]

[18] Hosseinnezhad, H., Hatungimana, D., & Ramyar, K. (2021). Mechanical properties of roller compacted concrete containing recycled concrete aggregate. *J Constr, 20*(2), 277-290. [CrossRef]

[19] Alghader, A., Sarıışık, A., & Can, S. Geri Dönüştürülmüş beton agregasının kendiliğinden yerleşen betonun performansına etkisi. *Harran Üniv Müh Derg, 8*(2), 91-107. [CrossRef]

[20] Kanagaraj, B., Kiran, T., Anand, N., & Al Jabri, K. (2023). Development and strength assessment of eco-friendly geopolymer concrete made with natural and recycled aggregates. *Constr Innov, 23*(3), 524-545. [CrossRef]

[21] Tan, J., Cai, J., Huang, L., Yang, Q., Mao, M., & Li, J. (2020). Feasibility of using microwave curing to enhance the compressive strength of mixed recycled aggregate powder based geopolymer. *Constr Build Mater, 262*, 120897. [CrossRef]

[22] Gültekin, A. (2024). Investigation of usability of recycled aggregate in SIFCON production. *J Sustain Constr Mater Technol, 9*(1), 36-44. [CrossRef]

[23] Eryılmaz, K., Polat, R., Turhan, D., & Karagöl, F. (2023). Geopolimer beton atıklarından elde edilen agregaların geopolimer betonda kullanılabilirliğinin araştırılması. *J Inst Sci Technol, 13*(1), 419-431. [CrossRef]

[24] Sriravindrarajah, R., Wang, N. D. H., & Ervin, L. J. W. (2012). Mix design for pervious recycled aggregate concrete. *Int J Concr Struct Mater, 6*, 239-246. [CrossRef]

[25] Nazari, M., Mousavi, S. Y., Davoodi, S. R., & Mirgozar Langaroudi, M. A. (2024). Recycling of different types of brick aggregates in pervious concrete. *Eur J Environ Civ Eng, 28*(2), 1-22. [CrossRef]

[26] Brasileiro, K. P. T. V., de Oliveira Nahime, B., Lima, E. C., Alves, M. M., Ferreira, W. P., dos Santos, I. S., Filho, C. P. B., & dos Reis, I. C. (2024). Influence of recycled aggregates and silica fume on the performance of pervious concrete. *J Build Eng, 82*, 108347. [CrossRef]

[27] Barnhouse, P. W., & Srubar III, W. V. (2016). Material characterization and hydraulic conductivity modeling of macroporous recycled-aggregate pervious concrete. *Constr Build Mater, 110*, 89-97. [CrossRef]

[28] Türk Stardartları Enstitüsü. (2012). *Çimento - Bölüm 1: Genel çimentolar - Bileşim, özellikler ve uygunluk kriterleri. Ankara, Türkiye*. TS EN 197-1.

[29] Türk Stardartları Enstitüsü. (2019). *Beton - Sertleşmiş beton deneyleri - Bölüm 3: Deney numunelerinin basınç dayanımının tayini, Ankara, Türkiye*. TS EN 12390-3

[30] Türk Stardartları Enstitüsü. (2019). *Beton - Sertleşmiş beton deneyleri - Bölüm 5: Deney numunelerinin eğilme dayanımının tayini, Ankara, Türkiye*. TS EN 12390-5.

[31] Türk Stardartları Enstitüsü. (2019). *Beton - Sertleşmiş beton deneyleri - Bölüm 6: Deney numunelerinin yarmada çekme dayanımının tayini, Ankara, Türkiye*. TS EN 12390-6.

[32] China Standard Press. (2009). *Standard for test method of long-term performance and durability of ordinary concrete, Beijing, China*. GB/T 50082-2009.

[33] Yang, J., Guo, Y., Tam, V. W., Shen, A., Qin, X., Tan, J., Zhang, J. & Zhang, C. (2024). Research on the purification efficiency and mechanism for road runoff pollutants in pervious concrete with recycled aggregates. *J Environ Manag, 353*, 120180. [CrossRef]

[34] Nazeer, M., Kapoor, K., & Singh, S. P. (2023). Impact of recycled concrete aggregates on the strength and durability properties of pervious concrete. *Mag Concr Res, 76*(6), 1-20. [CrossRef]

[35] Li, J., Chen, L. L., Wang, Z. F., & Wang, Y. Q. (2023). Effect of modification and replacement rate of recycled coarse aggregate on properties of recycled aggregate concrete. *Iran J Sci Technol, 47*(6), 3321-3332. [CrossRef]

[36] Malayali, A. B., Chokkalingam, R. B., & Muthukannan, M. (2022). Strength properties of geopolymer concrete modified with recycled aggregates. *Iran J Sci Technol, 46*(1), 77-89. [CrossRef]

[37] Zhang, J., Sun, H., Shui, X., & Chen, W. (2023). Experimental investigation on the properties of sustainable pervious concrete with different aggregate gradation. *Int J Concr Struct Mater, 17*(1), 64. [CrossRef]

[38] El-Hassan, H., Kianmehr, P., Tavakoli, D., El-Mir, A., & Dehkordi, R. S. (2023). Synergic effect of recycled aggregates, waste glass, and slag on the properties of pervious concrete. *Dev Built Environ, 15*, 100189. [CrossRef]

[39] Tuan, N. K., Minh, P. Q., Giang, N. H., Dung, N. T., & Kawamoto, K. (2023). Porosity and permeability of pervious concrete using construction and demolition waste in Vietnam. *Geomate J, 24*(101), 12-21. [CrossRef]

[40] Lyu, Q., Dai, P., & Chen, A. (2024). Correlations among physical properties of pervious concrete with different aggregate sizes and mix proportions. *Road Mater Pave Des, 25*(12), 2747-71. [CrossRef]

[41] Liu, H. B., Li, W. J., Yu, H., Luo, G. B., & Wei, H. B. (2019). *Mechanical properties and freeze-thaw durability of recycled aggregate pervious concrete*. In IOP Conference Series: Materials Science and Engineering (Vol. 634, No. 1, p. 012011). IOP Publishing. [CrossRef]

[42] Wu, R., Shi, S., Shen, Y., Hu, C., Luo, M., Gan, Z., Xiao B, & Wang, Z. (2022). Effects of different factors on the performance of recycled aggregate permeable pavement concrete. *Materials, 15*(13), 4566. [CrossRef]

[43] Yan, K., Li, G., You, L., Zhou, Y., & Wu, S. (2020). Performance assessments of open-graded cement stabilized macadam containing recycled aggregate. *Constr Build Mater, 233*, 117326. [CrossRef]